

Universidad Autónoma de Madrid  
Departamento de Física Teórica

Uniformity of the Electromagnetic  
End-Cap Calorimeter of ATLAS

**Ph.D. Thesis**  
**Concepción Celia Oliver Amorós**

**Supervisor: Prof. José del Peso**

“Als meus pares,  
a mon germà i a Natalia.”



## Agradecimientos

No quiero dejar pasar esta oportunidad que me brinda la tesis para agradecer a todas las personas que me han ayudado y apoyado durante todo este tiempo.

Gran parte de este trabajo es debida a la dedicación y a la ayuda que me ha prestado en todo momento mi director de tesis, José del Peso. Desde el primer día ha sabido orientarme y aconsejarme en cada paso del análisis.

A Fernando Barreiro le debo mi estancia en este grupo de la Autónoma. Siempre he agradecido su buena acogida, las agradables conversaciones y su ayuda en todo momento.

De Luis Labarga admiro su pasión por el trabajo bien realizado, su visión analítica de la física, sus sabios consejos.

No puedo dejar de mencionar al resto del grupo de Altas Energías de la Autónoma: a Juan, Claudia, Manuel, Marcos, y a los últimos en llegar, Carolina y Eduardo. Un especial recuerdo a los que se fueron, Juan Pablo, Juan, Rafa y Matti, quien tanto me ayudó.

Dentro de nuestro grupo y en el laboratorio, se encuentran las personas que más me han animado, apoyado y han sabido ser antes amigos que compañeros de trabajo. No puedo olvidar los buenos momentos vividos, las risas, las cenas juntos. De Pachi admiro su amplitud de conocimientos, su disponibilidad para ayudarme en cualquier momento y sobre cualquier tema. Jorge ha sido un gran amigo para todo, siempre con buenos consejos. A Stephane le agradezco su ayuda en el análisis, pero sobre todo le agradezco el transmitirme su vitalidad. Hay tantas cosas que agradecer a Juanjo, desde su ayuda en el mundo de la informática a las numerosas horas que ha pasado escuchándome.

Si hay algo en la vida de lo que me siento orgullosa, es de la familia que tengo. Son ellos los que me motivan a seguir adelante y a los que debo y dedico todo reto que consiga en la vida. Por mis padres siento una profunda admiración, por su fe en mí, su dedicación absoluta, su incondicional ayuda. De ellos he aprendido a valorar la importancia de las cosas, el esfuerzo por luchar por los sueños. Mi hermano y Natalia me han apoyado en los buenos y malos momentos, confiando siempre en mí. A Mostar, por todos los días y noches a mi lado estudiando. Un especial recuerdo al resto de mi familia, a mis abuelos

(aunque ya no todos están), a mis tíos, a mis primos, a los que nunca olvido.

Mi total agradecimiento a la gente de Hondón de los Frailes que tanto me ha ayudado. Una mención especial se merecen mis amigos, por su gran calidad humana, su eterna e incondicional amistad, su apoyo en la distancia.

Por último agradezco a todas las personas (compañeros de carrera, de piso, amigos de Madrid, ...) que a su manera han estado presentes durante esta etapa de mi vida.

## Introduction

One of the main events in the field of particle physics at the beginning of this century will be the operation of the Large Hadron Collider (LHC), in 2007. This is installed into the existing Large Electron Positron (LEP) tunnel at the CERN laboratory across the Franco-Swiss border west of Geneva.

The LHC machine and the four planned experiments have been designed to study the extrapolation of the present knowledge in particle physics to the LHC energy scale and to detect the signatures of a new and possibly unexpected physics above the TeV energy threshold. The Standard Model (SM) describes very well the results of present experiments, nevertheless some fundamental questions remain still unanswered. The most important of them is probably the origin of the mass of the Z and W vector bosons of the electroweak interactions. The most accredited explanation is the existence of a Higgs field. One of the main goals of LHC is the discovery of the associated gauge boson, the Higgs particle. The experiments are designed to cover the different physics signatures of the Higgs, consisting in the identification of the predicted decay modes, with statistical significance over all the mass range. The detail studies on Yukawa couplings between the Higgs boson(s) and various fermions will give insights to the origin of mass. Other important topics in LHC are top-quark physics, CP-violation in the B-sector, possible signals of the formation of the quark-gluon plasma (QGP) and search for supersymmetric particles.

One of the four experiments of LHC, ATLAS, is a multipurpose detector which has a wide physics program, spanning from precision measurement of  $W^\pm$  bosons, top and bottom quark properties, to Higgs boson or supersymmetric particle searches. In most cases, the electromagnetic calorimeter of ATLAS will play a key role in measuring energy, position and time of electrons and photons.

The ATLAS electromagnetic calorimeter is a lead-liquid Argon (LAr) sampling calorimeter with an accordion geometry, that guarantees a full azimuthal average. This is composed by three sub-detectors, one barrel and two end-caps, each segmented in depth in three sampling compartments (front, middle, back) and with a fine granularity in  $\eta$  and  $\phi$  directions. Calorimeter prototype and production modules have been tested under electron beams at CERN during the last five years. An uniformity better than 0.6% is required in order to keep the global constant term of the energy resolution lower than 0.7%. In this thesis, the results of the test beams are presented and compared to ATLAS requirements. It is organized as follows.

Chapter 1 is meant as a theoretical introduction about particle physics and a general description of the LHC. A more detailed review of the multipurpose experiment ATLAS is also given.

Chapter 2 summarizes the basic principles of particle detection, necessary in order to understand the behaviour of the electromagnetic calorimeter.

A detailed description of the electromagnetic end-cap calorimeter of ATLAS (geometry and readout electronics) is given in chapter 3. The construction and quality control of the calorimeter module are discussed.

Chapter 4, in the first place, describes the testbeam facilities and the modeling of the detector response. The ATLAS liquid Argon electromagnetic calorimeter uses a digital filtering technique to reconstruct the signal amplitude from the ionization pulse sampling. The digital filtering coefficients computation requires the knowledge of the ionization pulse profile in each cell. The current work is based upon the method developed in [70] in which an algorithm is proposed to predict the shape of the physics pulses from the calibration pulses so the optimal filtering coefficients can be computed. The method makes up of the fact that most of the signal path is the same for calibration and physics pulses and can therefore be factorized.

After that, the uniformity analysis framework is defined and corrections to electron energy for high voltage, lateral leakage,  $\phi$ -modulation and  $\phi$ -asymmetry effects are analysed. Finally, results on the outer wheel response uniformity are given.

The dependence of the uniformity on the signal reconstruction method is shown in chapter 5. In this chapter, we describe three additional methods, which use time convolution to predict the physics pulse shape, starting from the calibration pulse shape, in order to compute the optimal filtering coefficients to reconstruct energy and time for electromagnetic cells of the liquid Argon electromagnetic end-cap calorimeter. The first one uses a simple description of readout electronics, while the second and third methods take into account some effects, like reflections in the cables. The effects of the signal reconstruction method on response uniformity are also shown.

Finally, conclusions are given in chapter 6.

# Contents

<b>1</b>	<b>The LHC and the ATLAS project</b>	<b>23</b>
1.1	Introduction . . . . .	23
1.1.1	The Standard Model . . . . .	23
1.1.2	Spontaneous symmetry breaking . . . . .	25
1.1.3	Higgs mechanism . . . . .	27
1.1.4	Higgs properties . . . . .	30
1.1.5	Successes and failures of Standard Model . . . . .	32
1.2	The LHC . . . . .	33
1.2.1	LHC physics . . . . .	38
1.2.2	Physics requirements . . . . .	40
1.3	The ATLAS detector . . . . .	41
1.3.1	Detector requirements . . . . .	43
1.3.2	General description . . . . .	43
1.3.3	The inner detector . . . . .	44
1.3.4	Calorimetry . . . . .	49
1.3.5	The muon spectrometer . . . . .	54
1.3.6	The magnet system . . . . .	56
1.3.7	Trigger and data acquisition . . . . .	58



<b>2</b>	<b>Principles of calorimetry</b>	<b>61</b>
2.1	Introduction . . . . .	61
2.2	Energy loss of charged particles . . . . .	61
2.2.1	Energy loss due to ionization . . . . .	62
2.2.2	Energy loss by radiation: Bremsstrahlung . . . . .	65
2.2.3	Critical energy . . . . .	68
2.2.4	Energy Straggling: the energy loss distribution . . . . .	68
2.3	Scattering of charged particles . . . . .	71
2.3.1	Rutherford Scattering . . . . .	71
2.3.2	Multiple Scattering . . . . .	72
2.4	Interactions of photons with matter . . . . .	73
2.4.1	The photoelectric effect . . . . .	73
2.4.2	Compton scattering . . . . .	73
2.4.3	Pair creation . . . . .	75
2.4.4	Absorption coefficient . . . . .	77
2.5	Electromagnetic showers . . . . .	78
2.6	Hadronic showers . . . . .	80
2.7	Calorimeters . . . . .	81
<b>3</b>	<b>The EMEC of ATLAS</b>	<b>87</b>
3.1	Introduction . . . . .	87
3.2	EMEC description . . . . .	89
3.2.1	High voltage law varying by step . . . . .	95
3.2.2	Energy resolution . . . . .	100
3.3	Mechanical components of EMEC . . . . .	102
3.3.1	The absorbers . . . . .	102

3.3.2	The electrodes . . . . .	110
3.3.3	The honeycomb spacers . . . . .	114
3.4	The electronics . . . . .	114
3.4.1	The cold electronics . . . . .	115
3.4.2	The warm electronics . . . . .	116
3.5	Changes since pre-production module . . . . .	124
3.6	Module assembly . . . . .	124
3.7	Tests for modules validation . . . . .	126
3.7.1	Sagging measurements . . . . .	130
3.7.2	Electrical tests . . . . .	131
<b>4</b>	<b>Uniformity studies</b>	<b>141</b>
4.1	Test beam . . . . .	142
4.1.1	Test beam setup . . . . .	142
4.1.2	Test beam data . . . . .	143
4.2	Calorimeter response . . . . .	145
4.3	Signal reconstruction . . . . .	147
4.3.1	Reconstruction of the signal amplitude . . . . .	147
4.3.2	Prediction of physics pulse . . . . .	151
4.3.3	The LAPP method . . . . .	156
4.3.4	Electronics calibration . . . . .	159
4.3.5	Cluster energy . . . . .	160
4.4	Uniformity analysis framework . . . . .	163
4.5	Electron energy corrections . . . . .	165
4.5.1	High Voltage correction . . . . .	166
4.5.2	Capacitance correction . . . . .	172

4.5.3	Lateral leakage correction . . . . .	183
4.5.4	$\phi$ -modulation correction . . . . .	185
4.6	Uniformity results . . . . .	188
<b>5</b>	<b>Dependence on signal reconstruction</b>	<b>193</b>
5.1	Method Hec . . . . .	195
5.2	Method Hecref . . . . .	197
5.3	Method Hecref $2\omega$ . . . . .	201
5.4	Several modifications . . . . .	201
5.5	TDC dependence of the cluster energy . . . . .	203
5.6	Uniformity dependence . . . . .	205
<b>6</b>	<b>Conclusions</b>	<b>207</b>
<b>A</b>	<b>Calculation of parameter <math>\alpha</math></b>	<b>209</b>
<b>B</b>	<b>Resumen en español</b>	<b>211</b>
B.1	LHC y el proyecto ATLAS . . . . .	211
B.1.1	Introducción . . . . .	211
B.1.2	El LHC . . . . .	212
B.1.3	El detector ATLAS . . . . .	213
B.2	Principios de detección de partículas . . . . .	214
B.2.1	Introducción . . . . .	214
B.2.2	Energía perdida por los partículas cargadas . . . . .	214
B.2.3	Dispersión de partículas cargadas . . . . .	215
B.2.4	Interacciones de los fotones con la materia . . . . .	215
B.2.5	Cascadas electromagnéticas . . . . .	216
B.2.6	Cascadas hadrónicas . . . . .	216

B.3	Calorímetro electromagnético de ATLAS . . . . .	216
B.3.1	Descripción del módulo . . . . .	216
B.3.2	Componentes mecánicos . . . . .	217
B.3.3	Montaje de los módulos . . . . .	218
B.3.4	La electrónica . . . . .	218
B.3.5	Pruebas de validación de los módulos . . . . .	219
B.4	Estudios de la uniformidad . . . . .	220
B.4.1	Pruebas con el haz . . . . .	220
B.4.2	Reconstrucción de la señal . . . . .	220
B.4.3	Análisis de la uniformidad . . . . .	221
B.4.4	Correcciones de la energía del electrón . . . . .	222
B.4.5	Resultados de la uniformidad . . . . .	223
B.5	Dependencia con la reconstrucción de la señal . . . . .	224
B.5.1	Diversos métodos . . . . .	224
B.5.2	Dependencia del TDC . . . . .	225
B.5.3	Dependencia de la uniformidad con la reconstrucción de la señal . . . . .	225
B.6	Conclusiones . . . . .	225



# List of Figures

1.1	Elementary particles in the Standard Model . . . . .	25
1.2	Higgs boson production mechanisms: (a) gluon fusion, (b) vector boson fusion, (c) associated production with a gauge boson, (d) production with a top quark and (e) corresponding production cross-section calculated with NLO corrections. . . . .	31
1.3	Branching ratios of the Higgs boson decays. . . . .	31
1.4	$pp$ cross-section as a function of center of mass energy. . . . .	35
1.5	Accelerators complex at CERN. . . . .	36
1.6	A view of the LHC project. . . . .	38
1.7	ATLAS detector. . . . .	42
1.8	Characteristic signal of different particles in the ATLAS detector. . . . .	44
1.9	The inner detector of ATLAS. . . . .	45
1.10	The pixel detector of ATLAS. . . . .	47
1.11	A barrel module of SCT tracker. . . . .	48
1.12	The transition radiation tracker of ATLAS. . . . .	49
1.13	A three dimensional view of the ATLAS calorimetry. . . . .	50
1.14	End-cap of the electromagnetic calorimeter. . . . .	51
1.15	The principle of the Tile Calorimeter design. . . . .	52
1.16	Hadronic end-cap module. . . . .	53
1.17	The muon spectrometer. . . . .	55

1.18	A MDT module. . . . .	56
1.19	The central solenoid magnet. . . . .	57
1.20	The end-cap toroidal magnet. . . . .	58
1.21	The ATLAS trigger system. . . . .	60
2.1	Ionization energy loss per unit of length in liquid hydrogen, gaseous helium, carbon, iron and lead. . . . .	64
2.2	Feynman diagram for bremsstrahlung. . . . .	66
2.3	Energy loss per unit of length as a function of the energy. . . . .	69
2.4	Critical energy as a function of $Z$ . . . . .	69
2.5	Photons cross-sections on carbon and lead. . . . .	74
2.6	The photoelectric effect. . . . .	75
2.7	Compton scattering. . . . .	76
2.8	Feynman diagrams for pair creation. . . . .	77
2.9	An electromagnetic shower. . . . .	78
2.10	Longitudinal development of electromagnetic shower. . . . .	80
2.11	An hadronic shower. . . . .	81
2.12	Energy deposit of pions as a function of calorimeter depth. . . . .	82
3.1	Photograph of a barrel module. . . . .	89
3.2	Representation of an electromagnetic end-cap calorimeter. . . . .	90
3.3	Front side photograph of the stacked module ECC1. . . . .	91
3.4	A schematic view of a gap electrode-absorber. . . . .	92
3.5	At the top, sketch of accordion absorbers with a simplified geometry. At the bottom, sketch of the end-cap from the front sight. . . . .	93
3.6	The production of the signal inside the calorimeter. . . . .	95
3.7	End-cap longitudinal section for different radii. . . . .	98
3.8	Liquid Argon gap versus radius. . . . .	99

3.9 High voltage variation along  $\eta$  for a uniform calorimeter response (open circles) together with the solution adopted in practice (solid triangles). . . . . 99

3.10 Outer and inner wheel flat electrode schematic views. Sampling regions are represented as well as high voltage sectors. High voltage values are indicated for each sector at liquid Argon temperature. . . . . 100

3.11 From top to bottom, lead plate thickness measured with X-ray techniques, with ultrasound techniques and comparison between both. . . . . 104

3.12 Thickness mean and RMS of the large lead plates used in module 0, module 2 (ECC1) and for 15 modules. . . . . 105

3.13 Presses used to bend large and small absorbers into accordion geometry. . . . . 106

3.14 Illustrating the bending process for large absorbers. . . . . 107

3.15 Mould with pre-glued absorber. . . . . 107

3.16 Mould in a vacuum bag before entering the autoclave which is shown open. . . . . 108

3.17 Precision 3D measuring table. . . . . 108

3.18 Thickness distribution measured at the acute (obtuse) side on the left (resp. right) hand side for all the outer absorbers produced for, from top to bottom, module 0, module 2 (ECC1) and for 15 modules. . . . . 109

3.19 A picture of an electrode, right hand side, and an illustration of its internal structure, left hand side. . . . . 110

3.20 Electrodes are bent fold by fold. A machined knife (top) push the electrode against a foam block (bottom). . . . . 111

3.21 Segmentation of the outer wheel of an EMEC module. The blue region corresponds to the cluster central cells considered for the analysis of the fourth chapter of this thesis. . . . . 112

3.22 Photograph of a D honeycomb spacer. . . . . 115

3.23 Photograph of an R honeycomb spacer. . . . . 116

3.24 Photograph of a HV board. . . . . 119

3.25 Photograph of summing boards. . . . . 120

3.26 Front (back) side of a stacked module with all HV and SB cards plugged in, on the top (resp. bottom). . . . . 121



3.27	A picture of a mother board. . . . .	122
3.28	Schematic of the calorimeter readout. . . . .	123
3.29	Structure elements bolted to the stacking frame (back side). . . . .	125
3.30	Picture of the high voltage test bench for outer wheel spacers. . . . .	126
3.31	View of a fully stacked module with all HV, SB and MB cards plugged in (top) and cabled (bottom). . . . .	127
3.32	ECC wheel assembly at CERN. . . . .	128
3.33	ECC wheel. . . . .	129
3.34	Sagitta measurements for absorber 36 in ECC1, as a function of wave number at four pseudorapidity values, left hand side. Sagitta measurements as a function of absorber number for two central pseudorapidity values, right hand side. . . . .	131
3.35	High voltage test bench, left hand side. Evolution with time of the current drawn in sector three when 1300 V is applied, right hand side. . . . .	132
3.36	Input (full circles) and output (open circles) TBF signal shapes, for a front side outer (inner) wheel channel, left (resp. right) hand side. . . . .	134
3.37	Capacitance measurements for the first six modules stacked at UAM. . . . .	135
3.38	Distribution of the kapton capacitance relative dispersion for the six modules stacked so far at UAM. . . . .	136
3.39	Capacitance measurements for TBF channel 17 as a function of azimuthal angle, for a given back cell. The solid line represents the result of a straight line fit. . . . .	137
3.40	Gap capacitances $C$ versus gap number for the outer wheel regions of the module ECC5. . . . .	138
4.1	Schematic view of the H6 beam line instrumentation. Scintillators are labeled $S$ and beam chambers $BC$ . . . . .	143
4.2	Beam profiles in the horizontal $x$ and vertical $y$ directions for two chambers located far (left hand side) and near (right hand side) the front face of the detector. The $x$ and $y$ coordinates are in the plane orthogonal to the beam direction: $x$ corresponds to $\eta$ and $y$ corresponds to $\phi$ direction. . . . .	144
4.3	Schematic view of the calorimeter readout electronics (taken from [51]). . . . .	146

- 4.4 Typical physics pulses (left) and calibration pulses (right) for front, middle and back cells. . . . . 148
- 4.5 The triangle shape corresponds to the signal as a function of time just after electrode and the bell shape to the signal after crossing the shaper. Dots represent the recorded amplitudes separated by 25 ns. . . . . 152
- 4.6 Bias between calibration and physics pulse amplitudes versus  $\eta$  for the outer wheel middle cells of the three tested modules. All points are averaged over  $\phi$ . . . . . 155
- 4.7 Bias between calibration and physics pulse amplitudes versus  $\eta$  for the outer wheel middle cells of the three tested modules. All points are averaged over  $\phi$ . . . . . 156
- 4.8 Comparison between predicted (red dotted line) and measured (dark solid line) physics pulses for 120 GeV electrons at the ECC1 beam test. . . . . 158
- 4.9 Averaged energy per cell of the front sampling (left) and the middle sampling (right). . . . . 161
- 4.10 Averaged energy per cell of the back sampling. . . . . 162
- 4.11 Distribution of the signal after all corrections and cuts have been applied. The Gaussian fit is also shown as a red line. . . . . 163
- 4.12 Segmentation of the outer wheel of an EMEC module. The blue region corresponds to the cluster central cells considered for this analysis. . . . . 165
- 4.13 The open circles represent the continuously varying high voltage value needed for the response to be constant over  $\eta$ . The black triangles represent the nominal values applied in different sectors in  $\eta$ . . . . . 167
- 4.14 First (left) and second (right) step of the high voltage correction, using the method of the independent sectors. Energy (GeV) as a function of  $\eta$ , for  $\phi_{cell} = 16$ , without corrections (left) and corrected with the weights  $w_{a_1}^{(s)}(\eta_j)$  (right). The blue line is the result of a linear fit. . . . . 168
- 4.15 Left: energy (GeV) without corrections (black dots) as a function of  $\eta$ , for a given  $\phi$  ( $\phi_{cell} = 22$ ) and the outcome of adding the constants  $k^{(s)}$  to the energy (blue dots). Right: energy (GeV) without corrections with the addition of the  $k^{(s)}$  parameters (blue dots) as a function of  $\eta$  for  $\phi_{cell} = 22$ . The solid line represents the fit to the curve  $a_1 + a_2 \eta^{a_3}$ . . . . . 170

- 4.16 Left: energy (GeV) obtained from the fit to a curve  $a_1 + a_2 \eta^{a_3}$  and where the parameters  $k^{(s)}$  have been subtracted (blue dots), as a function of  $\eta$ , for  $\phi_{cell} = 22$ . The initial energy without corrections is shown as black dots. Right: energy (GeV) after the fit to a  $a_1 + a_2 \eta^{a_3}$  curve and after the subtraction of the  $k^{(s)}$  parameters (blue dots), as a function of  $\eta$ , for  $\phi_{cell} = 22$ . The solid line represents the result of a linear fit. . . . . 170
- 4.17 Left: energy corrected with the weights  $w_{a_2}^{(s)}(\eta_j)$  (black dots) and energy corrected with  $w_{a_2}^{(s)}(\eta_j)$  after adding the constants  $k^{(s)}$  (blue dots), as a function of  $\eta$ , for  $\phi_{cell} = 22$ . Right: energy corrected with  $w_{a_2}^{(s)}(\eta_j)$  after adding the constants  $k^{(s)}$  (blue dots), as a function of  $\eta$ , for  $\phi_{cell} = 22$ . The solid line represents the fit to a  $a'_1 + a'_2 \eta^{a'_3}$  curve. . . . . 171
- 4.18 Left: energy (GeV) obtained from the fit to a curve  $a'_1 + a'_2 (\eta)^{a'_3}$  and where the parameters  $k^{(s)}$  have been subtracted (blue dots) as a function of  $\eta$ , for  $\phi_{cell} = 22$ . Black dots are the initial energy corrected by  $w_{a_2}^{(s)}(\eta_j)$ . Right: energy (GeV) after the fit to a  $a'_1 + a'_2 (\eta)^{a'_3}$  curve and after the subtraction of the  $k^{(s)}$  parameters, as a function of  $\eta$ , for  $\phi_{cell} = 22$ . The solid line represents the result of a linear fit. . . . . 172
- 4.19 Parameters  $\alpha^{(s)}$  versus  $\phi_{cell}$  and versus module. . . . . 173
- 4.20 Parameters  $\beta^{(s)}$  versus  $\phi_{cell}$  and versus module. . . . . 174
- 4.21 Mean values of the parameters  $\alpha^{(s)}$  and  $\beta^{(s)}$  versus HV sector  $s$  and versus module. . . . . 175
- 4.22  $\alpha$  parameter distribution over all  $\phi$  values of the six HV zones studied, and for the three tested modules. . . . . 176
- 4.23 Variation along the  $\phi$  direction of the ECC0 energy measured in beam test for a cell with a fixed value of  $\eta = 1.8875$  (red circles) and capacitance measured at the stacking frame for this  $\eta$  (blue stars). The capacitance values have been multiplied by a factor in order to make easy the comparison between the energy and capacitance measurements, so the units of  $C$  are arbitrary. There is a good correlation between the cluster energy and capacitance measured at the stacking frame for each middle cell. . . . . 177

4.24	Measurement results of the middle cell capacitance non-uniformity along $\phi$ for the ATLAS EMEC modules, at the stacking site. All capacitance measurements were performed at the middle cell level, on the summing boards, except for ECC5, whose measurements were performed at the gap level, on the electrodes. Five modules have not been measured. Only the relative variation with respect to the mean value is plotted. The dispersion is given for each module. . . . .	180
4.25	Capacitance measurements (in $pF$ ) performed at the ECA wheel for several $\eta_{cell}$ . A correlation between the measurements is observed. . . . .	181
4.26	Capacitance measured at $\eta_{cell} = 39$ for ECC1 (in middle cell units corresponds to $\eta = 2.3875$ ) on the wheel. At $\phi_{cell} = 24$ there is a step decrease due to a change in the grounding of the capacimeter used for the measurements. . . . .	181
4.27	Capacitance measured at $\eta_{cell} = 39$ (in middle cell units corresponds to $\eta = 2.3875$ ) for ECC0 on the wheel (red circles) and on the stacking frame (blue stars). . . . .	182
4.28	Response signal of the network analyzer as a function of the input frequency. The minimum of the output function is obtained when the frequency equals $\frac{1}{\sqrt{LC}}$ of the cell. . . . .	183
4.29	Cluster energy versus $\eta$ incident position of the beam on cell 14 (middle cell units). . . . .	184
4.30	Parameter $K$ of the lateral leakage correction, averaged over $\phi$ , as a function of $\eta$ , for ECC0, ECC1 and ECC5 modules. Its $\eta$ dependence (averaged over $\phi$ and over modules) has been parametrized by a line $K = p_0 + p_1\eta$ , being $p_0 = 68.3 \pm 7.6$ and $p_1 = -59.6 \pm 4.0$ . . . . .	185
4.31	Photograph of an electrode sandwiched between two consecutive absorbers thanks to the spacers. . . . .	186
4.32	Cluster energy versus $\phi$ for $\eta = 1.5625$ (left) and $\eta = 2.2125$ (right). The quantity $\phi_{abs}$ is in units of the thickness between two consecutive absorbers. The solid line represents the results of a fit to a Fourier polynomial. . . . .	188
4.33	$\phi$ -mean coefficient $a_1, a_2, b_1$ and $\phi_0$ of $\phi$ -modulation versus $\eta_{cell}$ and versus module. The dependence on $\eta$ is fitted to polynomials, whose parameter values are in table 4.6. . . . .	189
4.34	Distribution of the mean cluster energy for ECC0, ECC1 and ECC5. . . . .	190
5.1	Drift time $\tau_d$ dependence on $\eta_{cell}$ for front, middle and back cells. . . . .	197

5.2	Comparison of frequency (GHz) obtained from a fit to test beam data using Hec method (red circles) and direct measurements (blue stars), for a given $\phi_{cell}$ middle cell, as a function of $\eta_{cell}$ . The measurements were performed on the ECC wheel using a network analyzer device. . . . .	198
5.3	Comparison between predicted pulse using the Hec method (red line) and measured physics pulse (dark line), both in GeV, for 120 GeV electrons of the ECC1 beam test, for a middle cell ( $\eta_{cell} = 28$ and $\phi_{cell} = 19$ ). . . . .	198
5.4	Residual $r^{(i)}$ of middle cells for the three signal reconstruction methods Hec (black full line), Hecref (red dashed line) and Hecref2 $\omega$ (blue dotted line). . . . .	199
5.5	Comparison of frequency (GHz) obtained from a fit to test beam data using Hecref method (red circles) and direct measurements (blue stars), for a given $\phi_{cell}$ middle cell, as a function of $\eta_{cell}$ . The measurements were performed on the ECC wheel using a network analyzer device. . . . .	200
5.6	Comparison between predicted pulse using the Hecref method (red line) and measured physics pulse (dark line), both in GeV, for 120 GeV electrons of the ECC1 beam test, for a middle cell ( $\eta_{cell} = 28$ and $\phi_{cell} = 19$ ). . . . .	200
5.7	Comparison between predicted pulse using the Hecref2 $\omega$ method (red line) and measured physics pulse (dark line), both in GeV, for 120 GeV electrons of the ECC1 beam test, for a middle cell ( $\eta_{cell} = 28$ and $\phi_{cell} = 19$ ). . . . .	202
5.8	Cluster energy as a function of the TDC time using signal reconstruction method Hec (left) and method Hecref (right). The red line represents a parabolic fit. . . . .	204
5.9	Cluster energy as a function of the TDC time using signal reconstruction method Hecref2 $\omega$ (left) and method LAPP (right). The red line represents a parabolic fit. . . . .	205
5.10	Cluster energy as a function of the TDC time using signal reconstruction method of parabola. . . . .	206
A.1	Description of the parameters used for the calculation of $\alpha$ : front (left picture) and profile (right picture) view of the wheel. . . . .	210

# List of Tables

1.1	Fundamental fermions in the Standard Model [2]. . . . .	24
1.2	Gauge bosons in the Standard Model [2]. . . . .	25
1.3	LHC parameters. . . . .	35
1.4	Transverse granularity ( $\Delta\eta, \Delta\phi$ ) of the Electromagnetic Calorimeter in $\eta$ . . . . .	51
1.5	Transverse granularity ( $\Delta\eta, \Delta\phi$ ) of the hadronic calorimeter. . . . .	53
2.1	Critical energy and radiation length for different materials. . . . .	70
3.1	The seven high voltage region chosen in the outer wheel. . . . .	97
3.2	Contributions to the constant term of the energy resolution. . . . .	101
3.3	Transverse granularity ( $\Delta\eta, \Delta\phi$ ) of the EMEC in pseudorapidity. . . . .	113
3.4	Characteristics of the different types of HV boards. . . . .	117
3.5	Characteristics of the different types of summing boards. . . . .	118
3.6	High voltage settings for the test of the spacers. . . . .	125
3.7	High voltage settings for the HV tests. . . . .	133
4.1	Cluster size $\Delta\phi \times \Delta\eta$ as a function of the region in $\eta$ . For the front sampling two cells along $\phi$ are taken when the beam is incident near the boundary between two cells. . . . .	162
4.2	Number of cluster central cells kept for the uniformity analysis. . . . .	166
4.3	RMS of the deviation of $\eta$ scan energy from the mean value, integrated over all $\phi$ , using several high voltage correction methods. . . . .	175

4.4	Mean values of the high voltage correction parameters $\alpha^{(s)}$ and $\beta^{(s)}$ for several high voltage sectors averaged over the three tested modules. . . . .	175
4.5	$C$ measurements performed for the three beam-tested modules. For ECC0 the measurements at the stacking frame were done on the summing boards connectors, while for ECC5 module were measured at the gap level combining several sectors in $\eta$ . The measurements at the wheel were done on the mother boards connectors. All measurements correspond to cells of the middle layer. . . . .	180
4.6	Parameters of the $\phi$ -modulation correction. We have fitted the average value of the three modules ECC0, ECC1, and ECC5 to a polynomial, whose degree depends on the $\eta$ region. . . . .	187
4.7	Deviation from uniformity for the three modules analyzed. . . . .	190
4.8	Deviation from uniformity for the three modules analyzed. The $\eta$ region is restricted to 8-35 in middle cell units and the gap to gap fluctuations is corrected using the test beam data. . . . .	191
4.9	Deviation from uniformity for ECC0 and ECC1. The $\phi$ -asymmetry is corrected using capacitance measured at stacking frame for ECC0 and test beam data for ECC1 in the first row and using capacitance measured in the wheel in the second row. . . . .	191
5.1	Deviation from horizontal of TDC dependence of the cluster energy for the different signal reconstruction methods. For the parabola method only 75 ns around the signal maximum are used to obtain $r_{max}$ . For the OF-based methods the whole range, 125 ns, is used to obtain $r_{max}$ . . . . .	204
5.2	Deviation from uniformity for ECC1 as a function of the signal reconstructed method. . . . .	206

# Chapter 1

## The LHC and the ATLAS project

### 1.1 Introduction

#### 1.1.1 The Standard Model

The Standard Model [1] of particle physics is a quantum field theory, based on the gauge symmetry  $SU(3)_C \times SU(2)_L \times U(1)_Y$ , which describes the strong, weak and electromagnetic fundamental forces, as well as the fundamental particles that make up all matter. This gauge group includes the symmetry group of the strong interactions  $SU(3)_C$  and the symmetry group of the electroweak interactions,  $SU(2)_L \times U(1)_Y$ . The symmetry group of the electromagnetic interactions  $U(1)_{em}$  appears in the SM as a subgroup of the  $SU(2)_L \times U(1)_Y$  and it is in this sense that the weak and electromagnetic interactions are said to be unified. The gravitation interaction is not included in the Standard Model.

The Standard Model contains both fermionic and bosonic fundamental particles. Fermions are particles with half-integer spin which form totally-antisymmetric composite quantum states. As a result, they are subject to the Pauli exclusion principle, which states that no fermions can share the same quantum state, and obey Fermi-Dirac statistics. Bosons are particles which form totally-symmetric composite quantum states. They obey Bose-Einstein statistics and they have integer spin. Because bosons do not obey the Pauli exclusion principle, it is much harder to form stable structures with bosons than with fermions and, therefore, all ordinary matter is constituted by fermions.

The fermions are classified into leptons and quarks. The known leptons are the electron  $e^-$ , the muon  $\mu^-$  and the  $\tau^-$  with electric charge  $Q = -1$  (all charges are given in units of the elementary charge  $e$ ) and the corresponding neutrinos  $\nu_e$ ,  $\nu_\mu$  and  $\nu_\tau$  with  $Q = 0$ . Their interactions (weak and electromagnetic) fall off rapidly with distance. The known quarks



are of six different flavors:  $u, d, s, c, b$  and  $t$  and have fractional charge  $Q = \frac{2}{3}, -\frac{1}{3}, -\frac{1}{3}, \frac{2}{3}, -\frac{1}{3}$  and  $\frac{2}{3}$  respectively. The quarks have an additional quantum number, the colour, which can be of three types, generally denoted as  $q_i, i = 1, 2, 3$ . The strong force between quarks gets stronger with distance, so that they are always found in colourless combinations called hadrons. These colourless composite particles are classified into baryons and mesons. The baryons are fermions made of three quarks,  $qqq$ , and the mesons are made of one quark and one antiquark,  $q\bar{q}$ . The mass of such aggregates exceeds that of the components due to their bending energy.

The fundamental fermions in the Standard Model are given in the table 1.1 [2].

Family	Quarks	Mass (GeV)	Q ( $q_e$ )	Leptons	Mass (MeV)	Q ( $q_e$ )
1	d	0.003-0.007	-1/3	e	$0.51099892 \pm 0.00000004$	-1
	u	0.0015-0.0030	+2/3	$\nu_e$	< 0.002	0
2	s	$0.095 \pm 0.025$	-1/3	$\mu$	$105.658369 \pm 0.000009$	-1
	c	$1.25 \pm 0.09$	+2/3	$\nu_\mu$	< 0.19	0
3	b	$4.20 \pm 0.07$	-1/3	$\tau$	$1776.99 \pm 0.28$	-1
	t	$174.2 \pm 3.3$	+2/3	$\nu_\tau$	< 18.2	0

Table 1.1: Fundamental fermions in the Standard Model [2].

The fermions can be arranged in three families (see figure 1.1) with identical properties except for mass. The first one is consisting of the electron, electron neutrino, and the up and down quarks. All ordinary matter is made from first generation particles; the higher generation particles decay quickly into the first generation ones and can only be generated for a short time in high-energy experiments. Experimental results, as the analysis of Z partial decay in hadrons, leptons and neutrinos in LEP1 ([3], [4]) have showed there are three families and no more.

A gauge theory means that it models the forces between fermions by coupling them to bosons. The Lagrangian of each set of mediating bosons is invariant under a transformation called gauge transformation, so these bosons are referred to as *gauge bosons*. The bosons in the Standard Model are:

- Photons,  $\gamma$ , which mediate the electromagnetic interaction. They are massless, chargeless and non-selfinteracting.
- $W^\pm$  and  $Z^0$  bosons, which mediate the weak nuclear force. They are massive particles and also selfinteracting. The  $W^\pm$  are charged with  $Q = \pm 1$  respectively and the  $Z^0$  is electrically neutral.

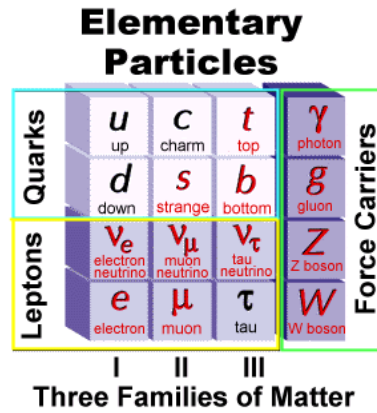


Figure 1.1: Elementary particles in the Standard Model

- Eight species of gluons,  $g_\alpha, \alpha = 1, \dots, 8$ , which mediate the strong nuclear force. They are massless, electrically neutral and carry colour quantum number.
- The Higgs bosons, which induce spontaneous symmetry breaking of the gauge groups and are responsible for the existence of inertial mass.

The Higgs boson is the only boson in the theory which is not a gauge boson. Gravitons, the bosons believed to mediate the gravitational interaction, are not accounted for the Standard Model. The gauge bosons properties are shown in the table 1.2 [2].

Interaction	Particle	Symbol	Spin	Mass ( $GeV$ )	Q ( $q_e$ )
Electromagnetic	photon	$\gamma$	1	0	0
Weak nuclear force		Z	1	$91.187 \pm 0.002$	0
		$W^\pm$	1	$80.403 \pm 0.029$	$\pm 1$
Strong force	gluons	$g$	1	0	0

Table 1.2: Gauge bosons in the Standard Model [2].

### 1.1.2 Spontaneous symmetry breaking

A system will be said to possess a symmetry that is spontaneously broken if the Lagrangian describing the dynamics of the system is invariant under this symmetry transformation, but the vacuum of the theory is not invariant. The Goldstone model is a simple model with

spontaneous symmetry breaking (SSB). Starting with a classical theory, take a Lagrangian density

$$\mathcal{L} = \partial^\mu \varphi^* \partial_\mu \varphi - V(\varphi),$$

where  $\varphi$  is a complex field

$$\varphi = \frac{\sqrt{2}}{2}(\varphi_1 + i\varphi_2)$$

and  $V(\varphi)$  the potential energy

$$V(\varphi) = \mu^2 |\varphi|^2 + \lambda |\varphi|^4.$$

The constants  $\mu^2$  and  $\lambda$  are real with  $\lambda$  positive to make the total field energy bounded from below. It should be noted that  $\varphi$  is a function of the spacetime coordinate  $x$  which is suppressed to simplify the notation. This Lagrangian is invariant under the global  $U(1)$  transformation describing rotations in the complex plane. Requiring that the vacuum, the lowest energy state, is invariant under Lorentz transformations and translations implies that  $\varphi(x)$  is a constant in this vacuum state. Two different possibilities exist for the vacuum state depending on the parameter  $\mu^2$ .

If  $\mu^2$  is positive the situation is quite normal with the minimum potential energy when  $\varphi = 0$ . If instead  $\mu^2$  is negative, the minimum energy no longer corresponds to a unique value of  $\varphi$  but is instead degenerate with the minimum as a ring in the complex plane

$$\varphi V_{min} = \sqrt{\frac{-\mu^2}{2\lambda}} e^{i\theta}, \quad 0 \leq \theta \leq 2\pi$$

As the Lagrangian  $\partial^\mu \varphi^* \partial_\mu \varphi - V(\varphi)$  is invariant under rotations in the complex plane of  $\varphi$ , each direction is equally good and setting  $\theta = 0$  such that

$$\varphi V_{min} = \sqrt{\frac{-\mu^2}{2\lambda}} \equiv \frac{v}{\sqrt{2}}$$

can be done without loss of generalization. A theory where the vacuum has less symmetry than the Lagrangian is called a theory with spontaneous symmetry breaking. The deviation from the chosen minimum can be described by the two real field  $\sigma$  and  $\eta$  defined through

$$\varphi = \frac{\sqrt{2}}{2}(v + \sigma + i\eta).$$

Therefore, we can rewritten the Lagrangian in terms of  $\sigma$  and  $\eta$ :

$$\mathcal{L} = \frac{1}{2}\partial^\mu\sigma\partial_\mu\sigma - \lambda v^2\sigma^2 + \frac{1}{2}\partial^\mu\eta\partial_\mu\eta - \lambda v\sigma(\sigma^2 + \eta^2) - \frac{1}{4}\lambda(\sigma^2 + \eta^2)^2 + c$$

with  $c$  a constant of interest only for general relativity. Taking the higher order terms as interaction terms the free Lagrangian reads:

$$\mathcal{L} = \frac{1}{2}\partial^\mu\sigma\partial_\mu\sigma - \lambda v^2\sigma^2 + \frac{1}{2}\partial^\mu\eta\partial_\mu\eta$$

It is seen that  $\sigma$  and  $\eta$  in fact are two real Klein-Gordon fields. By quantizing these fields the Lagrangian describes two different spin 0 particle fields. The  $\sigma$  boson will have mass

$$m_\sigma = v\sqrt{2\lambda}$$

arising from the  $\sigma^2$  term while the  $\eta$  boson will be massless. The masslessness of the  $\eta$  boson are a direct consequence of the minimum being degenerate. The remaining terms in the complete Lagrangian can be treated as interactions among the  $\sigma$  and  $\eta$  particles through perturbation theory.

This is an example of the prediction of the so called Goldstone theorem which states that when an exact continuous global symmetry is spontaneously broken, i.e. it is not a symmetry of the physical vacuum, the theory contains one massless scalar particle for each broken generator of the original symmetry group.

### 1.1.3 Higgs mechanism

When a spontaneous symmetry breaking takes place in a gauge theory the so-called Higgs mechanism ([5]) operates. It implies the appearance of massive vector particles. The Higgs mechanism is the mechanism that gives masses to all elementary particles in particle physics. This is accomplished by requiring that the Lagrangian that exhibits the spontaneous symmetry breakdown is also invariant under *local*, rather than global, gauge transformations. This procedure fits very well in the requirements for a gauge theory of electroweak interactions where the short range character of this interaction requires a very massive intermediate particle. The discovery of the  $W^\pm$  and  $Z$  gauge bosons at CERN in 1983 ([6]) may be considered as the first experimental evidence of the SSB phenomenon in electroweak interactions.

In the SM, the symmetry breaking is realized linearly by a scalar field which acquires a non-zero vacuum expectation value. The resulting physics spectrum contains not only the massive intermediate vector bosons and fermionic matter fields but also the Higgs

particle, a neutral scalar field which has escaped experimental detection until now. The main advantage of the SM picture of symmetry breaking lies in the fact that an explicit and consistent formulation exists, and any observable can be calculated perturbatively in the Higgs self-coupling constant.

Here it will be shown the Higgs mechanism for a U(1) theory. Let us consider again the charged self-interacting scalar Lagrangian  $\mathcal{L} = \partial^\mu \varphi^* \partial_\mu \varphi - V(\varphi)$  with the potential  $V(\varphi) = \mu^2 |\varphi|^2 + \lambda |\varphi|^4$ , and let us require a invariance under the local phase transformation,

$$\varphi \rightarrow e^{[iq\alpha(x)]} \varphi,$$

with  $\alpha$  any differentiable function.

We introduce a gauge boson  $A_\mu$  and the covariant derivative  $D_\mu$ , so that the Lagrangian becomes invariant:

$$\begin{aligned} \partial_\mu &\rightarrow D_\mu = \partial_\mu + iqA_\mu \\ A_\mu &\rightarrow A'_\mu = A_\mu - \partial_\mu \alpha(x) \end{aligned}$$

The new Lagrangian is:

$$\mathcal{L} = D^\mu \varphi^* D_\mu \varphi - V(\varphi) - \frac{1}{4} F_{\mu\nu} F^{\mu\nu}.$$

Continuing in exactly the same way as for the Goldstone model with a negative  $\mu^2$  and expressing the Lagrangian in terms of the variables  $\sigma$  and  $\eta$  as we defined before the result is

$$\begin{aligned} \mathcal{L} &= \frac{1}{2} \partial^\mu \sigma \partial_\mu \sigma - \lambda v^2 \sigma^2 + \frac{1}{2} \partial^\mu \eta \partial_\mu \eta - \frac{1}{4} F_{\mu\nu} F^{\mu\nu} \\ &+ \frac{1}{2} q^2 v^2 A_\mu A^\mu + qv A^\mu \partial_\mu \eta + \text{higher order terms} \end{aligned}$$

The Lagrangian clearly has a massive vector boson field  $A_\mu$ , with mass  $M_A = qv$ , a massless scalar boson  $\eta$  (the Goldstone boson) and a scalar field  $\sigma$  with mass  $M_\sigma = \sqrt{-2\mu^2}$ . However the presence of the term  $qvA^\mu \partial_\mu \eta$  is quite inconvenient since it mixes the propagators of  $A_\mu$  and  $\eta$  particles. In order to eliminate this term, we can choose the gauge parameter to be proportional to  $\eta$  as

$$\alpha(x) = -\frac{1}{qv} \eta(x)$$

In this way the field  $\varphi(x)$  has the form

$$\varphi(x) = \frac{\sqrt{2}}{2} (v + \sigma(x))$$

With this choice of gauge (called unitary gauge) the Goldstone boson  $\eta$  disappears, and we get the Lagrangian

$$\mathcal{L} = \frac{1}{2}\partial^\mu\sigma\partial_\mu\sigma - \lambda v^2\sigma^2 - \frac{1}{4}F_{\mu\nu}F^{\mu\nu} + \frac{1}{2}g^2v^2A'_\mu A'^\mu + \text{higher order terms}$$

The corresponding degree of freedom of the Goldstone boson was absorbed by the vector boson that acquires mass. In summary, it is seen that a complex scalar field  $\varphi$  and a massless vector field  $A_\mu$ , both with two degrees of freedom, as a result of the Higgs mechanism were transformed into one real scalar field  $\sigma$  with one degree of freedom and a massive vector boson field  $A'_\mu$  with 3 degrees of freedom.

The Higgs mechanism was demonstrated here for a  $U(1)$  gauge invariant Lagrangian. To extend it to  $SU(2)_L \times U(1)_Y$  gauge invariant Lagrangian of the electroweak theory is relatively simple. The starting point is a Lagrangian with a complex scalar doublet and four massless vector bosons. Through the Higgs mechanism the Lagrangian is transformed into one real scalar, three massive vector and one massless vector boson. The massless vector boson is of course to be identified with the photon and the single remaining scalar with the Higgs boson. The three massive vector bosons correspond to  $W^\pm$ ,  $Z^0$ . The masses of the particles in the Standard Model are given as

$$m_H = \sqrt{2\lambda}v = \left(\frac{\sqrt{2}}{G_F}\right)^{\frac{1}{2}}\sqrt{\lambda}, \quad m_W = \frac{1}{2}vg, \quad m_Z = \frac{m_W}{\cos\theta_W},$$

where  $g$  is the weak coupling constant and  $\theta_W$  the Weinberg angle. The vacuum expectation value is easily extracted as

$$v = \frac{2m_W}{g} = 247 \text{ GeV},$$

but there is no way to measure the value of  $\lambda$  before a discovery of the Higgs. Therefore, the Higgs mass  $M_H$  is not predicted in the Standard Model and can take any value. There are some bounds on this mass from the requirement of the consistency of the theory. Unitarity gives an upper bound around 860 GeV, triviality gives an upper bound of 640 GeV, and vacuum stability arguments provides a lower bound around 132 GeV. The current lower mass limit on the Higgs boson mass is from direct searches at LEP and is 114.4 GeV [7]. Precision measurements at LEP indicate that the SM Higgs boson is unlikely to be heavier than 260 GeV [8].

The discovery of this particle is one of the challenges of the high-energy colliders. This is the most important missing piece of the Standard Model and its experimental verification could furnish very important information on the spontaneous breaking of the electroweak symmetry and on the mechanism for generating fermion masses.

### 1.1.4 Higgs properties

The Higgs boson couples to all particles that get mass ( $\propto v$ ) through the spontaneous symmetry breaking of  $SU(2)_L \times U(1)_Y$ . Therefore it will be produced in association with heavy particles and it will decay into the heaviest particles that are accessible kinematically. The neutral and weak interacting Higgs boson can interact with photons through loops of charged particles that share the weak and electromagnetic interactions: leptons, quarks and W boson. In the same way the Higgs couples indirectly with gluons via loops of quarks.

The Higgs boson can be produced in electron-positron collisions via the Bjorken mechanism ( $e^+ + e^- \rightarrow Z \rightarrow ZH$ ), or vector fusion ( $e^+ + e^- \rightarrow \nu\bar{\nu}(WW) \rightarrow \nu\bar{\nu}H$  and  $e^+ + e^- \rightarrow e^+e^-(ZZ) \rightarrow e^+e^-H$ ). At LEP I and II the Higgs production is dominated by the Bjorken mechanism and they were able to rule out from very small Higgs masses up to 95.2 GeV. At the future  $e^+e^-$  accelerators, the production of Higgs with mass between 100 and 200 GeV will be dominated by the WW fusion.

At  $pp$  collisions the Higgs boson can be produced via (see figure 1.2):

- the gluon fusion mechanism

$$p\bar{p} \rightarrow gg \rightarrow H,$$

- through the vector boson fusion ( $V = W^\pm, Z^0$ )

$$p\bar{p} \rightarrow VV \rightarrow H,$$

- in association with a  $W^\pm$  or a  $Z^0$

$$p\bar{p} \rightarrow q\bar{q}' \rightarrow VH.$$

At the Fermilab Tevatron the Higgs is better produced in association with vector boson and they look for the  $VH(\rightarrow b\bar{b})$  signature. At LHC, that will operate with  $\sqrt{s} = 14 \text{ TeV}$ , the dominant production mechanism is through the gluon fusion and it is sensitive to a fourth generation of quarks. We expect that the LHC can explore up to  $M_H \sim 700 \text{ GeV}$  with an integrated luminosity of  $\mathcal{L} \sim 100 \text{ fb}^{-1}$ .

### Higgs Decays

The possible decay modes of the Higgs boson are essentially determined by the value of its mass. In figure 1.3 we present the Higgs branching ratios for different  $M_H$ . It is clear that branching ratios change dramatically across the possible range of the Higgs mass

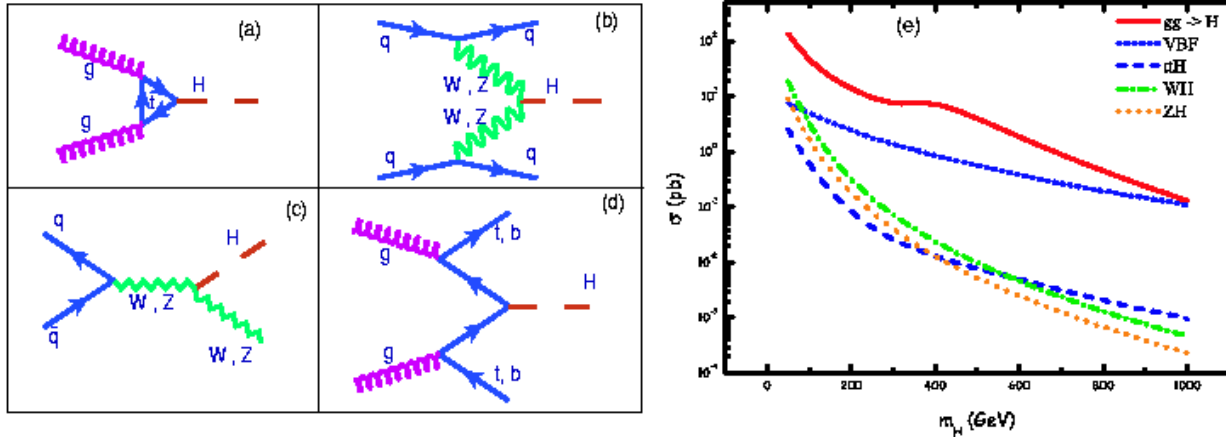


Figure 1.2: Higgs boson production mechanisms: (a) gluon fusion, (b) vector boson fusion, (c) associated production with a gauge boson, (d) production with a top quark and (e) corresponding production cross-section calculated with NLO corrections.

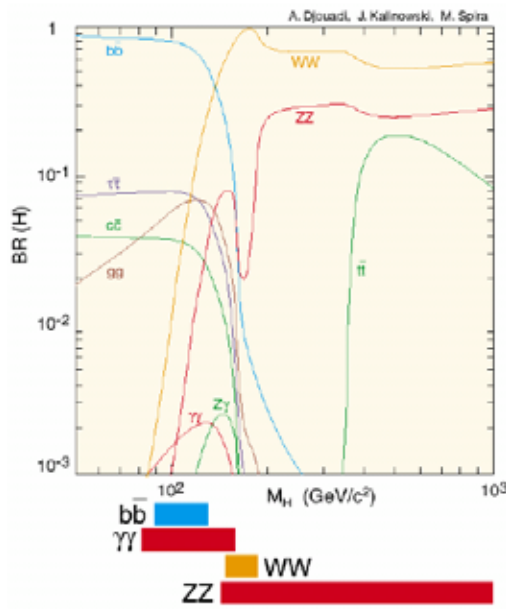


Figure 1.3: Branching ratios of the Higgs boson decays.



making it necessary to have different strategies for the Higgs identification depending on its mass.

When the Higgs boson mass lies in the range  $95 \text{ GeV} < M_H < 130 \text{ GeV}$ , the Higgs is quite narrow  $\Gamma < 10 \text{ MeV}$  and the main branching ratios come from the heaviest fermions that are accessible kinematically:

$$\begin{aligned} BR(H \rightarrow b\bar{b}) &\sim 90\% \\ BR(H \rightarrow c\bar{c}) &\simeq BR(H \rightarrow \tau\bar{\tau}) \sim 5\% \end{aligned}$$

For a heavier Higgs, i.e.  $M_H > 130 \text{ GeV}$ , the vector boson channels  $H \rightarrow VV^*$ , with  $V=W^\pm, Z^0$  are dominant

$$\begin{aligned} BR(H \rightarrow W^+W^-) &\sim 65\% \\ BR(H \rightarrow Z^0Z^0) &\sim 35\% \end{aligned}$$

For  $M_H \simeq 500 \text{ GeV}$  the top quark pair production contributes with  $\sim 20\%$  of the width.

### 1.1.5 Successes and failures of Standard Model

The Standard Model predicted the existence of W and Z bosons, the gluon, the top quark and the charm quark before these particles had been observed. Their predicted properties were experimentally confirmed with good precision. The Large Electron-Positron collider (LEP) at CERN tested various predictions about the decay of Z bosons and found them confirmed. The Higgs detection is necessary in order to get a complete validation of the Standard Model.

Nevertheless, although the Standard Model has had great success in explaining experimental results, it has never been accepted as a complete theory of fundamental physics. This is because it has several important defects:

1. The model contains 19 free parameters, such as particle masses which must be determined experimentally. These parameters cannot be independently calculated.
2. The model does not describe the gravitational interaction.
3. The SM did not accommodate massive neutrinos, but, in 1998 Super-Kamiokande published results indicating neutrino oscillation, which implied the existence of non-zero neutrino masses. Since then, physicists have revised the Standard Model to allow neutrinos to have mass, which make up additional free parameters beyond the initial 19.

4. Even if the Higgs exists, all is not perfectly well with the Standard Model alone. The same mechanism that gives all masses would drive the Higgs to the Planck scale. Then it is not understood why the Higgs mass is so low.
5. In addition, due to cosmological reasons the Standard Model is believed to be incomplete. Within it, matter and antimatter are symmetric, but there is a preponderance of matter in the universe. Furthermore, the Standard Model provides no mechanism to generate the cosmic inflation.

Since the completion of the Standard Model, many efforts have been made to address all these problems. One attempt to address these defects is known as grand unification. The so-called grand unified theories (GUTs) hypothesized that the  $SU(3)$ ,  $SU(2)_L$  and  $U(1)$  groups are actually subgroups of a single large symmetry group. At high energies (far beyond the reach of current experiments), the symmetry of the unifying group is preserved; at low energies, it reduces to  $SU(3) \times SU(2)_L \times U(1)$  by the process known as spontaneous symmetry breaking. A further extension of the Standard Model can be found in the theory of supersymmetry, which proposes that each elementary particle has a super-partner whose spin differs by  $1/2$  from that of the particle.

## 1.2 The LHC

The Large Hadron Collider (LHC) [9] is the next generation collider at “*Centre Européen de Physique Nucléaire*” (CERN), in Geneva, Switzerland. The LHC will collide protons on protons, in 2007, at a centre of mass energy of  $\sqrt{s} = 14 \text{ TeV}$ <sup>1</sup>. The LHC superconducting magnets will be installed in the old LEP tunnel whose circumference is of the order of  $27 \text{ km}$ . The two proton beams will circulate in opposite directions and guided by a  $8.34 \text{ T}$  field generated by superconducting magnets. The proton-proton collisions let reaching higher energies than in the  $e^-e^+$  collider (for which the synchrotron radiation is very important). For while a proton-antiproton collider has the advantage that both counter-rotating beams can be kept in the same beam pipe, producing the enormous amounts of antiprotons required for the high luminosity is not realistic and would be more expensive than the proton-proton solution with separate beam pipes. Besides protons, the LHC will also accelerate and collide beams of lead nuclei.

The average number of interactions per crossing  $N$  is given by the well known expression:

$$N = \sigma_{in} \times \mathcal{L} \times \Delta T$$

---

<sup>1</sup>The highest centre of mass energy available today is that of the FNAL Tevatron which is  $2 \text{ TeV}$ .

where  $\sigma_{in}$  is the inelastic  $pp$  cross-section (of the order of  $80 \text{ mb}$ , see figure 1.4),  $\mathcal{L}$  the luminosity and  $\Delta T$  the time it takes a bunch to complete a turn in the storage ring divided by the number of protons in that bunch. It is calculated to be  $\Delta T = 31 \text{ ns}$ . The cross-section is, at a given centre of mass energy, a fixed number dependent only on the specific physics process while the luminosity is controlled by the parameters of the collider. The luminosity for a collider is:

$$\mathcal{L} = \frac{1}{4\pi} \frac{N^2 f}{t A_T},$$

where  $N$  is the number of protons in each bunch,  $t$  the time between individual bunches,  $A_T$  the transverse dimension of the bunches at the interaction points and  $f$  the fraction of bunch positions actually containing protons.

For the LHC the time between bunches (bunch crossing time) will be 25 ns corresponding to a bunch separation of 7.5 m. The proton bunches will have a length of a few centimeters and transverse dimensions of a few micrometers. To be able to fill new bunches into the LHC and operate the beam dump it is necessary to order the proton bunches in bunch trains followed by some empty bunches. In total 2835 of the 3557 available spaces with 25 ns separation will contain protons corresponding to  $f=0.80$ . The only remaining way to increase the luminosity is to increase the number of protons in each bunch. This is limited by electromagnetic forces between the colliding bunches. In LHC, each bunch will contain approximately  $10^{11}$  protons.

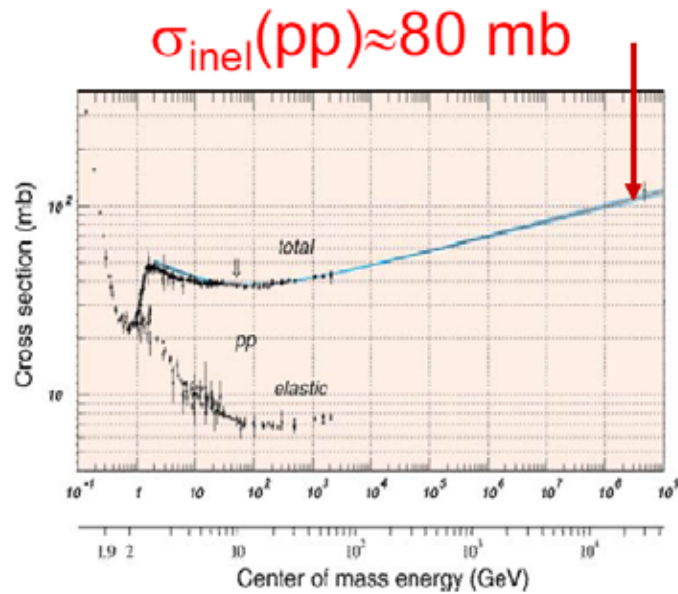
For the first years of running it is foreseen to run at low luminosity  $\mathcal{L}_{\text{low}} = 10^{33} \text{ cm}^{-2}\text{s}^{-1}$  and gradually increasing it to the high luminosity  $\mathcal{L}_{\text{high}} = 10^{34} \text{ cm}^{-2} \text{ s}^{-1}$ . For the lead ion runs, the design luminosity is  $0.5 \times 10^{27} \text{ cm}^{-2}\text{s}^{-1}$ . With these numbers one expects on the average 20 interactions per crossing in the high luminosity running mode. We can see some LHC mechanical parameters in the table 1.3.

Proton acceleration starts in the 50 MeV proton LINAC, followed by injection into the 1.4 GeV Proton Synchrotron Booster (PSB). The Proton Synchrotron (PS) itself will accelerate the protons to 26 GeV and deliver a beam of 135 bunches, containing  $10^{11}$  protons, spaced at 25 ns. The Super Proton Synchrotron (SPS) will accelerate the protons to 450 GeV, at which point they will be injected into the LHC. Finally protons will be accelerated to 7 TeV in separate magnetic channels inside a single twin bore magnet, making use of the same yoke and cryostat. A layout of the LHC injection scheme is shown in figure 1.5.

In these operating conditions, we will find one *good* event containing a Higgs decay and approximately 20 extra *bad* (minimum bias) interactions. The pile up of minimum bias

Beam energy	7.0 TeV
Bunch separation	24.95 ns
Time between collisions	14.95 ns
Luminosity	$0.1 \text{ a } 1 \cdot 10^{34} \text{ cm}^{-2} \cdot \text{s}^{-1}$
Circumference	26.659 km
Particles per bunch	$1.05 \cdot 10^{11}$ protons
Beam length ( $\sigma_z$ )	7.5 cm
Beam width ( $\sigma_x$ )	15.9 $\mu\text{m}$
Number of bunches	2835
DC beam current	0.56 A
Magnetic field	8.34 T
Magnetic dipole temperature	1.9 K
Energy loss per turn	7 keV
Total radiated power/beam	3.8 kW
Stored energy per beam	350 MJ

Table 1.3: LHC parameters.

Figure 1.4:  $pp$  cross-section as a function of center of mass energy.

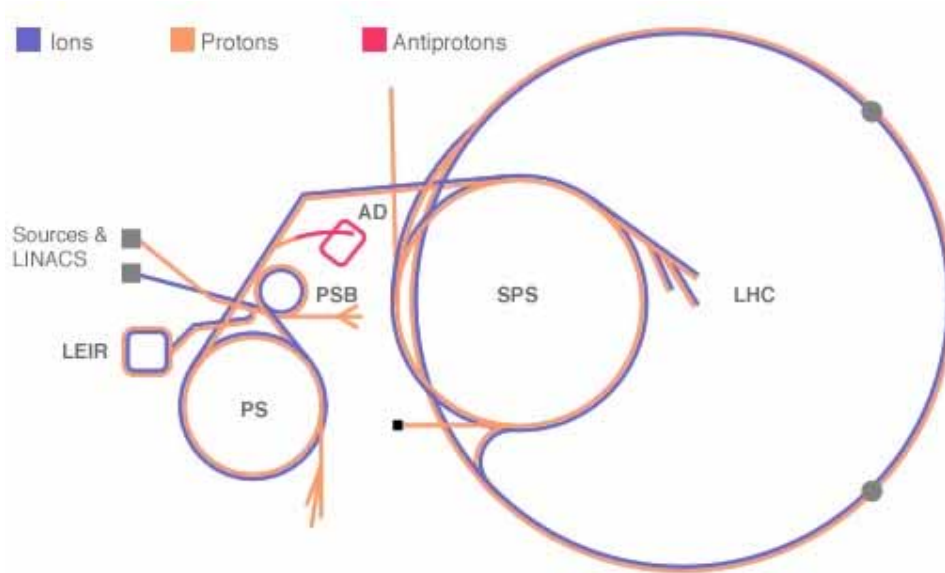


Figure 1.5: Accelerators complex at CERN.

events implies some requirements on the detector design:

- LHC detectors must have fast response. Otherwise will integrate over many bunch crossing, which implies a large pile-up. The typical response time will be 20-50 ns, requiring a very challenging readout electronics.
- LHC detectors must be highly granular, in order to minimize probability that pile-up particles be in the same detector element as interesting object (e.g.  $\gamma$  from  $H \rightarrow \gamma\gamma$  decays). That results in a large number of electronics channels (for CMS  $\sim 40 \times 10^6$ ) and in a high cost.

The high flux of particles from  $pp$  collision produces a high radiation environment. For instance, in forward calorimeters, we will find up to  $10^{17} n/cm^2$  in 10 years of LHC operation and up to  $10^{17} Gy$ <sup>2</sup>. As detectors and electronics are required to survive 10 years of operation, the radiations have a big impact on detectors:

- Detectors may need special environment for long term viability. For instance, silicon must be run at low temperature to limit leakage current and avoid reverse annealing (which is equivalent to high bias operation).
- Radiation deteriorates performances and induces time-dependent variations, as the attenuation of light transmission in crystals or scintillators.

<sup>2</sup>  $1 Gy = 1 \text{ Joule/kg}$  is a unit of absorbed energy.

- It forbids the use of some rather usual materials. For instance, many plastics or glues are not radiation hard, tantalum capacitors are forbidden, and some materials become highly activated by neutrons.
- Radiation restrict access for maintenance.
- It is necessary a quality control for every piece of material.

Five experiments, with huge detectors, will explore particle collisions at the LHC (see figure 1.6). These experiments are: ATLAS (A Toroidal LHC ApparatuS), CMS (Compact Muon Solenoid), LHCb (The Large Hadron Collider Beauty Experiment), ALICE (A Large Ion Collider Experiment) and TOTEM.

ATLAS and CMS are the two general purpose experiments, while LHCb, ALICE and TOTEM have a narrowly defined purpose.

The ATLAS detector has been designed to be a multi-purpose detector capable of making precise measurements during both low and high luminosity runs with a  $\eta$  coverage of  $|\eta| < 5$ . In order to explore the discovery potential for new physics at the LHC, this detector has been optimized to be especially precise for measurements of leptons ( $e$  and  $\mu$ ), photons, jets and missing transverse energy,  $E_{Tmiss}$ . In addition, ATLAS will also perform precise measurements for a large number of physics channels.

Similarly to ATLAS, CMS is a general purpose detector. The design goals for the CMS detector included a high performance muon system, the best possible electromagnetic calorimeter, high quality central tracking and a hermetic hadron calorimeter. Achieving these goals will enable CMS to identify and measure muons, photons and electrons with high precision.

The basic principle of ATLAS and CMS detectors is an experiment covering as much of the solid angles as possible ( $4\pi$ ) since we do not know how new physics will manifest itself. The momentum and charge of tracks and secondary vertexes (e.g. from b-quark decays) are measured in central tracker (Silicon layers plus gas detectors). The energy and positions of electrons and photons are measured in electromagnetic calorimeters, while the energy and position of hadrons and jets are measured mainly in hadronic calorimeters. The external muon spectrometer (+ central tracker) identifies the muons and measures their momentum. Neutrinos are *detected* and *measured* through measurement of missing transverse energy ( $E_T^{miss}$ ) in calorimeters.

LHCb is a detector designed to study the physics of B-mesons. The study of charge-parity (CP) violation which results in a difference in the decay rate of particles and anti-particles, is one of the main goals of the LHCb experiment.

The ALICE detector (A Large Ion Collider Experiment) is being built as a dedicated

heavy-ion detector to investigate the unique physics potential of nucleus-nucleus interactions at LHC energies. One of the key physics aims of ALICE is to study the physics of strongly interacting matter at extreme energy densities, where the formation of a new phase of matter, the quark-gluon plasma, is expected.

The TOTEM detector will be dedicated to measuring the total cross-section, elastic scattering and diffractive dissociation at the LHC. The experimental apparatus consists of elastic scattering detectors based on a system of Roman pots, and a forward inelastic detector which will be integrated into CMS detector.

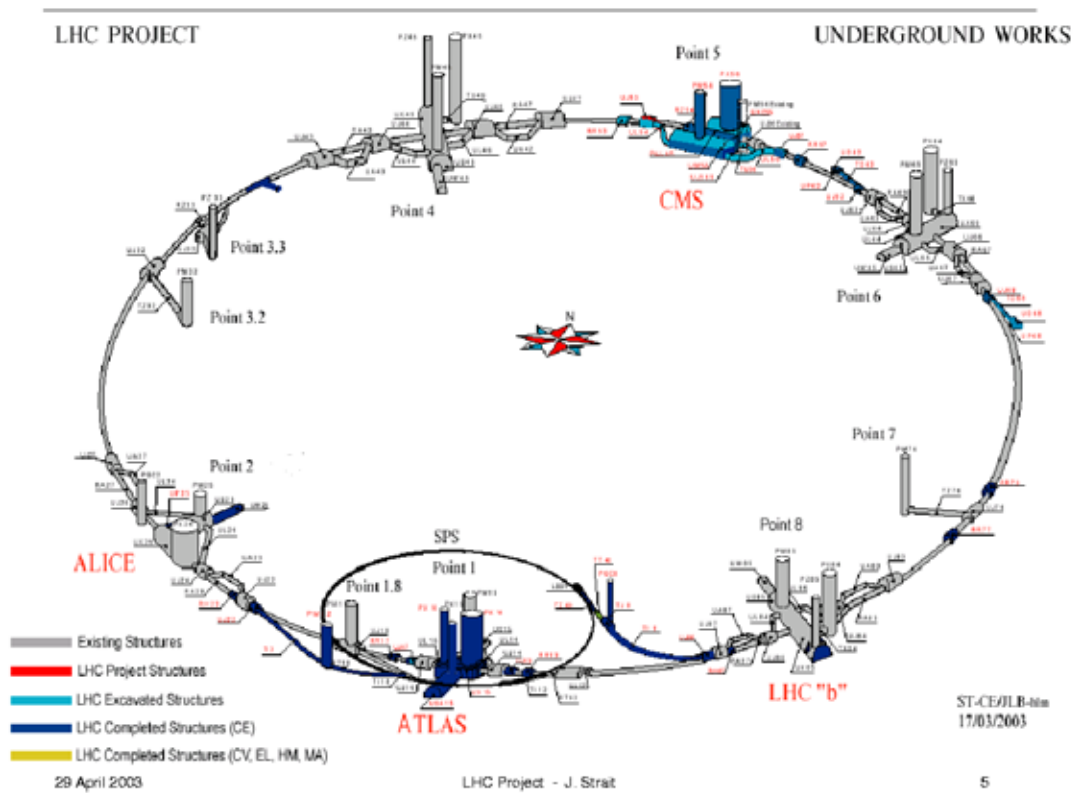


Figure 1.6: A view of the LHC project.

### 1.2.1 LHC physics

The LHC machine and the planned experiments have been designed to investigate many different types of physics that might become detectable in the energetic collisions of the LHC. Some of these are confirmations or improved measurements of the Standard Model, while many others are searches for new physical theories.

- **Discovery of the Higgs boson**

As we have seen before, the Standard Model does not predict the Higgs mass. The experiments are designed to cover the different physics signatures of the Higgs, consisting in the identification of the predicted decay modes, with statistical significance over all the mass range.

**An intermediate mass Higgs,  $m_Z < m_H < 2m_Z$**

To find a Higgs particle below the threshold for the  $H \rightarrow ZZ$  decay and above the limit set by the searches at LEP will be difficult. The obvious way to detect a Higgs would be in the dominant  $H \rightarrow b\bar{b}$  channel. In order to identify the jets with b-quarks, it will be used a method based either on the long lifetime of the b-quarks which causes secondary vertexes or on the high amount of leptons in B meson decays. This decay channel is dominant and accounts for 90% of all possible decays. However, it is masked by a very high background coming from QCD processes.

The other way of identifying a Higgs in the intermediate mass region is to select an exotic decay as the  $H \rightarrow \gamma\gamma$  decay. The trigger is two isolated electromagnetic clusters. While the channel suffers from a branching ratio around  $10^{-3}$  (its branching ratio is suppressed by three orders of magnitude with respect to the previous decay), the backgrounds are also much lower than in the case of the  $H \rightarrow b\bar{b}$  decay due to the clear signature of two isolated photons in the final state. In fact, the main reducible backgrounds comes from jet pair production each of them containing a leading  $\pi^0$ . Therefore, in order to be able to discern a Higgs signal from background the electromagnetic calorimeters are required to exhibit a good  $\gamma/\pi^0$  separation capability. Monte Carlo studies further indicate that the mass resolution necessary to discover the Higgs into two photons should not be worse than 1%. This requires a  $10\%/\sqrt{E}$  resolution in the electromagnetic calorimetry of ATLAS.

In the upper limit of this mass interval the branching ratio to vector bosons reaches significant levels. However, at least one of the vector bosons will not be on the mass shell.

**A heavy Higgs,  $2m_Z < m_H \leq 700 \text{ GeV}$**

If a Standard Model Higgs is having a mass above twice the Z mass the discovery will be easy through the decay channel  $H \rightarrow ZZ \rightarrow l^+l^-l^+l^-$ , with  $l = e, \mu$ . Obviously, here again, the electromagnetic calorimeters will be instrumental together with the muon detection systems. Both lepton pairs will have an on-shell Z mass making it possible to reduce many types of backgrounds. The main irreducible background is direct ZZ production, but a requirement for at least one of the Z bosons to have a



transverse momentum above half the Higgs mass will strongly suppress this background. A good momentum resolution for low momenta leptons, large geometric acceptance and efficient lepton isolation at high luminosity are also required.

### A very heavy Higgs, $m_H \geq 700 \text{ GeV}$

With the fixed collision energy of the LHC, the production cross-section of a Higgs particle falls with an increasing Higgs mass. The rate in a selective decay channel like the four lepton channel is thus no longer high enough for the highest Higgs masses. With the decays to vector bosons totally dominating, the only possible detection channels left are with at least one of the vector bosons decaying to neutrinos or jets,  $H \rightarrow ZZ \rightarrow ll\nu\nu$ ,  $H \rightarrow ZZ^* \rightarrow lljet - jet$ ,  $H \rightarrow WW \rightarrow lvjet - jet$ .

- **New physics studies**

In the LHC supersymmetry and extradimensions will be studied. Both predict new particles in the TeV scale, which, if they exist, should be observed in LHC.

- **Electroweak and top studies**

In the LHC precise measurements of top and W masses and electroweak bosons coupling will be done. These measurements will help to limit the parameters of the combined theory.

- **B Physics**

In the LHC the hadrons-B decay will be studied and therefore they will limit the mixing matrix *Cabibbo-Kobayashi-Maskawa* parameters, including precise measurements of CP violation in B-mesons decays.

- **Strong interactions**

We could perform measurements of the strong coupling constant,  $\alpha_s$ , and of the partonic density functions.

- **Heavy ions**

During the collision phase of Pb-Pb ions, the very high density and temperature will cause a phase transition from ordinary hadronic matter to a deconfined quark-gluon plasma.

## 1.2.2 Physics requirements

As a summary, there are several physics requirements for ATLAS, for example:

- Good charged particle reconstruction in inner tracker
  - B and  $\tau$  tagging (pixel detector)
- Good electromagnetic resolution for  $|\eta| < 2.5$ 
  - $< 1\%$  di-electron mass resolution at  $100 \text{ GeV}/c^2$
  - Primary vertex localization and/or  $\gamma$  angular measurement
  - $\pi^0$  rejection
  - Lepton isolation
- Good muon identification and momentum resolution for  $|\eta| < 2.5$ 
  - $< 1\%$  di-muon mass resolution at  $100 \text{ GeV}/c^2$
  - Ability to measure unambiguously charge up to  $> 1 \text{ TeV}/c$
- Good missing  $E_T$  and di-jet mass resolution
  - Large hadronic calorimeter coverage  $|\eta| \sim 5$
  - Lateral segmentation  $\Delta\eta \times \Delta\phi < 0.1 \times 0.1$

### 1.3 The ATLAS detector

As we mentioned previously, ATLAS (A Toroidal LHC ApparatuS) [10] is a multi-purpose detector designed to exploit the physics potential of the LHC, see figure 1.7. The detector is being built by an international collaboration of about 2000 physicists, engineers and technicians from 34 countries. The construction is scheduled to be completed in 2007.

The necessity to withstand several years in a high radiation environment while providing data for a widely varied physics programs defines the design of the detector. The detector is cylindrical, having a total length of 44 meters, a diameter of 22 meters and a overall weight of 7000 tons (while CMS detector has a length of 22 m and a diameter of 15 m).

The ATLAS coordinate system is a spherical system defined in terms of the  $z$  direction (beam axis), a polar angle measured from this axis ( $\theta$ ) and an azimuthal angle ( $\phi$ ). In practice the polar angular coordinate is not expressed in terms of  $\theta$ , but rather in terms of pseudorapidity defined as:

$$\eta = -\ln\left(\tan\left(\frac{\theta}{2}\right)\right)$$

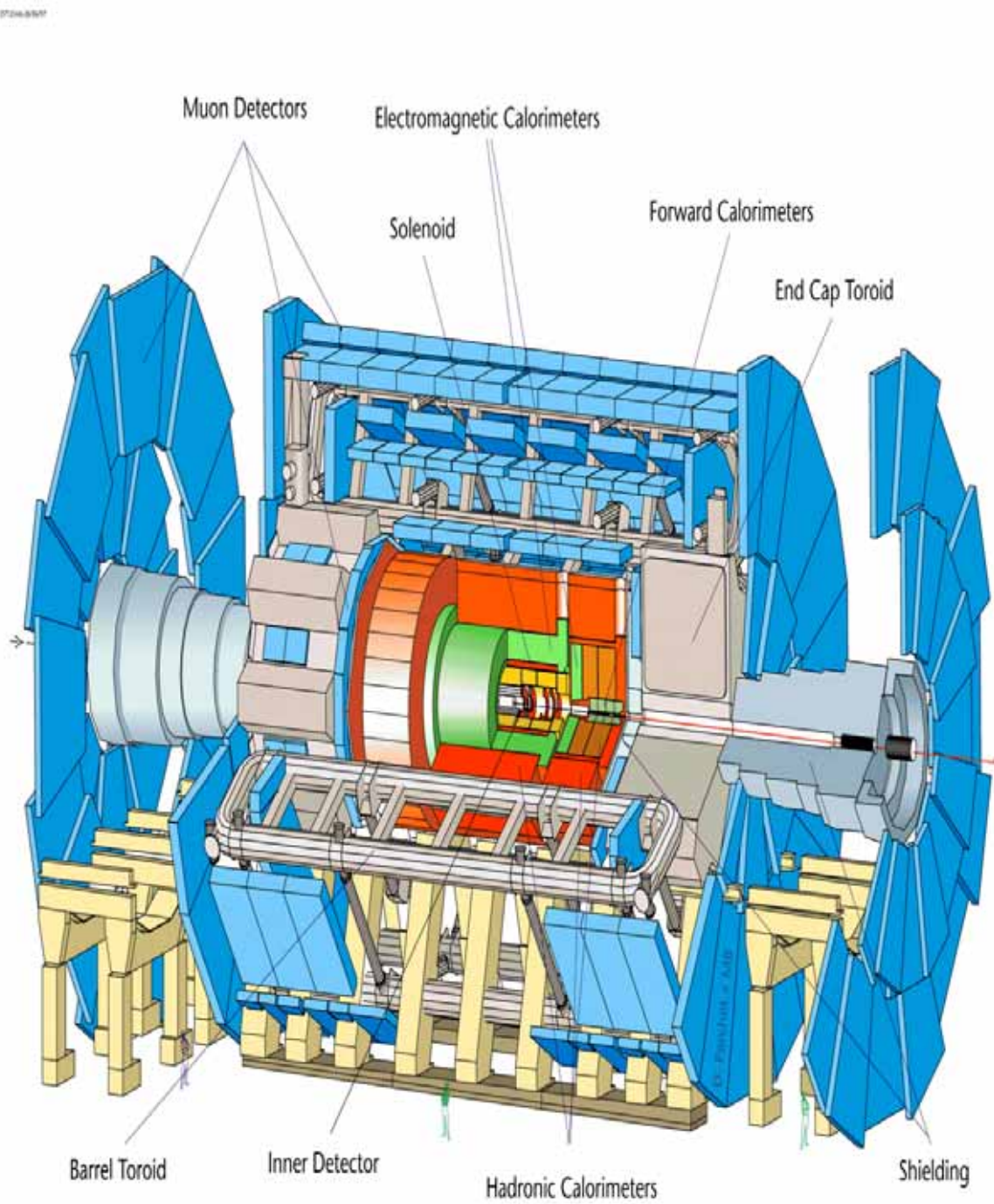


Figure 1.7: ATLAS detector.

The distribution of charged particles from minimum bias events is approximately uniform in pseudorapidity. Physically this means that detector cells of equal size in pseudorapidity contain an approximately equal particle multiplicity.

### 1.3.1 Detector requirements

In order to do the physics studies mentioned before, the main ATLAS detector requirements are:

- Very good electromagnetic calorimetry for electron and photon identification and measurements, complemented by hermetic jet and missing  $E_T$  calorimetry;
- Efficient tracking at high luminosity for lepton momentum measurements, for b-quark tagging, and for enhanced electron and photon identification, as well as  $\tau$  and heavy-flavour vertexing and reconstruction capability of some B decay final states at lower luminosity;
- Stand-alone, precision, muon-momentum measurements up to highest luminosity, and very low- $p_T$  trigger capability at lower luminosity.

### 1.3.2 General description

The detector is made up of four major sub-detector systems:

- the inner detector,
- the calorimeters, both electromagnetic and hadronic,
- the muon spectrometer,
- the magnet system.

These detectors will measure the energy and momentum of charged and neutral particles produced in the interaction point as a result of proton-proton collisions (see figure 1.8). The only particle identification possible at LHC energies will be lepton, i.e. electron or muon, and photon. The neutrinos are *detected* through the study of the missing energy.

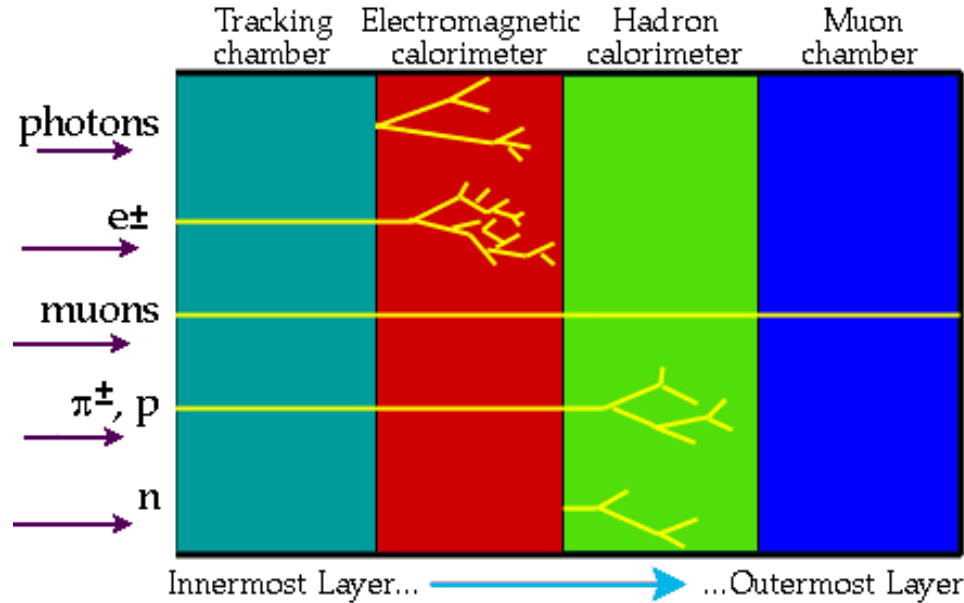


Figure 1.8: Characteristic signal of different particles in the ATLAS detector.

### 1.3.3 The inner detector

The inner detector [11] is designed to reconstruct particle tracks and decay vertex in any event with high efficiency. Using additional information from the calorimeter and muon systems, the inner detector also contributes to electron, photon and muon recognition, and supplies extra signatures for short lived particle decay vertexes. The magnetic field surrounding the entire inner detector causes charged particles to curve; the direction of the curve reveals a particle's charge and the degree of curvature reveals its momentum.

Important physics considerations for the inner detector are:

- Tracking coverage over the range  $|\eta| \leq 2.5$ .
- Excellent momentum and impact parameter resolution for tracks with  $p_T > 0.5 \text{ GeV}$  up to very high momentum.
- Momentum resolution  $p_T \times \sigma(\frac{1}{p_T}) < 0.3$  at  $p_T = 500 \text{ GeV}$  for  $|\eta| \leq 2$  and  $< 0.5$  at  $|\eta| = 2.5$ .
- Polar angular resolution  $\sigma(\theta) \leq 2 \text{ mrad}$ .
- High track finding efficiency whilst keeping the rate from fake tracks low.
- Identification of the charge of high- $p_T$  tracks, electrons, photons and jets.

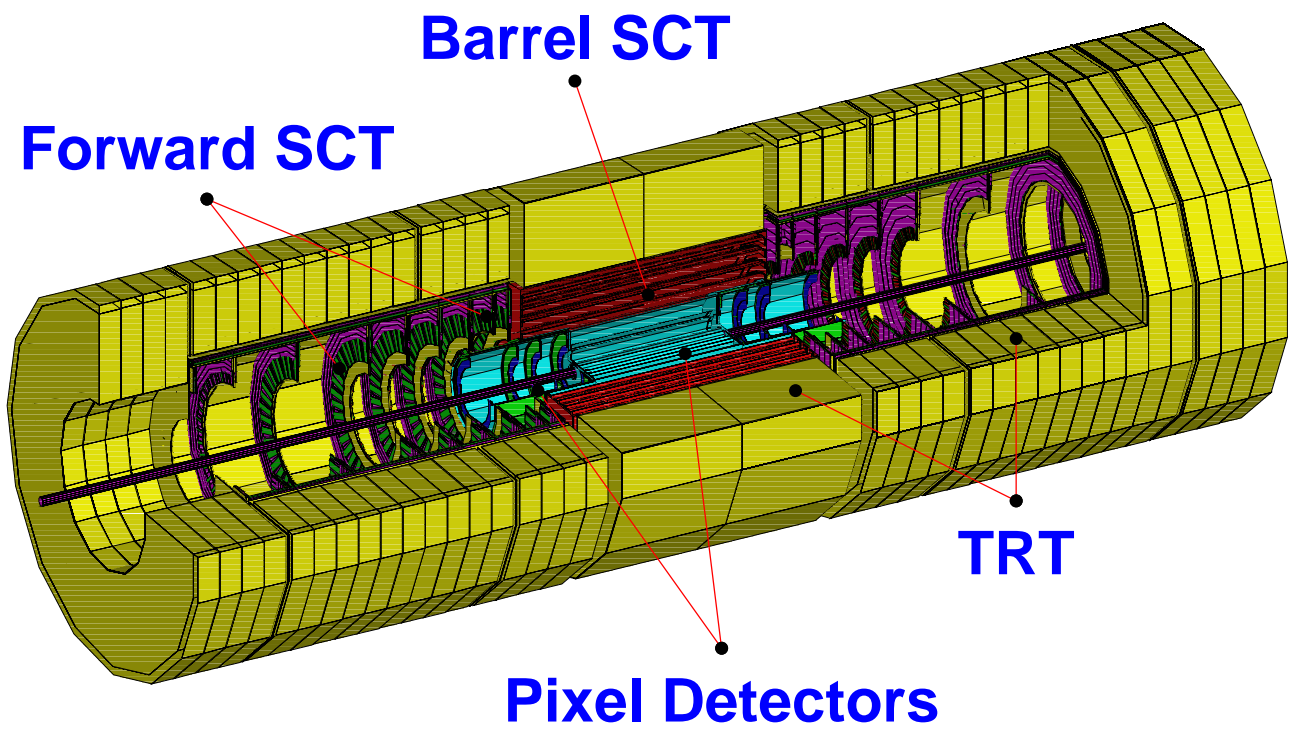


Figure 1.9: The inner detector of ATLAS.

- Tagging of b-jets originating from b-quarks.
- Identification of the primary vertex.
- Reconstruction of soft electrons and secondary vertexes from b-decays and  $\tau$ -decays.

The ATLAS inner detector consists of three distinct subdetector systems (as we can see in the figure 1.9): high resolution pixel detectors at innermost radius, silicon microstrips detectors of the Semi-Conducting Tracker (SCT) at intermediate radius and continuous tracking detectors of the Transition Radiation Tracker (TRT) at outer radius. The inner detector is contained within a solenoid magnet of central field 2T. It occupies the cylindrical cavity defined by the boundaries of the electromagnetic calorimeter cryostats, with a radius  $R = 115 \text{ cm}$  and  $z = 345 \text{ cm}$ .

The beam pipe, 1 mm thick beryllium corresponding to  $0.3 X_0$  at normal incidence, has a diameter of 5 cm. The inner detector shows a transition from barrel to disk geometry at  $\eta = 1$  in order to minimize the amount of material traversed by particles. The products of collisions emitted a low pseudorapidity will be detected in the barrel part, constituted by concentric cylinders around the beam axis, while the particles emitted at high  $\eta$  will be detected at the end-caps, constituted by a disk perpendicular to the beam axis.

Due to the high rate of interaction in the LHC, the detectors will be work with a big radiation flux, being the tracking detectors based in silicon particularly sensible. The high radiation dose degrade the sensible parts of silicon and damage the electronic. As this damage depends strongly on the temperature, the silicon detectors will be located in a cold region, working normally in a temperature range around -5 and 10 centigrade degrees. This induces large material budget (cooling pipes and ledges).

### The pixel detector

The pixel detector (see figure 1.10) is designed to provide a very high-granularity and high-precision set of measurements as close to the interaction point as possible. The system consists of three barrel layers at average radius of 4 cm, 11 cm and 14 cm, and four disks in each end-cap between radius of 11 and 20 cm, which complete the angular coverage. The basic unit of the pixel detector is the module. A module is a rectangular active device approximately 6 cm by 2 cm with 46080 pixels, each  $50 \mu\text{m}$  in  $(r, \phi)$  and  $400 \mu\text{m}$  in  $z(r)$ , which explains the effectiveness of the pixel detector system in producing good track separation. At a radius of 4 cm from the beampipe, it will be necessary to replace it periodically due to radiation damage.

The pixel detector provides three to four measurements along a track. There are overlaps

in  $z$  (barrel) or  $r$  (end-cap) and in  $(r, \phi)$ . It is therefore possible for a single track to give two hits in a single plane in a small region of the detector.

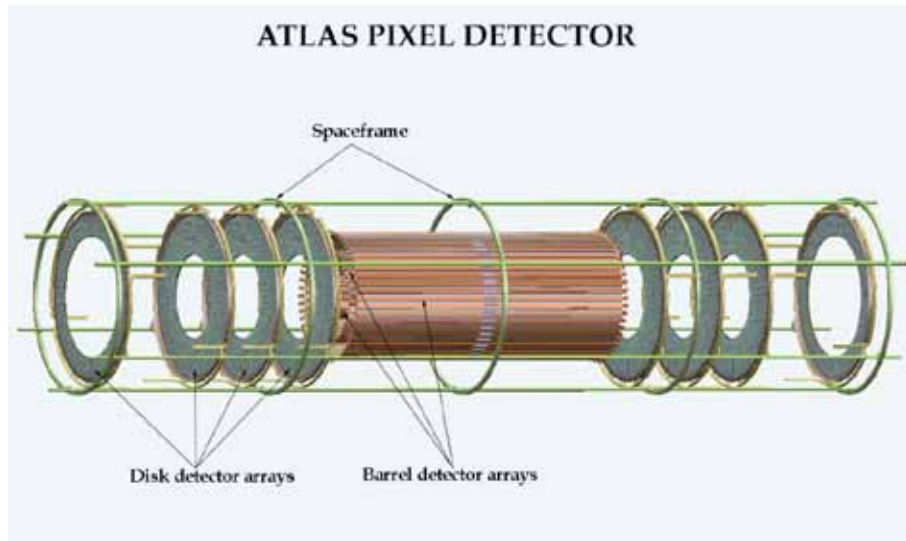


Figure 1.10: The pixel detector of ATLAS.

### Semiconductor tracker (SCT)

The semiconductor tracker (SCT) is designed to provide four high precision measurements per track in the intermediate radial range, contributing to the measurement of momentum, impact parameter and vertex position, as well as providing good pattern recognition by the use of high granularity. The barrel SCT consists of four layers of silicon microstrip detector at radii 300 cm, 373 cm, 447 cm and 520 cm. Each silicon detector is  $6.36 \times 6.40 \text{ cm}^2$ , containing 768 readout strips, each of  $80 \mu\text{m}$  pitch. Pairs of detectors are bonded end-to-end together to form 12.8 cm strips. A barrel SCT module (see figure 1.11) consists of two such detector pairs glued back-to-back at an angle of 40 mrad, separated by a heat transport plate, and the electronics is mounted above the detectors on a hybrid. In the end-caps, nine wheels provide measurements in  $z$ - $\phi$  and  $r$ . The end-cap modules are constructed in a similar way but use tapered strips. In the barrel, the strips are parallel to the beam direction whereas they are radial in the end-caps. Both the pixel and SCT detectors provide 10 hits with a precision of 10 to 20  $\mu\text{m}$ .



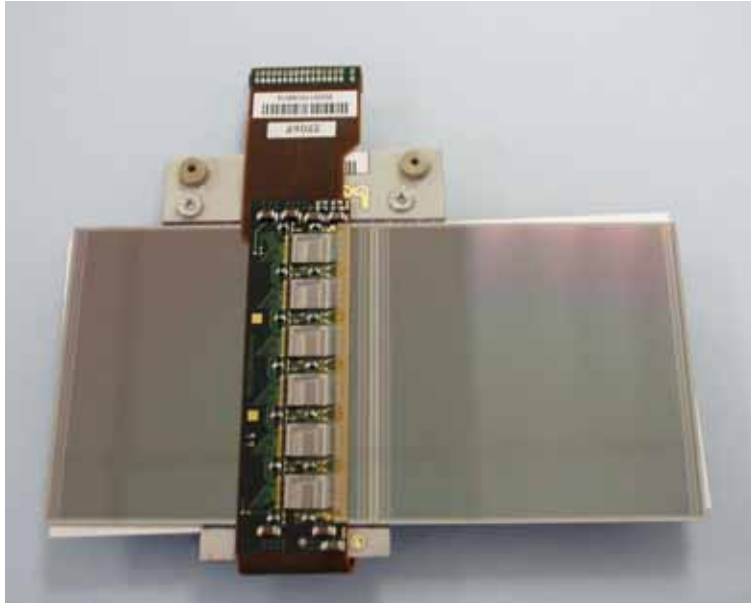


Figure 1.11: A barrel module of SCT tracker.

### Transition radiation tracker (TRT)

The transition radiation tracker (TRT), see figure 1.12, uses straw detectors, each one being 4 mm in diameter and of maximum length 150 cm. One straw acts as a cathode and is kept at high voltage of negative polarity. In the centre of this there is a  $30\mu\text{m}$  diameter gold-plated tungsten sense wire. The straws are filled with a gas mixture based on xenon (70%) with the addition of  $\text{CO}_2$  (27%) and  $\text{O}_2$  (3%). They can operate at the very high rates expected at the LHC by virtue of their small diameter and the isolation of the sense wires within individual gas envelopes. The layer of straws are interleaved with the radiators (polypropylene foils or fibers).

The TRT consists of a barrel with a half-length of 74 cm and two end-caps in the region  $83\text{ cm} < |z| < 335\text{ cm}$ . The barrel contains  $\sim 55000$  straws parallel to the beam axis and the end-caps  $\sim 320000$  radial straws. Typically the TRT will provide 36 measurements per track, albeit with a lower spatial precision than that of the SCT, of  $170\mu\text{m}$  in  $r\text{-}\phi$ , and a drift time measurement. The maximum drift time is 40 ns, significantly larger than the bunch crossing time of 25 ns, implying that the TRT must cope with high occupancy. Xenon gas in the TRT aids electron identification through the detection of transition radiation photons created in the radiator between the straws.



Figure 1.12: The transition radiation tracker of ATLAS.

### 1.3.4 Calorimetry

The calorimeters must measure, with sufficient resolution, the energy and direction of jets, electrons and photons, and  $E_{Tmiss}$  over a wide rapidity interval; the ability to identify the bunch crossing, and some capability to identify muons are also important requirements. In addition to energy measurement, particle identification is important, as  $\gamma/\pi^0$  and  $e/\pi$  separation.

The calorimeters are situated outside the solenoidal magnet that surrounds the inner detector. Unlike tracker subsystems, the intrinsic energy resolution of calorimeters improves with increasing energy, making them particularly suitable for use at high energy colliders. Fast detector response ( $< 50$  ns) and fine granular are required to minimize the impact of the pile-up on the physics performance. High radiation resistance is also needed, given the high particle fluxes expected over a period of operation of at least ten years.

The ATLAS calorimetry covers the range  $|\eta| < 5$  using different techniques and devices as best suited for the different requirements and radiation environment. A three dimensional view of the ATLAS calorimetry is shown in the figure 1.13. The ATLAS calorimetry consists of :

- an electromagnetic calorimeter composed of a barrel ( $|\eta| < 1.475$ ) and two end-caps ( $1.375 < |\eta| < 3.2$ )
- an hadronic calorimeter, with a barrel ( $|\eta| < 1.7$ ) and two end-caps ( $1.5 < |\eta| < 3.2$ )

- a forward calorimeter in order to improve the calorimeter hermeticity in the region  $3.2 < |\eta| < 4.9$ .

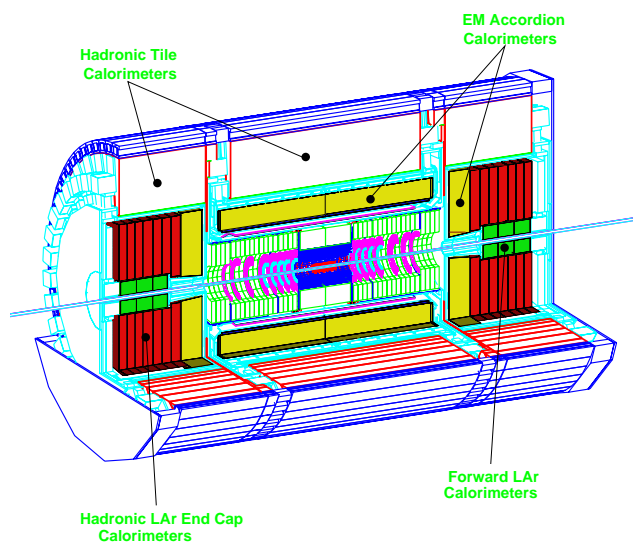


Figure 1.13: A three dimensional view of the ATLAS calorimetry.

The different calorimeters are segmented transversally (in  $\eta$  and  $\phi$  projective cells) and longitudinally (in depth) in samplings. The granularity of the different cells depends on the sampling and  $\eta$  for each calorimeter.

### The electromagnetic calorimeter

The electromagnetic (EM) calorimeter absorbs energy from particles that interact electromagnetically, which include charged particles and photons. It is a lead-liquid Argon sampling calorimeter with accordion shaped absorber plates and interleaved readout electrodes. The accordion calorimeter combines hermeticity with excellent energy and position resolution.

It covers the region of pseudorapidity up to  $|\eta| < 3.2$  and has three longitudinal samplings. Table 1.4 summarizes the granularity of the EMEC in pseudorapidity. The barrel covers  $|\eta| < 1.475$  and the two identical end-caps (see figure 1.14) cover  $1.375 < |\eta| < 3.2$ . The two EMEC cylinders are located inside the end-cap cryostat at  $z \sim -350$  cm and  $z \sim 350$  cm of the nominal interaction point. The total amount of material traversed by

particles prior to the calorimeter face is about  $2.3X_0$  at  $\eta = 0$ , increasing in  $\eta$  due to the angle of the particle. A presampler in front of the electromagnetic barrel  $|\eta| < 1.52$  and in front of the EMEC  $1.5 < |\eta| < 1.8$  is needed in order to measure the energy loss in the material in front of the calorimeter: the inner detector, solenoid and cryostat walls. It also helps in measuring the direction of electromagnetic shower with the necessary accuracy. In the transition region between the barrel and end-caps, i.e. the boundary between the two cryostats, the amount of material reaches  $7X_0$ , which is corrected for by inserting a scintillator slab in the gap between the barrel and end-cap cryostat. A more detailed study of this detector will be done at the third chapter.

	$\eta$ Range	Front	Middle	Back
Barrel	$ \eta  \leq 1.475$	$0.025/8 \times 0.1$	$0.025 \times 0.025$	$0.05 \times 0.025$
end-cap	$1.375 \leq  \eta  \leq 1.425$	$0.05 \times 0.1$	$0.05 \times 0.025$	-
	$1.425 \leq  \eta  \leq 1.5$	$0.025 \times 0.1$	$0.025 \times 0.025$	-
	$1.5 \leq  \eta  \leq 1.8$	$0.025/8 \times 0.1$	$0.025 \times 0.025$	$0.050 \times 0.025$
	$1.8 \leq  \eta  \leq 2.0$	$0.025/6 \times 0.1$	$0.025 \times 0.025$	$0.050 \times 0.025$
	$2.0 \leq  \eta  \leq 2.4$	$0.025/4 \times 0.1$	$0.025 \times 0.025$	$0.050 \times 0.025$
	$2.4 \leq  \eta  \leq 2.5$	$0.025 \times 0.1$	$0.025 \times 0.025$	$0.050 \times 0.025$
	$2.5 \leq  \eta  \leq 3.2$	-	$0.1 \times 0.1$	$0.1 \times 0.1$

Table 1.4: Transverse granularity ( $\Delta\eta, \Delta\phi$ ) of the Electromagnetic Calorimeter in  $\eta$ .

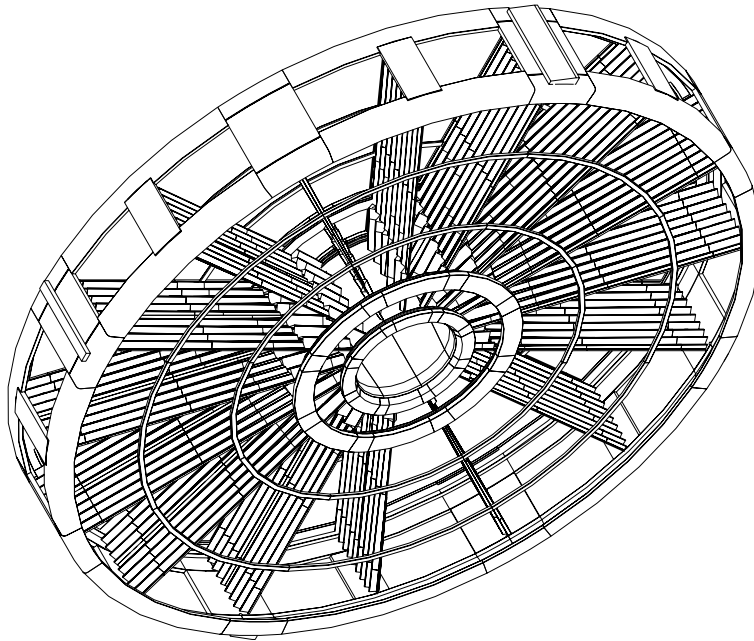


Figure 1.14: End-cap of the electromagnetic calorimeter.

### The hadronic calorimeter

The main function of the hadronic calorimeter is the identification, reconstruction and measurement of jets, and the measurement of the missing  $E_T$  in an event. It is primarily concerned with jet mass reconstruction, and the calorimeter energy resolution is not the dominant contribution ( $\frac{\sigma}{E} = \frac{50\%}{\sqrt{E(GEV)}} \oplus 3\%$ ). Instead the hadronic end-cap calorimeter design aim is for a compact, reliable, radiation tolerant design of minimum cost. It is necessary a forward coverage to  $|\eta| < 5$  and a fine lateral granularity at very high- $p_T$  (for very collimated jets).

The hadronic calorimetry [13] covers the pseudorapidity region  $|\eta| < 3.2$  and uses a combination of two technologies. The barrel is composed of a central part ( $|\eta| < 1.0$ ) and two extended barrels  $0.8 < |\eta| < 1.7$ . They are divided into 64 modules and employ a technique using iron scintillator tiles with wave length shifts (WLS) fiber readout (Tilecal). The iron plates and scintillator plates are perpendicular to the beam axis and staggered in depth, simplifying the mechanical construction and the fiber routing (see figure 1.15). Light is collected by WLS fibers running on either side of scintillator plates.

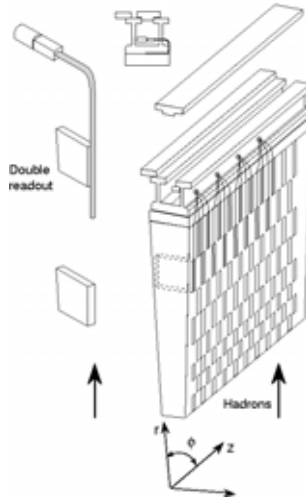


Figure 1.15: The principle of the Tile Calorimeter design.

In the range  $1.5 < |\eta| < 3.2$ , there are two end-cap hadronic calorimeters, HEC1 and HEC2, and each end-cap consists of 32 modules (see figure 1.16). For those, copper absorber plates in liquid Argon are used. Among other aspects this technique alleviates radiation resistance problems. The copper plates are perpendicular to the beam axis. The HEC has a lateral modularity of  $\Delta\eta \times \Delta\phi = 0.1 \times 0.1$  out to pseudorapidity of 2.5, and  $\Delta\eta \times \Delta\phi = 0.2 \times 0.2$  beyond 2.5. The end-caps will be in the same cryostat as EMEC.

Table 1.5 summarizes the granularity of the hadronic calorimeter.

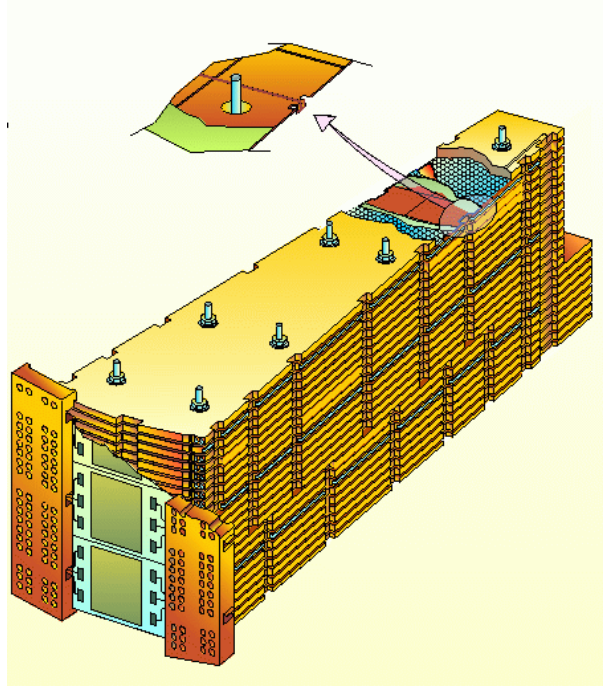


Figure 1.16: Hadronic end-cap module.

	$\eta$ Range	Front	Middle	Back
Barrel	$ \eta  \leq 1.0$	$0.1 \times 0.1$	$0.1 \times 0.1$	$0.2 \times 0.1$
	$0.8 \leq  \eta  < 1.7$	$0.1 \times 0.1$	$0.1 \times 0.1$	$0.2 \times 0.1$
end-cap	$1.5 \leq  \eta  < 2.5$	$0.1 \times 0.1$	$0.1 \times 0.1$	$0.1 \times 0.1$
	$2.5 \leq  \eta  < 3.2$	$0.2 \times 0.2$	$0.2 \times 0.2$	$0.2 \times 0.2$

Table 1.5: Transverse granularity ( $\Delta\eta, \Delta\phi$ ) of the hadronic calorimeter.

In both technologies the hadronic shower develops through interactions of the hadrons with the high  $Z$  nuclei, iron or copper, and one measures the ionization energy left by charged tracks in the cascade in the active material, scintillator or liquid Argon. The hadronic cascade is initiated usually in the electromagnetic sections, this is particularly so in the barrel, so that one needs to add the signals from both electromagnetic and hadronic sections. Reconstruction algorithms are being developed making use of data taken with prototypes for both calorimeter types exposed to test beams at CERN.

### The forward calorimeter

In order to achieve a good hermeticity, thus providing excellent resolution in missing transverse energy, a forward calorimeter (FCAL) completes the coverage for jets in ATLAS in the pseudorapidity region  $3.2 < |\eta| < 4.9$ . Owing to the extreme particle and energy flux environment at these high values of rapidity, radiation hardness is the prevailing requirement. The annual radiation fluency at the FCAL is  $10^{16}$  *neutrons cm<sup>-2</sup>* and  $2 \times 10^6$  *Gy*. Due to the energy of the particles in this region, the stochastic term in the energy resolution is not the most important, and the lateral modularity has to be chosen such that the angular resolution does not dominate the transverse energy resolution. In order to achieve a  $E_T$  resolution of 10%, the requirement on the energy resolution is  $\frac{\sigma}{E}(\text{jets}) \leq \frac{70\%}{\sqrt{E(\text{GeV})}} \oplus 7\%$  and the lateral modularity is  $\Delta\eta \times \Delta\phi = 0.2 \times 0.2$ .

ATLAS has decided to integrate the forward calorimeter into the end-cap calorimeter at a distance of 5 m from the interaction point. The forward calorimeter is segmented longitudinally in three modules: FCAL1 (electromagnetic module) and FCAL2 and FCAL3 (hadronic module). The structure of the FCAL2 and FCAL3 consists of a paraxial arrangement of tungsten rods inside copper tubes; the liquid Argon gap between the rod and tube providing the ionization region. FCAL1 is very similar except that the matrix and the electrode rods are made of copper. FCAL1 contains the maximum of electromagnetic showers, and thus the maximum ionization and heat load; hence the use of copper.

### 1.3.5 The muon spectrometer

The muon spectrometer is required to:

- Identify, reconstruct and measure the momenta of muon tracks, as well as provide an association with measurements in the inner detector. Good transverse momentum resolution must be maintained down to 5 GeV as well as a coverage in pseudorapidity of up to 3.
- Trigger on both single-muon and multi-muon events. The trigger system must have a wide acceptance, be efficient and selective.
- All muons must be unambiguously associated with the correct bunch crossing using timing information provided by the trigger chambers.

Momentum and mass resolutions of the order of 1% are important for the reconstruction of narrow final states with two or four muons, for background rejection and for charge identification. The muon spectrometer must also measure a second coordinate in the non

bending plane for muon tracks, with a spatial resolution of  $5 - 10 \text{ mm}$  to ensure good track reconstruction and momentum measurement.

The ATLAS muon spectrometer (see figure 1.17) consists of three layers of measuring stations using four different types of chambers. The precision measurement is performed by the so-called Monitored Drift Tube chambers (MDT), see figure 1.18, covering most of the acceptance ( $|\eta| < 2$ ), supplemented by the 32 Cathode Strip Chambers (CSC) in the very forward region ( $2 < |\eta| < 2.7$ ) at higher particles. Each of the MDT chambers consist of two assemblies of three or four layers of high pressure drift tubes, separated by supports in which are integrated optical alignment systems monitoring the geometrical deformations of the large (up to 6 meter long) chambers. The resolution of the individual drift tube is  $\sim 80 \mu\text{m}$ . About 1200 MDT chambers are required to cover the large area of  $5500 \text{ m}^2$ . The CSC are multiwire proportional chambers, with a resolution of  $\sim 60 \mu\text{m}$ .

In the barrel region (up to  $|\eta| = 1$ ), the trigger function is provided by 1136 Resistive Plate Chambers (RPC). They cover an area of  $3650 \text{ m}^2$  and have a very good space time resolution of  $1 \text{ cm} \times 1 \text{ ns}$ . In the forward region ( $1.0 < |\eta| < 2.4$ ), as a trigger chambers, we have 1584 Thin Gap Chambers (TGC), at higher particle fluxes and with  $2900 \text{ m}^2$ . These chambers are similar to multiwire proportional chambers, the trigger signals are obtained from the wires and read-out strips oriented orthogonal to the wires.

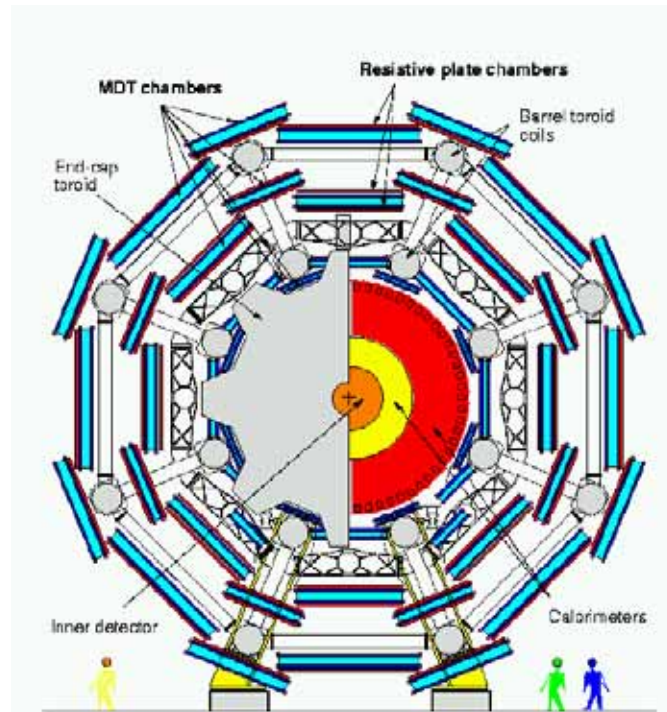


Figure 1.17: The muon spectrometer.



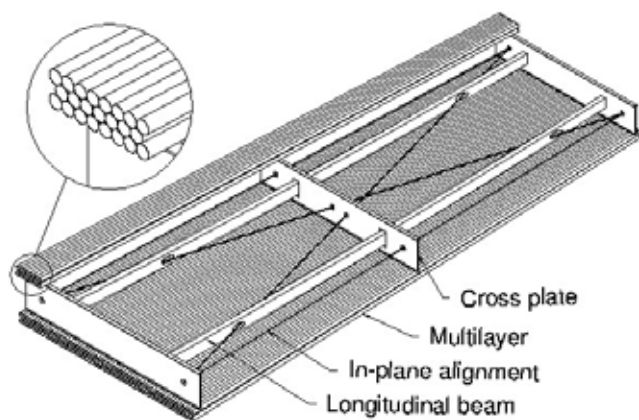


Figure 1.18: A MDT module.

### 1.3.6 The magnet system

The ATLAS detector uses two large magnet systems to bend charged particles so that their momenta can be measured.

#### The central solenoid

The ATLAS central solenoid (see figure 1.19) is a superconducting magnet of length 5.3 *m* designed to provide an axial magnetic field of 2 T in the inner tracking volume. The positioning of the central solenoid in front of the electromagnetic calorimeter allows the use of a more compact design and reduces the overall weight of the detector. This design also results in a smaller magnetic field in the electromagnetic calorimeter, reducing the transverse shower spread. The 2 T magnetic field allows even very energetic particles to curve enough for their momentum to be determined, and its nearly uniform direction and strength allow measurements to be made very precisely. The presence of extra material in front of the electromagnetic calorimeter however degrades the calorimeter performance. To minimize this degradation, the coils have been designed to be as thin as is both reliably and safely possible. Therefore, optimum electromagnetic calorimeter performance requires that there be a minimum of material in front of the calorimetry, whilst for the

inner detector, uniformity and a maximum field are required.

The yoke for the magnetic flux return is the iron absorber of the tile calorimeter. This is separate from the solenoid coil end resulting in a non uniform field in the inner detector tracking volume. The main consequences of such a non-uniform field are:

- Deviation of the track trajectory from that of a perfect helix. This has consequences for pattern recognition algorithms and level-2 track searches.
- Reduced bending power, resulting in a degradation in  $p_T$  resolution.



Figure 1.19: The central solenoid magnet.

### The aircore toroids

The outer toroidal magnetic field is produced by eight very large air-core superconducting barrel loops and two end-caps (see figure 1.20), all situated outside the calorimeters and within the muon system. This magnetic field is 26 meters long and 20 meters in diameter, and it stores 1.2 GJ of energy. Its magnetic field is not uniform, because a solenoid magnet of sufficient size would be impossible (or at least prohibitively expensive) to build. Fortunately, measurements need to be much less precise to measure momentum accurately in the large volume of the muon system.

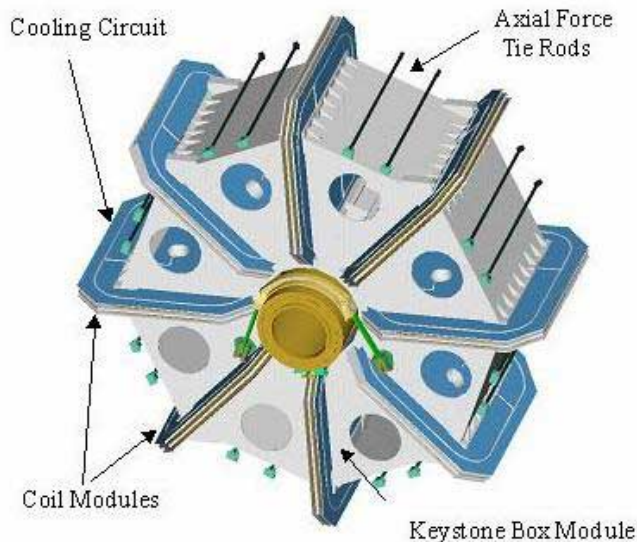


Figure 1.20: The end-cap toroidal magnet.

### 1.3.7 Trigger and data acquisition

The total inelastic non-diffractive proton-proton cross-section at the LHC of  $80 \text{ m}\sigma$ , which corresponds to an interaction rate of  $10^9 \text{ Hz}$  at the design luminosity, places rigorous requirements upon the trigger systems of all LHC experiments. Data must be accepted at the full bunch crossing rate of  $40 \text{ MHz}$ , requiring decisions to be made every  $25 \text{ ns}$ . At the design luminosity, each bunch crossing contains approximately 23 events. Significantly smaller cross-sections for physics processes of interest as well as small branching ratios to final states require that a high rate background be rejected whilst good efficiency for physics processes is maintained.

The ATLAS trigger (see figure 1.21) must be capable of triggering on the final states of decays which comprise the ATLAS physics program. The following trigger objects must be triggered on:

- Both low and high  $p_T$  decays of charged leptons for B-physics and decays of heavy objects respectively.
- High- $p_T$  quark and gluon jets.
- Electroweak gauge bosons.

- Missing  $E_T$  of weakly interacting particles.

The ATLAS trigger system [15] comprises three distinct levels of online event reconstruction and selection: level-1, level-2 and the event filter (EF). Each subsequent level reduces the rate of data by applying selection criteria. The final output rate to storage can be no more than approximately 100 Hz, requiring a rejection against minimum-bias events (events that have not been selected for specific properties) of  $\sim 10^7$ .

- **Level-1 trigger (LVL1)**

The principal requirement of this level is that it identify unambiguously interesting physics events, whilst reducing the overall rate. No tracking information is used at level-1 due to timing restrictions and the inherent complex nature of the information from the inner detector. It takes into account information from calorimeters with reduced granularity and from muon detectors. The time taken to make a decision in this level is approximately  $2 \mu s$ , during which time event data from the different sub-detector systems is stored in pipeline memories. This level reduce the events rate to lower than 100 KHz (initially is around 40 MHz).

- **Level-2 trigger (LVL2).**

Level-2 processors make use of full granularity information from the inner detector as well as from the muon detectors and calorimetry to extract features of interest, measure track  $p_T$  and reconstruct decay vertexes. The output rate is approximately 3 KHz.

- **Event filter (EF)**

Complete event reconstruction is performed by the event filter on those events passing the level-2 trigger. The time available for a decision at the event filter is 1 s and so more “offline-like” algorithms can be employed to reject background. The final event size is expected to be approximately 1MB at 100 Hz resulting in  $\sim 10^{15}$  bytes of data per year.

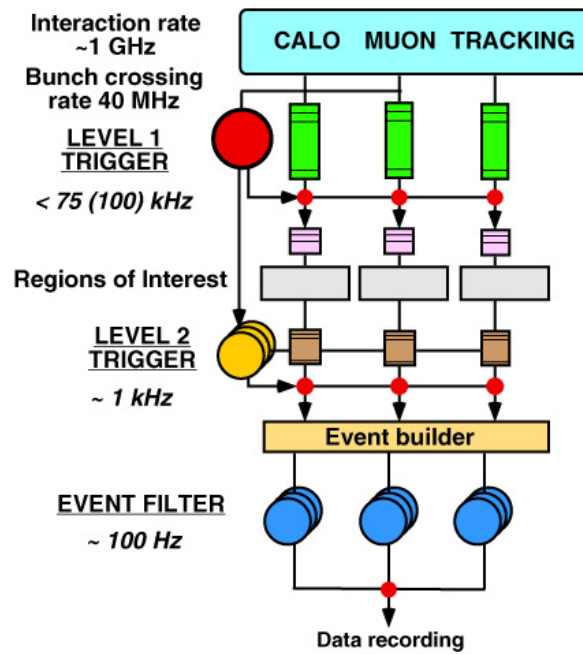


Figure 1.21: The ATLAS trigger system.

# Chapter 2

## Principles of calorimetry

### 2.1 Introduction

In this chapter the basic interaction mechanisms of charged and neutral particles are presented [16]. These processes are the basis of all current particle detection devices and thus determine the sensitivity and efficiency of a detector. The ionization energy loss of charged particles is fundamental to most particle detectors and is therefore described in more detail. Photons are measured via the photoelectric effect, Compton scattering or pair production, and neutrons through their nuclear interactions.

In the following we distinguish between the interaction of charged and neutral particles. In most cases the observed signature of a particle is its ionization, where the liberated charge can be collected and amplified, or its production of electromagnetic radiation which can be converted into a detectable signal. In this sense neutral particles are only detected indirectly, because they must first produce in some kind of interaction a charged particle which is the measured in the usual way.

### 2.2 Energy loss of charged particles

Charged particles interact with a medium via electromagnetic interactions by the exchange of photons. If the range of photons is short, the absorption of virtual photons constituting the field of the charged particle will give rise to ionization of the material. If the medium is transparent Cherenkov radiation can be emitted above a certain threshold. But also sub-threshold emission of electromagnetic radiation can occur, if discontinuities of the dielectric constant of the material are present (transition radiation). The emission of

real photons by decelerating a charged particle in a Coulomb field also constitutes an important energy loss (bremsstrahlung).

Basically, when electrons or positrons traverse a block of matter they lose energy in two different ways, each of them dominant in two different energy ranges. Namely:

- by ionization i.e. through collisions with electrons in the atomic medium
- through radiation due to the acceleration of the incoming leptons in the Coulomb field of the nuclei.

The energy loss per unit length can be written as follows:

$$\left(\frac{dE}{dx}\right)_{tot} = \left(\frac{dE}{dx}\right)_{ionization} + \left(\frac{dE}{dx}\right)_{radiation}$$

As we will discuss next, the energy loss by ionization is the dominant process at low energies while bremsstrahlung is dominant at high energies.

### 2.2.1 Energy loss due to ionization

Let us consider a heavy particle, with charge  $ze$ , mass  $M$  and velocity  $v$  traversing a block of matter. Let us assume that at a distance  $b$  of the incident particle direction an atomic electron is found. One can use a semi-classical approximation assuming the electron to be free and at rest during the time the interaction takes place. One usually further assumes that the direction of the incident particle is not changed as it is much heavier than the atomic electron.

*General case: the Bethe-Bloch formula*

Within these approximations, Bohr obtained expressions for energy loss of heavy particles ( $\alpha$  particles of heavy nuclei), which were found to properly describe experimental data. For lighter particles like protons a disagreement with experiment was found, because quantum effects were not taken into account. The correct quantum-mechanical calculation was first performed by Bethe and Bloch, obtaining this formula:

$$-\left(\frac{dE}{dx}\right)_{ioniz} = 2\pi N_a r_e^2 m_e c^2 \rho \frac{Z z^2}{A \beta^2} \left[ \ln \left( \frac{2m_e \gamma^2 v^2 W_{max}}{I^2} \right) - 2\beta^2 \right]$$

- $E$  : incident particle energy  
 $x$  : path length  
 $N_a$  : Avogadro's number ( $6.022 \times 10^{23} \text{ mol}^{-1}$ )  
 $r_e$  : classical electron radius ( $2.817 \times 10^{-13} \text{ cm}$ )  
 $m_e$  : electron mass  
 $\rho$  : density of absorbing material  
 $A$  : atomic weight of absorbing material  
 $Z$  : atomic number of absorbing material  
 $z$  : charge of incident particle in units of  $e$   
 $\beta$  :  $v/c$  of the incident particle  
  
 $\gamma$  :  $1/\sqrt{(1 - \beta^2)}$   
 $W_{max}$  : maximum energy transfer in a single collision  
 $I$  : mean excitation potential

In practice, two more corrections are needed, the so called density effect and the shell effect [17]:

$$-\left(\frac{dE}{dx}\right)_{ioniz} = 2\pi N_a r_e^2 m_e c^2 \rho \frac{Z}{A} \frac{z^2}{\beta^2} \left[ \ln \left( \frac{2m_e \gamma^2 v^2 W_{max}}{I^2} \right) - 2\beta^2 - \delta - 2\frac{\zeta}{Z} \right]$$

$\delta$ : density effect correction, which arises from the fact that the electric field of the particle also tends to polarize the atoms along its path.

$\zeta$ : shell effect correction, which accounts for effects when the velocity of the incident particle is comparable or smaller than the orbital velocity of the bound electrons.

The maximum energy transfer occurs in head on collisions between the incident particle and the atomic electron. By simple kinematics considerations one obtains

$$W_{max} = \frac{2m_e c^2 \eta^2}{1 + 2s\sqrt{1 + \eta^2} + s^2}$$

with  $s = m_e/M$  and  $\eta = \beta\gamma$ .

The excitation potential  $I$  is given by  $h\bar{\nu}$  where  $\bar{\nu}$  is the mean orbital frequency for electrons in the material. Theoretically it can be calculated as the logarithmic average of the orbital frequencies in the various atomic levels. In practice this is not so easy. For different materials one uses a semi-empirical formula:



$$\frac{I}{Z} = 12 + \frac{7}{Z} eV \quad Z < 13$$

$$\frac{I}{Z} = 9.76 + 58.8 Z^{-1.19} eV \quad Z \geq 13$$

which gives a reasonable approximation for most cases.

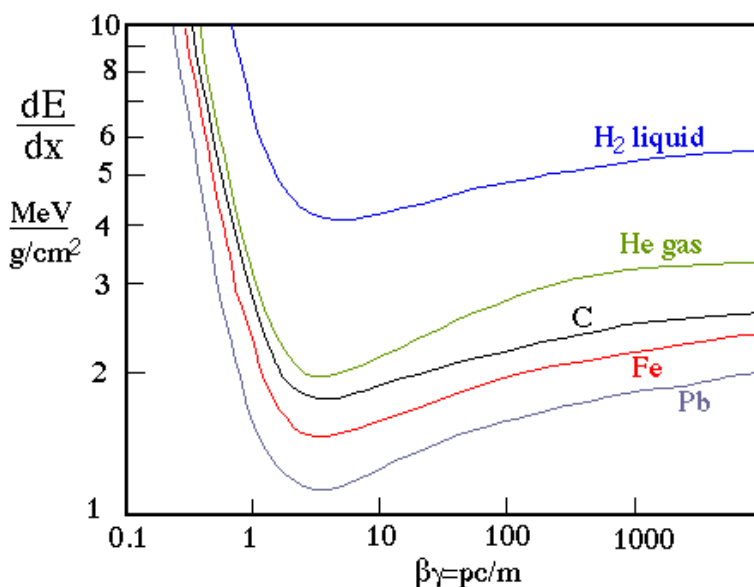


Figure 2.1: Ionization energy loss per unit of length in liquid hydrogen, gaseous helium, carbon, iron and lead.

The energy loss per unit length depends on the energy of the incident particle. It exhibits a sharp fall off, proportional to  $1/\beta^2$  for low  $\beta$  values, it reaches a minimum known as the ionization minimum (around  $\beta\gamma = 3$ ), and finally shows a logarithmic increase (relativistic rise) leading to a plateau (*the Fermi plateau*), see figure 2.1. For energies bigger than the ionization minimum, each particle shows a characteristic curve. It can be used to identify particles in this energy range.

The ionization energy loss is statistically distributed around its mean value. The distribution, often referred to as *energy straggling*, is approximately gaussian for thick absorbers, but develops asymmetry and a tail towards high energies for decreasing thickness; it becomes a Landau distribution for very thin absorbers (as we will see later).

#### *The case for electrons and positrons*

If one wishes to go from the general case discussed above to that of energy loss by electrons (or positrons) one will have to modify the Bethe-Bloch formula in order to take into account that the mass of the incident particle is as light as that of the target atomic electrons. Furthermore one has to consider Fermi statistics.

The maximum energy transfer simplifies to  $W_{max} = T_e/2$  where  $T_e$  is the kinetic energy of the incident particle. One obtains:

$$-\left(\frac{dE}{dx}\right)_{ioniz} = 2\pi N_a r_e^2 m_e c^2 \rho \frac{Z}{A} \frac{1}{\beta^2} \left[ \ln \left( \frac{\tau^2(\tau+2)}{2(I/m_e c^2)^2} \right) + F(\tau) - \delta - 2\frac{\zeta}{Z} \right]$$

with  $\tau$  the incident electron (or positron) kinetic energy in units of  $m_e c^2$ , i.e.:

$$\tau = T_e / (m_e c^2)$$

and  $F(\tau)$  is given by:

$$F(\tau) = 1 - \beta^2 + \frac{\frac{\tau^2}{8} - (2r+1)\ln(2)}{(\tau+1)^2}$$

for  $e^-$  and

$$F(\tau) = 2\ln 2 - \frac{\beta^2}{12} \left( 23 + \frac{14}{\tau+2} + \frac{10}{(\tau+2)^2} + \frac{4}{(\tau+2)^3} \right)$$

for  $e^+$ .

### 2.2.2 Energy loss by radiation: Bremsstrahlung

If a charged particles is decelerated in the Coulomb field of a nucleus a fraction of its kinetic energy will be emitted in form of real photons (bremsstrahlung). The electron and positron are the only particles for which energy loss by bremsstrahlung is significantly important, see figure 2.2 for a diagrammatic representation.

In fact the semi-classical calculation for the bremsstrahlung cross-section for any given particle of mass  $M$  reads [18]:

$$\left(\frac{d\sigma}{dk}\right)_{rad} \simeq \frac{5e^2}{\hbar c} z^4 Z^2 \left(\frac{mc}{Mv}\right)^2 \frac{r_e^2}{k} \ln \left(\frac{Mv^2\gamma^2}{k}\right)$$

with  $k$  the energy of the produced photon, i.e.

$$\left(\frac{d\sigma}{dk}\right)_{rad} \propto M^{-2}$$

Thus, the bremsstrahlung cross-section for a muon,  $m_\mu = 105.7$  MeV, is approximately 44000 times smaller than that for an electron,  $m_e = 0.51$  MeV. We can also note that the

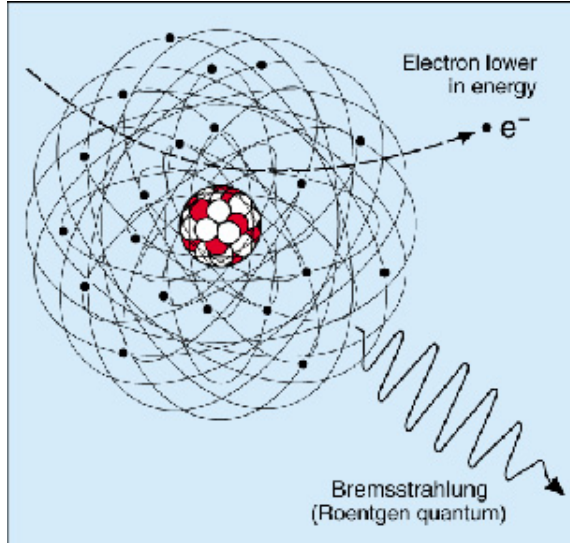


Figure 2.2: Feynman diagram for bremsstrahlung.

cross-section is proportional to  $Z^2$ , i.e. to the atomic number squared of the traversed material. This explains the use of high  $Z$  materials ( Fe, Cu, Pb, U) in calorimeters, in order to get a bigger energy loss by radiation. Finally we can add that cross-section for bremsstrahlung shows the typical ultraviolet divergence for  $QED$  processes, i.e. the cross-section becomes very large as the radiated photon becomes very soft.

Up to now we have only dealt with the interaction of the incident particle with the nuclear Coulomb field. Obviously one has to take into account the screening effect due to the atomic electrons. This effect is parametrized in terms of the quantity [19]  $\xi = \frac{100m_e c^2}{Z^{1/3}} \frac{k}{E_i E_f}$ , where  $E_i$  and  $E_f$  are the initial and final electron (positron) energies and  $k$  the energy of the radiated photon. In the case of negligible screening, something which happens for low  $Z$  materials i.e. very few atomic electrons,  $\xi \gg 1$ , the cross-sections can be written as

$$\left(\frac{d\sigma}{dk}\right) = \frac{4\sigma_0}{k} \left(1 + w^2 - \frac{2}{3}w\right) \left[\ln\left(\frac{2E_i E_f}{m_e c^2 k}\right) - \frac{1}{2} - f(Z)\right]$$

with:

$$w = E_f/E_i$$

$$\sigma_0 = \alpha Z^2 r_e^2$$

with  $\alpha = \frac{e^2}{\hbar c}$

The function  $f(Z)$  is a small correction to the Born approximation which takes into

account the interaction of the final state electron with the nucleus Coulomb field. Davies found the following parametrization:

$$f(Z) \simeq a^2[(1 + a^2)^{-1} + 0.020206 - 0.0369a^2 + 0.0083a^4 - 0.002a^6]$$

with  $a = Z/137$ .

Full screening corresponds to the limit  $\xi \simeq 0$  ( $\xi \ll 1$ ). This happens for high  $Z$  values. In this case, the cross-section reads:

$$\left(\frac{d\sigma}{dk}\right) = \frac{4\sigma_0}{k} \left\{ \left(1 + w^2 - \frac{2}{3}w\right) \left[\ln\left(\frac{183}{Z^{1/3}}\right) - f(Z)\right] + \frac{w}{9} \right\}$$

The energy loss due to radiation can now be calculated by integrating the cross-section times the photon energy over the allowable energy range, i.e.,

$$-\left(\frac{dE}{dx}\right)_{rad} = \int_0^{k_{max}} kn_a \left(\frac{d\sigma}{dk}\right)_{rad} dk$$

with  $k_{max} = E_i - mc^2$  the maximum photon energy and  $n_a = \rho N_a/A$ ,  $n_a$  the number of atoms/cm<sup>3</sup>. Let  $-\left(\frac{dE}{dx}\right)_{rad} = n_a E_i \sigma_{rad}$  with:

$$\sigma_{rad} = \frac{1}{E_i} \int_0^{k_{max}} k \left(\frac{d\sigma}{dk}\right)_{rad} dk$$

In the case of full screening and with  $E_i \gg mc^2/\alpha Z^{1/3}$  one obtains:

$$\sigma_{rad} = 4\sigma_0 \left[ \ln\left(\frac{183}{Z^{1/3}}\right) + \frac{1}{18} - f(Z) \right]$$

Note that in most cases,  $\sigma_{rad}$  is independent of the initial electron energy. Thus, the energy loss  $-(dE/dx)_{rad}$  is proportional to  $E_i$ .

The radiation length,  $X_0$ , is defined as the distance an electron needs to penetrate in a block of matter in order that its energy be degraded by a factor  $e^{-1}$ . Since as we have deduced:

$$\frac{dE}{E} = -n_a \sigma_{rad} dx$$

with  $\sigma_{rad}$  independent of the energy.

Therefore:

$$E = E_i e^{-(n_a \sigma_{rad} x)} = E_i e^{-\left(\frac{x}{X_0}\right)}$$

When  $x = X_0$ , we find  $E = E_i e^{-1}$ . Thus, we conclude:

$$X_0 = (n_a \sigma_{rad})^{-1}$$

If the traversed block of matter is made up of different materials, then we will obtain:

$$\frac{1}{X_0} = \sum_{i=1}^n \omega_i \left(\frac{1}{X_0}\right)_i$$

with  $\omega_i$  the massic fraction of element  $i$  and  $(X_0)_i$  its radiation length of the material  $i$ . In table 2.1 we show typical values for the radiation length for several materials.

### 2.2.3 Critical energy

The critical energy  $E_c$  (see figure 2.4) is defined as that energy at which the energy loss by radiation equals that by ionization, i.e.

$$\left(\frac{dE}{dx}\right)_{rad} = \left(\frac{dE}{dx}\right)_{ioniz}$$

for  $E = E_c$ .

Above this critical energy, the energy loss by radiation will become dominant. An approximate formula by Bethe-Heitler for  $E_c$  reads [20]:

$$E_c \simeq \frac{1600 m_e c^2}{Z}$$

Figure 2.4 and table 2.1 show values for critical energies for some solids and liquids.

We end this subsection with the remark that in modern particle physics experiments one is dealing with very energetic electrons, so that indeed energy loss by bremsstrahlung is the dominant process in the development of the electromagnetic showers.

### 2.2.4 Energy Straggling: the energy loss distribution

We have studied the mean energy loss suffered by charged particles when passing through matter. For any given particle, however, the amount of energy lost will not, in general,

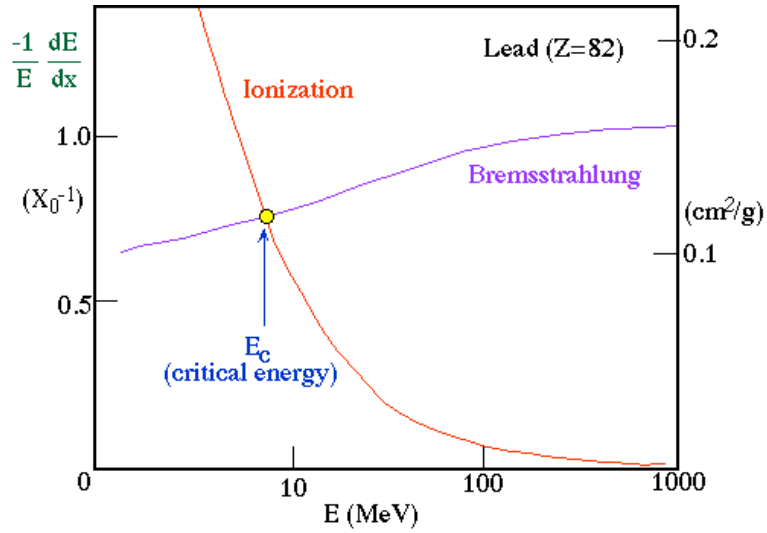


Figure 2.3: Energy loss per unit of length as a function of the energy.

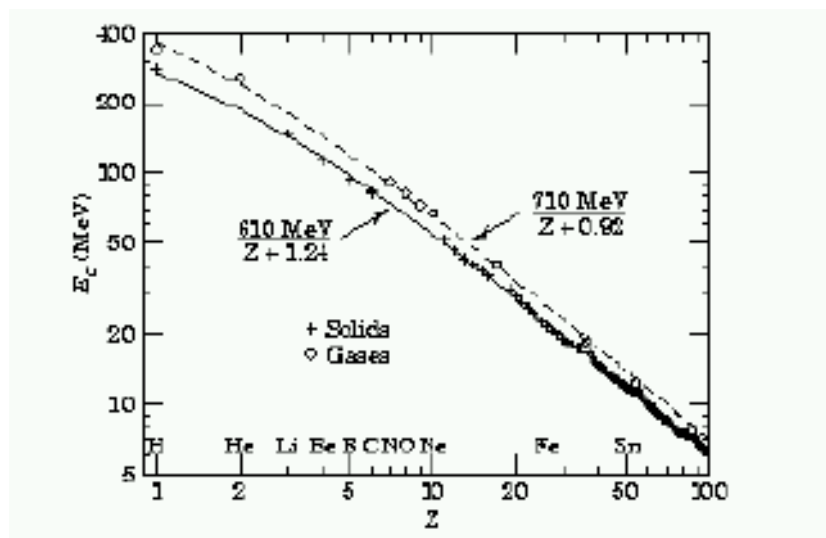


Figure 2.4: Critical energy as a function of  $Z$ .

Material	Critical Energy (MeV)	Radiation Length (cm)
Air	102	30050
$H_2O$	92	36.1
Argon	45.6	14.0
Al	51	8.9
Fe	27.4	1.76
Cu	24.8	1.43
Pb	9.51	0.56

Table 2.1: Critical energy and radiation length for different materials.

be equal to this mean value because of the statistical fluctuations which occur in the number of collisions suffered and in the energy transferred in each collision. Theoretically, calculating the distribution of energy losses for a given thickness of absorber is a difficult mathematical problem and is generally divided into two cases: thick absorbers and thin absorbers.

- *Thick absorber*

We talk about thick absorber when the number of collisions is very high as in the case of an electron impinging on a lead plate with a thickness given by several radiation lengths. In that case it can be proved that the distribution of the energy loss is a Gaussian. This is a consequence of the central limit theorem, which states that the sum of  $N$  random variables tends to a Gaussian when  $N$  becomes very large. In our case the random variable is  $\delta E$ , the energy loss due to ionization in a single collision. The total energy loss will be the sum over a many independent  $\delta E$ , all of them following the same distribution function. In the limit that the number of collisions is large, then we obtain a Gaussian

$$f(x, \Delta) \propto \exp\left(\frac{-(\Delta - \bar{\Delta})^2}{2\sigma^2}\right)$$

with  $x$  the absorber thickness and  $\Delta$  the energy lost in the absorber.

For non-relativistic heavy particles the spread  $\sigma_0$  of this Gaussian was calculated by Bohr to be:

$$\sigma_0^2 = 0.1569\rho\frac{Z}{A}x[MeV^2],$$

where  $\rho$ ,  $Z$  and  $A$  are the density, atomic number and atomic weight of the material respectively.

This is why, in forthcoming analysis, when we show the distribution of energy measured in the calorimeter, it will always be Gaussian shaped.

- *Thin absorbers*

In contrast to the situation discussed above, one says that a particle traverse a thin layer of material when the number of collisions  $N$  is small, so that application of the central limit theorem is not justified. This is the situation of an electron or photon traversing a block of matter a fraction of a radiation length or a muon traversing any finite size material

This case has been originally treated by Landau. A simple approximate function which describes the energy loss of a charged particle traversing a thin layer of material is given by the Moyal function:

$$f(\lambda) = \frac{1}{\sqrt{2\pi}} \exp -\frac{1}{2}(\lambda + \exp -\lambda)$$

where the reduced energy variable  $\lambda$  represents the normalized deviation from the most probable energy loss  $(\Delta E)_{mp}$ :

$$\lambda = \frac{\Delta E - (\Delta E)_{mp}}{\xi}$$

where  $\xi = K \frac{Z}{A} \frac{\rho}{\beta^2} x$ .

This function is not Gaussian shaped and exhibits the characteristic tail at high energy losses.

## 2.3 Scattering of charged particles

### 2.3.1 Rutherford Scattering

In addition to inelastic collisions with the atomic electrons, when a charged particle traverses a block of matter, we have to consider Coulomb interactions with the nuclei (although its probability is lower than one for inelastic collisions). The scattering of a spin 0 particle of charge  $z$  on a target of nuclear charge  $Z$  is mediated by the electromagnetic interaction. The cross-section for this process is given by the well-known Rutherford formula:

$$\frac{d\sigma}{d\Omega_R} = Z^2 z^2 r_e^2 \left( \frac{Mc}{\beta p} \right) \frac{1}{4 \sin^4 \theta / 2}$$



where  $p$  denotes the incident momentum.

The scattering angle is:

$$\theta = \frac{2zZe^2}{\beta cb} \frac{1}{p}$$

For spin  $\frac{1}{2}$  particles, like electrons, one has according to Mott:

$$\frac{d\sigma}{d\Omega_M} = \frac{d\sigma}{d\Omega_R} \left(1 - \beta^2 \sin^2(\theta/2)\right)$$

Because of its  $\theta$  dependence, the vast majority of these collisions result, therefore, in a small angular deflection of the particle. We assume here that the nuclei are much more massive than the incident particles so that the small energy transfer to the nucleus is negligible. The particle thus follows a random zigzag path as it traverses the material. The accumulative effect of these small angle scattering is, however, a net deflection from the original particle direction. Both expressions show the typical singularity at small scattering angles  $\Theta$ .

### 2.3.2 Multiple Scattering

From the previous section one can see that the average scattering angle  $\langle\theta\rangle$  is zero. Multiple scattering is the effect of Coulomb scattering acting on a particle and summing up in the way of many relatively small random changes of the direction of flight. To characterize the different degrees of scattering when a particle passes through an absorber one normally uses the so-called “average scattering angle”  $\sqrt{\langle\theta^2\rangle}$ . The projected angular distribution of scattering angles in this sense leads to an average scattering angle of

$$\sqrt{\langle\theta^2\rangle} = \theta_{plane} = \frac{13.6 MeV}{\beta cp} a \sqrt{\frac{x}{X_0}} \left\{1 + 0.038 \ln \frac{x}{X_0}\right\}$$

with  $p$  in Mev/c and  $x$  the thickness of the scattering medium measured in radiation lengths  $X_0$ . The average scattering angle in three dimension is

$$\theta_{space} = \sqrt{2}\theta_{plane}$$

The case of multiple Coulomb scattering is solved using statistical methods resulting in a given distribution function for the angular deviation. A good approximation at low angles is a Gaussian distribution.

## 2.4 Interactions of photons with matter

Photons are attenuated in matter via the processes of the photoelectric effect, Compton scattering and pair production. Each of them is dominant in a different energy range. The photoelectric effect is dominant for low energies, up to 500 keV, pair production is dominant at high energies, i.e. above 50 MeV while Compton scattering may be important in between. In figure 2.5 we present a summary of photon cross-sections on lead and carbon.

### 2.4.1 The photoelectric effect

When a photon of energy  $k = h\nu$  traverses a block of matter, it can be absorbed by an atomic electron (see figure 2.6). If the photon energy is larger than the electron binding energy  $E_l$ , the atom might be ionized and a free electron, with energy equal to the incident photon energy minus the binding energy, will be created:

$$E_{e^-} = k - E_l = h\nu - E_l$$

The calculation of the cross-section is complicated due to the discontinuities associated to the different binding energies corresponding to the various shells. For high energy photons (of the order of a few MeV),  $\sigma_{photoelectric}$  decreases as  $Z^5/k$ . This makes photoelectric absorption negligible at very high energies.

### 2.4.2 Compton scattering

Next, we are going to discuss Compton scattering on free electrons, see figure 2.7. Of course in reality one is generally looking at Compton scattering on a bound electron. For practical purposes, though, whenever the photon energy is much larger than the atomic binding energy, the target electron could be considered quasi-free.

The cross-section for Compton scattering was historically one of the first QED calculations and is given by the well known Klein-Nishina formula [21]

$$\frac{d\sigma}{d\Omega} = \frac{r_e^2}{2} \frac{1}{[1 + \gamma(1 - \cos \theta)]^2} \left( 1 + \cos^2 \theta + \frac{\gamma^2(1 - \cos \theta)^2}{1 + \gamma(1 - \cos \theta)} \right)$$

with  $\gamma = h\nu/m_e c^2$ .

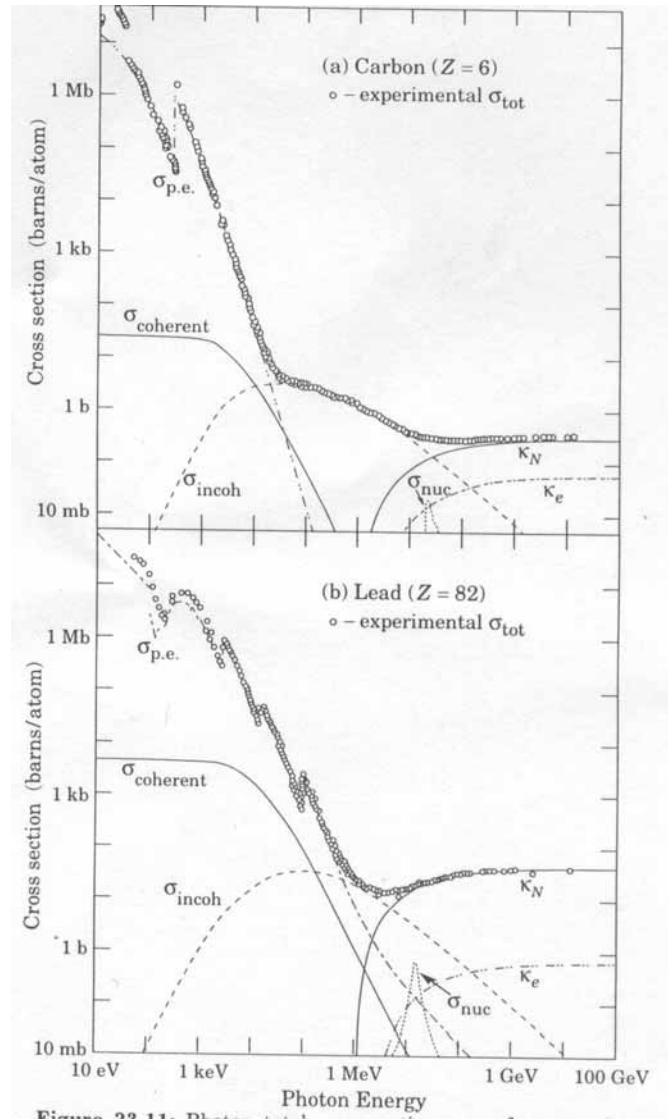


Figure 2.5: Photons cross-sections on carbon and lead.

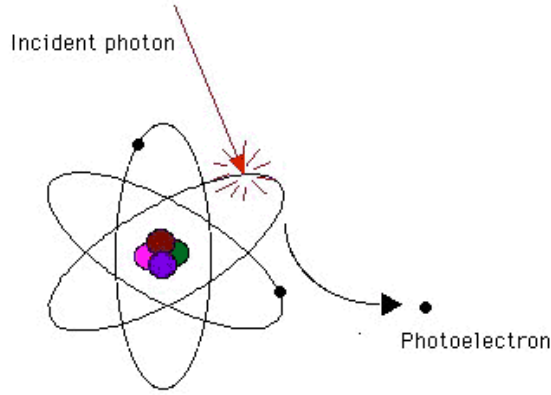


Figure 2.6: The photoelectric effect.

After integration over  $d\Omega$  one obtains:

$$\sigma_{Compton} = 2\pi r_e^2 \left\{ \frac{1+\gamma}{\gamma^2} \left[ \frac{2(1+\gamma)}{1+2\gamma} - \frac{1}{\gamma} \ln(1+2\gamma) \right] + \frac{1}{2\gamma} \ln(1+2\gamma) - \frac{1+3\gamma}{(1+2\gamma)^2} \right\}$$

### 2.4.3 Pair creation

Last, but not least, we shall discuss the conversion of a photon into an  $e^-e^+$  pair. For obvious kinematic reasons, this is a process which can only occur above a threshold given by twice the electron mass, i.e.  $h\nu \geq 1.022$  MeV.

The Feynman diagram for pair creation (see figure 2.8) can be derived by crossing from that for bremsstrahlung. Therefore screening effects are similar in both cases. This effect can be also parametrized in terms of the variable  $\xi$ , in analogy to bremsstrahlung

$$\xi = \frac{100m_e c^2}{Z^{1/3}} \frac{k}{E_+ E_-}$$

with  $E_-$  the energy of the outgoing electron,  $E_+$  that of the outgoing positron and  $k = h\nu = E_+ + E_-$ .

For negligible screening, i.e.  $\xi \gg 1$ , we obtain:

$$\left( \frac{d\sigma}{dE_+} \right)_{pair} = \frac{4\sigma_0}{k} \left( \omega_+^2 + \omega_-^2 + \frac{2}{3}\omega_+\omega_- \right) \left[ \ln \left( \frac{2E_+E_-}{m_e c^2 k} \right) - \frac{1}{2} - f(Z) \right]$$

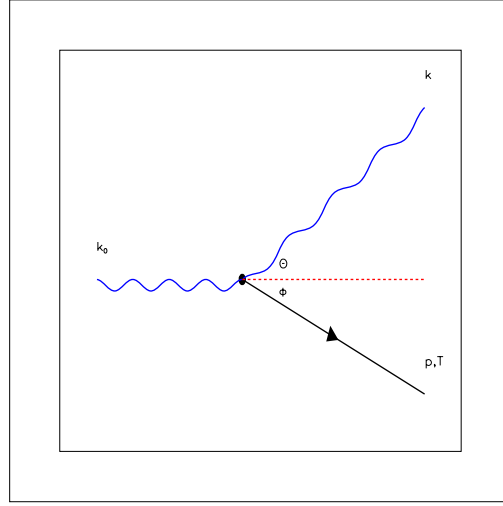


Figure 2.7: Compton scattering.

and for full screening, i.e.  $\xi \rightarrow 0$ , one finds:

$$\left( \frac{d\sigma}{dE_+} \right)_{pair} = \frac{4\sigma_0}{k} \left\{ \left( \omega_+^2 + \omega_-^2 + \frac{2}{3}\omega_+\omega_- \right) \left[ \ln \left( \frac{183}{Z^{1/3}} \right) - f(Z) \right] - \frac{\omega_+\omega_-}{9} \right\}$$

with  $\sigma_0 = \alpha Z^2 r_e^2$ ,  $\alpha = \frac{e^2}{\hbar c}$  and  $\omega_- = \frac{E_-}{k}$  and  $\omega_+ = \frac{E_+}{k}$ . The function  $f(Z)$  was already defined for bremsstrahlung.

For no screening, the total cross-section reads:

$$\sigma_{pair} = 4\sigma_0 \left[ \frac{7}{9} \left( \ln \frac{2k}{m_e c^2} - f(Z) \right) - \frac{109}{54} \right]$$

For full screening and with  $k \gg 137m_e c^2 / Z^{1/3}$ , the total cross-section is given by:

$$\sigma_{pair} = 4\sigma_0 \left\{ \frac{7}{9} \left[ \ln \left( \frac{183}{Z^{1/3}} \right) - f(Z) \right] - \frac{1}{154} \right\}$$

The mean free path  $\lambda_{pair}$  is usually defined as the distance a photon must traverse in order to be converted into an  $e^-e^+$  pair, i.e.:

$$\lambda_{pair} = \frac{1}{n_a \sigma_{pair}}$$

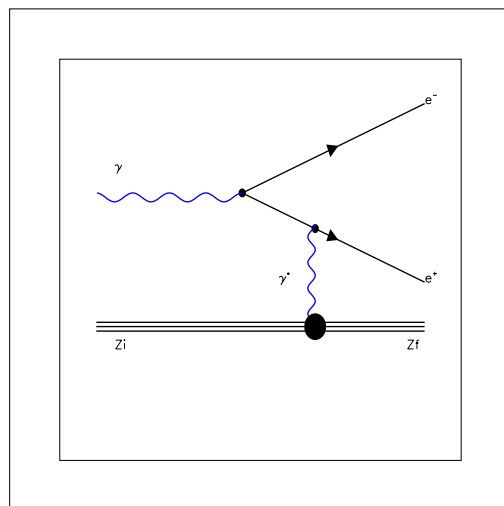


Figure 2.8: Feynman diagrams for pair creation.

We realize that  $\sigma_{pair} \simeq \frac{7}{9}\sigma_{radiation}$  and therefore:

$$\lambda_{pair} \simeq \frac{9}{7}X_0.$$

#### 2.4.4 Absorption coefficient

The total cross-section per atom for a photon interacting with a block of matter will be given by the sum of the three cross-sections we have previously discussed, i.e.

$$\sigma_{tot} = \sigma_{photoelectric} + Z\sigma_{Compton} + \sigma_{pair}$$

Note that the Compton cross-section  $\sigma_{Compton}$  has been multiplied by  $Z$  in order to take into account that the photon can indeed interact with the  $Z$  electrons in the material. The absorption coefficient  $\mu$  is defined as the product of the cross-section times the density of the material. The intensity of a photon beam varies in matter according to

$$I = I_0 e^{-\mu x}.$$

Therefore if we have a beam with  $N_0$  photons at a depth  $x_0$ , the number of surviving photons after traversing a distance  $x$  will be given by:

$$N = N_0 \exp(-\mu x)$$

## 2.5 Electromagnetic showers

The development of cascades induced by electrons, positrons or photons is governed by bremsstrahlung of electrons and pair production of photons. Secondary particle production continues until photons fall below the pair production threshold, and energy losses of electrons other than bremsstrahlung start to dominate: the number of shower particles decays exponentially.

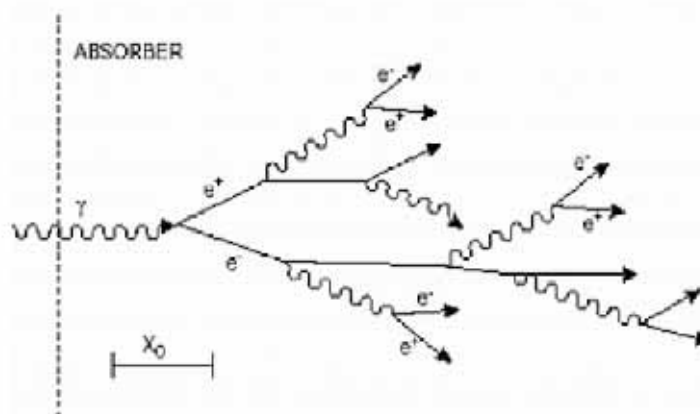


Figure 2.9: An electromagnetic shower.

A very simple model can describe the main features of particle multiplication in electromagnetic cascades, see figure 2.9. We consider an electron incident on a block of matter with energy much larger than the critical energy for the material. As we have discussed in previous subsections, the dominant energy loss mechanism is radiation. Therefore, on average, once the electron passes through a radiation length of a given material, the number of particles in the shower will be two because the initial electron will have radiated a photon. Emitted photons are going to be converted into  $e^-e^+$  pairs. Then in turn, and as long as their energies are above critical, they are going to radiate. By using this argument it is easy to estimate that at a depth given by  $t$  radiation lengths the number the particles will be:

$$N = 2^t$$

and the average energy of particles found at a depth  $t$  will be:

$$\epsilon = \frac{E_0}{N} = E_0 \cdot 2^{-t}$$

Those particles with energy below the critical energy  $E_c$  cannot radiate any longer. Therefore the maximal depth for a block of matter to contain an electromagnetic shower will

be given by:

$$t_{max} = \frac{\ln E_0/E_c}{\ln 2}$$

If we denote by  $\langle T \rangle$  the average total path traversed by the particles in the cascade, assuming that on the average every secondary passes through on radiation length of material, we will have that  $\langle T \rangle$  equals the number for particles in the cascade:

$$\langle T \rangle = \sum_{i=0}^{t_{max}} 2^i = \frac{2^{t_{max}} - 1}{2 - 1} \simeq 2^{t_{max}} = \frac{E_0}{E_c} = N$$

As the shower develops itself, a small fraction of the energy is lost by ionization. This fraction is proportional to  $\langle T \rangle$ , as every secondary particle in the shower deposits an amount of energy per unit length which is independent of its own energy, i.e.:

$$E_{ionization} \propto \langle T \rangle = \frac{E_0}{E_c}$$

This relation is the key to our understanding of calorimeters. If one would be able to measure the energy of the secondaries i.e. particles created in the cascade, one would be able to determine the incident energy. Calorimeters are built for this purpose, and they should therefore be designed deep and wide enough so as contain the whole shower.

Of course, the discussion presented so far is somewhat qualitative and for details one has to resort to Monte Carlo simulations. They implement details such as the dependence of the cross-sections on the material and energy as well as a description of the energy loss due to ionization is a function of energy.

The characteristic length of the electromagnetic shower is the aforementioned radiation length  $X_0$ . If we study the longitudinal development of the electromagnetic shower (see figure 2.10), we will conclude it is necessary a depth of  $> 25X_0$  to contain a high energy electromagnetic shower.

Although we have kept the issue aside until now, an electromagnetic shower develops itself not only longitudinally, as we have discussed this far, but also laterally. The lateral development is due to:

- multiple scattering of electrons
- bremsstrahlung photons are emitted within the characteristic angle  $\theta_{bremsstrahlung} \simeq p_e/m_e$



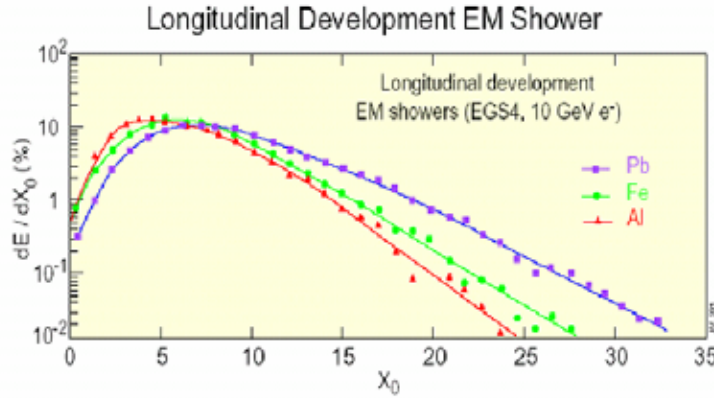


Figure 2.10: Longitudinal development of electromagnetic shower.

- the lateral spread between electron and positron coming from photon conversions which is typically of the order of  $\langle\theta\rangle \simeq \frac{m_e c^2}{E}$ .

In order to give a figure of merit for the lateral development of an electromagnetic shower, one defines the Molière radius as:

$$R_M = X_0 \frac{E_s}{E_c}$$

with  $E_s = \sqrt{\frac{4\pi}{\alpha}} m_e c^2 = 21.2 \text{ MeV}$ . This gives us:

$$R_M \simeq 7 \frac{A}{Z} \text{ g.cm}^{-2}.$$

Thus, a cylinder of radius  $2R_M$  ( $3R_M$ ) around the incident electron direction will contain 95% (99%) of the shower energy.

## 2.6 Hadronic showers

The hadronic showering process (figure 2.11) is dominated by a succession of inelastic hadronic interactions. At high energy, these are characterized by multiparticle production ( $\pi^0, \pi^\pm, K, \dots$ ) and particle emission originating from nuclear decay of excited nuclei. Secondaries are mostly pions and nucleons. Due to the relatively frequent generation of  $\pi^0$ 's, there is also an electromagnetic component present in hadronic showers. The hadronic multiplication process is measured at the scale of nuclear interaction length  $\lambda_L$ , which is essentially energy-independent. About  $10 \lambda_L$  are necessary to contain 99% of energy of 200 GeV pion (see figure 2.12).

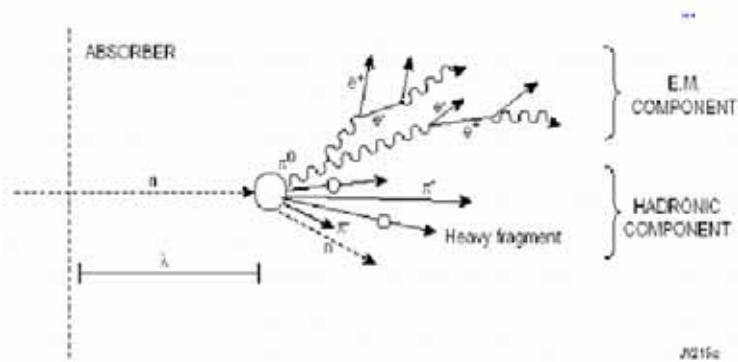


Figure 2.11: An hadronic shower.

Parts of the energy of the incident hadron is spent to break up nuclear bonds. This fraction of the energy is invisible in hadron calorimeters. Further energy is lost by escaping particles like neutrinos and muons as a result of hadron decays. Since the fraction of lost binding energy and escaping particles fluctuates considerably, the energy resolution of hadron calorimeters is systematically inferior to electron calorimeters.

Contrary to electromagnetic showers, which develop in subnanosecond time, the physics of hadronic shower is characterized by different time scales, the slowest of which (de-excitation of heavy nuclei) may reach a microsecond.

## 2.7 Calorimeters

A calorimeter is a composite detector using total absorption of particles to measure the energy and position of incident particles or jets. In the process of absorption, showers are generated by cascades of interactions. Characteristic interactions with matter (e.g. atomic excitation, ionization) are used to generate a detectable effect, via particle charges.

Calorimeters detector have two advantages over tracking detectors: firstly, they are sensitive to both charged and neutral particles, and secondly, when we used them to measure the energy of the particle, their accuracy increases with the energy of the particle. This is because the fluctuations in the shower process decrease as the number of particles in the shower increases, i.e. as the energy increases. In contrast, the use of curvature in a magnetic field to determine momentum gives a fractional error proportional to the momentum of the particle. At high enough energy, the calorimeter must always therefore

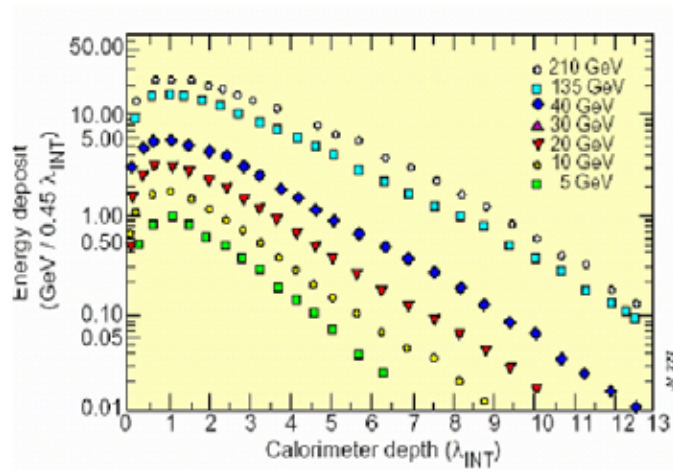


Figure 2.12: Energy deposit of pions as a function of calorimeter depth.

have a better energy resolution.

Often a combined electromagnetic-hadronic device is built, consisting of an initial electromagnetic section followed by a hadronic section. Typically, incident electromagnetic particles (e.g. electrons and photons) are fully absorbed in the electromagnetic calorimeter, which is made of the first layers of a composite calorimeter. An electromagnetic shower is produced until the average energy of the products drops below the critical energy. The number of charged particles in the shower (or the track length of these particles) is proportional to the energy of the primary particle. The electromagnetic calorimeter construction takes advantage of the comparatively short and concentrated electromagnetic shower shape to measure energy and position with optimal precision for these particles (which include  $\pi^0$ 's, decaying electromagnetically). Electromagnetic showers have a shape that fluctuates within comparatively narrow limits; its overall size scales with the radiation length.

Incident hadrons, on the other hand, may start their showering in the electromagnetic calorimeter, but will nearly always be absorbed fully only in later layers, i.e. in the hadronic calorimeter, built precisely for their containment. Hadronic showers have a widely fluctuating shape; their average extent does not scale with the calorimeter's interaction length, but is partly determined by the radiation length.

Discrimination, often at the trigger level, between electromagnetic and hadronic showers is a major criterion for a calorimeter; it is, therefore, important to contain electromagnetic showers over a short distance, without initiating too many hadronic showers. The critical quantity to maximize is the ratio  $\frac{\lambda_c}{X_0}$ , which is approximately proportional to  $Z^{1.3}$ ; hence the use of high-Z materials like lead, tungsten or uranium for electromagnetic calorimeters.

The pattern of energy deposition of a high-energy electrons in a calorimeter, as well as the correlation of deposited energy with magnetically-measured momentum, can be used to distinguish electrons from other charged particles. Since high-energy photons also create electromagnetic showers in high-Z materials, electromagnetic calorimetry can also be used to identify photons and measure their energy. Photons are distinguishable from electrons since they do not give observable tracks in tracking telescopes.

Calorimeters can also provide signatures for particles that are not absorbed: muons and neutrinos. Muons do not shower in matter, but their charge leaves an ionization signal, which can be identified in a calorimeter if the particle is sufficiently isolated, and then can be associated to a track detected in tracking devices inside the calorimeter, or/and in specific muon chambers (after passing the calorimeter). Neutrinos, on the other hand, leave no signal in a calorimeter, but their existence can sometimes be inferred from energy conservation; in a hermetically closed calorimeter, at least a single sufficiently energetic neutrino, or an unbalanced group of neutrinos, can be *observed* by forming a vector sum of all measured momenta, taking the observed energy in each calorimeter cell along the direction from the interaction point to the cell. The precision of such measurements, usually limited to the transverse direction, requires minimal leakage of energy in all directions, hence a major challenge for designing a practical calorimeters.

From the construction point of view, one can distinguish between:

- Homogeneous calorimeter

Although not all of the shower energy is deposited in the form of ionization, the measurable signal will be proportional to the energy of the incident particle as long as the shower is fully contained. Thus the energy of the incident particle can be reconstructed by measuring the signal produced by a fully contained electromagnetic shower. Such a device is known as a homogeneous calorimeter. In these calorimeters the functions of passive particle absorption and active signal generation and readout are combined in a single material. Such materials are almost exclusively used for electromagnetic calorimeters, e.g. crystals, composite materials or, usually for low energy, liquid noble gases. Since they are not subject to sampling fluctuations, homogeneous electromagnetic calorimeters generally have better energy resolution than sampling calorimeters (for example,  $\frac{5\%}{\sqrt{E}}$  achieved by the OPAL collaboration using lead glass).

- Heterogeneous or sampling calorimeters

In sampling calorimeters the functions of particle absorption and active signal readout are separated. This allows optimal choice of absorber materials and a certain freedom in signal treatment. These calorimeters consist of alternate layers of an active medium and a passive absorber such that only a fraction of the shower is

sampled. Heterogeneous calorimeters are mostly built as sandwich counters, sheets of heavy-material absorber (e.g. lead, iron, uranium) alternating with layers of active material (e.g. liquid or solid scintillators, or proportional counters). Only the measurable signal produced in the active medium is collected and used to reconstruct the incident particle energy. The fraction of the shower energy which produces a measurable signal in the active medium is referred to as the sampling fraction,  $f_s$ . The denser absorbing medium serves to reduce the physical thickness of the calorimeter necessary to fully contain the shower. The number of active layers per radiation length of material is denoted the sampling frequency. Hadron calorimeters, needing considerable depth and width to create and absorb the shower, are necessarily of the sampling calorimeter type.

In practical constructions the ratio of energy loss in the passive and active material is rather large, typically of the order of 10. Although performance does not strongly depend on the orientation of active and passive material, their relative thickness must not vary too much, to ensure an energy resolution independent of direction and position of showers. Only a few percent of the energy lost in the active layers is converted in detectable signal.

The measurable signal ought to lie above a given threshold  $\eta$ . However, only a fraction of the total length of the cascade  $\langle T \rangle$  will be measured (sampled). In fact the measured path  $\langle T_d \rangle$  is:

$$\langle T_d \rangle = F(\eta) \cdot \langle T \rangle = F(\eta) \cdot \frac{E_0}{E_c}.$$

Let  $d$  be the distance in units of radiation lengths between two consecutive absorbers. Thus, the sampled path is given by:

$$N_s \simeq \frac{\langle T_d \rangle}{d} = F(\eta) \cdot \frac{E_0}{E_c \cdot d}.$$

### Energy resolution of calorimeters

Two are the main contributions to the energy resolution in a calorimeter. We will discuss them next.

#### *Intrinsic fluctuations*

These are due to fluctuations in the total path  $\langle T \rangle$  coming from the shower development. We have seen that  $\langle T \rangle$  is proportional to the number of secondaries in the shower  $N$ .

Typically,  $N$  is large enough so that the standard deviation is  $\sigma \sim \sqrt{N}$ . Thus:

$$\frac{\sigma(E_0)}{E_0} \simeq \frac{\sigma(N)}{N} = \frac{\sqrt{N}}{N} = \frac{1}{\sqrt{N}} \propto \frac{1}{\sqrt{E_0}}$$

This relation imposes a lower limit on the precision one can obtain. Homogeneous calorimeters can reach resolutions of the order of  $\frac{\sigma}{E} \simeq \frac{1\%}{\sqrt{E}}$ .

#### *Sampling fluctuations*

For sampling calorimeters one has to add to the intrinsic fluctuations discussed above those related with the sampling process itself. The energy resolution can be parametrized as [22]:

$$\left(\frac{\sigma(E_0)}{E_0}\right)_{\text{sampling}} \simeq R \sqrt{\frac{d[X_0]}{E_0[\text{GeV}]}}$$

where  $R$  is a constant dependent on the passive material of our choice. This sampling fluctuations which are proportional to the square root of  $d$  are larger than the intrinsic fluctuations.

Over much of the useful range of calorimeters, this two terms dominate energy resolution.

#### *Additional contributions*

Additional contributions are due to noise in the electronic read-out chain. In  $pp$  colliders there is also a term due to pile up. These terms are proportional to  $b/E_0$ . This component may limit the low-energy performance of calorimeters.

Finally we would also like to mention that non uniformities both in the mechanical construction as well as in the read out chain give rise to contributions which remain constant i.e. do not vanish with energy. Therefore the constant term is associated with mechanical imperfections of the calorimeter, non-uniformity signal generation and/or collection, the cell to cell intercalibration error, quality of the detection medium, the fluctuation in the amount of energy leakage, fluctuation in the electromagnetic component for hadronic shower, uniformity of response and stability with time. This component,  $c$ , sets the limit for the performance at very high energies.

To summarize, the energy resolution can be parametrized as:

$$\frac{\sigma}{E} = \frac{a}{\sqrt{E}} \oplus \frac{b}{E} \oplus c$$

The first term is known as the stochastic or sampling term and accounts for the statistical fluctuation in the number of primary signal generating processes, the second, noise term, includes the energy equivalent of the electronics noise and the pile-up (the fluctuation of

energy entering the measurement area from other sources), and the third term or constant term, which dominates at very high energies, is related to the non uniformities in the calorimeter response. In this thesis the non-uniformity of response of the calorimeter and, therefore, the constant term of the energy resolution are studied.

The two types of calorimeters have markedly different characteristics:

1. Electromagnetic calorimeter

Energy measurement in sampling calorimeters is limited in resolution due to statistical fluctuations in the ratio of the energy deposited in the active layers to that in the inactive layers. There are also fluctuations arising from Landau distribution. Typical performance for electromagnetic showers is relative rms energy uncertainty  $\frac{\sigma(E)}{E} = \frac{10\%}{\sqrt{E}}$ , where E is expressed in GeV. At the highest energies, as this quantity goes to zero, other contributions (for example, calibration uncertainties) dominate. It is difficult to measure energy in sampling calorimeters to better than a few percent.

2. Hadronic calorimeter

The poor energy resolution of hadronic sampling calorimeters arises from random fluctuations in the shower composition (e.g. in the relative numbers of neutral vs. charged pions produced) and from energy loss mechanisms (such as breakup of nuclei in the inactive layers) not yielding signal in the sampling medium. The decay of the neutral pion into a pair of photons converts hadronic energy into electromagnetic energy, which degrades the energy resolution due to the differing response to electromagnetic and hadronic energy. Typical resolutions are  $\frac{\sigma(E)}{E} = \frac{50\%}{\sqrt{E}}$ , where E is expressed in GeV.

# Chapter 3

## The EMEC of ATLAS

### 3.1 Introduction

Calorimetry will be a crucial tool for the understanding of proton-proton collisions at the LHC, since many physics processes will manifest themselves through final states with electrons or photons. The  $H \rightarrow ZZ^* \rightarrow 4e$  and  $H \rightarrow \gamma\gamma$  channels place the most stringent requirements on the electromagnetic calorimeter in terms of acceptance, energy resolution and range, and particle identification. For physics simulations, it has been determined that the electromagnetic calorimeter should meet the following requirements:

- Searches for rare processes require an excellent coverage in pseudorapidity, as well as the measurement of the missing transverse energy of the event and the reconstruction of jets.
- In the mass range of interest, an energy resolution of 1% is required. It implies that the global constant term of the energy resolution remain less than 0.7% and that the sampling term be kept at a level of  $\sim \frac{10\%}{\sqrt{E(\text{GeV})}}$ . The global constant term is determined by the uniformity of the detector response over the full calorimeter acceptance. It requires a uniformity better than 0.6%.
- The electromagnetic calorimeter is required to reconstruct electrons and photons in the energy range 20 MeV to 2 TeV, i.e. from the typical noise level in one cell up to the single cell energy deposition in the case of the decays  $Z' \rightarrow e^+e^-$  and  $W' \rightarrow e\nu$ , which may have masses up to 5 TeV.
- Backgrounds to electrons and photons come predominantly from hadronic jets. To obtain a photon efficiency of 80%, a jet rejection factor of 5000 is needed in the



range  $25 \text{ GeV} < p_T < 100 \text{ GeV}$  to suppress  $\gamma$ -jet and jet-jet backgrounds to the  $H \rightarrow \gamma\gamma$  channel. Electron-jet separation and rejection of isolated high- $p_T$   $\pi^0$ 's is necessary.

- The impact of noise on the calorimeter performance must be as small as possible. At LHC, contributions to the calorimeter resolution from noise arise from pile-up and from the electronic noise of the readout chain. These contributions are particularly important at low energy ( $E < 20 \text{ GeV}$ ) where they can dominate the accuracy of the calorimeter energy and position measurements. Minimization of the pile-up noise requires fast detector response and fast electronics; minimization of the electronic noise requires high calorimeter granularity and high-performance electronics.
- The EM calorimeters will have to withstand neutron fluencies of up to  $10^{15} \frac{n}{\text{cm}^2}$  and radiation doses of up to 200 kGy (integrated over ten years of operation).
- The photon direction must be measured with high accuracy, so that the angular contribution to the width of the reconstructed  $\gamma\gamma$  invariant mass in the  $H \rightarrow \gamma\gamma$  channel is not dominant over the contribution from the energy resolution. This implies a very good transverse and longitudinal segmentation, with a measurement of the shower direction in  $\theta$  with an angular resolution of  $\sim \frac{50 \text{ mrad}}{\sqrt{E(\text{GeV})}}$ .
- The time resolution should be around 100 ps for background rejection and for the identification of some decay modes with non-pointing photons.
- It is necessary to obtain a linearity better than 0.1%.

The electromagnetic calorimeter (ECAL) ([12], [23]) is a sampling calorimeter constituted by lead/liquid Argon, with high granularity and with an accordion geometry. A good particle identification is achieved with the lateral and longitudinal segmentation of the calorimeter. The electromagnetic calorimeter is split up into two main parts:

- one barrel
- two end-caps.

The barrel (see figure 3.1) is composed of two half barrels centered over the  $z$  axis and it covers a pseudorapidity up to  $\eta = 1.475$ . In the barrel the segmentation is  $\Delta\eta \times \Delta\phi = 0.003 \times 0.1$  ( $0.025 \times 0.025$ ,  $0.05 \times 0.025$ ) in the first (second and third, respectively) sampling. The general geometry of the barrel is very similar to the one used in the end-caps.

The end-caps cover a pseudorapidity range from  $\eta = 1.375$  to  $\eta = 3.2$ .



Figure 3.1: Photograph of a barrel module.

The electromagnetic calorimeter covers less than 24 radiation lengths in the barrel and 26 in the end-caps. Due to the two radiation length of material (including the cryostat and the solenoid) in front of the main calorimeters, a presampler is used to correct for the energy loss in the region  $\eta < 1.375$ . The end-cap presampler is placed in front of the electromagnetic end-cap calorimeter in the region  $1.5 < \eta < 1.8$  and the barrel presampler is placed in  $\eta < 1.5$ .

We are going to limit the calorimeter description to the end-cap, and in practice to those modules which were stacked and cabled at UAM.

## 3.2 EMEC description

The electromagnetic calorimeter is based on the accordion geometry [24] [25]. Each of two wheels (EMEC), with internal and external radii of about 30 cm and 2 m, respectively, is constituted by two parts: the inner wheel, which covers a pseudorapidity range between  $\eta = 2.5$  and  $\eta = 3.2$ , and the outer wheel, which covers the range from  $\eta = 1.375$  to  $\eta = 2.5$  (see figure 3.2). In order to facilitate handling and logistics, each end-cap is subdivided into 8 octants also named as modules. The 16 modules have been stacked in the CPPM<sup>1</sup> and UAM<sup>2</sup> clean rooms. Figure 3.3 shows a front side photograph of one stacked and cabled octant, module 2 named ECC1.

The wheels consist of accordion shaped lead absorbers interleaved with electrodes (see figure 3.4). The absorber plates are mounted in a radial arrangement, while the accordion

<sup>1</sup>Centre de Physique des Particules de Marseille

<sup>2</sup>Universidad Autónoma de Madrid

waves are parallel to the front and back edges of the wheel and run in depth. There are 768 electrodes and absorbers in the outer wheel while there are 256 in the inner one. Moreover, honeycomb spacers are used to separate the electrodes and absorbers, resulting in approximately 4 mm gaps. The gap, when the module is inside the cryostat, is filled with liquid Argon. A high voltage is applied between the absorbers and electrodes, producing an electric field in the gap electrode-absorber. In this way, when high-energy photons or electrons traverse the lead, will produce an electromagnetic shower giving electrons or positrons, whose total number will be proportional to the incident energy. The charged particles of the electromagnetic shower will traverse the active material, ionizing the liquid Argon. Electron-ion pairs will be created, and due to the electric field, they will be derived to the electrode where the shower will be detected.

The design is symmetrical in  $\phi$  and projective to the interaction point in  $\eta$ . In particular the cells drawn in the electrodes point to the nominal ATLAS interaction point.

The end-cap presampler is placed in front of the electromagnetic end-cap calorimeter in the region  $1.5 < |\eta| < 1.8$ . It is divided into 768 cells (per end-cap wheel) of  $\Delta\eta \times \Delta\phi = 0.025 \times 2\pi/64$ , and 32 identical azimuthal sectors (modules). Each module consists of two 2 mm thick active liquid Argon layers, formed by three electrodes parallel to the front face of the EM end-cap calorimeter.

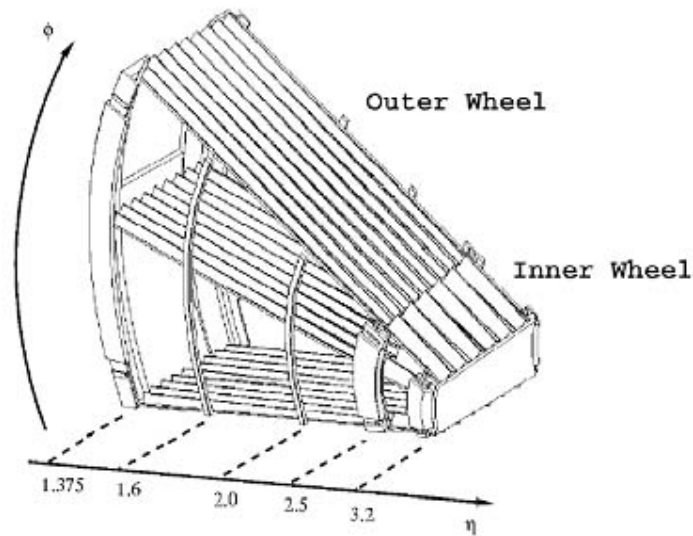


Figure 3.2: Representation of an electromagnetic end-cap calorimeter.

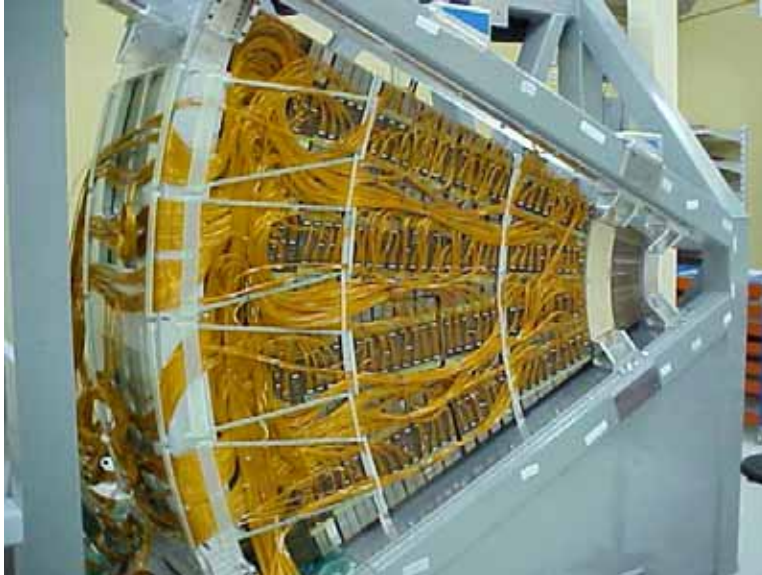


Figure 3.3: Front side photograph of the stacked module ECC1.

### Choice of active and passive materials

The ATLAS collaboration chose finally a sampling calorimeter, where the active material is lead and the passive one is liquid Argon. The lead has a radiation length value of  $0.56\text{ cm}$ , allowing a compact calorimeter. Moreover it has a critical energy ( $6.9\text{ MeV}$ ) lower than this value for the rest of materials which are used usually in calorimetry.

There are several requirements for the active component:

- Very low energy to produce an ionization electron
- Non chemical reactivity
- High purity to avoid recombination events
- Resistance to radiations
- Density to allow particles which traverse it to produce a big number of electron-ion pairs (it is better to use a liquid than a gas).
- Ability to tolerate a high voltage

The noble liquids with a high atomic number  $Z$  carry out all these requirements. Due to the electronic orbit saturation, it is possible the ionization electron drift without risk of capture, and moreover, these elements are very resistant to radiations. To get a low

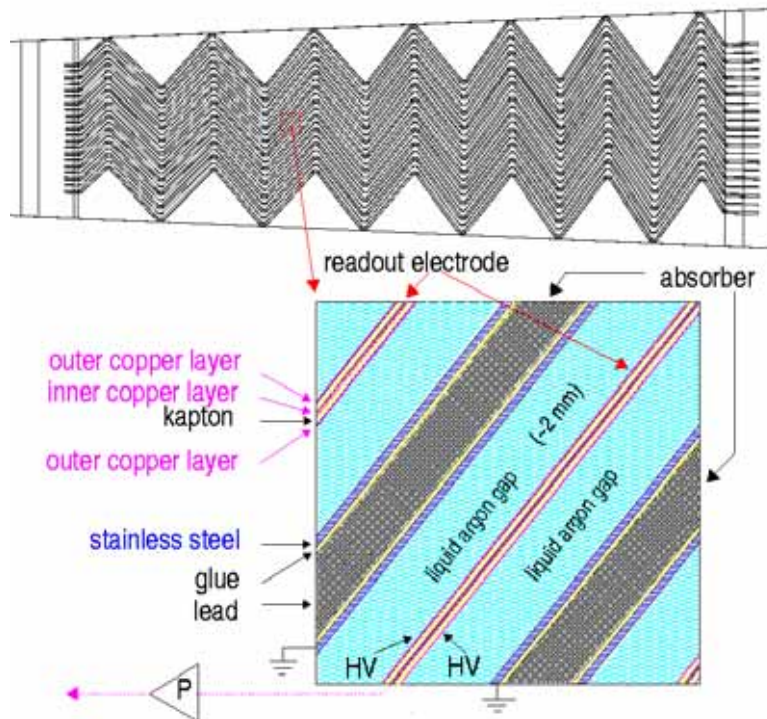


Figure 3.4: A schematic view of a gap electrode-absorber.

radiation length and ionization energy small, it is necessary a high  $Z$  material. The noble liquid with highest atomic number is the xenon, but is very expensive (because it is very difficult to find it). The ATLAS collaboration doubted between krypton and Argon. The krypton has as the advantage the improvement of the sampling term in 30% and the noise term in a factor of 1.6. However, it would be a very expensive detector, given the requirements for a high purity and mechanical tolerances. For this reason, the liquid Argon<sup>3</sup> was chosen. It has to be maintained at 90 K, requiring a cryogenic system.

### Consequences of the accordion geometry

A classic sampling calorimeter is constituted by parallel plates of passive material. It is not hermetic due to the cables, which should go out by some place. This is a problem because we should compute the lost energy in those cracks and, moreover, the cable length would introduce noise due to the overlap. The adopted solution was the accordion geometry, which reduce totally the hermeticity problem (no cracks in  $\phi$ ) and solve partially the problem coming from the cable length, because all the electronic is located on front or

<sup>3</sup>The radiation length for liquid Argon is shorter than for gaseous state.

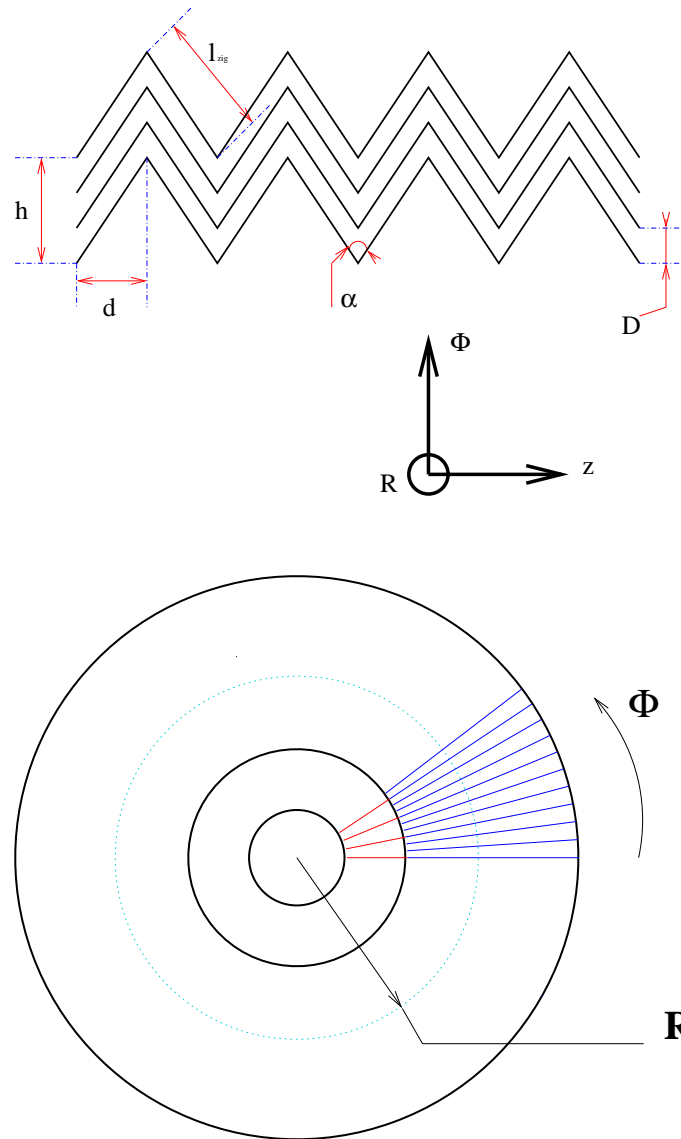


Figure 3.5: At the top, sketch of accordion absorbers with a simplified geometry. At the bottom, sketch of the end-cap from the front sight.

on back of the calorimeter. In addition, the accordion geometry minimizes inductances in the signal paths, allowing the use of the fast shaping needed for operation with 25 ns bunch intervals between collisions at LHC.

At the top of figure 3.5, a sketch of the simplified absorber geometry is shown. A more realistic description should take into account the curvature radius in a fold region instead of sharp angles.

The height of one absorber peak  $h$  is proportional to the distance between two neighbouring absorbers  $D$  so that:

$$h = \beta \cdot D$$

where  $\beta$  is an integer which is equal to 3 in our case. Moreover we can calculate the distance between two consecutive absorbers in another way. At the bottom of figure 3.5, a sketch of the end-cap front sight exhibits a  $\phi$  symmetry so that the gap distance between two absorbers can be calculated as follows:

$$D = \frac{2\pi R}{N}$$

where  $N$  is the number of absorbers. If we name  $L$  the projected width of one absorber over the  $z$  axis and  $M$  the waves number in the  $z$  direction, then:

$$d = \frac{L}{2M}$$

A very easy relation could be extracted from figure 3.5:

$$\tan \frac{\alpha(R)}{2} = \frac{d}{h}$$

and therefore:

$$\alpha(R) = 2 \arctan \left( \frac{1}{\beta} \cdot \frac{N}{2\pi R} \cdot \frac{L}{2M} \right)$$

From this formula, we can deduce that  $\alpha$ , the folding angle, depends on  $L$ , the projected width of the absorber, and  $R$ . For mechanical reasons,  $L$  is constant so the folding angle  $\alpha$  is a function of  $R$ . Then, the smaller is the radius  $R$ , the bigger is the pseudorapidity  $\eta$  and the more obtuse is the angle  $\alpha$ .

We can also remark that:

$$\frac{\tan(\alpha_{in}/2)}{\tan(\alpha_{out}/2)} = \frac{R_{out}}{R_{in}}$$

Limitations in the technologies used in the production of the absorbers imply that the bending angle  $\alpha$  should be kept in the following boundaries:

$$60^\circ < \alpha < 120^\circ$$

so that

$$\frac{R_{out}}{R_{in}} < 3$$

But according to the overall dimensions of the end-cap calorimeter  $R_{out}/R_{in} = 6.7$ . As it is impossible to require that in all pseudorapidity range with the accordion geometry, each end-cap calorimeter is constituted by two coaxials wheels, the outer wheel from  $\eta = 1.375$  to  $\eta = 2.5$  and the inner wheel from  $\eta = 2.5$  to  $\eta = 3.2$ . There is a crack between them of 3 mm of width which is filled with a low density material.

### 3.2.1 High voltage law varying by step

The incident particle deposits the main part of its energy in the absorber, producing a electromagnetic shower, with less energetic secondary particles. When these particles traverse the active material (see figure 3.6), they ionize the liquid Argon, producing a uniform distribution of pairs electrons-positive ions along the particle path. Due to the electric field applied to the gap, the electrons are derived to the electrode with a velocity of various millimeters per *ns* and the ions are derived to the absorber more slowly. An electrical signal is obtained due to the electrons derive to electrode.

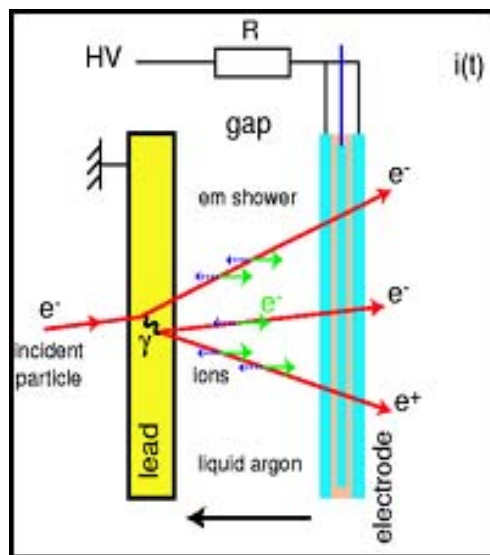


Figure 3.6: The production of the signal inside the calorimeter.

The generated signal in the electrode has a triangle shape which can be described as



follows ([24], [25], [26]):

$$I_p(t) = I_p^0 Y(t) Y(t - \tau_d) \left(1 - \frac{t}{\tau_d}\right)$$

where  $I_p^0$  is the maximum intensity

$$I_p^0 = \frac{Q}{\tau_d}$$

being  $\tau_d = \frac{g}{v_d}$  the maximum drift time of electrons inside liquid Argon (approximately 400 ns), and  $Q$  is the deposited charge in the liquid Argon.  $Y(t)$  is the Heavyside function.

The electrons drift velocity  $v_d$  in the liquid Argon is given by

$$v_d = k \times \left(\frac{U}{g}\right)^b$$

with  $b \simeq 0.4$  (experimentally determined [27]),  $U$  the high voltage in  $kV$ ,  $g$  is the liquid Argon gap in  $cm$  and  $k$  a constant.

For a given deposited energy  $E_0$ , the expression for the deposited charge  $Q$  is the following:

$$Q = \frac{E_0}{W_i} \times f_s$$

with  $W_i$  the ionization energy (for the liquid Argon  $W_i = 23.6 eV$ ) and  $f_s$  the sampling fraction.

Eventually the following formula is obtained:

$$\frac{I_p^0}{E_0} = \frac{k \cdot f_s}{W_i} \times \frac{U^b}{g^{(1+b)}}.$$

In order for the response to be constant, we need  $\frac{k \cdot f_s}{W_i} \times \frac{U^b}{g^{(1+b)}}$  to be constant too. Since we also know that  $\frac{f_s}{g}$  is approximately constant, it is required that the ratio  $U/g$  to be constant.

The liquid Argon gap in the end-cap calorimeter<sup>4</sup> follows the law which can be understood very simply with the sketch in figure 3.5:

$$g = \frac{2\pi R}{N} \sin \frac{\alpha}{2} - e_{abs}$$

---

<sup>4</sup>In the barrel the LAr gap can be kept at constant (2.1 mm half-gap) thickness from front to back by opening the folds of the accordion. The HV value is the same for all gaps (2 KV).

where  $N$  is the absorbers number,  $R$  the radius,  $\alpha$  the accordion aperture angle and  $e_{abs}$  the absorber thickness. A complication is added due to the fact that the angle  $\alpha$  decreases as the radius increases (see figure 3.7). For the outer wheel, the LAr gap thickness between the absorber and the electrode decreases continuously from 2.8 mm (at  $\eta = 1.375$ ) to 0.9 mm (at  $\eta = 2.5$ ) when  $\eta$  increases. For the inner wheel, the gap decreases continuously from 3.1 mm (at  $\eta = 2.5$ ) to 1.8 mm (at  $\eta = 3.2$ ) when  $\eta$  increases. As seen in figure 3.8, the gap depends on the position  $R$  (and consequently on  $\eta$ )<sup>5</sup>.

There are two ways to make the response uniform (that is, as we have said before,  $U/g$  constant). Firstly, we can make the lead thickness variable with  $R$  so that  $g$  remains constant, and use a high voltage constant. Other possibility is use a lead thickness constant with  $R$  but tuning the high voltage in order for the term  $\frac{U}{g}$  to be constant. For technical reasons, the first idea was given up.

### High voltage selected distribution

To achieve a uniform response, we need a high voltage which follows something similar to a linear behaviour over  $\eta$ . Certainly a difference between inner and outer wheel is necessary. Nevertheless in the real layout, a high voltage varying continuously is an unrealistic technical option. Instead a voltage setting which varies by steps was adopted. Seven high voltage regions in the outer wheel and two in the inner wheel were chosen as illustrated in fig 3.9.

The seven high voltage region chosen in the outer wheel are showed in the table 3.1 whereas the figure 3.10 shows a schematic view of the HV side of flat electrodes. These HV values have been determined by a MonteCarlo simulation [25] based on GEANT3.

HV region	1	2	3	4	5	6	7
	F	B1	B2	B3	B4	B5	B6
$\eta$ range	[1.4-1.5]	[1.5-1.6]	[1.6-1.8]	[1.8-2.0]	[2.0-2.1]	[2.1-2.3]	[2.3-2.5]
HV values	2500 V	2300 V	2100 V	1700 V	1500 V	1250 V	1000 V

Table 3.1: The seven high voltage region chosen in the outer wheel.

---

<sup>5</sup>This is not true for the barrel since in the barrel  $R$  is not correlated with  $\eta$  but with the depth.

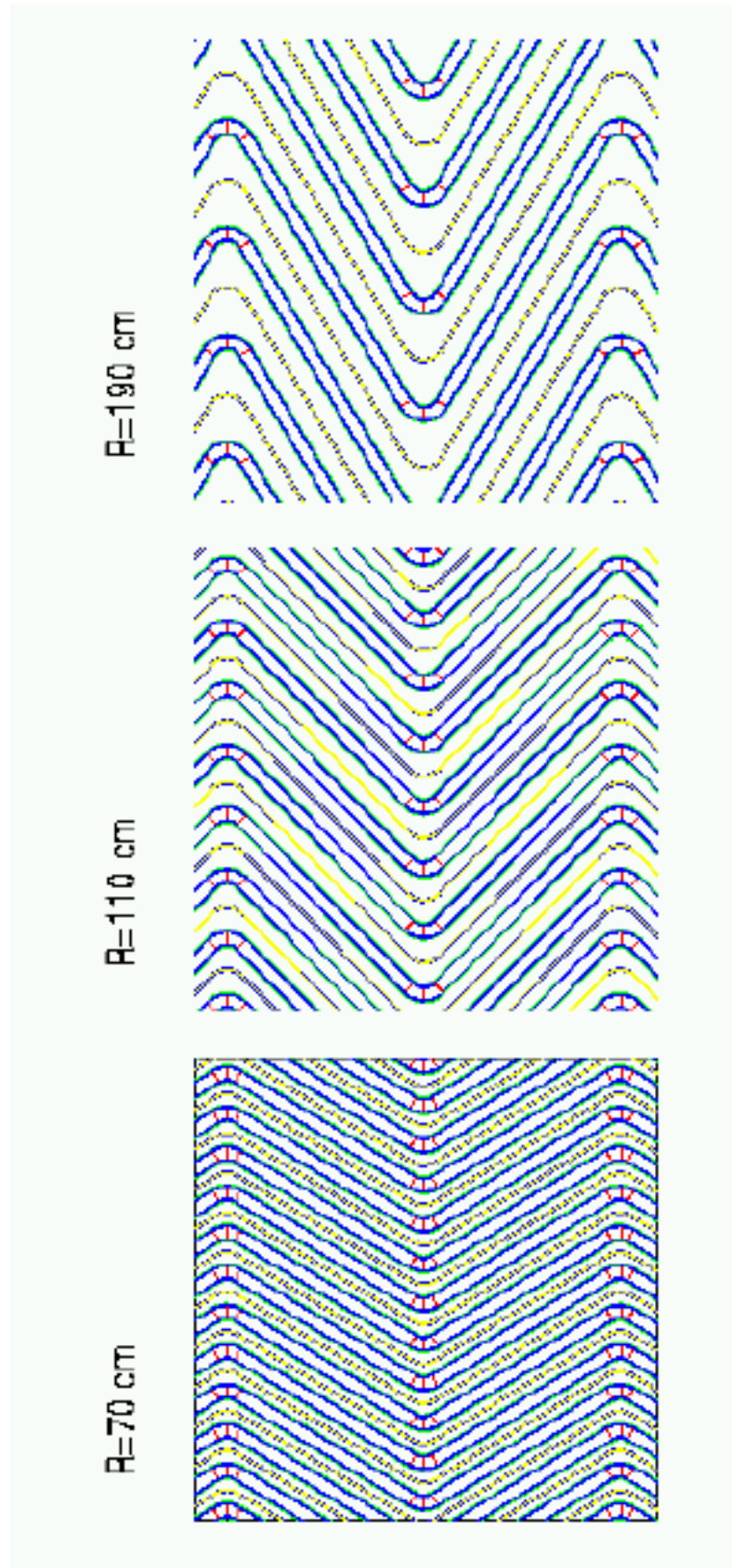


Figure 3.7: End-cap longitudinal section for different radii.

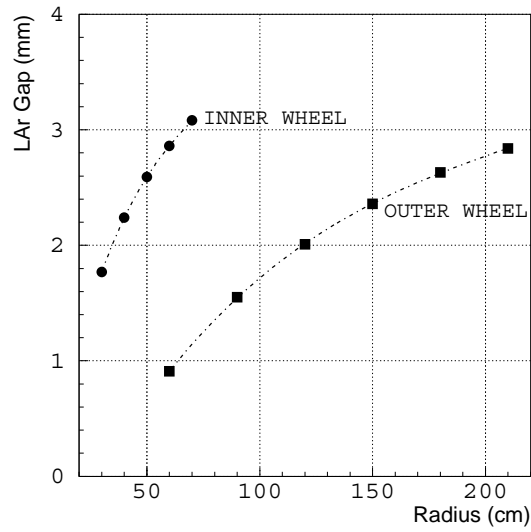


Figure 3.8: Liquid Argon gap versus radius.

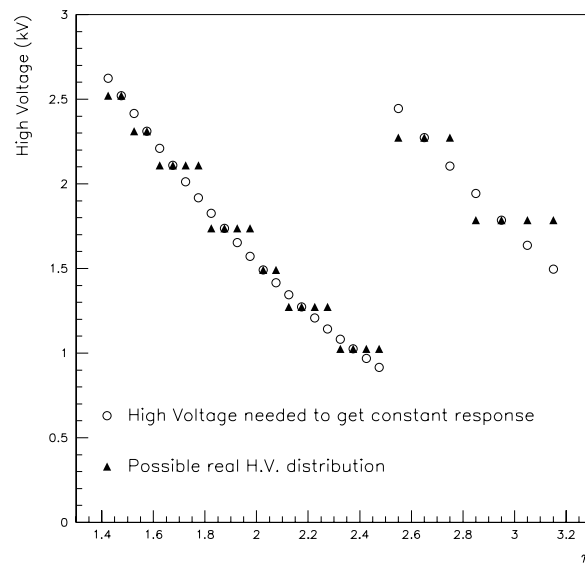


Figure 3.9: High voltage variation along  $\eta$  for a uniform calorimeter response (open circles) together with the solution adopted in practice (solid triangles).

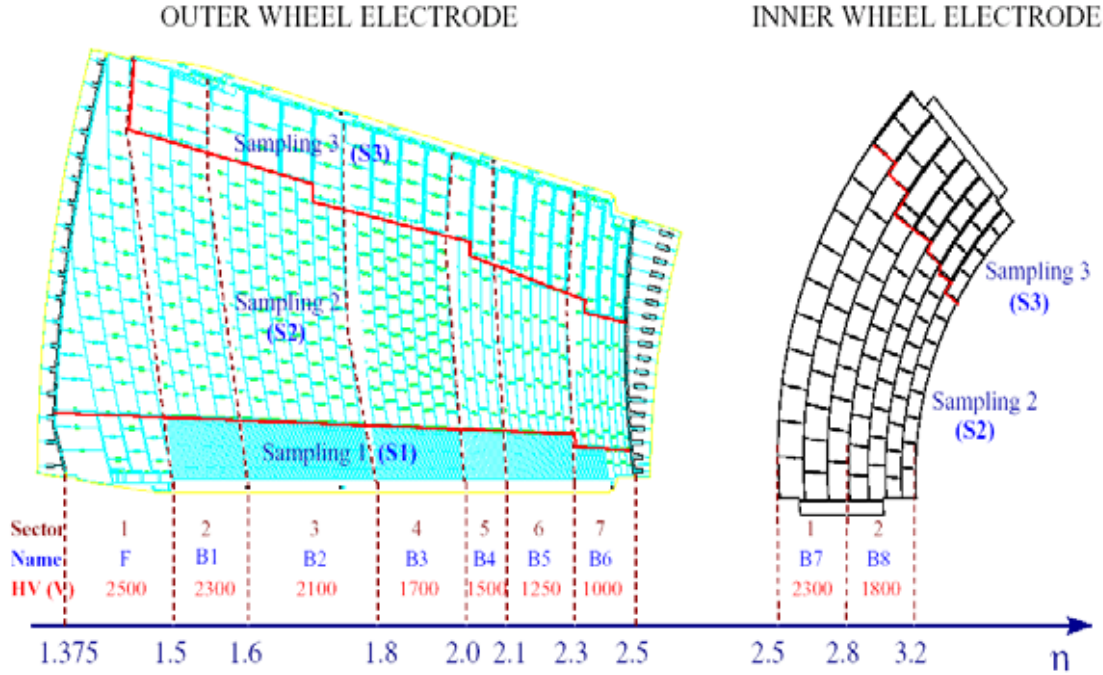


Figure 3.10: Outer and inner wheel flat electrode schematic views. Sampling regions are represented as well as high voltage sectors. High voltage values are indicated for each sector at liquid Argon temperature.

### 3.2.2 Energy resolution

As we have seen in the previous chapter, the energy resolution can be written in this way:

$$\frac{\sigma}{E} = \frac{a}{\sqrt{E}} \oplus \frac{b}{E} \oplus c$$

where

- The  $a$  term, called sampling term, is due to the distribution of the electromagnetic shower energy between the passive and active material and to the intrinsic fluctuations related with the sampling process itself.
- The  $b$  term, or noise term, is due to the noise fluctuations width in the readout chain. It is independent of the deposited energy by a particle in the liquid Argon.
- The  $c$  term, or constant term, is due to the different non-uniformities of the energy response, that means, to the different local or global inhomogeneities. In the table 3.2 we summarize the different contributions to the constant term.

Type		Contribution
Mechanical	Absorbers (thickness)	<0.2%
	Argon ( electrode-absorber gap)	<0.15%
	Accordion geometry ( $\phi$ -modulation)	<0.2%
Calibration method	Amplitude (measurement precision)	<0.25%
	Readout stability	$\simeq 0.1\%$
	Difference between the physics and calibration signals	<0.2%
Others	Liquid Argon impurity	<0.1%
	Temperature inhomogeneity	$\simeq 0.2\%$
	High voltage variation	<0.1%
Total		$\sim 0.55\%$

Table 3.2: Contributions to the constant term of the energy resolution.

At low energy, the noise term is the most important, but at high energies the constant term is the dominant. To minimize  $c$  the assembly quality should be improved, requiring therefore very severe mechanical tolerances in the calorimeter construction.

The requirements imposed by the ATLAS collaboration (in order to get a 1% resolution on the low mass Higgs) are:

- sampling term,  $a \leq 10\%$
- noise term,  $b \leq 300 \text{ MeV}$
- constant term,  $c \leq 0.7\%$

Among these requirements, the most stringent, in order to control the energy resolution over the wide energy range accessible at the LHC, is to achieve a global constant term of 0.7% or better over the full detector coverage devoted to precision physics ( $\eta < 2.5$ ). The first contribution to this term comes from the local (over one cell) constant term, which is mainly related to the intrinsic calorimeter geometry. A second contribution comes from the non-uniformity of the detector response from cell to cell, arising for instance from mechanical, geometrical, calibration or material effects. To meet the requirements on the global constant term, the local constant term must be lower than 0.5%, and therefore, the response non-uniformity has to be around 0.6% over  $\Delta\eta \times \Delta\phi \sim 0.2 \times 0.4$  regions. These regions could then be intercalibrated using  $Z^0 \rightarrow e^+e^-$  events to obtain the desired accuracy after few days at LHC [28].

### 3.3 Mechanical components of EMEC

#### 3.3.1 The absorbers

The absorbers [27] are made of 1.7 mm (2.2 mm) thick lead plates for the outer (resp. inner) wheel, clad with two 0.2 mm stainless steel sheets. They are glued with 0.15 mm thick glass-fiber prepreg. The stainless steel jacket ensures the absorber rigidity (which allows that the liquid Argon gap uniformity is maintained in the level of 100  $\mu m$ ) and a smooth surface for high voltage. The glass-fiber prepreg provides the needed rigidity after its polymerization.

The absorbers have nine (six) waves in the outer (resp. inner) wheel. In order to keep the contribution to the constant term below 0.3% [12], stringent tolerances must be imposed on the absorber thickness, whose nominal values are 2.4 mm (2.9 mm) in the outer (resp. inner) wheel. Along the two straight edges of the folded absorbers, corresponding to the front and back sides of the end-cap calorimeter, two longitudinal glass-epoxy bars are glued. To increase the absorber rigidity, a bar transverse to the waves is glued on the edge at the large radii of each absorber. These bars are used to position the absorbers with a precision of the order of 0.1 mm during stacking.

Two types of absorbers are used in the EMEC: large absorbers for the outer wheel and small absorbers for the inner wheel. The weight of a large (small) absorber is roughly 26 kg (7.5 kg respectively). In order to get a projective region between the outer and inner wheel, the lead length is different in the front and back sides.

The steps of the absorber construction are the following:

- The lead plates were produced at Rohr GmbH, Krefeld (Germany). An online monitoring is performed during the rolling process [29]. This is based on an X-ray source emitting from above and seven phototubes located below the lead sheet as it is being rolled. These phototubes, at fixed positions, measure the attenuation of the X-ray beam intensity in a time window so that each measurement is indeed a thickness averaged over a distance of roughly 10 – 15 cm. The lead plates before their bending are approximately  $1.5 \times 1 \text{ m}^2$  for the larger absorbers and  $0.5 \times 1 \text{ m}^2$  for the small ones. The lead plates are sent to Talleres Mendiaraiz, Zumaya (Spain) where they are cleaned mechanically and laser cut into their designed shapes. They are chemically cleaned by CHIMIMECA (Morians, France).
- The stainless steel sheets are produced by Allegheny Rodney metals, Sprockhovel (Germany). Their thickness tolerance is 6  $\mu m$ . Then they are sent to CPPM, Marseille (France) for inspection and after that, they are laser cut in Mendiaraiz,

Zumaya (Spain), with the same dimensions as the lead plates. They are chemically cleaned by CHIMIMECA, Moirans (France).

- The fiber-glass prepreg was produced by HEXCEL Composites and is of the type Brochier Vicotex 1454NC/50%/120 – 120 *cm*.
- In order to have a very precise 2D thickness map of the lead plates and to check their quality, their thickness is measured at UAM by means of ultrasound techniques [30]. Using this technique, the plates for the first 4 modules were thickness mapped in a lattice consisting of some 400 points. A good correlation between X-ray and ultrasound measurements is observed, as illustrated in fig 3.11. So for the rest of the modules, we decided to restrict the ultrasound measurements to some 20% of the plates randomly sampled within each roll.

Figure 3.12 shows the mean and standard deviation for the average thickness measured over each large plate for Module 0 ([31], [32]), Module 2 (ECC1) and the whole production. To summarize, the standard deviations for the lead thickness measurements which we find to be 7  $\mu m$  (10  $\mu m$ ) are well below the design specifications which are 17  $\mu m$  (22  $\mu m$ ) for the outer (resp. inner) wheel.

- The longitudinal and transversal bars are fabricated in Chatillon sur Seine (France), by *Compreforme*. They are performed with complex material with the following characteristics: non conductor, dilatation coefficient similar to the absorber one, resistance to radiations, non contamination of the liquid Argon and easy manufacture.
- Once all these operations are over, both the lead and stainless steel sheets are sent to Fibertecnic, Vitoria (Spain) where the absorber will be fabricated [33].
- The flat lead and stainless steel plates are pre-glued, and, furthermore along their two straight edges, which will correspond to the front and back sides of the end-cap calorimeter, two longitudinal epoxy bars are glued to them. In order to obtain the accordion shape, they are bent using two presses as illustrated in figs 3.13. Four snapshots of the bending process are shown in fig 3.14.
- In order for the prepreg to polymerize the accordion shaped absorbers undergo a temperature/pressure cycle of (120°C/2.7 bars) using an autoclave technique. For financial reasons, each autoclave cycle is used to cure ten (four) large (resp. small) absorbers. For this purpose, moulds have been designed and built where the bent absorbers are placed, see fig 3.15. These moulds are precision machined with a mechanical reproducibility at the level of 40  $\mu m$ .

The moulds are wrapped in a vacuum bag and put in the autoclave, see fig 3.16. The autoclave cycle lasts for approximately eight hours.



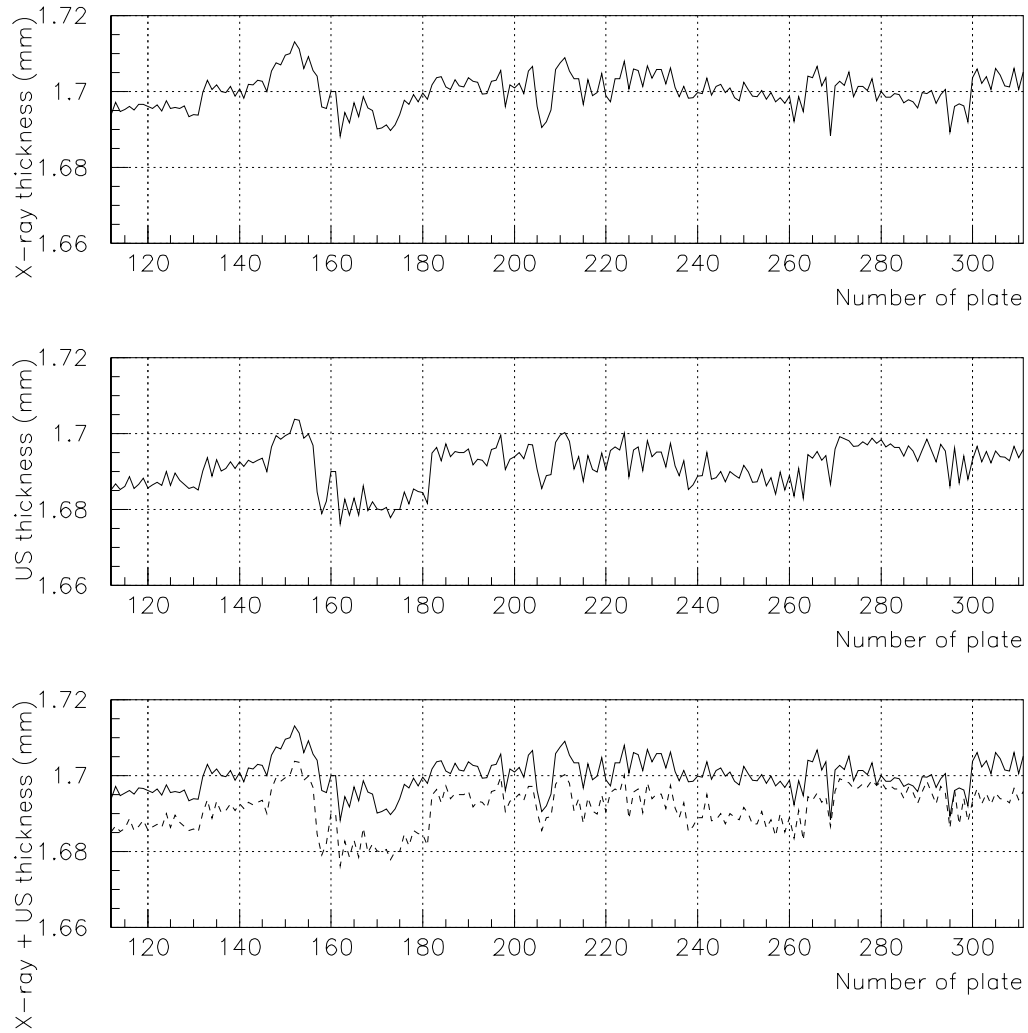


Figure 3.11: From top to bottom, lead plate thickness measured with X-ray techniques, with ultrasound techniques and comparison between both.

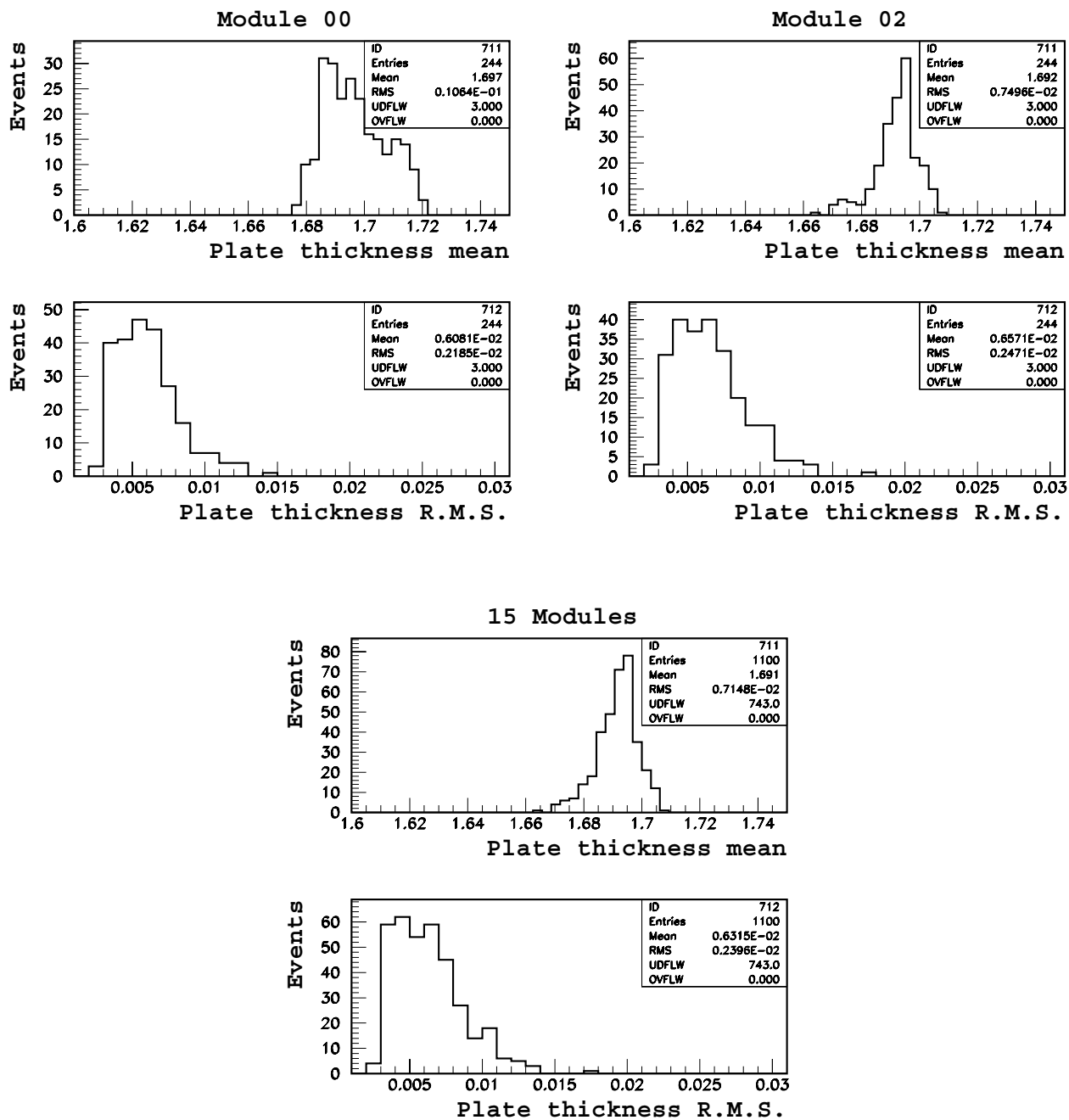


Figure 3.12: Thickness mean and RMS of the large lead plates used in module 0, module 2 (ECC1) and for 15 modules.



Figure 3.13: Presses used to bend large and small absorbers into accordion geometry.

- Once the autoclave cycle is finished the absorbers are cleaned, i.e. rests of the pre-preg are taken away, and visually inspected.
- Thickness and widths at predefined positions are measured with a manual technique (Palmer). Furthermore, for 10% of the absorbers a complete 3D mapping is performed [34], see fig. 3.17. The thickness in each wave is measured in both the acute and obtuse sides. Measurements of the bending angles are also performed. Fig 3.18 shows that indeed the thickness measurements conform to expectations with a standard deviation of the order of  $24 \mu m$  ( $35 \mu m$ ) in the acute (resp. obtuse) side of the absorber. The specifications per module for the acute (obtuse) side are  $110 \mu m$  (resp.  $36 \mu m$ ) [33].
- Finally, the absorbers are sent to the two stacking sites, CPPM and UAM, where a bar transverse to the waves is glued on the edge at large radii of each absorber. These bars are used to help the positioning of the absorbers and reduce their sagging.

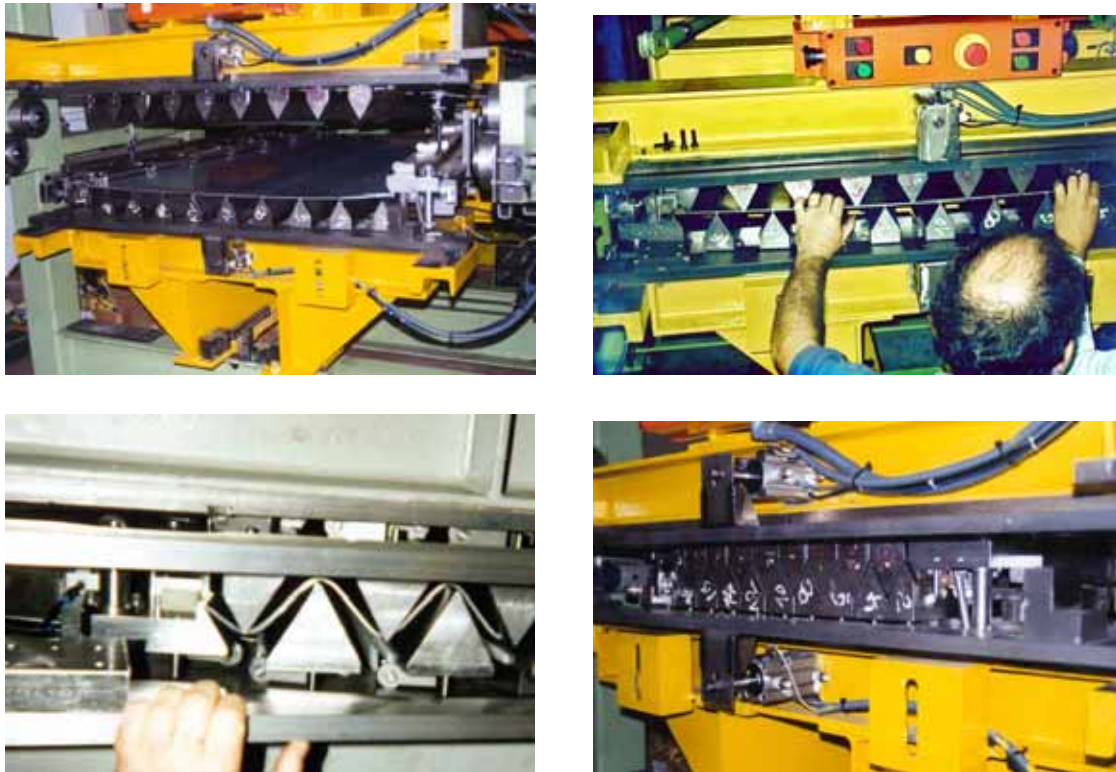


Figure 3.14: Illustrating the bending process for large absorbers.



Figure 3.15: Mould with pre-glued absorber.

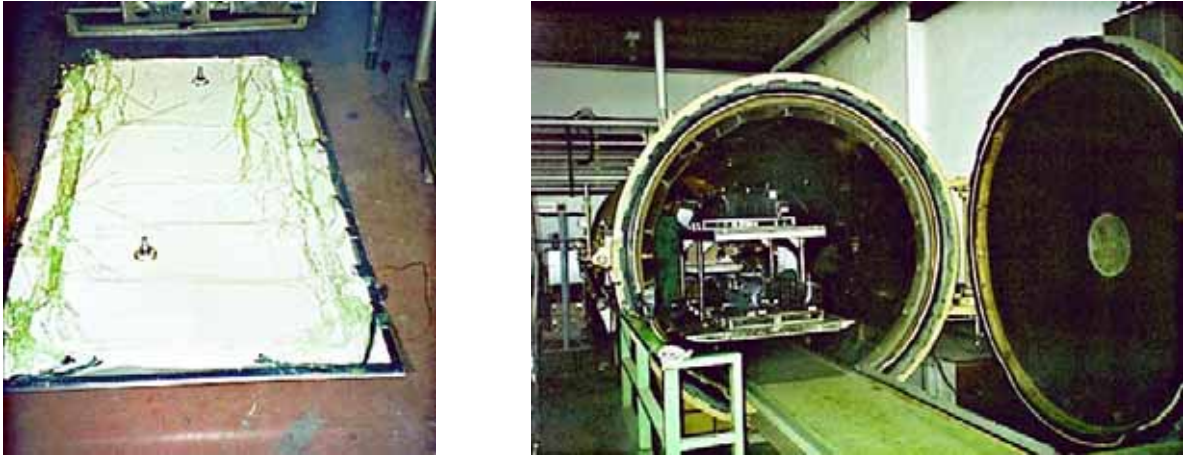


Figure 3.16: Mould in a vacuum bag before entering the autoclave which is shown open.

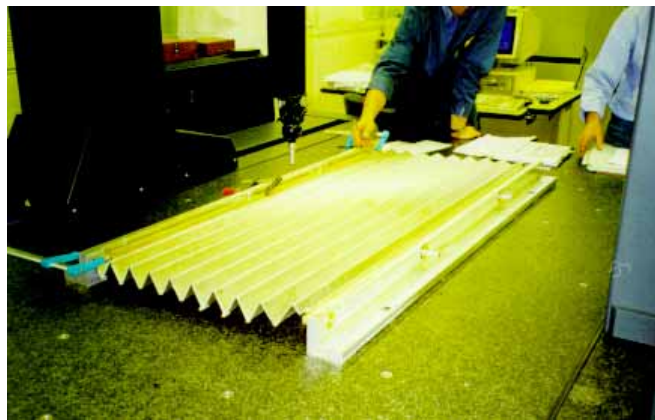


Figure 3.17: Precision 3D measuring table.

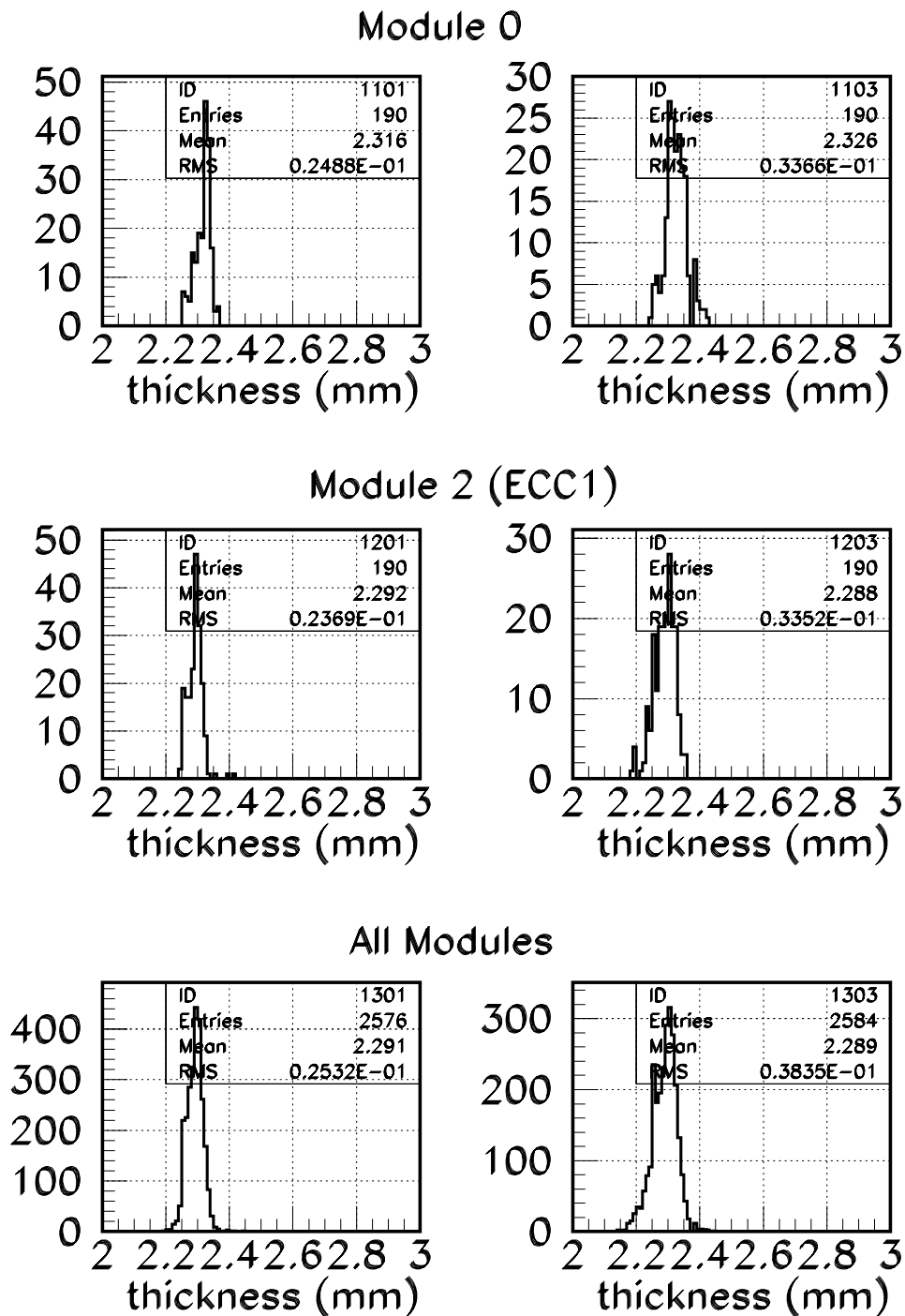


Figure 3.18: Thickness distribution measured at the acute (obtuse) side on the left (resp. right) hand side for all the outer absorbers produced for, from top to bottom, module 0, module 2 (ECC1) and for 15 modules.

### 3.3.2 The electrodes

The readout electrodes [35] are flexible printed circuit boards folded with the same geometry as the absorbers. The electrode thickness is  $275 \mu\text{m}$  and consists of three layers of  $35 \mu\text{m}$  copper, insulated by two  $50 \mu\text{m}$  kapton polyimide sheets (see figure 3.19). This structure combines the functions of the charge collection anode and of the blocking capacitor for the high voltage. The external layers, HV1 and HV2, provide the high voltage to the liquid Argon gaps, while the internal layer allows the signal collection by capacitive coupling. The  $\eta$  granularity is defined in the electrodes as copper strips using kapton as electrical isolator between two strips and between signal and high voltage copper strips. The  $\phi$ -segmentation is defined by connecting the signal paths of the  $n$  electrodes corresponding to  $n$  layers, using summing boards. A module has 3888 readout channels or cells.

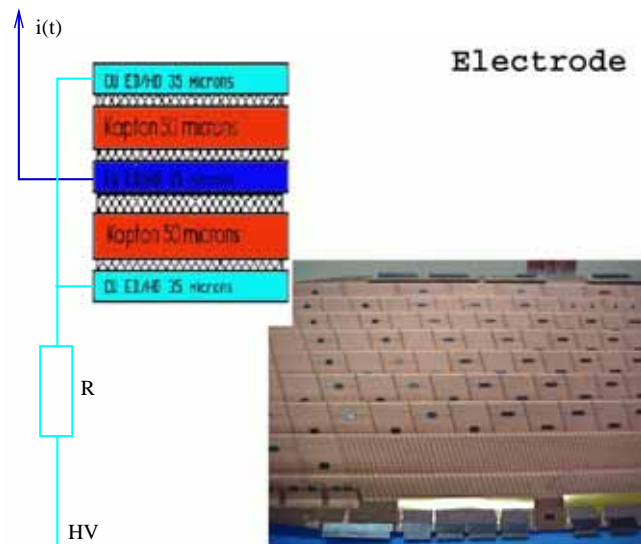


Figure 3.19: A picture of an electrode, right hand side, and an illustration of its internal structure, left hand side.

The electrodes consist of polyimide material, copper, glue and additional metallic and plastic elements used for electrical connections and mechanical support. All the materials should be validated for operation at cryogenic temperature (the electrodes are immersed in liquid Argon kept at about 89 K) and should be tolerant. Moreover, they should not pollute the liquid Argon and should have compatible thermal expansion coefficients among them.

The electrodes have been built by Cicorel S.A. (Switzerland) and MCB Industrie (France).

The bending machine is a single knife associated with a press, adapted to obtain a variable folding angle [36], see figure 3.20. The knife pushes the electrode against an elastic support, foam plate, so that the electrode is bent without longitudinal stress, the fold being symmetrical with respect to the knife axis. A precise positioning of each fold before bending is required and this is achieved with two rectangular indexing holes per fold, which are machined in extra material added on both edges of each electrode. This extra material is cut and removed after bending. For a more detailed analysis in construction of the electrodes refer to [37].

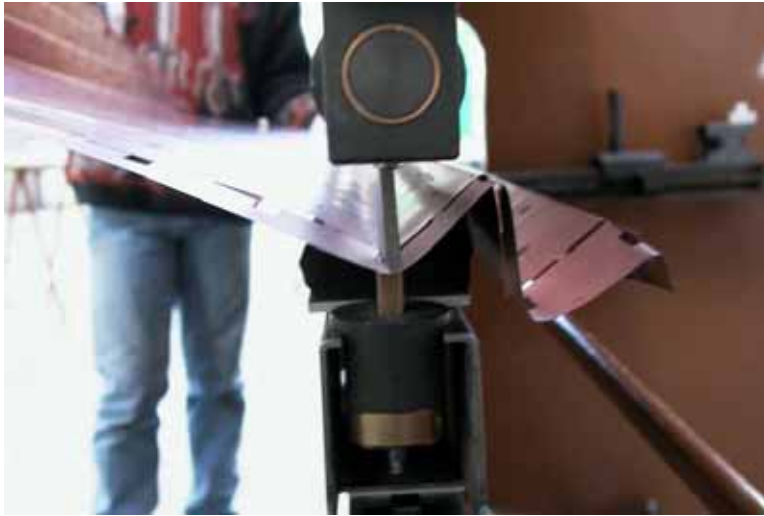


Figure 3.20: Electrodes are bent fold by fold. A machined knife (top) push the electrode against a foam block (bottom).

The electrodes are segmented in depth in three (two) sections in the outer (resp. inner) wheel. Contrary to the outer wheel, the main goal of the  $\eta$  region above 2.5 is to detect missing energy in LHC collisions. Therefore a coarser granularity and only two samplings (middle and back) are necessary in the inner wheel. A schematic view of the module segmentation is plotted in figure 3.21. The three samplings front, middle and back are denoted by  $s_1$ ,  $s_2$  and  $s_3$  respectively. Cell numbers for the three samplings are indicated along  $\eta$  (abscissas) and along  $\phi$  (ordinates). Middle cells are represented by a square and the correspondence with  $\eta$ -units and  $\phi$ -radians can be obtained easily for the three samplings. To be precise, the granularity for the outer and inner wheel are:

- S1, the front section (only for the outer wheel), covering the pseudorapidity interval  $[1.375, 2.5]$  is finely segmented in narrow strips in  $\eta$  except for the regions  $[1.375, 1.5]$  and  $[2.4, 2.5]$ , which correspond to the frontiers with the barrel and the inner wheel respectively. For a given  $\Delta\eta=0.025$  (one middle cell), the number of strips decreases with  $\eta$ . Some  $\eta$  strips of adjacent electrodes are summed by 12 to construct a cell in  $\phi$  ( $\Delta\phi = 2\pi/64 \sim 0.1$ ). The front section is about  $7 X_0$  and it has been designed to be



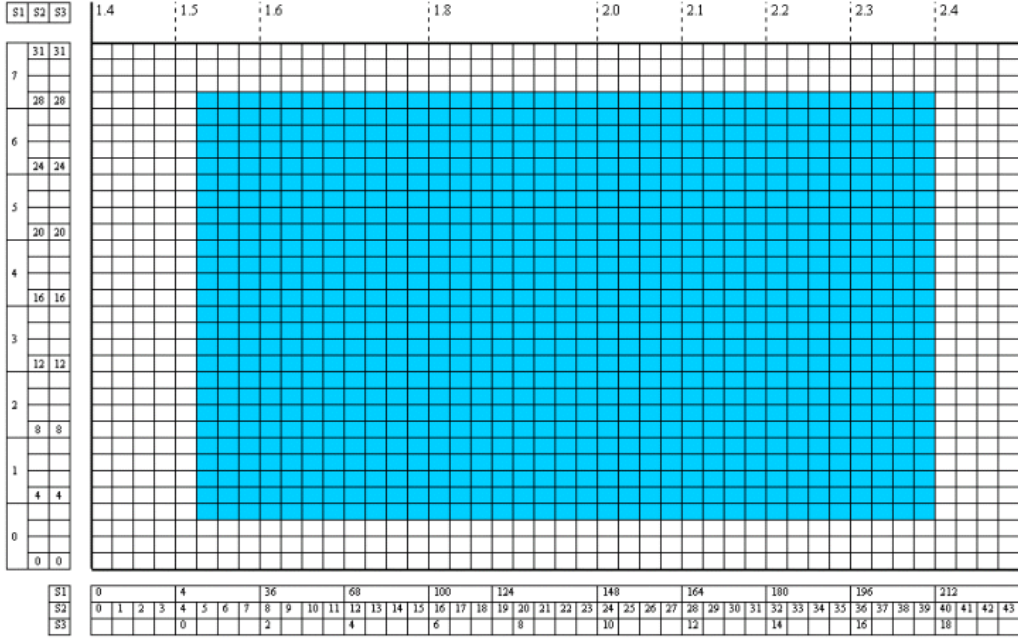


Figure 3.21: Segmentation of the outer wheel of an EMEC module. The blue region corresponds to the cluster central cells considered for the analysis of the fourth chapter of this thesis.

instrumental in the detection of  $H \rightarrow \gamma\gamma$  since it performs precise  $\gamma/\pi^0$  separation. It can also be used for the precise calculation of the particle  $\eta$  position.

- S2, i.e. the middle section, has a constant granularity in pseudorapidity of  $\Delta\eta = 0.025$  ( $\Delta\eta = 0.1$ ) in the outer (resp. inner) wheel, except for a small region in the outer wheel. Together with S1, it will provide an angular resolution of  $50 \text{ mrad}/\sqrt{E(\text{GeV})}$ . This is necessary to measure the Higgs boson mass with a resolution of 1% in the aforementioned decay channel. Three adjacent electrodes with the same  $\eta$  cell are summed in  $\phi$  ( $\Delta\phi = 2\pi/256 \sim 0.025$ ) for the outer wheel, whereas for the inner wheel four adjacent electrodes are ganged together ( $\Delta\phi = 2\pi/64 \sim 0.1$ ). Both the front and middle sections account for  $24 X_0$  and, therefore, the main part of energy deposited in the calorimeter will be those measured in this section.
- S3, i.e. the back section, covering the region  $[1.5, 3.2]$  has a constant segmentation in pseudorapidity which is twice as large (the same) as that in S2 in the outer wheel (resp. inner wheel). This section adds  $4-12 X_0$  ( $2-8 X_0$ ) in the outer (resp. inner) wheel. It has been designed to measure the electrons/positrons energy and high-energy photons, and to improve the particle identification. The back section recovers high energy tails and helps to separate hadronic to electromagnetic particles.

Table 3.3 summarizes the granularity of the EMEC in pseudorapidity.

Wheel	$\eta$ Range	Front	Middle	Back
Outer	[1.375,1.425]	$0.05 \times 0.1$	$0.05 \times 0.025$	-
	[1.425,1.5]	$0.025 \times 0.1$	$0.025 \times 0.025$	-
	[1.5,1.8]	$0.025/8 \times 0.1$	$0.025 \times 0.025$	$0.050 \times 0.025$
	[1.8,2.0]	$0.025/6 \times 0.1$	$0.025 \times 0.025$	$0.050 \times 0.025$
	[2.0,2.4]	$0.025/4 \times 0.1$	$0.025 \times 0.025$	$0.050 \times 0.025$
	[2.4,2.5]	$0.025 \times 0.1$	$0.025 \times 0.025$	$0.050 \times 0.025$
Inner	[2.5,3.2]	-	$0.1 \times 0.1$	$0.1 \times 0.1$

Table 3.3: Transverse granularity ( $\Delta\eta, \Delta\phi$ ) of the EMEC in pseudorapidity.

The distribution of the HV to the utter layers of the electrodes is realized by means of resistive silk-screened pads of carbon-loaded epoxy ink. The layout of the resistor pads, which can be seen on fig 3.19, was driven by the following criteria:

- avoid cross-talk between calorimeters cells.
- protect the input of the preamplifiers.
- minimize dead regions in the front sampling.
- protect the front end electronics against sparking. It requires high resistance values.
- minimize the high voltage drop induced by minimum bias pile-up events. It requires low values of R.

Some of these requirements are conflicting, so a compromise is reached with a nominal resistance value of  $1 M\Omega$  at room temperature, which maintains a relative drift velocity variation at the level of 0.1%, and consequently a negligible contribution to the constant term [38].

In the outer wheel, signals from the front section (S1) are routed to the front side of the detector. Except for  $\eta < 1.5$ , signals from the middle (S2) and back (S3) sections are routed to the back side (as well as in the inner wheel). Output connectors are stapled and soldered on both flat edges of the electrodes. A coppered kapton foil, called flap, glued on a cylindrical plastic tube, is soldered on the ground pad of the electrode to ensure proper grounding of the absorber.

### 3.3.3 The honeycomb spacers

The fluctuation of this gap is a very important source of non-uniformity. In order to maintain the electrode centred in between two consecutive absorbers, insulating honeycomb spacers were used. The spacers are made of NOMEX paper impregnated with phenolic resin, laid in the flat areas of the accordion. This is a very low density material i.e.  $\rho = 32 \text{ kg/m}^3$ . The strips are cut from plates produced with linearly variable thickness, with a tight tolerance of  $+0.05 \text{ mm}$  and  $-0.25 \text{ mm}$ . They consist of hexagonal cells which are similar to honeycombs and are capable to bear the weight of the absorber plates. Even if the width of the flat parts of the accordion varies as a function of the radius, it is kept constant to make easy the honeycomb strip cutting. They are linked together with glass-fiber wires glued only in contact with the honeycomb material. The relative position of the strips is given by jigs used to have the glue set. See figure 3.22 for illustration.

Originally the spacer thickness was chosen to be the nominal one i.e. the gap thickness and two spacers were used for the outer wheel. While stacking module 0, an overbulging effect was seen. On the short term, the problem was solved by mechanically constraining the absorbers with the drawback of inducing short circuits between electrodes and absorbers. On the long term, the solution found for the overbulging effect was to cut the honeycomb spacers a few tens of microns thinner. We will see in a forthcoming section how the sagitta measurements do show that the mechanical deformations are kept under control. Additionally, to avoid short circuits in the obtuse part of the outer wheel (due to a possible contact of an electrode with an absorber) a third type of continuous honeycomb spacer has been added for module series production, see figure 3.23.

In summary, in order to take into account the electrode-absorber gap variation, three honeycomb strips (C, D, R) are used to cover the overall length of the outer wheel absorber for series production modules. Two (A, B) are used for the inner wheel.

## 3.4 The electronics

The electronics are divided into two parts: the electronics inside the cryostat, in the liquid Argon, called cold electronics, and the electronics outside the cryostat or warm electronics.

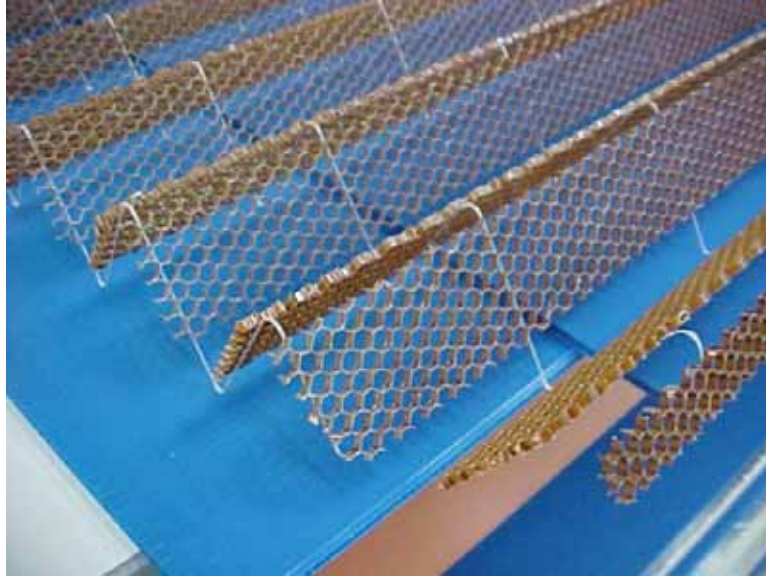


Figure 3.22: Photograph of a D honeycomb spacer.

### 3.4.1 The cold electronics

#### The HV and summing boards

Two types of boards made of multilayer PCBs are plugged on the electrode connectors. The first one, HV board, distributes the high voltage to  $\phi$  sectors consisting of 24 (8) electrodes in the outer (resp. inner) wheel. There are two HV cables soldered on the board, to supply the lower and upper gaps separately. The different types of boards needed for the EMEC as well as their dimensions are summarized in the table 3.4. The PCBs were fabricated by ELATE S.A., Madrid (Spain). The boards were manufactured and quality controlled at the stacking sites at CPPM and at UAM. A detail of a HV board is shown in fig 3.24.

The second type, the summing boards (SB), performs the signal summation in  $\phi$  thus defining the granularity. In fact, 12 adjacent electrodes are summed for a front cell and 3 (4) for middle and back cells in the outer (resp. inner) wheel. A detail of the summing boards is shown in fig 3.25. The different types of summing boards with their dimensions and number of layers are summarized in table 3.5.

The summing boards for module 0 were single layered, and for series production their design was turned into multilayered in order to reduce cross-talk effects. The summing boards are impedance controlled, with a tolerance of 10%. The PCBs themselves were also manufactured by ELATE S.A., Madrid (Spain). The boards were fabricated by TEYDISA, Madrid (Spain). The quality control was performed in our laboratory at



Figure 3.23: Photograph of an R honeycomb spacer.

UAM.

The front (back) side of the outer wheel with HV and summing boards plugged in is on the top (resp. bottom) left part of figure 3.26.

### The mother boards

Mother boards are plugged on top of the summing boards. They collect the ionization signal and distribute the calibration signal through resistive networks. We use them to inject a current pulse with known amplitude in the lecture chain, simulating the pulse which comes from the calorimeter cells, in order to get a precise calibration of the readout electronic. This pulse is generated by a calibration board located in the outer wall of the cryostat. Using the resistances of the mother board, the voltage is converted in current. A detail of a MB is shown in figure 3.27.

### 3.4.2 The warm electronics

The warm electronics [39] correspond to the electronics which are located outside the cryostat. For all the ATLAS LAr detectors, i.e. the electromagnetic and hadronic calorimeters, the warm electronics are identical. The signal cables exit from the mother boards to the internal walls of the cryostat and they go towards outside, where the front end crate (FEC) is located.

		Length (mm)	Width (mm)	Boards
F1	hv-f	350	50	72
B1	hv-b1	340	50	72
B2	hv-b2	320	50	72
B3	hv-b3	260	50	72
B3	hv-b4	220	50	72
B4	hv-b5	200	50	72
B4	hv-b6	170	50	72
IB	hv-b7	220	60	36
IB	hv-b8	180	60	36

Table 3.4: Characteristics of the different types of HV boards.

The FEC (see figure 3.28), situated above the cryostat, contains the following types of boards:

- Front-end boards (FEBs), which amplify, shape, store the signal during the trigger latency and then digitize the selected signals. The FEBs provide virtually dead-time free operation up to 75 kHz trigger rate. They treat 128 channels in 16 groups of 8 channels. Each block includes: 2 four-channel preamplifiers, 2 four-channel shapers, 2 twelve-channel analog memories or SCA (Switched Capacitor Arrays) and one 12-bit ADC running at 5 MHz. The dispersion of the electronic gains on a FEB is determined to be about 2%.
  - A preamplification is done in order to decrease the electronic noise influence inside the readout chain. The preamplifiers are of current sensitive type to provide fast signals over the large dynamic range needed for operation at the LHC. A protection network is added in front of the preamplifier in order to withstand potential HV sparks in the detector gaps.
  - Since the bunch crossing time will be 25 ns, much smaller than the response time of detector ( $\sim 450$  ns), additional signals from different beam crossing could be added, leading a pile-up noise. To solve this problem, a shaper chip, with a  $CR - RC^2$  architecture, is located immediately after the preamplifier. One differentiation removes the long trailing tail of the LAr signal and two integrations limit the useful bandwidth and reduce electronics noise. We can optimize the relation signal to noise choosing the value of its time constant (the integration time of the input signal): the electronics noise (pile-up noise) decrease (increase) when this time decrease. In order to minimize the total

	Length (mm)	Width (mm)	Layers	Boards
F1-S	170	40	8	128
F2-S1	160	60	2	128
F2-S2	160	60	2	128
F3-S1	150	70	2	128
F3-S2	140	70	2	128
F3-S3	140	70	2	128
F3-S4	130	70	2	128
F4-S1	120	50	2	128
F4-S2	120	50	2	128
F4-S3	110	50	2	128
F4-S4	110	50	2	128
F5-S1	100	70	2	128
F5-S2	90	70	2	128
F5-S3	90	70	2	128
F5-S4	80	70	2	128
F5-S5	70	30	2	128
B1-S	170	50	8	128
B2-S1	160	50	8	128
B2-S2	150	50	8	128
B3-S1	140	50	2	128
B3-S2	120	50	2	128
B3-S3	110	50	2	128
B4-S1	100	50	2	128
B4-S2	90	50	2	128
B4-S3	90	40	2	128
B4-S4	80	40	2	128
IB-S1	120	50	2	64
IB-S2	100	50	2	64

Table 3.5: Characteristics of the different types of summing boards.

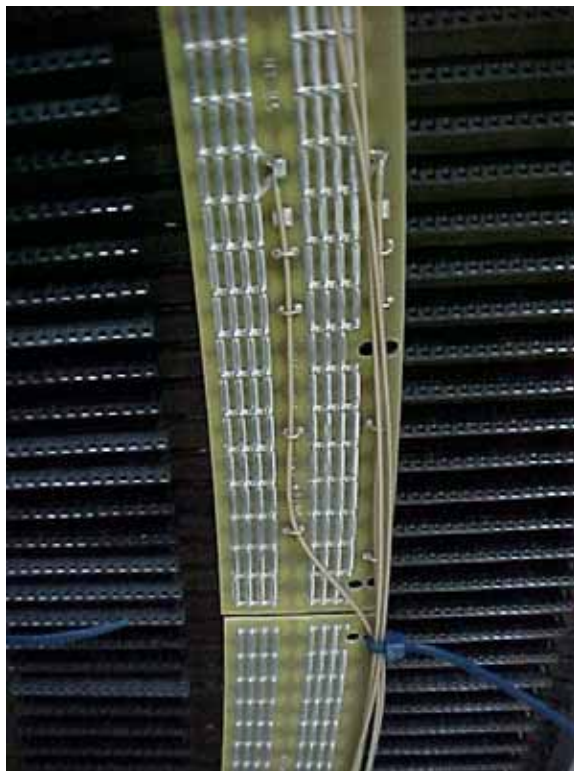


Figure 3.24: Photograph of a HV board.

noise, a  $\tau_s = 15$  ns have been chosen<sup>6</sup>.

- The signal is amplified with three different gains: high, medium and low gain. The gain ratio is approximately 1:9.3:93.
- The Tower Builder board sums the calorimeter cells by trigger tower, with  $\Delta\eta \times \Delta\phi = 0.1 \times 0.1$ .
- After shaping the signal is sampled at 40 MHz (each 25 ns) and stored in an analogical memory, switch capacitor array (SCA).
- Seven amplitudes sampled are stored and digitized in 12-bits 5 MHz ADCs, until the trigger signal is received. In the testbeam, this trigger signal comes from the external machine while in ATLAS is the First Level Trigger (FLT). The choice of which signal (gain) is to be digitized is either done automatically by the hardware (free gain) or the digitization of one, two or three gains can be programmed. For the free gain mode, the gain selector compares a predefined sample in medium gain after digitization to two thresholds. If the signal is less than the first threshold, the high gain will be chosen. If the signal is greater than the second one, the low gain will be chosen.

---

<sup>6</sup>We have chosen a mean value for this time constant although it depends on luminosity and  $\eta$  position.



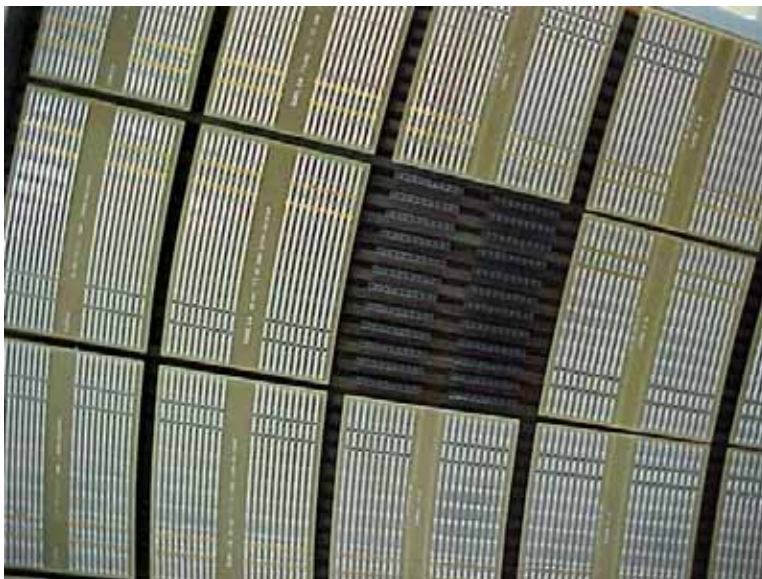


Figure 3.25: Photograph of summing boards.

- Event output data is formatted and sent in 32-bit words at 40 MHz to the miniROD (Read Out Device) board.
- Calibration boards
 

The front end crate (FEC) also houses the calibration boards (CALIB) [40], which generate high precision calibration pulses. One of the contributions to the constant term comes from the electronic readout chain. In order to reduce this contribution, all channels must be calibrated with a good precision. The calibration board must provide fast signals resembling closely the ionization signal in order to study the readout channel influence. Several requirements are demanded for the calibration signal:

  - The calibration signal must have a rising time of  $\sim ns$  and a decreasing time of  $\sim 450 ns$ , as the ionization signal.
  - It must be linear over a large dynamic range, from  $200 nA$  (noise amplitude) up to  $10 mA$  (amplitude equivalent of 3 TeV of deposited energy in one calorimeter middle cell).
  - It must be uniform ( $< 0.25\%$  including signal distribution).
  - It must be radiation tolerant and it must be able to operate inside magnetic fields of  $\sim 10 mT$ .

The injection signal which come from the calibration board has a decreasing exponential shape:



Figure 3.26: Front (back) side of a stacked module with all HV and SB cards plugged in, on the top (resp. bottom).

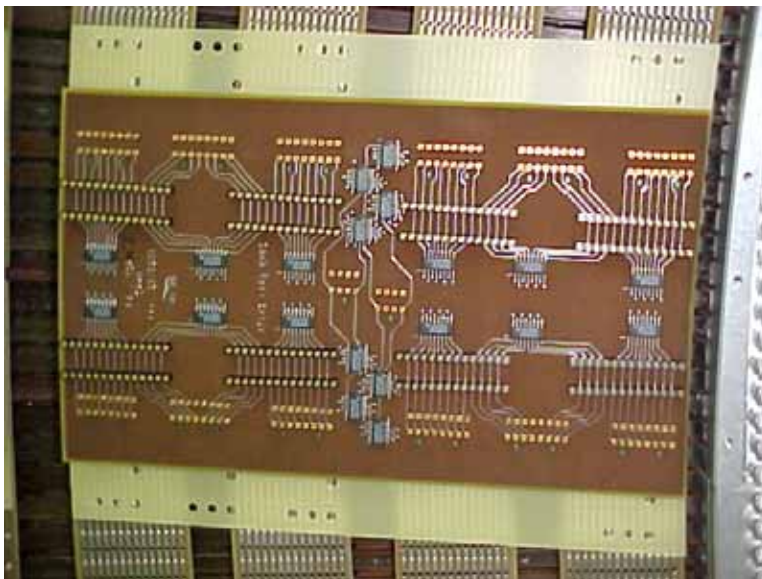


Figure 3.27: A picture of a mother board.

$$V_c(t) \propto I_c e^{-\frac{t}{\tau}}$$

where  $I_c$  is the current produced in a 18 bits numeric-analogic converter DAQ. The signal is injected inside the cells through an injection resistance  $R_{inj}$  (see figure 3.28), which is on the mother boards, in order to provide a current. This is not affected by the inductance between the mother boards and the detector. Finally, the calibration signal which come from the cells, go through the same readout electronic as the physics signal and the same treatment is applied.

The calibration signal is different from ionization signal and the injection points are also different (the calibration signal is injected on mother boards whereas the ionization signal is injected on electrodes).

- The FEC contains control boards to receive and distribute the 40 MHz clock, the level-1 accept signal, as well as other fast synchronous signals, and to receive and distribute control information to configure and control the various boards in the crate.
- Finally, the front end crate also contains monitoring boards to read out various monitors.

To each FEC is associated a read-out driver crate (ROD) which contains:

- a CPU connected to the network to control the electronics;

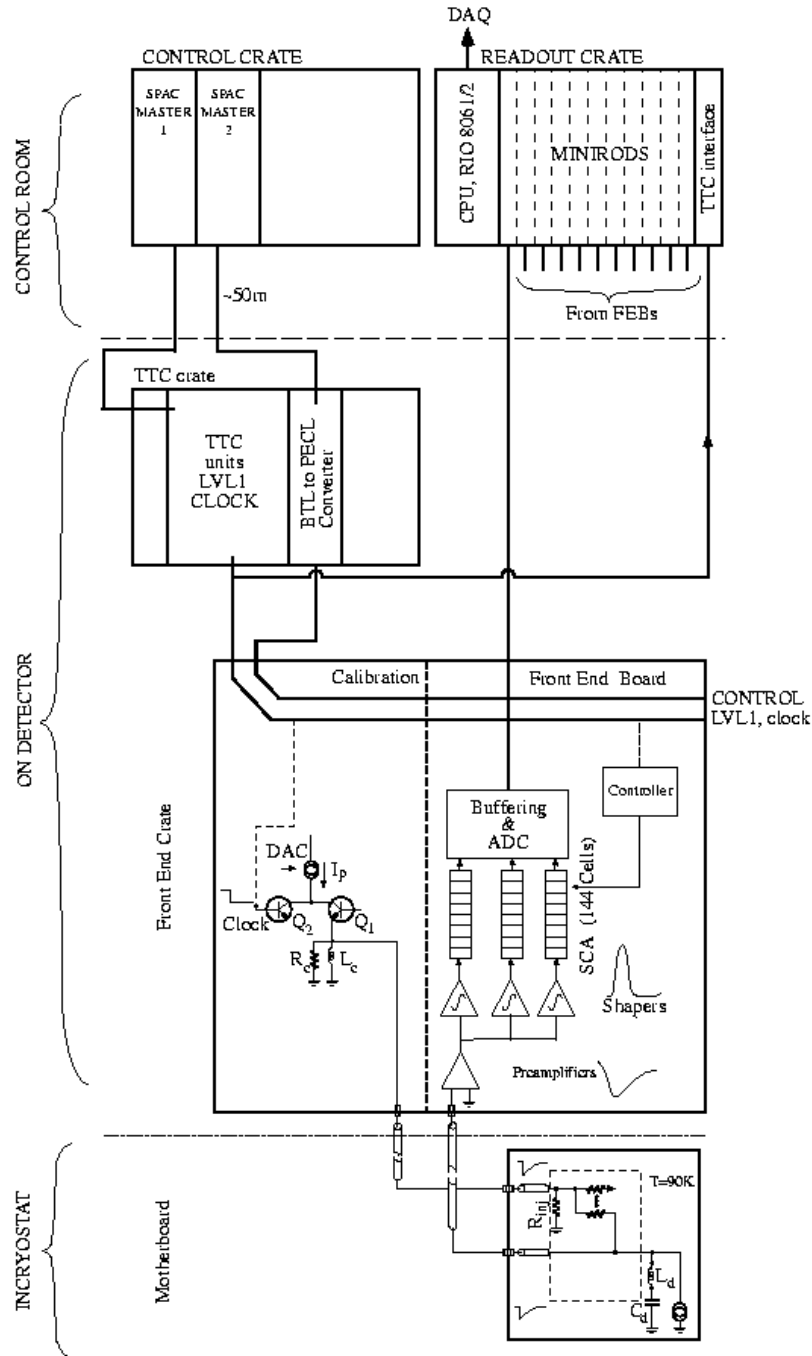


Figure 3.28: Schematic of the calorimeter readout.

- a communication module to configure or down-load parameters into the various boards of the FEC or to read back registers;
- Read Out Driver (ROD) modules, which receive raw data from the FEBs and produce the corresponding energy, time and some form of data quality measure, sending the result to the DAQ.

### 3.5 Changes since pre-production module

Several small modifications were introduced after the EMEC prototype module beam test in 1999. Firstly, in order to reduce the inductive cross-talk to an acceptable level ( $< 1\%$ ) [41] the summing and mother boards were redesigned. Secondly, a ground connection was added on every electrode connector to obtain a better uniformity of the middle cell inductances along  $\eta$ . Additionally, stricter quality controls were introduced for module production and the cleanliness of the stacking room was improved. Honeycomb spacers were modified in rigid honeycomb nets, facilitating their positioning. Moreover, high voltage tests are done on the spacers before stacking. As we have said previously, for the serie production modules three honeycomb spacers have been used (instead of two spacers for the module 0) in the outer wheel, and the spacers were cut a few tens of microns thinner.

### 3.6 Module assembly

The stacking [27] has been performed at two sites: Madrid and Marseille. At each site, it is performed in a clean room, sealed from external air penetration, with a small atmospheric overpressure and a constant temperature of  $20^{\circ}C$ . Humidity is controlled. The total weight of the detector is supported mainly by two large external aluminum rings (see figure 3.29). However, in order to minimize the width of the crack between the outer and inner wheels and link these two wheels together, intermediate rings are used at  $\eta = 2.5$ . The front one is made of composite material to reduce the amount of dead material in front of the detector. The back one is made of aluminum. They have been manufactured at the INP Novosibirsk (Russia). Five additional lighter aluminum rings are added, two on each side of the outer wheel to control the gap thickness, and one on the circumference in between the two external rings to minimize the absorber deformation.

The stacking operation starts by handling one large absorber, previously vacuum and alcohol cleaned, with a lifting beam equipped with suckers. The heads of the longitudinal bars are inserted into the grooves of the rings and slide down along them. The position of



Figure 3.29: Structure elements bolted to the stacking frame (back side).

each absorber is then precisely defined by inserting pins and screws into centering holes drilled in both absorber bars and support rings.

A first layer of honeycomb spacers is then put in place. These honeycomb spacers have been previously HV tested in two separate bench tables (for outer and inner wheel), built at ISN Grenoble (France), see figure 3.30. The spacers are placed in between two absorbers, one grounded and the other one kept at a given voltage, thus mimicking a real electrode-absorber gap. The voltage settings are even much higher than the nominal ones, see the table 3.6, in order to have an additional safety margin.

Spacer type	A	B	C	D	R
Voltage (V)	2200	1800	3300	2700	2200

Table 3.6: High voltage settings for the test of the spacers.

After vacuum and alcohol cleaning, the electrode is installed and kept in position. A second layer of spacers is put on the electrode and the complete gap is closed with the next absorber (which is fixed with pins and screws). The rest of the gaps which complete



Figure 3.30: Picture of the high voltage test bench for outer wheel spacers.

the module are stacked in the same way.

Once the module stacking is finished and all tests are good successfully passed, the summing and mother boards are connected over the electrodes, and the module is cabled.

Figure 3.31 shows the back side of an electromagnetic end-cap module with the complete cold electronics, i.e. HV, SB and MB, inside the stacking frame in the clean room at UAM. The readout cable harnesses, 64 channel kapton coaxial cables, are plugged on the MB and routed out of the module, see the bottom part of the figure. To reduce the noise contribution, cables with  $25 \Omega$  and  $50 \Omega$  characteristic impedance are used for the middle-back and front sections, respectively.

Finally the modules have been integrated in the two electromagnetic calorimeter end-caps. The ECC wheel assembly and integration are shown in figures 3.32 and 3.33.

### 3.7 Tests for modules validation

The quality of the stacking is monitored by the following tests sequence [42]:

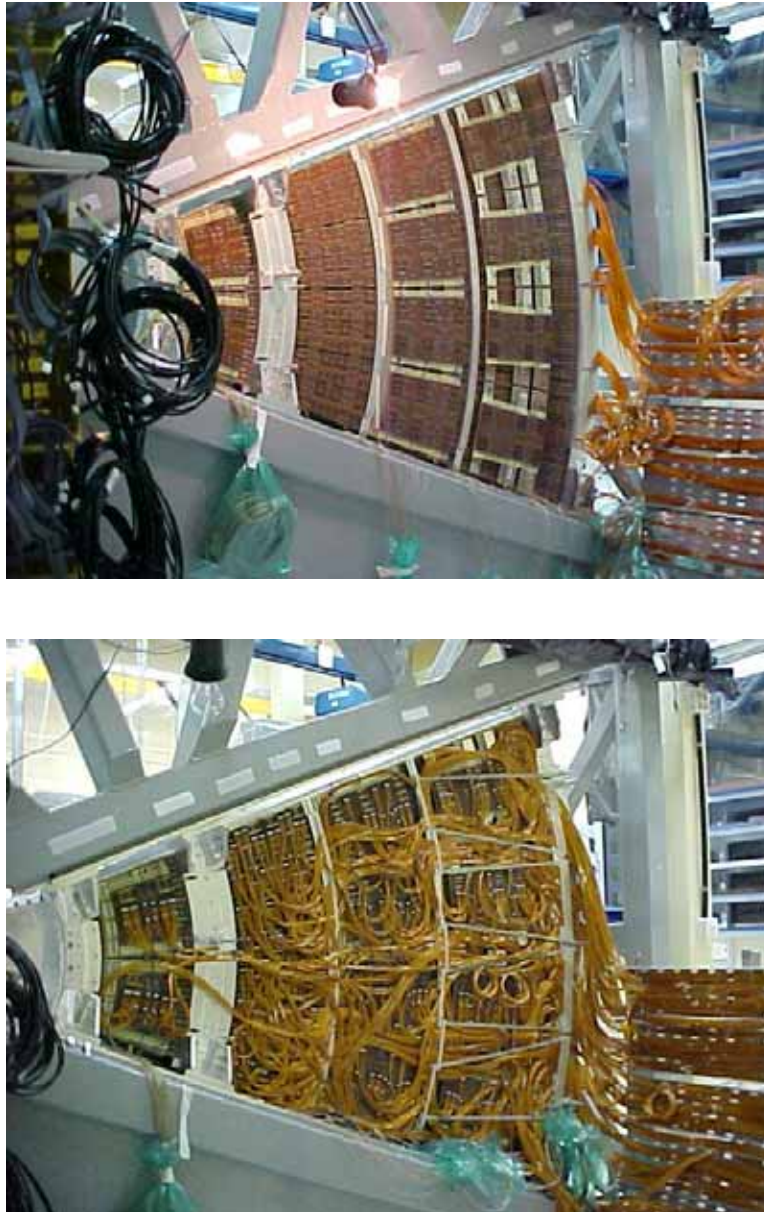


Figure 3.31: View of a fully stacked module with all HV, SB and MB cards plugged in (top) and cabled (bottom).





Figure 3.32: ECC wheel assembly at CERN.

- sagging measurements on the last stacked absorber
- a HV test after each stacked gap to check the voltage holding of the gap between electrodes and absorbers
- a low frequency test (TBF) after every mounted gap to check the correct distribution of the high voltage and the electrical continuity of the signal readout
- an overnight HV test on the gaps stacked during each day
- a long time (week-end) HV test on the last  $\sim 24$  stacked gaps
- a final high voltage test over the whole module, at the end of the stacking, and after tightening the position pins and screws again
- gap capacitance measurements (CAPAGAP), at the end of the stacking, to electrically control the gap thickness uniformity and the mechanical assembly quality
- cell capacitance and inductance measurements, after stacking, to map the module readout characteristics for future signal reconstruction

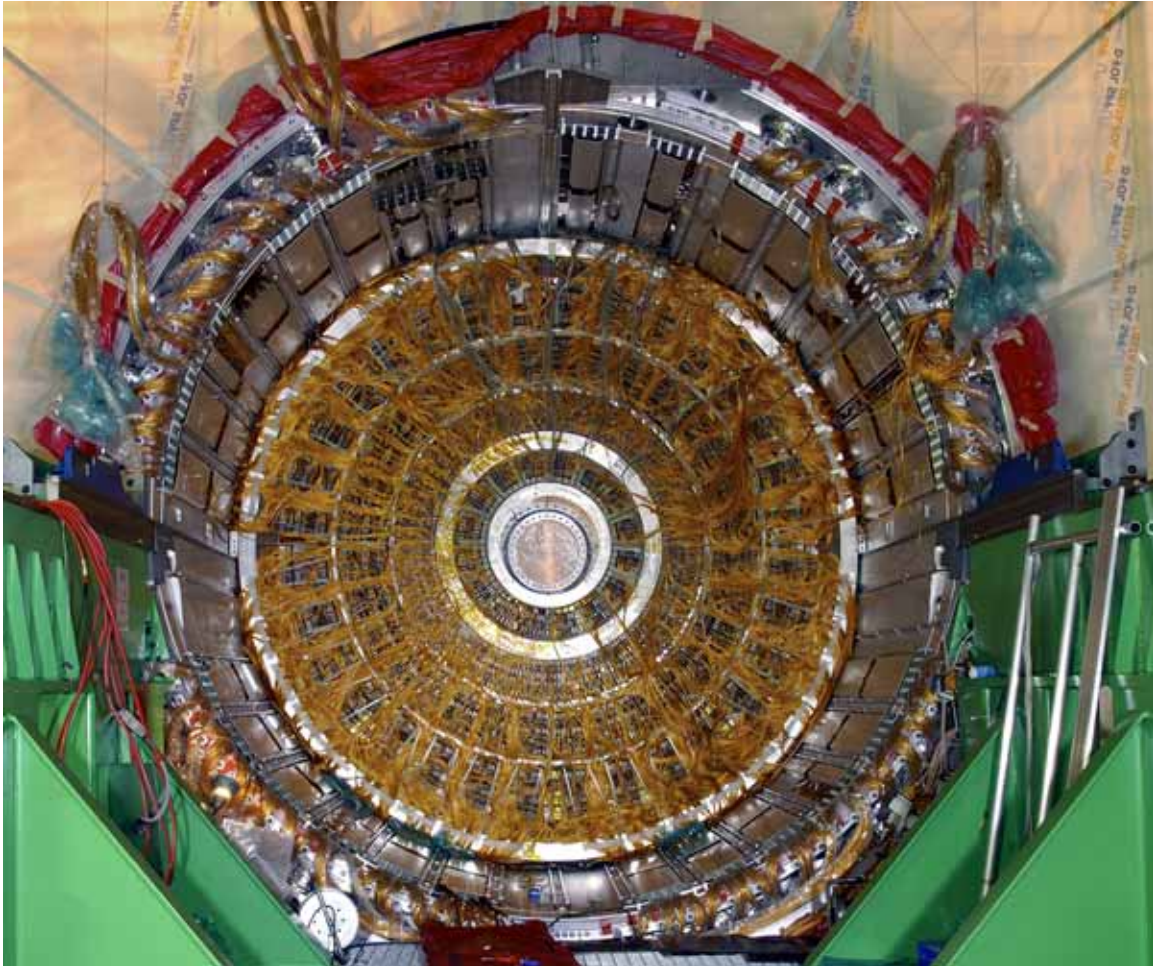


Figure 3.33: ECC wheel.

- cold and warm high voltage tests at CERN
- cold electronic resistive network measurements, during cold tests at CERN, to check the resistance values and their small dispersion (0.1%)
- cell response measurements with calibration pulses (TPA), during cold tests at CERN, to check cable continuity and signal output shape.

The three last tests are made at CERN, while the rest of tests are made at the stacking sites (Marseille or Madrid).

### 3.7.1 Sagging measurements

Sagitta measurements have been performed systematically as a way to monitor the stacking process. While stacking module 0, a total sagitta of 3 *mm* was measured on the absorber central wave after stacking of the first 12 absorbers plates. At that time the adopted short term solution was to mechanically stress the absorbers by putting some load on them. On the longer term the solution chosen was to cut the spacers a few tens of microns thinner than nominal.

To control the possible mechanical deformation of the detector, the relative height of each wave along four (one) equidistant lines, orthogonal to the front and back sides of the module, in the outer (resp. inner) wheel is measured, after one absorber is fixed. For the outer wheel they roughly correspond to  $\eta \sim 1.5, 1.8, 2.1$  and  $2.4$ .

These mechanical deformations have several consequences: they complicate the stacking and the assembly of the wheels. Physically, a deformation produces a variation in the gap, inducing an electric field variation and therefore, it implies a variation in the signal height. That could be an important source of detector response non-uniformity.

Out of the many plots that one can choose to illustrate the magnitude of these possible deformations, we show in figure 3.34:

- the sagitta measurements for absorber number 36 in ECC1 along the four pseudo-rapidity values previously mentioned as a function of wave number, left hand side. Notice the parabolic deformation shape, whose maximum located at the fifth wave number, increases with increasing  $\eta$ . This is expected as due to the central back pin in the transversal bars.
- the sagitta measurements for the fifth wave at  $\eta = 1.8, 2.1$  as a function of the absorber number, right hand side. The distribution is rather uniform, almost overall positive definite and with an absolute average value of the order of 0.3 *mm* and 0.8 *mm*.

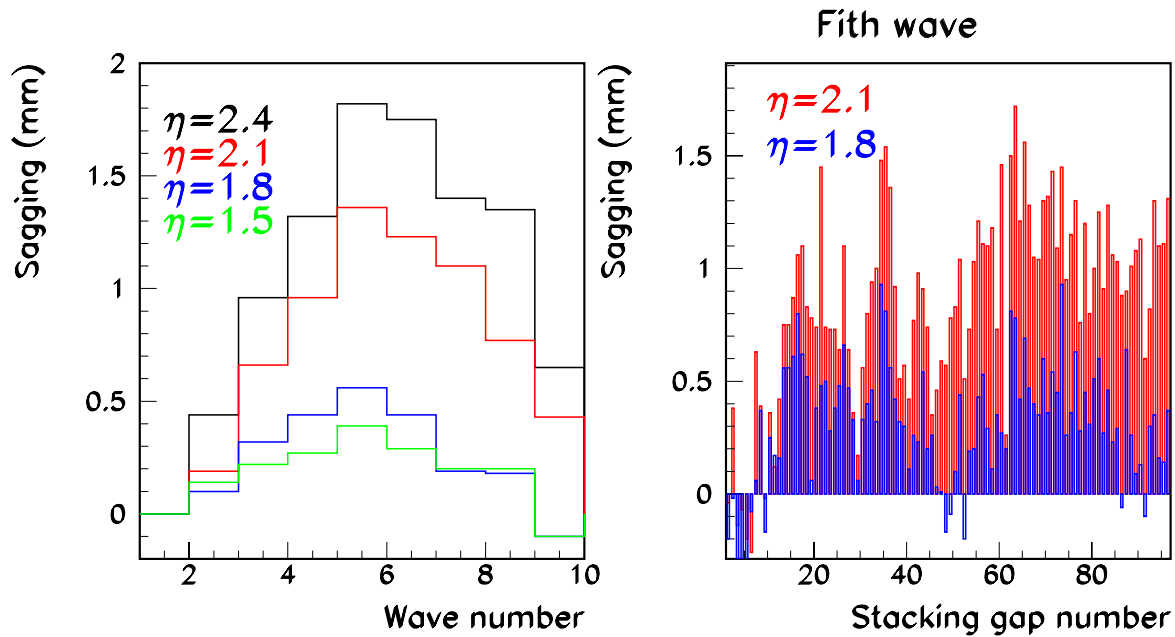


Figure 3.34: Sagitta measurements for absorber 36 in ECC1, as a function of wave number at four pseudorapidity values, left hand side. Sagitta measurements as a function of absorber number for two central pseudorapidity values, right hand side.

### 3.7.2 Electrical tests

The tests HV, TBF, CAPAGAP and TPA [42] are performed with similar benches located at each stacking sites and at CERN. They are based on:

- A computer with a *GPIB bus* which controls the electronic modules;
- A crate with a custom VME-like base plane and controller board (IGPIB), power supplies and several electronic boards:
  - a MUXCAPA board used as a low frequency sinusoidal signal generator for the TBF test and as a multiplexer for the CAPAGAP test,
  - a TBF board which distributes the low frequency signal,
  - MUX boards which multiplex readout signals, with respectively 2 (25) boards for the TBF (TPA) test,
  - a TPA board which generates input signal for the cell response measurements,

- a CQHT board, which is a secure multiplexer for the HV and TBF tests;
- A digital oscilloscope used to readout signals from the TBF or TPA tests;
- A 30 MHz bandwidth RLC meter used in the CAPAGAP test;
- A computer controlled power supply, with a 10 nA current sensitivity.

### High voltage tests

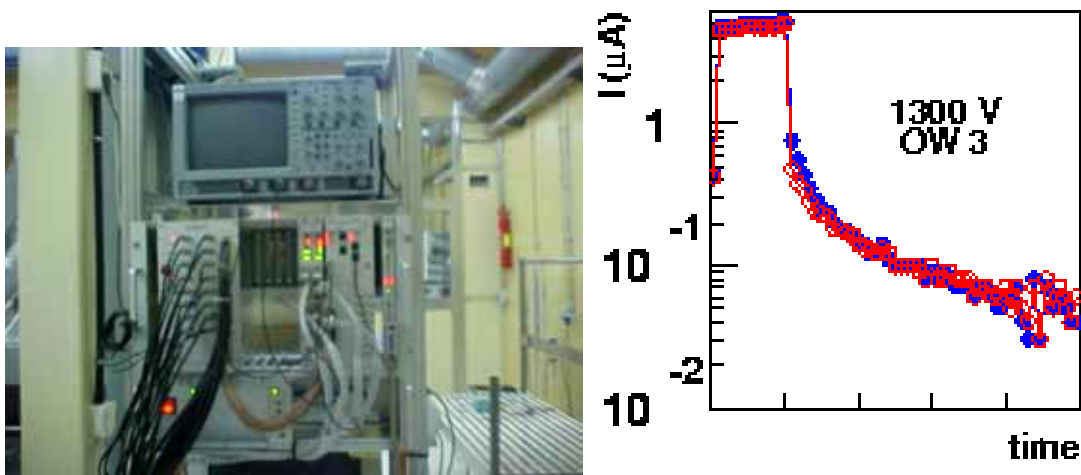


Figure 3.35: High voltage test bench, left hand side. Evolution with time of the current drawn in sector three when 1300 V is applied, right hand side.

This test is performed to detect any high voltage problem by measuring the leakage current of each electrode side and each high voltage sectors. A tension is applied to the electrodes and the leakage currents are recorded. The high voltage tests are performed using a power supply with a current sensitivity of 1.0  $\mu A$ , see figure 3.35.

High voltages are distributed on both electrode sides, HV1 and HV2. The high voltage settings vary stepwise as a function of  $\eta$ . In the outer (inner) wheel there are seven (resp. two) HV sectors. For the first four modules, the settings were chosen at the values corresponding in air to those in Argon at cold. For modules fifth and beyond we set more stringent limits and the HV settings were the nominal ones at LAr temperature (see table 3.7). Because the ratio of the dielectric constant in Argon and air is 1.6 we thought this gave us a safe margin.

The electrode and the associated gaps behave like capacitances charged during the HV ramp up ( $\frac{\Delta V}{\Delta t}$ ). The ramp up is set between 5 and 11 V/s with respect to the number of

tested electrodes. During the voltage increase, the measured current  $I$  is almost constant and corresponds to the charged capacitance  $C$  which is related to the HV sector surface, the liquid Argon gap and the electrode capacitance. When the voltage reaches its nominal values, the current decreases following a  $\frac{1}{RC}$  law.

The high voltage test will be positive if the leakage current is lower than  $10 \mu A$ . If it is bigger than this value, the electrode will be replaced by another one. A failure in this test can be due to several reasons: metallic particles between the electrode and the absorber, incorrect spacer positioning or imperfections which allow contact between the electrode and the absorber.

	Outer wheel							Inner wheel	
HV Sector	1	2	3	4	5	6	7	1	2
Voltage (V)	2500	2300	2100	1700	1500	1250	1000	2300	1800

Table 3.7: High voltage settings for the HV tests.

The high voltage tests of long time (the overnight and weekend tests) were added after the fourth production module, ECC7. With the previous production modules experience, we were aware that some high voltage problems could appear a posteriori. To prevent that and in addition to those two new tests, the high voltage settings were increased up to  $\sim 1.6$  times (as we have seen previously) the nominal high voltage values at cold and the spacers cleanliness was tested.

### Low frequency test

This test is designed to check the continuity of the electrical circuit and the electrode connections including the high voltage distribution. The test originally developed for the barrel [43] was implemented for the end-cap in [42]. In order to increase the signal to noise ratio and therefore to improve the measurement quality, signal cells are grouped. In the front (middle plus back), 37 (resp. 14) TBF channels are considered where each channel has a summation index which varies with  $\eta$ .

The principle is to send a low frequency sinusoidal signal on the HV lines of an electrode to obtain an output signal on the signal layer by capacitive coupling. Figure 3.36 shows typical input and output signals. Using two different frequencies, chosen to maximize the phase difference between input and output signals, the coupling capacitance, i.e. the kapton capacitance, can be calculated.

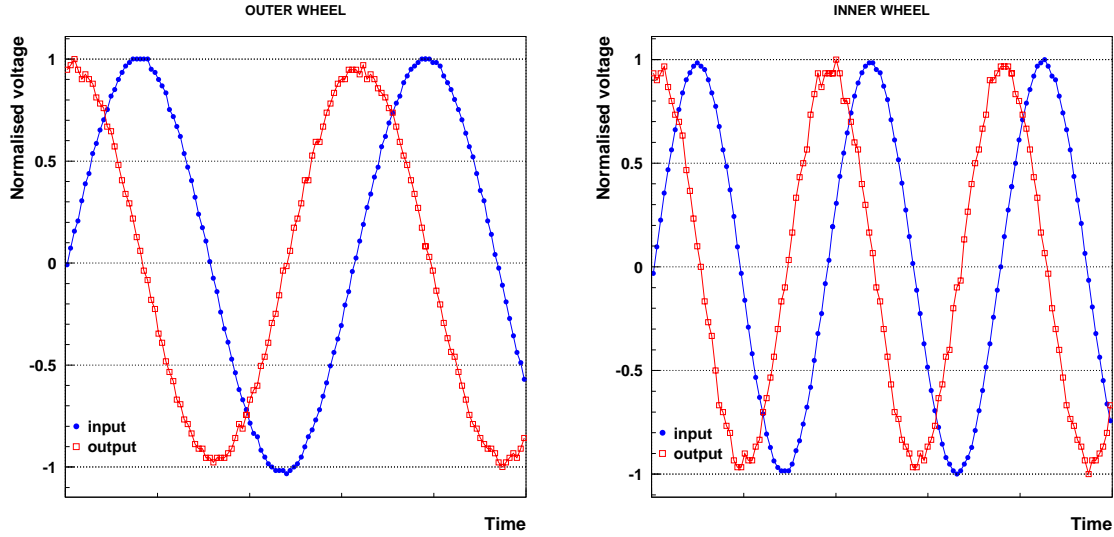


Figure 3.36: Input (full circles) and output (open circles) TBF signal shapes, for a front side outer (inner) wheel channel, left (resp. right) hand side.

In order to successfully pass the TBF test, each channel must satisfy the following criteria:

- back channels: their kapton capacitance has to be within 10% of the mean value computed with the electrodes of the first production module
- front channels: each kapton capacitance has to be greater than the corresponding one with a missing strip

$$C_{miss} = \frac{i - 1}{1} \times C_{mean}$$

with  $i$  the number of cells summed to create a channel.

The average capacitance, over  $\phi$ , for each of the six modules stacked so far at UAM, is plotted in figure 3.37. We would like to remark the excellent reproducibility in the capacitance measurements, since essentially one cannot distinguish between the various symbols associated to each module.

In the outer wheel, for each module and for one of the 96 gaps, we measure the kapton capacitance of 102 channels (37 channels in the front and 14 in the back by 2 sides). For each module and for a given channel, we extract from the data the average capacitance over  $\phi$ ,  $C_{mean}$ , and the standard deviation,  $\sigma_C$ , so that we can calculate the dispersion of the channel capacitance, i.e.  $\sigma_C/C_{mean}$  for the six modules built at UAM. Figure 3.38 shows the distribution of the kapton capacitance relative dispersion for the six modules

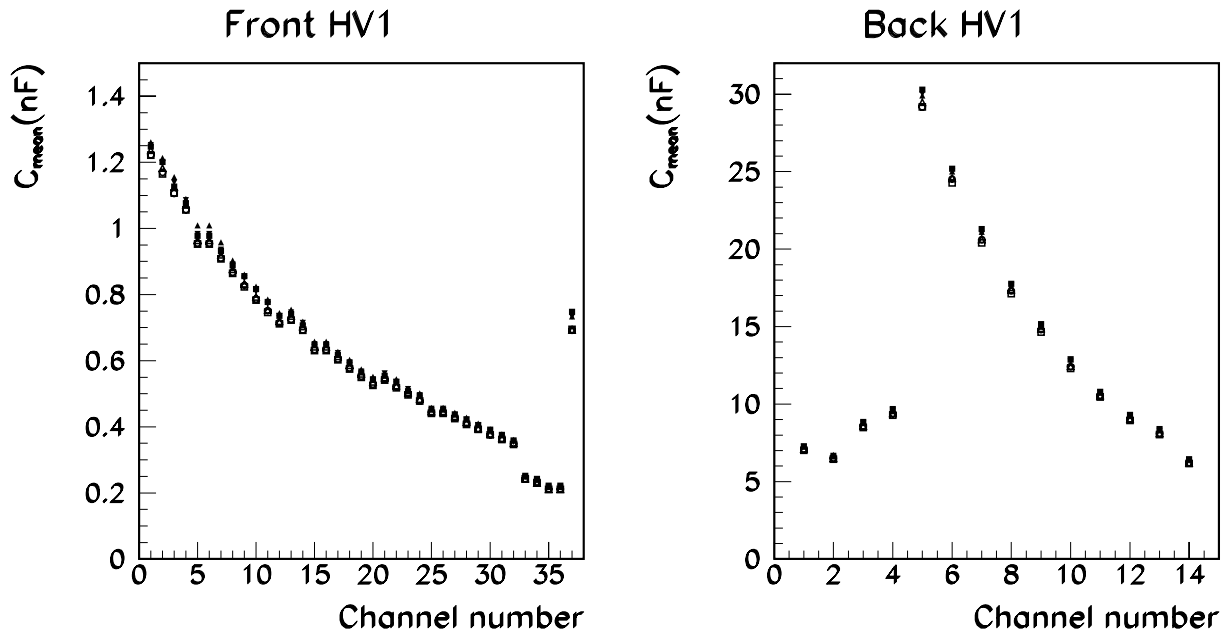


Figure 3.37: Capacitance measurements for the first six modules stacked at UAM.

built at UAM. A mean value around 2% is obtained. Figure 3.39 shows for a given back cell, the variation of the capacitance as a function of the azimuthal angle. Notice that the capacitances are globally constant with the gap number.

### Gap capacitance measurements (CAPAGAP)

This test, which measures the electrode-absorber gap, is performed at the end of the stacking and only, for technical reason, at the Marseille site. The goal is to control the gap thickness uniformity and identify possible geometrical problems after the module completion such as over thickness. The considered electrode regions are the high voltage sectors except for the inner wheel where the two sectors are grouped. The capacitance between electrodes and absorber (also called gap capacitance) is:

$$C = \frac{\varepsilon a}{\langle g \rangle}$$

where  $a$  and  $\langle g \rangle$  are respectively the surface and the mean gap of the tested zone. As the gap thickness is varying with  $\eta$ , the gap capacitance measured is an average over the considered sector surface. The capagap measurements are performed by using a RLC-



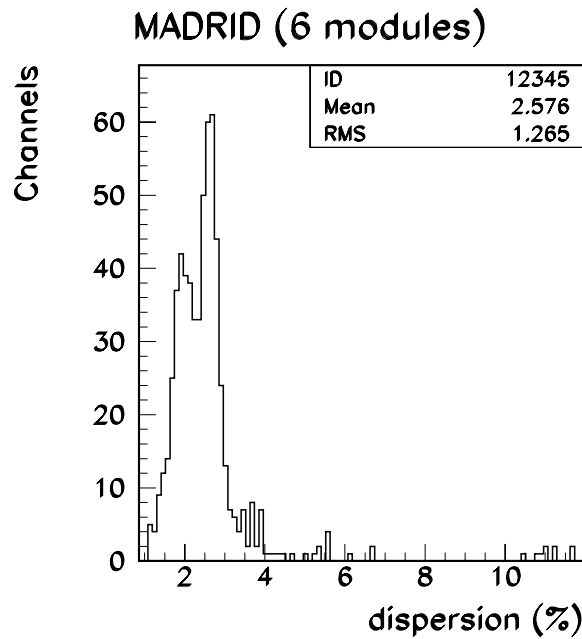


Figure 3.38: Distribution of the kapton capacitance relative dispersion for the six modules stacked so far at UAM.

metre with a 150 KHz frequency and 2V amplitude. The precision of the capacitance measurements is approximately 200 pF (the measurements are between 500 and 1000 pF). The mean gap thickness could be used to correct for the non-uniformity in electrode-absorber gap, as we will see in the next chapter.

Figure 3.40 shows the outer wheel gap capacitances as a function of the gap number, for the outer wheel regions of the module ECC5. The gap capacitances are globally constant with the gap number in each sector, apart from a small 5% decrease, visible for the last gaps and explained by a limited load on the last absorbers. The two sectors (F and B1) are not affected by this effect because of antiflexion pins, inserted on the transversal bars at the outer radius of the absorbers. On the contrary, the effect is maximum for sector B6 and is visible on the last 10 gaps. Similar results have been obtained for the inner wheel and for the other modules.

The contribution to the energy resolution constant term of the dispersion of gap thickness can be calculated (see annexe of [44]). For instance, a global dispersion of 1.9% (if the last gaps are removed) is obtained for ECC3, that converts into a 0.18% contribution to the constant term, compatible with the required 0.15% [23].

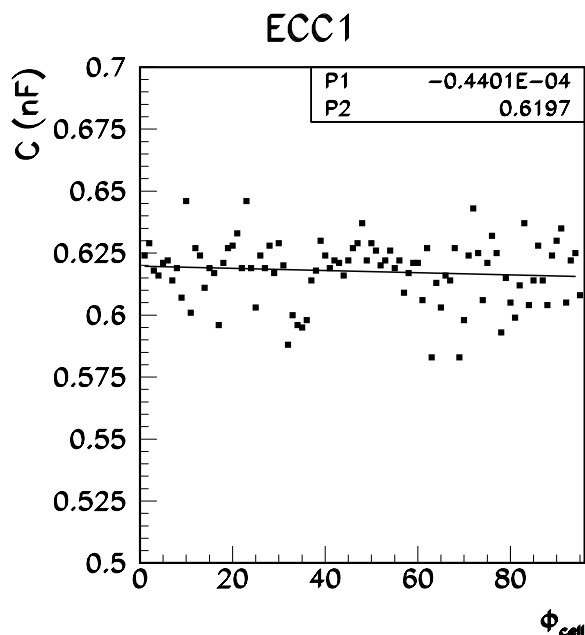


Figure 3.39: Capacitance measurements for TBF channel 17 as a function of azimuthal angle, for a given back cell. The solid line represents the result of a straight line fit.

### Cell capacitance and inductance measurements

For some of the produced modules, at the end of the stacking and after the summing board plugging, absolute cell inductance and capacitance measurements are performed. The cell capacitances are slowly decreasing with  $\phi$  (variation of 8%), because the total load on absorbers decreases with  $\phi$ .

Due to technical reasons, cell capacitance and inductance and capagap measurements are not performed on all modules. The measurements are available on [45].

### Measurements done at CERN

Once the production module is cabled and validated at the production side, it is shipped to the north experimental area at CERN to be tested in liquid Argon before its integration in the end-cap wheel. Four tests can be done: cold and warm high voltage tests, cold electronic (mother boards) resistive network measurements, calibration and beam tests.

After its arrival at CERN, the tested module is placed in a cryostat equipped with two ATLAS-like front end crates (standard and special FEC), associated to the three

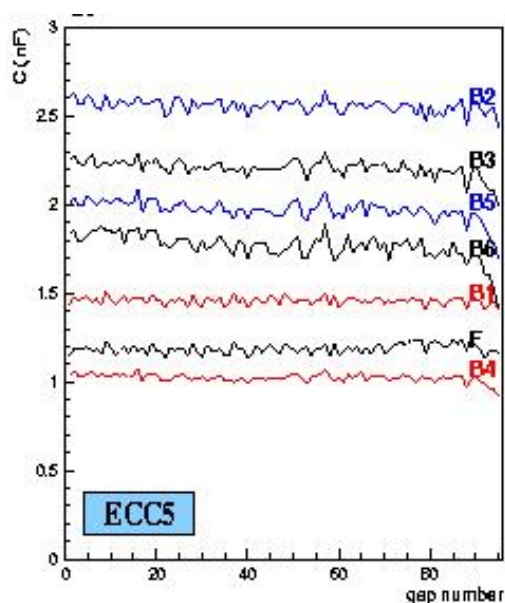


Figure 3.40: Gap capacitances  $C$  versus gap number for the outer wheel regions of the module ECC5.

feedthroughs (FT0-2) which link the cold and warm electronics.

- High voltage tests

Once the module is at CERN and is installed in a clean room, a HV test is performed, before the module insertion in the cryostat. HV values at liquid Argon temperature divided by 2 are used. This allows to identify potential problems such as short circuits or disconnected HV channels. After the module insertion in the cryostat and its filling up with liquid Argon, a test is carried out at the nominal high voltage values. After module re-heating, possible problems are then cured in a clean room. A last HV test is performed before the storage of the module for future integration.

- Cold electronic resistive network measurements

During tests at CERN, signal output and calibration input resistances are mapped out at room and/or cold (liquid Argon) temperature in the front end crate baseplane. Measurements have been carried out on several production modules and confirm the quality of the resistance networks used. Damaged networks have been found on some motherboards that have been replaced. Dead channels have been investigated and cured.

- TPA test

This test perform a crude calibration of the production modules, checking their electrical continuity and the cabling quality. The principle is to send a 20 V amplitude and 2 ns rise time step signal produced by a 64 channels TPA board through the cold electronic (mother boards and summing boards) and read all signal lines. Detector cells are only viewed as cell capacitance. The TPA test was replaced by the precise calibration done with ATLAS-like electronics for modules ECC0, ECC1 and ECC5 tested with a beam.

- Beam tests

Three production modules of the EMEC (ECC0, ECC1 and ECC5) were exposed to electron beams. These tests will be studied in more detail in the fourth chapter.



# Chapter 4

## Uniformity studies

Test beam measurements are extremely important to check that the modules meet the requirements for the LHC physics.

In summer 1999 the Module 0 prototype [46] [47] was tested at CERN using electron beams. Unfortunately, only a small region of the module could be equipped with electrodes hence the study of the uniformity could not be performed for this prototype. The test was then devoted to energy and position resolutions and uniformities restricted to very small regions only [27].

Three of the sixteen EMEC production modules, stacked in Madrid and Marseille, were exposed to electron beam to check the electron response reproducibility between modules and to control the quality of the production by measuring the detector response uniformity over its whole acceptance. Modules ECC0 (from Marseille) and ECC1 (from Madrid) were tested in summer 2001 and module ECC5 (from Marseille) in May-June 2002, in the H6 beam line of the North Experimental Area at CERN. It is important to notice that ECC0 and ECC1 are the two first stacked modules, and, since stacking quality improved with time, they present more local defects (for instance, high voltage problems) than the other modules. Moreover, modules coming from the two stacking sites were tested under beam, which is important to check the performance reproducibility. Several studies were done with the test beam measurements, as the linearity response, time and angular resolution or uniformity studies, which will be studied in more detail in this chapter.

## 4.1 Test beam

### 4.1.1 Test beam setup

A 120 GeV electron beam was used to study the calorimeter response as a function of the point of incidence ([23] [48]). The 450 GeV SPS protons are sent over a target, producing an hadronic shower. The resulting electrons, muons and hadrons are directed to several beam lines (P0, H6 and H8). The electron and hadron separation is done by using magnets which bend their trajectory. For the H6 beam line, electron beams with a dynamic range between 10 and 200 GeV/c were obtained<sup>1</sup>. For the 119.1 GeV electrons used in this uniformity study, the beam momentum spread was  $\sim 0.07\%$ . The system was equipped with motors to move the module along the two orthogonal directions  $\eta$  and  $\phi$  independently, keeping the projectivity of the cells to the nominal ATLAS interaction point.

The calorimeters were inserted in the cryostat of the former NA31 experiment [49], which was connected to a common cryogenic system [50] used by the ATLAS liquid Argon community and filled with liquid Argon. The Argon pressure was controlled with a precision of a few per mil leading to negligible temperature variations with time. The presence in the Argon of electronegative impurities ( $O_2, CO_2, \dots$ ), which may trap electrons drifting in the electric field, was measured to be less than 0.1 ppm  $O_2$  equivalent.

A sketch of the H6 beam line instrumentation is shown in figure 4.1. The beam profile can be studied with the help of four multiwire proportional chambers BC1, BC2, BC3 and BC4. One of these beam chambers, BC1, was situated some 18 m away from the detector while BC4 was located right in front of the calorimeter, i.e. only 0.25 m away. The others two were in between. Cuts were performed on the profile seen by BC4 in order to reject events in the beam tails. The particle path was reconstructed using these four beam chambers (with a resolution lower than 200  $\mu m$ ), readout by delay lines. The chamber efficiency was around 80% (70%) in 2001 (2002). Figure 4.2 shows the beam profile, in the plane perpendicular to the beam direction, as measured with BC1 and BC4. The beam spot size was about  $\pm 2$  cm in both directions, which was sufficient to completely cover a size of one middle cell in the outer wheel, but not in the inner wheel (the cells in the inner wheel are bigger).

The trigger was defined by the coincidence of a wide area scintillator (S1), 18 m upstream from the cryostat, plus two narrow ones (S2 and S3), located close to the entrance face of the cryostat. These scintillator counters in front of the calorimeter were also used to obtain the arrival time of the incident particle (thereafter called TDC time,  $t_{tdc}$ ). In addition, the analog signal recorded on  $S_\pi$  (placed just behind the cryostat) was used offline to

---

<sup>1</sup>The lower momentum electrons are obtained by using a tertiary target.

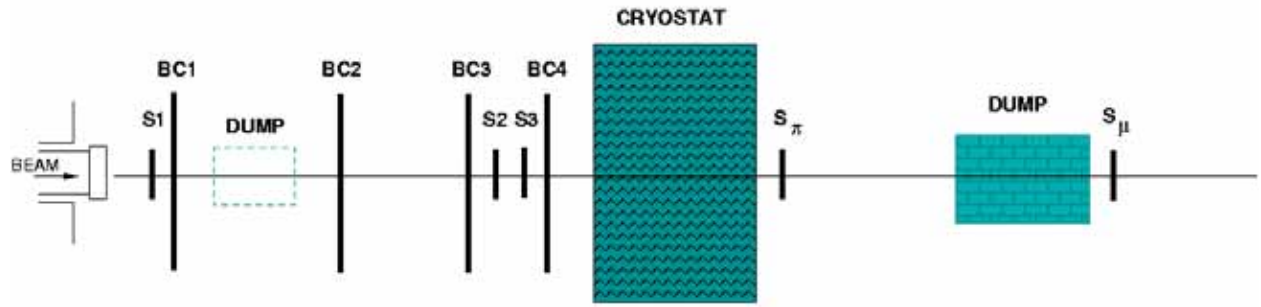


Figure 4.1: Schematic view of the H6 beam line instrumentation. Scintillators are labeled  $S$  and beam chambers  $BC$ .

flag pions, while muons could be vetoed in the trigger by  $S_\mu$  (located after the dump), to increase the electron purity. Thus,  $S_1 \cap S_2 \cap S_3 \cap S_\pi \cap S_\mu$  triggers an electron. Typically, 70% (60%) of the particles for ECC0 and ECC1 periods (for ECC5 period) were triggered as electrons using the information of the beam chambers and the scintillator counters.

Additionally, two concrete blocks, the first (second) between BC1 and BC2 (resp.  $S_\pi$  and  $S_\mu$ ) were used to absorber beam halo (resp. hadrons whose energy has not been completely absorber in the calorimeter).

The dead material thickness in front of the active part of the calorimeter (cryostat walls, cold electronics, cables, liquid Argon, ...) was almost constant with  $\eta$  and amounted to  $1.5 \pm 0.1 X_0$ . The presampler adds in the region  $1.5 < \eta < 1.8$  a thickness of the order of  $0.1 X_0$ . The presampler data is not used at all throughout this thesis.

ATLAS-like warm electronics has been used to read out the signal. On top of the cryostat, the front-end electronic is located in two crates which can house up to 38 Front End Boards (FEBs) and two calibration boards [39]. Three feedthroughs (FT0, FT1 and FT2) link the cold and warm electronics. The FEBs (128 channels each) amplify, shape and store the analog signals coming from the mother boards in the Switch Capacitor Array at a 40 MHz frequency during the trigger latency.

### 4.1.2 Test beam data

For runs with electron beam (*physics runs*), 10000 events (20000 events for a half of ECC5 runs) were recorded using two gains (high and medium) per event, including typically 500 random triggers. *Pedestal runs* of 2000 events (for each gain) were regularly taken, in which non signal was applied to the electrode, in order to measure the pedestal and the



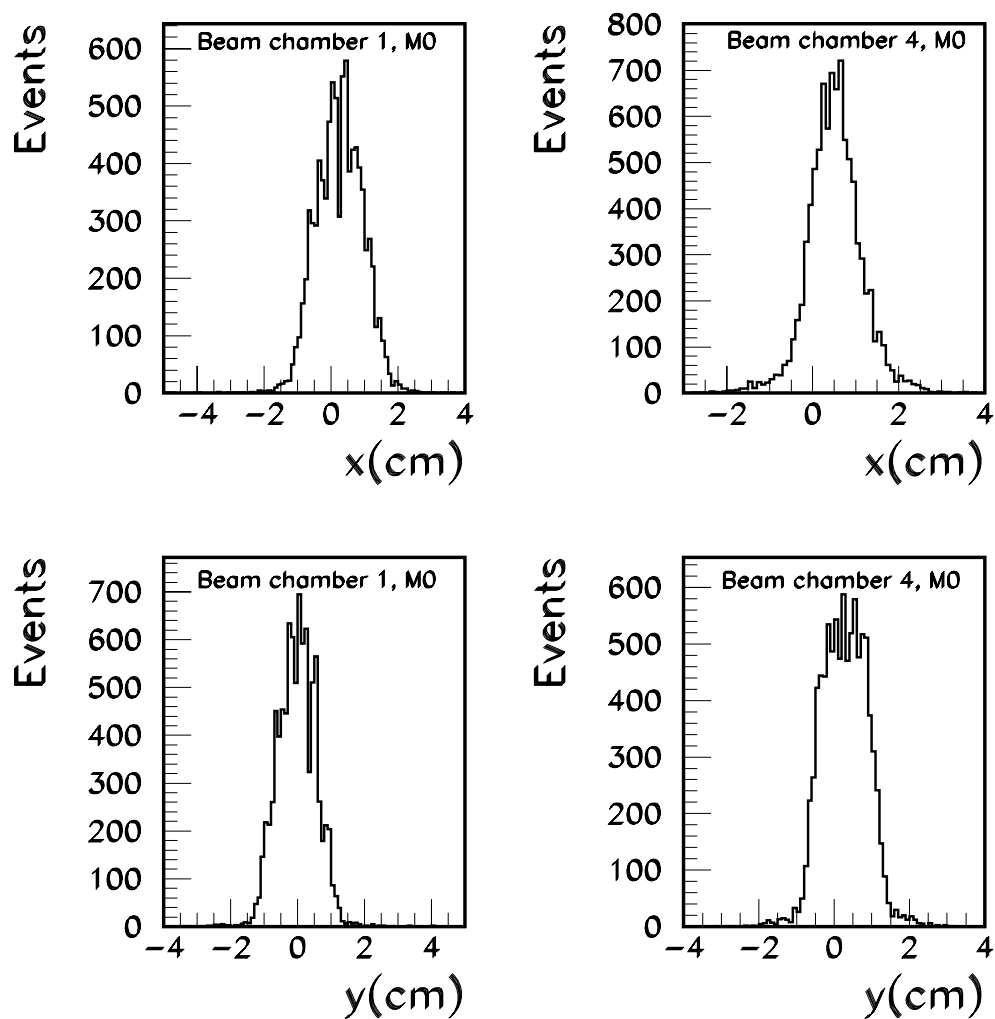


Figure 4.2: Beam profiles in the horizontal  $x$  and vertical  $y$  directions for two chambers located far (left hand side) and near (right hand side) the front face of the detector. The  $x$  and  $y$  coordinates are in the plane orthogonal to the beam direction:  $x$  corresponds to  $\eta$  and  $y$  corresponds to  $\phi$  direction.

noise of each electronic readout channel. Two kinds of calibration runs were recorded: *delay runs*, which allow to reconstruct the signal shape of each cell, and *ramp runs*, which compute the gain coefficient. For the delay runs the calibration board generates pulses with a fixed amplitude input value (fixed DAC) and a variable delay time for the pulse start (the delay of the calibration board is increased in steps of 1 ns). For the ramp runs, the calibration board generates pulses with linearly increasing input amplitude and a fixed time for the pulse start.

During the beam test, of the order of  $3 \times 10^6$  triggers were recorded as a function of the beam energy  $E$ , of the coordinates of the incidence point in the calorimeter ( $\eta$ ,  $\phi$ ) and of the high voltage. In particular, it is worth to study the dependence of the detector response as a function of one of these variables, while the others are kept constant. Thus, we speak of energy,  $\eta$ ,  $\phi$  or high voltage (HV) scans.

## 4.2 Calorimeter response

The figure 4.3 shows a schematic representation of the calorimeter readout. We can represent the detector cell as a capacitance  $C_d$  between the absorber (ground reference) and the readout electrode. The signal originated by the electromagnetic shower is represented by a triangular ionization current  $I_p(t)$  applied between the two capacitor plates. This signal is brought to the summing board and the mother board through a path on the electrode, which has an inductive behaviour:  $L_d$  is the total inductance of this path, including the SB and MB contributions. The signal travels through a  $25 \Omega$  cable in case of a middle or a back cell and a  $50 \Omega$  cable in case of a front cell. Immediately after the feedthrough of the cryostat the signal enters a Front End Board (FEB). To cope with the large dynamic range of LHC energies, a three gain shaper is used (ratio 1:9.3:93 called high, medium and low gain), but with the beam energy available (between 10 and 200 GeV) only high and medium gains are relevant<sup>2</sup>. To reduce the noise contribution, a gain selection is applied by software; namely for those cells with signal amplitude below (above) saturation the high (medium) gain response is chosen (the saturation of the high gain response occurs at about 20 GeV). The measured shaping signal  $g_d(t)$  is sampled by a Switch Capacitor Array (SCA) located in the FEB at a frequency of 40 MHz (equivalent to a period of 25 ns), that is at the nominal bunch crossing frequency of LHC beams. For each trigger, 7 samples<sup>3</sup> for each of the 2 gains are digitized by ADC located in the FEB and the numbers are transmitted to the miniRODs and the DAQ computing system in the control room.

---

<sup>2</sup>The low gain is needed for particles with energy typically greater than 300 GeV.

<sup>3</sup>Although in the beam test 7 samples per cell are stored, only 5 of them are used in the analysis, as will be explained later.

The Data Acquisition system (DAQ) performs the event building using informations coming from the beam chambers, scintillator counters and the calorimeter. At ATLAS, the 40 MHz DAQ clock will be synchronized with the bunch crossing, so that the particles will reach the calorimeter synchronously with the clock. On the contrary, during the beam test data taking, particles hit the detector at random times with respect to that clock. Therefore, since the beam is asynchronous the phase ( $t_{tdc}$ ) between the trigger and the next leading edge of a 40 MHz clock serves as time reference for the digitized samples. This phase is measured by a precise TDC, with a step of 50 ps.

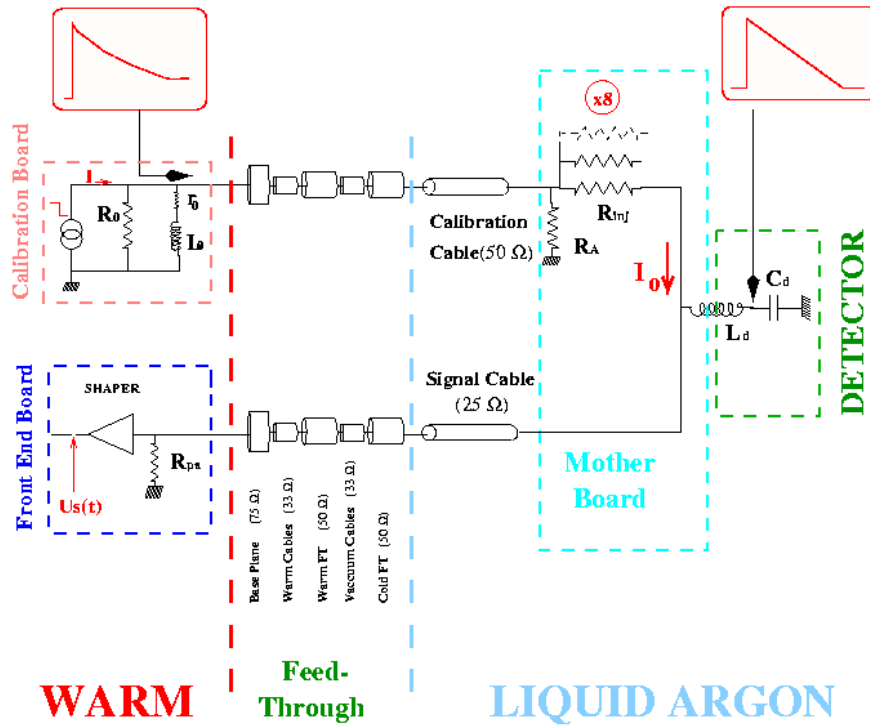


Figure 4.3: Schematic view of the calorimeter readout electronics (taken from [51]).

The physics pulse shape measured in beam tests,  $g_d(t)$ , can be obtained by representing the profile histogram of the response signal distribution (in ADC units) for a given gain as a function of the time measured with the TDC,  $t_{reco} = 25 \times i_{sample} - t_{tdc}$ , where  $t_{tdc}$  is between 0 and 24 ns and  $i_{sample}$  is one of the 7 samples of the signal (which takes values from 0 to 6). Left plots of figure 4.4 show typical physics pulse shapes for front, middle and back cells. Only electrons impacting at the center of the cell ( $\pm 15\%$ ) will be considered.

A calibration line is also represented in figure 4.3. An exponential signal  $I_c(t)$  is generated

in the Calibration Board that makes the role of the triangular ionization signal ( $I_p$ ) for physics events. The signal  $I_c$  pass the feedthrough to come into the cryostat and travels through a long cable up to the mother board. The detector is seen as a capacitance and an inductance as indicated in figure 4.3. The response to this injection signal continues through the same readout line as the ionization signal up to the SCA. The output is again 7 samples of the shaped signal  $g_c(t)$  digitized by ADC.

The calibration boards allow to set the amplitude of injected current  $I_c$  numerically. A DAC unit included in the calibration board, transforms this number into an analog amplitude. We will refer to this number as DAC value. Delay runs in medium (high) gain with a DAC value of 10000 (1000) units are considered for the signal reconstruction studies. Each calibration board is equipped with a delay unit, which allows to delay the injection from 0 to 24 ns in steps of 1 ns with respect to the leading edge of the 40 MHz clock ( $t_{delay}$ ). The calibration pulse  $g_c(t)$  is obtained by representing the sample heights as a function of  $25 \times i_{sample} - t_{delay}$ <sup>4</sup>. Typical calibration pulse shapes for front, middle and back cells are shown in the right plots of figure 4.4.

At DAC=0 the observed calibration pulse shape is not zero [40], which is due to several effects. Firstly, the DAC voltage is not exactly 0 when the DAC register contains  $0 \times 0$ . Secondly, the command sent to the calibration board causes a small signal called clock feedthrough and there is the so-called injected charge signal. Since the response of the detector to an ionization signal is not dependent on this residual signal, the corresponding DAC=0 pulse shape is subtracted from each calibration pulse shape. This should cancel spurious effects on the shape of  $g_c(t)$  introduced by the calibration board electronics.

## 4.3 Signal reconstruction

The objective of the signal reconstruction is to reconstruct the physics signal amplitude and, using the calibration system, obtain the energy inside each cell. Finally, the energy of the incident particle is obtained by summing the energy of different cells.

### 4.3.1 Reconstruction of the signal amplitude

The maximum of the shaped signal is proportional to the energy deposited in the cell. Therefore is very important to reconstruct the signal amplitude from the stored samples in order to measure the energy deposited inside one cell. Signal reconstruction consists in

---

<sup>4</sup>Every sample height is an average over 100 events taken for a given delay.

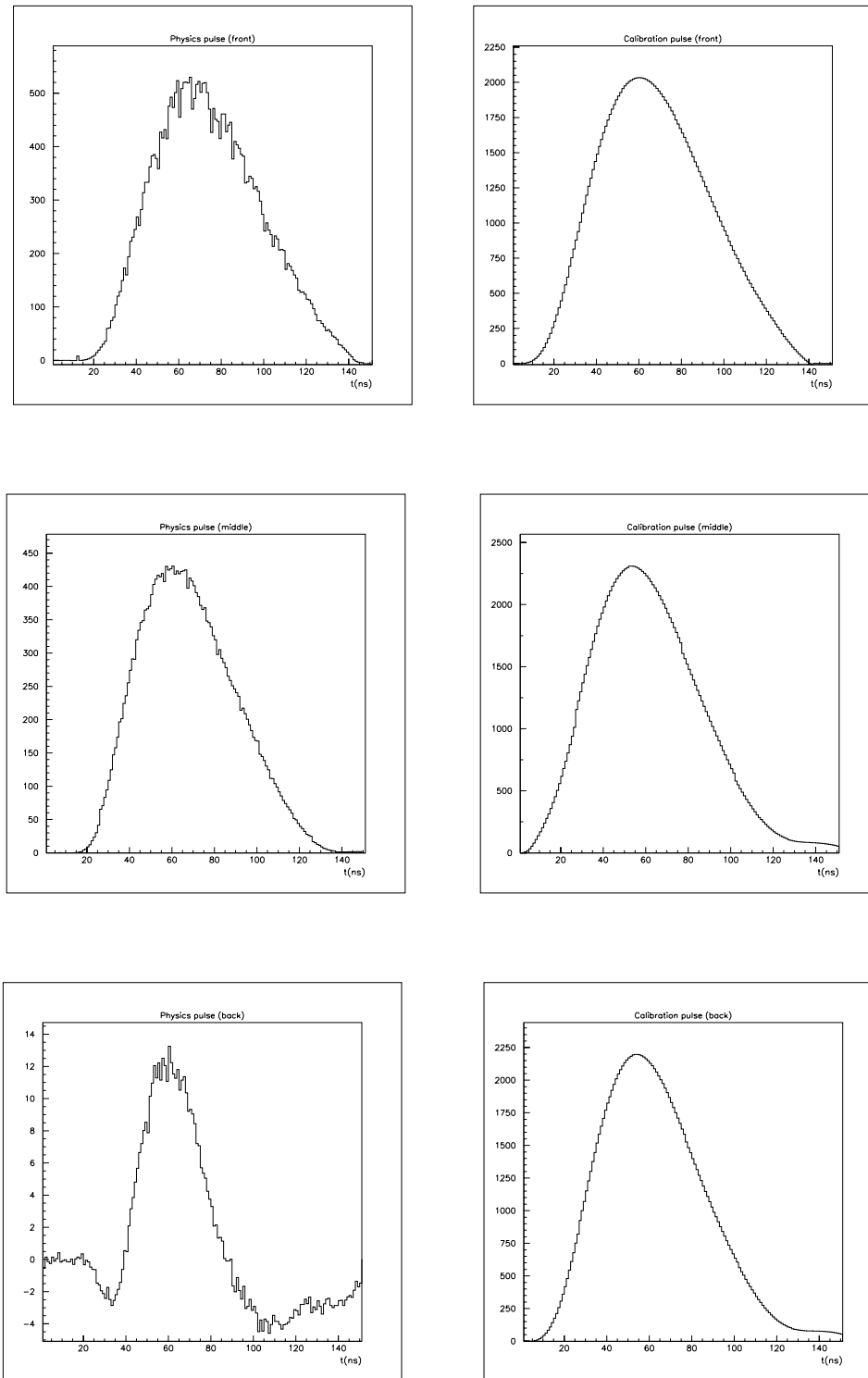


Figure 4.4: Typical physics pulses (left) and calibration pulses (right) for front, middle and back cells.

finding, after pedestal subtraction, the maximum of each cell response, using  $n$  (5 in our case) samples. To reconstruct this maximum, two methods are considered: a coarse one, so called parabola fitting, used during the data taking and a more precise one, named optimal filtering.

### Parabola fitting

Developed for online purpose, this method fits a parabola shape on the 3 highest amplitude samples. We consider the maximum of this parabola as the signal amplitude. This procedure does not rely on any signal shape and can be applied to all detector cells. The computed amplitude is thus only affected by a residual bias. However, this amplitude is not exactly correct (due to the signal shape around this three samples is not a perfect parabola) and moreover it shows a non negligible residual dependence on  $t_{tdc}$ .

### Optimal filtering

This method describes a technique for the determination of the amplitude and timing information of a shaped signal, using the stored samples. It uses the autocorrelation function of the samples, which is a function of the ratio of the thermal to pileup noise amplitudes, to maximize the signal/noise ratio for determination of the time origin  $\tau$  and the amplitude  $A$  of the signal [52].

In liquid ionization calorimeters operating in a high luminosity environment there are two principal sources of noise:

- Thermal noise

The amplitude of the thermal noise depends only upon the characteristics of the detector and the signal processing circuitry.

- Pileup or physics noise

This noise is due to the constant bombardment of calorimeter cells by products of collision reactions with high cross-sections, which occur simultaneously, in the same bunch crossing, with a hard process. The level of pileup noise depends on the luminosity of the machine and on the depth of the calorimeter section.

We assume that the form of the signal at the output of the circuit is known, except for its amplitude  $A$  and time origin  $\tau$ . So the samples  $S_i$  will have values:

$$S_i = Ag(t_i - \tau) = Ag(t_i) - A\tau g'(t_i) + n_i$$

where  $t_i$  is  $i \times 25$  ns,  $g$  is the normalized function of the signal after the shaper and  $n_i$  is a noise component.  $g'$  refers to  $g'(t) = dg/dt$  and use of the Taylor series expansion has been made. We also assume that the signal is sampled many times, giving a set of measurements,  $S_1, S_2, \dots, S_n$ . We wish to determine the parameters  $A$  and  $\tau$  from the data set  $S_i$  (in ADC units, after subtracting the pedestal). We define coefficients  $a_i$  and  $b_i$  and form the linear sums  $u$  and  $v$  of signal samples:

$$u = \sum_i a_i S_i$$

$$v = \sum_i b_i S_i$$

Requiring the expectation value of  $u$  to be  $A$  and the expectation value of  $v$  to be  $A\tau$ , demanding the average of noise (from electronics and pile-up) to be equal to 0 and minimizing the variances of the parameters  $u$  and  $v$  we obtain (using Lagrange multipliers) the values of coefficients  $a_i$  and  $b_i$ . These parameters are functions of the analytic parametrization of the normalized ionization pulse shape  $g$ , of its derivative  $g'$  and its transpose, and function of the inverse of the autocorrelation matrix  $R_{ij} = \langle n_i n_j \rangle$ . The noise autocorrelation between all samples can be extracted from pedestal runs.

Thus, the optimal filtering technique consists of a sum of weighted samples  $S_i$  to reconstruct the maximum of signal amplitude:

$$A = \sum_{i=1}^n a_i S_i$$

The time shift ( $\tau$ , in ns) between reconstructed and input shape maximum amplitude is computed as:

$$A \tau = \sum_{i=1}^n b_i S_i$$

where  $n$  is the number of samples and  $a_i$  and  $b_i$  are the optimal filtering coefficients computed for each gain and for all values of the phase between the trigger and the 40 MHz clock, by step of 1 ns. In our analysis, we consider only 5 of the seven measured samples (we choose the central samples), i.e.  $n = 5$ . This method demands the optimal filtering coefficients determination for each cell and each gain.

The two main advantages of the optimal filtering method are:

- it is not sensible to the temporal position of the highest amplitude sampling related to the peak position. It is very important since at the test beam the beam is

asynchronous. In ATLAS the beam is synchronous and therefore, a third sampling inside a  $\pm 2$  ns windows around the signal amplitude can be chosen.

- the noise dependence is minimize.

### 4.3.2 Prediction of physics pulse

As we have seen before, the shape of the signal pulse is needed to obtain the maximum of the signal from the recorded samples using the Optimal Filtering (OF) procedure. However, this shape is known only for the cells of the 3 modules tested with beams,  $g_d(t)$ . Therefore a procedure to reconstruct the physics signal shape,  $g_p(t)$  ( $g_p(t)$  refers to the predicted physics pulse shape) from a calibration pulse shape  $g_c(t)$  is foreseen for all modules installed in ATLAS.

The first attempt to find an analytical function for pulse shapes consists in building an electrical model [53] of the detector-preamplifier-shaper system, and to compute its response for calibration or electron signals. To have a complete electrical description of the electromagnetic calorimeter is not an easy task since the signal suffers deformations from several sources (as reflections and cross-talk in the readout lines). Trying to take into account these electrical effects would lead to add a non-negligible amount of free parameters that would be hard to constrain in order to provide a reliable electronic calibration.

Another procedure consists on extracting the shape of the physics response from the calibration pulse [51]. Although the readout path and electronics is the same for physics and calibration inputs, there are two differences at the injection point, namely:

- the physics input signal is produced inside a gap of the detector, while the calibration input is generated outside in a calibration board connected on a Front End Crate.
- the physics input signal has a triangular shape when represented as a function of time, while the calibration charge injection has an exponential shape.

The ionization electrons drift in the field provided on the LAr gap by the voltage, producing a current signal with amplitude proportional to the released energy. This current has the typical ionization-chamber triangular shape, with a rise time of the order of 1 ns followed by a linear decay for the duration of the maximum drift time  $\tau_d$ . Such a signal at the input of the cell capacitor in time domain is given by:

$$I_p(t) = I_p^0 Y(t) Y(\tau_d - t) \left(1 - \frac{t}{\tau_d}\right)$$



where  $Y$  is the *Heavyside* function and  $I_p^0$  is the amplitude of the ionization current. The drift time  $\tau_d$  in a 2 mm gap under a voltage of 2000 V is close to 400 ns. This time is a function of the pseudorapidity due to the change in the LAr gap and in the voltage, taking values in the range 200-600 ns. The signal in the Laplace domain is:

$$\hat{I}_p(s) = I_p^0 \left( \frac{1}{\tau_d s} - \frac{1 - e^{-\tau_d s}}{\tau_d^2 s^2} \right)$$

In figure 4.5 is shown the injected triangular signal together with the output signal after crossing the shaper. The sampled amplitudes each 25 ns are represented by dots. The maximum do not usually coincide with one of the samples.

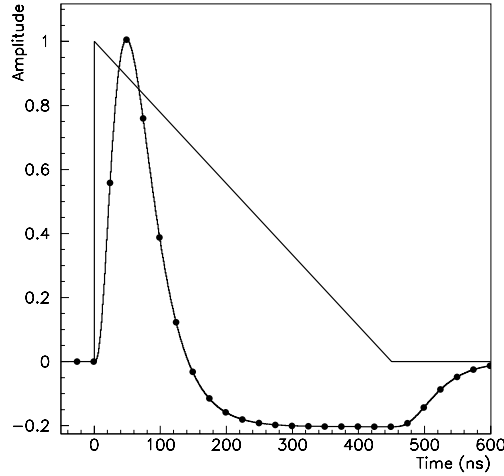


Figure 4.5: The triangle shape corresponds to the signal as a function of time just after electrode and the bell shape to the signal after crossing the shaper. Dots represent the recorded amplitudes separated by 25 ns.

The output physics signal can be written as:

$$g_p(t) = \int_{-\infty}^{+\infty} K_p(t - t') I_p(t') dt'$$

where  $K_p$  contains the information of the readout circuitry and  $I_p(t)$  is the ionization current at the input of the cell capacitor. In the Laplace domain (applying the “Convolution Theorem”), we find:

$$\hat{g}_p(s) = \hat{I}_p(s) \hat{K}_p(s)$$

where  $\hat{I}_p(s)$  is the Laplace transform of  $I_p(t)$ .

The calibration charge injection aims to mimic the ionization signal, in order to be able to measure the actual gain and properties of each channel thus assuring the proper cell equalization. An exponential signal with decay time  $\tau_c$  is generated by the calibration boards [40], whose pulser is based on a RL-circuit (see figure 4.3). The values of the  $R_0$  and  $L_0$  components are chosen in order to obtain the proper exponential decay constant  $\tau_c$ , which has been chosen to mimic the ionization signal decay slope. The non-ideal inductance  $L_0$  of the calibration board pulser circuit has a resistive component  $r_0$  that alters the exponential waveform baseline. According to figure 4.3, the calibration current in the time domain is:

$$I_c(t) = I_c^0 Y(t) (f + (1 - f)e^{-t/\tau_c})$$

where  $I_c^0$  is the amplitude of the injected current,  $Y(t)$  is the *Heavyside* step function,  $f$  (between 0 and 1) is the fraction of the total resistance ( $r_0 + \frac{R_0}{2}$ ) represented by the resistive component  $r_0$  of the non-ideal inductance  $L_0$  i.e.

$$f = \frac{r_0}{r_0 + \frac{R_0}{2}}$$

and  $\tau_c$  is the effective exponential decay constant (which value is approximately 360 ns)

$$\tau_c = \frac{L_0}{r_0 + \frac{R_0}{2}}$$

In the Laplace domain the calibration current reads:

$$\hat{I}_c(s) = I_c^0 \left( \frac{\tau_c(1-f)}{1 + \tau_c s} + \frac{f}{s} \right)$$

The output calibration signals in the time and Laplace domain are given by:

$$g_c(t) = \int_{-\infty}^{+\infty} K_c(t-t') I_c(t') dt'$$

$$\hat{g}_c(s) = \hat{I}_c(s) \hat{K}_c(s)$$

where  $K_c$  contains the information of the readout circuitry seen by the calibration current.

As we have seen before, there are two main differences between physics and calibration pulses: the input signal shape is different (triangular for physics and exponential for calibration), and it is not injected at the same point. The injection of the calibration current occurs outside the detector and sees a slightly different LC-circuit for the detector cell than the ionization current which occurs inside the detector gaps. For this reason, the functions  $\hat{K}_c$  and  $\hat{K}_p$  differ and therefore, the shaped pulse obtained at the end of the readout electronics chain (calibration pulse  $g_c(t)$ ) does not agree with the shaped pulse produced by a particle (physics pulse  $g_p(t)$ ). To obtain  $g_p$  from  $g_c$  these differences should have to be simulated, which is a difficult task. Let us factorize  $\hat{K}_c$  and  $\hat{K}_p$  as a term corresponding to the LC-circuit ( $\hat{H}_c$  for calibration and  $\hat{H}_p$  for physics) and a common part associated to the readout circuit ( $\hat{A}$ ). This function  $\hat{A}$  includes all effects induced by readout cables and the electronic that are not well known and hard to describe with an electrical model. Then:

$$\begin{aligned}\hat{K}_p(s) &= \hat{H}_p(s) \hat{A}(s) \\ \hat{K}_c(s) &= \hat{H}_c(s) \hat{A}(s)\end{aligned}$$

It can be shown that:

$$\begin{aligned}\hat{H}_p(s) &= \frac{\omega^2}{s^2 + \omega^2\tau s + \omega^2} \\ \hat{H}_c(s) &= \frac{s^2 + \omega^2}{s^2 + \omega^2\tau s + \omega^2}\end{aligned}$$

with  $\tau = R_{pa}C_d$  and  $\omega = \frac{1}{L_dC_d}$ , being  $L_d$  the inductance and  $C_d$  the capacitance of the calorimeter cell.  $R_{pa}$  is the input impedance of the preamplifier.

Dividing  $\hat{g}_p(s)$  and  $\hat{g}_c(s)$  the common part  $\hat{A}(s)$  cancels out obtaining the following relation between the physics and calibration pulses in the Laplace domain:

$$\hat{g}_p(s) = \hat{B}(s)\hat{g}_c(s)$$

where

$$\hat{B}(s) = \frac{\hat{H}_p(s) I_p(s)}{\hat{H}_c(s) I_c(s)}$$

In more detail:

$$\hat{B}(s) = \frac{\omega^2}{s^2 + \omega^2} \frac{\hat{I}_p(0) \left( \frac{e^{-\tau_d s} - 1}{\tau_d^2 s^2} + \frac{1}{\tau_d s} \right)}{\hat{I}_c(0) \left( \frac{\tau_c(1-f)}{1+\tau_c s} + \frac{f}{s} \right)}$$

In the method used for the uniformity analysis of this chapter, called LAPP method, the function  $\hat{B}(s)$  is discretized in the frequency domain of the Fourier transform  $\hat{B}(\nu)$  and afterwards the physics pulse  $g_p(t)$  in the time domain is predicted by applying the inverse Fourier transform using a Fast Fourier Transform numerical algorithm. In order to complete the computation of  $g_p(t)$ , the knowledge of the parameters set is required. To obtain the unknown parameters of the circuit (the frequency  $\omega = \frac{1}{\sqrt{L_d C_d}}$  and the starting time of the calibration and physics signals, basically), a fit of the predicted physics pulse  $g_p(t)$  to the test beam measured physics pulse  $g_d(t)$  is performed.

Because of the shape between the physics current and the injected calibration signal are different, the two pulses do not have the same amplitude after shaping. The ratio between the maximum of the predicted physics pulse and the calibration pulse ( $\frac{M_{phys}}{M_{cal}}$ ) is shown as a function of  $\eta$  in figure 4.7 for the middle cells of the three tested modules. It roughly decreases with  $\eta$  and is minimal around  $\eta = 2.2$ , which reflects at first order the cell inductance variation. A good agreement between modules is found. Since it shows a dependence on  $\eta$ , not taking into account this term would induce a non uniformity.

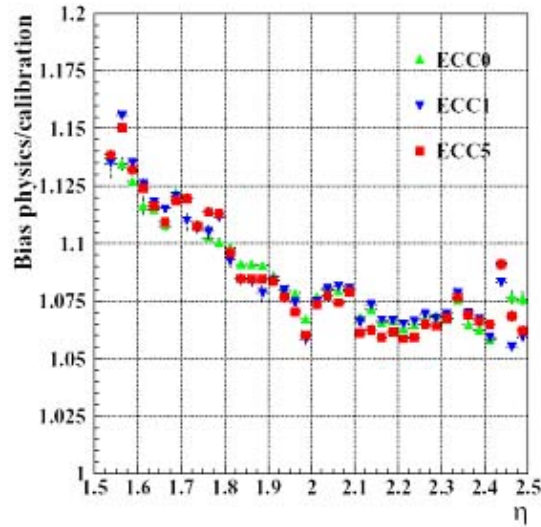


Figure 4.6: Bias between calibration and physics pulse amplitudes versus  $\eta$  for the outer wheel middle cells of the three tested modules. All points are averaged over  $\phi$ .

Once the circuit parameters are determined the physics pulse is predicted from the calibration pulse using either the FFT. After that, we can apply the optimal filtering procedure to obtain the maximum of the ionization signal, which is proportional to the energy deposited in the cell.

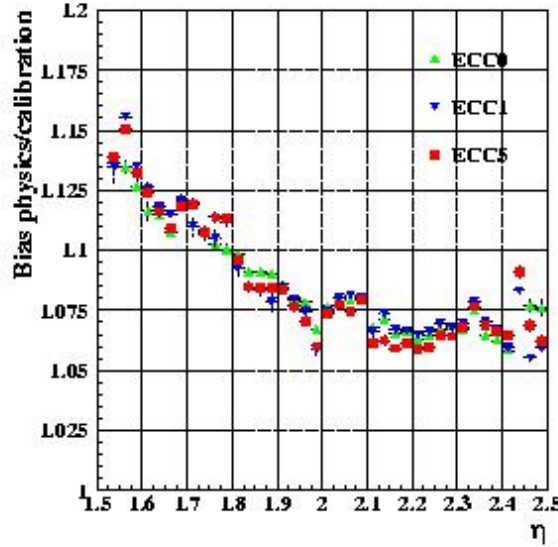


Figure 4.7: Bias between calibration and physics pulse amplitudes versus  $\eta$  for the outer wheel middle cells of the three tested modules. All points are averaged over  $\phi$ .

### 4.3.3 The LAPP method

In what follows in this chapter, we have used the LAPP method of the signal reconstruction which was developed by the LAPP group for EMBarrel beam test studies [51]. In this method, we have computed the function  $B$  in the domain of the Fourier transform  $\tilde{B}(\nu)$ . It is known that for a function  $f$  which satisfies  $f(t) = 0$  for  $t < 0$ , we find

$$(\hat{f})(-i\nu) = (\tilde{f})(\nu)$$

where  $\hat{f}$  and  $\tilde{f}$  refer to the functions in the Laplace and frequency domain respectively. Therefore, if we change  $s$  by  $-i\nu$  in

$$\hat{g}_p(s) = \hat{B}(s)\hat{g}_c(s) \quad \hat{B}(s) = \frac{\omega^2}{s^2 + \omega^2} \frac{I_p(s)}{I_c(s)}$$

we will find

$$(\tilde{g}_p)(\nu) = (\tilde{B})(\nu) (\tilde{g}_c)(\nu)$$

with

$$\tilde{B}(\nu) = \frac{\omega^2}{\omega^2 - \nu^2} \frac{\tilde{I}_p(\nu)}{\tilde{I}_c(\nu)}$$

In order to compute the Inverse Fourier transform a numerical method called Fast Fourier Transform (*FFT*) was used. This method demands a 2-power number of bins, choosing  $2^7 = 128$  in this case. So, the function  $\tilde{B}(\nu)$  and the pulses are discretized in the frequency domain of the Fourier transform, with a bin size of 1 ns, obtaining:

$$(\tilde{g}_p^k) = (\tilde{B}^k) (\tilde{g}_c^k), \quad k = 1, 2, \dots, 128$$

A pole is found for the frequency  $\nu = \pm \omega$ , which complicates the calculation since regularization of divergences needs to be applied. Finally, applying an inverse Fourier transform using a Fast Fourier Transform numerical algorithm we can obtain the predicted physics pulse in the time domain  $g_p(t)$ . Free parameters as LC are obtained from a fit of  $g_p(t)$  to test beam data  $g_d(t)$  corresponding to 120 GeV electrons. Existing *LC* measurements should avoid this fit, hence the method becomes applicable to modules that were not beam tested. This procedure is repeated for every cell of the calorimeter to obtain one predicted physics pulse  $g_p(t)$  per cell.

The parameters which take part in this analysis are the following:

### 1. Fixed parameters

- Parameter  $f$  of the calibration board. The value of  $f$  for EMBarrel modules was obtained from the 32 samples data in the H8 test beam period [54]. Unfortunately, these long delay runs were not taken in the EMEC test beam. One should not expect great differences since the calibration boards were the same for EMBarrel and for EMEC tests. Therefore, in this analysis, we have taken as  $f$  the mean of the values obtained for the EMBarrel modules. This value is  $f = 0.069$  [55].
- $\tau_c$ , the characteristic decay time of the exponentially decreasing current generated by the calibration board. Again, we have chosen the mean of the values from the EMBarrel modules, being  $\tau_c = 333.8$  ns [55].
- $\tau_d$ , the drift time. Its value was obtained from measurements on the calorimeter prototype Module 0. The values of  $\tau_d$  depend on  $\eta$  because of the cell size and the gap variation with  $\eta$  of the EMEC modules.

### 2. Free parameters

- Frequency  $\omega = \sqrt{\frac{1}{L_d C_d}}$
- Normalization constant

- Starting times of the calibration pulse  $t_c^0$  and of the physics pulse  $t_p^0$ .
- $\tau_s$ , the shaper time.

An idea of the quality of the prediction for  $g_p(t)$  can be seen in the figure 4.8 for the response of a particular middle cell. We define the residual as the relative difference between the prediction and the data histograms normalized to prediction peak, namely:

$$r^{(i)} = \frac{g_p^{(i)} - g_d^{(i)}}{\max(g_p^{(i)})} \quad i = 1, \dots, nbins$$

The maximum of this residual ( $r_{max}$ ) in absolute value is below 1% for all middle cells<sup>5</sup>.

Optimal Filtering coefficients for ECC0, ECC1 and ECC5 has been obtained, and recorded for general use, applying the LAPP method to these EMEC modules [57].

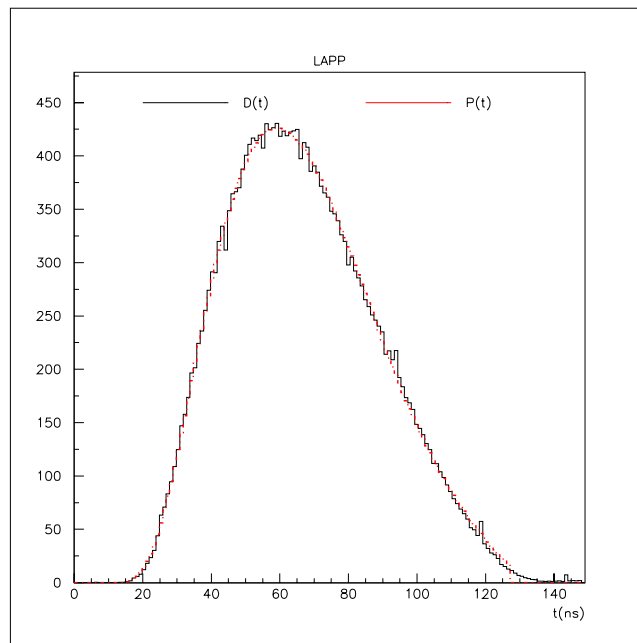


Figure 4.8: Comparison between predicted (red dotted line) and measured (dark solid line) physics pulses for 120 GeV electrons at the ECC1 beam test.

<sup>5</sup>Some "sparks" are observed every 25 ns due to an imperfection in the delay clock, that can be corrected [56].

### 4.3.4 Electronics calibration

The final step in order to get the energy deposited in one cell is convert the value of the ionization signal maximum obtained in ADC units to a GeV units.

To correct for the gain dispersion of the electronics chain and study the stability over time for all the detector cells, calibration runs (ramp runs) were regularly recorded (typically every 24 h) in high and medium gains. In these runs, 11 input calibration pulses with fixed start time and linearly increasing amplitudes<sup>6</sup> (DAC units) are sent, by calibration patterns (4 per sampling), to each input signal line through the mother boards. For each DAC value, the cell response amplitude (in ADC units) is reconstructed using the pulse shape extracted from the delay runs [58], after subtraction of the pedestal and the calibration board injected charge (DAC=0).

To convert ADC (reconstructed signal) in DAC values (injected signal), a second degree polynomial

$$DAC = r_1 ADC + r_2 (ADC - r_0)^2$$

is fitted with 3 parameters ( $r_0, r_1$  and  $r_2$ ). The values of these parameters are obtained for each cell in high and mediums gains. The linear term and the quadratic one, which takes into account small non-linearities, are the gain coefficients of the cell. Whenever it was possible, the closest ramp run preceding the physics run is used to calibrate the detector.

The expected factor  $\gamma_i$ , which converts amplitudes in DAC units to energy in GeV, depends on the sampling and is given by

$$E_i = \gamma_i \times DAC, \quad \gamma_i = \frac{1}{I_0^E} \times \frac{V_{Count}^{DAC}}{R_{inj}^i}$$

where  $i = 1, 2, 3$  refers to front, middle and back samplings, respectively,  $V_{Count}^{DAC}$  is the Volt per DAC conversion factor<sup>7</sup> and  $R_{inj}^i$  is the equivalent resistance of the calibration system on the mother boards<sup>8</sup> (see figure 4.3). The term  $I_0^E$  is the current density (the ratio between the induced current and the deposited energy), which value is  $2.45 \text{ nA/MeV}$  ( $1.97 \text{ nA/MeV}$ ) for the outer (inner wheel). The term  $\frac{V_{Count}^{DAC}}{R_{inj}^i}$  converts DAC units to Amperes [51] and the term  $\frac{1}{I_0^E}$  change from Amperes to GeV. Numerically, we obtain for

---

<sup>6</sup>0-1000 DAC in high gain with a step of 100 DAC, 0-10000 DAC in medium gain with a step of 1000 DAC.

<sup>7</sup>The maximum DAC, 5V, is coded on 17 bits, thus  $V_{Count}^{DAC} = \frac{5}{(2^{17}-1)}$ .

<sup>8</sup> $R_{inj}^i = 3000, 500, 1000\Omega$  for S1, S2 and S3, respectively.



the outer wheel<sup>9</sup> :

$$\gamma_2 = \gamma = 31.2 \text{ MeV}, \quad \gamma_1 = \frac{\gamma}{6}, \quad \gamma_3 = \frac{\gamma}{2}$$

A few cells ( $\sim 5\%$ ) suffered from calibration problems, linked to the mother boards. For these cells, the calibration gain coefficients of the neighbouring cell in  $\phi$  are used. The list of problematic cells can be found at [59]. A specific treatment was needed for ECC5 cells located in the half lower part of one of the three baseplanes used in testbeam. It corresponds to the region  $1.6 < \eta < 2.4$  and  $0.4 < \phi < 0.6$ . This baseplane was already used for the pre-production module beam test in 1999 and suffered probably of ageing effects. This part exhibited in 2002 a large resistive cross-talk affecting the calibration pulses [60], which spoiled the calorimeter response in some region. It has been corrected for in the calibration gain computation by subtracting the neighbouring cell contributions from the calibration shapes [61]. In this region the cell response amplitude is reconstructed using the parabola method and not using the pulse shape extracted from the delay runs (as we have done for the rest of the ECC5 and for the other modules).

### 4.3.5 Cluster energy

As we have seen, to obtain the energy deposited in one cell, we must subtract the pedestal to the 5 samples and reconstruct the signal amplitude from the optimal filtering coefficients. Afterwards, the electronic calibration weights (in order to get DAC from ADC) must be applied and finally we get the value in GeV using the  $\gamma_i$  coefficients.

Since the electromagnetic shower is not contained in one readout cell, the energy is measured in each compartment in a cluster of cells built around the most energetic one. The cluster size depends on the granularity which is not the same along the calorimeter. A cluster too small does not contain all the electromagnetic shower energy and a cluster too big is an unnecessary source of noise added and consequently the resolution is degraded. The choice of the cluster size is based on the optimization of the energy resolution.

In order to illustrate the shape of the shower profile, a lego plot showing the mean energy deposit in cells in the  $(\phi, \eta)$  plane, for a 100 GeV electron run, is presented both in figure 4.9 for the front and middle section of the calorimeter and in figure 4.10 for the back.

In the front sampling, since its segmentation depends on  $\eta$ , the cell numbers of the cluster for this layer depends on  $\eta$  as well<sup>10</sup> (see table 4.1). For the front sampling 1 or 2 cells in  $\phi$  are considered in the cluster depending on the beam point of incidence. If the beam is

---

<sup>9</sup>For the inner wheel, we have found  $\gamma_2 = \gamma = 38.8 \text{ MeV}$ ,  $\gamma_1 = \frac{\gamma}{6}$ ,  $\gamma_3 = \frac{\gamma}{2}$ .

<sup>10</sup>In the front sampling, the size of the cluster is always  $\pm 0.3$  around the central cell, but since the granularity depends on  $\eta$ , the cell numbers changes with  $\eta$ .

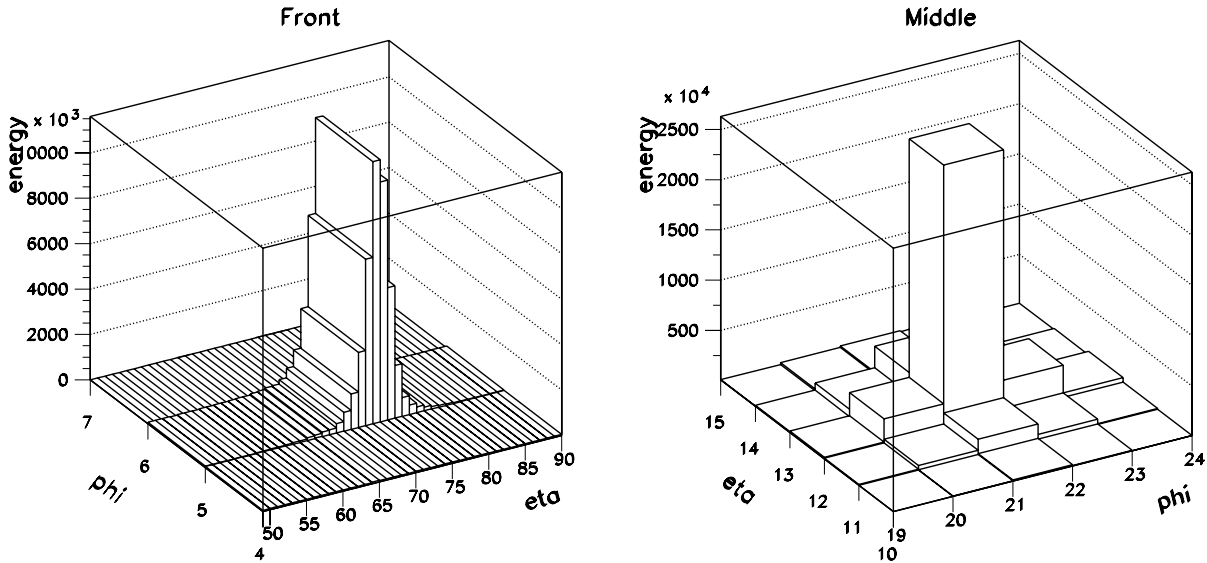


Figure 4.9: Averaged energy per cell of the front sampling (left) and the middle sampling (right).

incident at the cell center  $\pm 1/4$  times cell size, only 1 cell will be considered, otherwise a neighbour cell is added to the cluster. This cluster size guarantees a negligible lateral energy leakage of the electromagnetic cascade when the electron is incident on the center of the central cell.

Similarly, from the lego plot associated to the middle section of the calorimeter, a  $5 \times 5$  cluster size seems appropriate. We have checked that for several beam energies, the lego shape does not change, both for the middle and the front sampling, so that the cluster size is independent of the beam energy.

In contrast, the previous comments are not valid for the back sampling. We realized indeed that at low energies, the back sampling is dominated by noise while at high energies, i.e. above  $60 \text{ GeV}$ , it shows the expected peaked shape, see figure 4.10. A cluster size  $5 \times 3$  in the plane  $\phi \times \eta$  seems appropriate.

The electron energy is reconstructed from this cluster by adding the energies deposited in the three calorimeter sections, front, middle and back. No weights factors are introduced to reduce the effects of longitudinal leakage (negligible at  $120 \text{ GeV}$ ) and dead material in front (mainly from the cryostat wall).

The fraction of the total  $120 \text{ GeV}$  electron energy contained in the cluster is above 95% at high  $\eta$  and even more at low  $\eta$ .

The particle impact position on the calorimeter is estimated with energy weighted barycen-

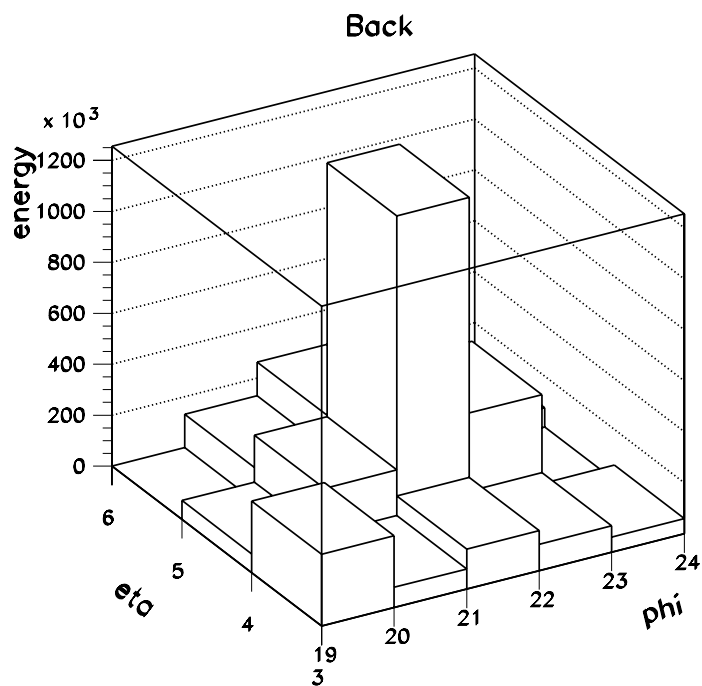


Figure 4.10: Averaged energy per cell of the back sampling.

$\eta$	Front	Middle	Back
1.5-1.8	1(2) $\times$ 23	5 $\times$ 5	5 $\times$ 3
1.8-2.0	1(2) $\times$ 15	5 $\times$ 5	5 $\times$ 3
2.0-2.4	1(2) $\times$ 11	5 $\times$ 5	5 $\times$ 3
2.4-2.5	1(2) $\times$ 3	5 $\times$ 5	5 $\times$ 3

Table 4.1: Cluster size  $\Delta\phi \times \Delta\eta$  as a function of the region in  $\eta$ . For the front sampling two cells along  $\phi$  are taken when the beam is incident near the boundary between two cells.

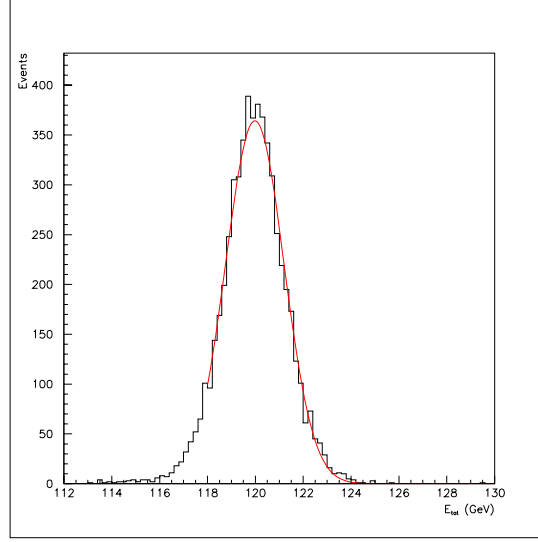


Figure 4.11: Distribution of the signal after all corrections and cuts have been applied. The Gaussian fit is also shown as a red line.

tre in the front sampling for the  $\eta$  (the middle sampling in the inner wheel) and the middle sampling for  $\phi$ . These barycentres are computed according the following formula:

$$\eta_{bar}^{S_1} = \sum_{j=1}^{N_j} \sum_{k=1}^{N_k} \frac{E_1(\eta_j, \phi_k) \times \eta_j}{E_{S_1}}, \quad \phi_{bar}^{S_2} = \sum_{j=1}^{N_j} \sum_{k=1}^{N_k} \frac{E_2(\eta_j, \phi_k) \times \phi_k}{E_{S_2}}$$

where  $N_j \times N_k$  is the number of cells in a  $\Delta\eta \times \Delta\phi$  cluster of the sampling  $S_i$ .

To guarantee the electron purity on the signal, standard selection cuts are applied to veto the small contamination from muons and pions in the beam line, cosmics and random triggers.

From a gaussian fit to the energy distribution (with typically 3000 events after cuts out of 10000) the mean energy and the energy resolution are extracted. Figure 4.11 shows this fit when the beam is incidente a  $\eta_{cell} = 20$ ,  $\phi_{cell} = 11$ . The fit starts at  $-1.5\sigma$  of the mean value, to reduce the influence of the low energy tail due mainly to residual pion contamination and loss of energy in the upstream material of the beam line.

## 4.4 Uniformity analysis framework

For the three tested modules the cell-to-cell non-uniformities have been measured over the full coverage. After a first preliminary analysis at UAM [62], two analysis of these

data have run in parallel and independently, one of the CPPM group [57] and another of the UAM group. We present here the results obtained by the UAM group concerning the uniformity of the three modules tested. These results have already been published by the UAM group as an ATLAS note [63].

We have only studied the uniformity in the precision region of the outer wheel. As we have seen before, an outer wheel module covers the region  $\Delta\eta \times \Delta\phi = [1.375, 2.5] \times [0.0, 0.8]$ , with a granularity of  $0.025 \times 0.025$  for the middle sampling cells. An outer wheel module is composed of  $44 \times 31$  middle cells, which are labeled in  $\eta_{cell}$  from 0 to 43 and in  $\phi_{cell}$  from 0 to 31. A planar representation of the outer wheel of an EMEC module is given in figure 4.12. The three samplings front, middle and back are denoted by s1, s2 and s3 respectively. Cell numbers for the three samplings are indicated along  $\eta$  (abscissas) and along  $\phi$  (ordinates). Middle cells are represented by a square and the correspondence with  $\eta$ -units and  $\phi$ -radians can be obtained easily for the three samplings.

To avoid border effects which are no more present in the ATLAS wheels, cells in region  $\phi_{cell} = 0$  and  $\phi_{cell} = 31$  in middle cell units are excluded for the cluster. The first of the three electrodes at the position  $\phi_{cell} = 0$  is not present on the tested modules because is the junction electrode between two modules, and is added during their integration in the ATLAS wheel. In addition, the LAr thickness corresponding to  $\phi_{cell} = 31$  is far from the nominal value due to the lack of weight from the neighbouring module. This effect will be seen in the capacitance measurements (see figure 4.23 lower curve) where the value for  $\phi_{cell} = 31$  suffers a deep decrease that implies a deep increase in the LAr gap thickness. These border effects in  $\phi$  are no more present in the ATLAS wheels when all the modules are integrated together.

In addition the following regions (at high and low  $\eta$ ) have not been considered to build the cluster because these are not precision regions:  $\eta_{cell} = 0, 1, 2$  and  $\eta_{cell} = 42, 43$  in middle cell units. The first region is located behind  $10 X_0$  of matter (barrel cryostat, solenoid and barrel) and will mainly recover the energy from the barrel/end-cap crack, whereas the second region is near to the crack between inner and outer wheel. Both regions do not have a constant depth in  $X_0$  and are poorly equipped (no strips and/or no back).

Therefore, taking into account the  $\eta$  and  $\phi$  border effects (including clustering) we have used the following region to analyze the module response uniformity:  $1.525 < \eta < 2.4$  and  $0.075 < \phi < 0.725$  corresponding to  $5 \leq \eta_{cell} \leq 39$  and  $3 \leq \phi_{cell} \leq 28$ . It includes 910 middle cells (marked in blue in figure 4.12), among which 874 on ECC0, 910 on ECC1 and 844 on ECC5 have been scanned.

There are some cells in the analysis region with a singular behaviour. On the one hand, there are problems which are only present during test beam period. These are related to setup, data taking problems or module problems that have been repaired after the beam test. For instance, there are dead cells (cells with no physical signal), noisy cells,

read-out and acquisition problems and connection problems (bad connected electrodes). We exclude all those cells related to known and resolved problems [64]. On the other hand, there are problems which will be present in ATLAS, as HV problems or strange signal shape. We keep all problems that are in ATLAS and correct for them. Table 4.2 shows the number of central cells of the cluster that are considered in this analysis.

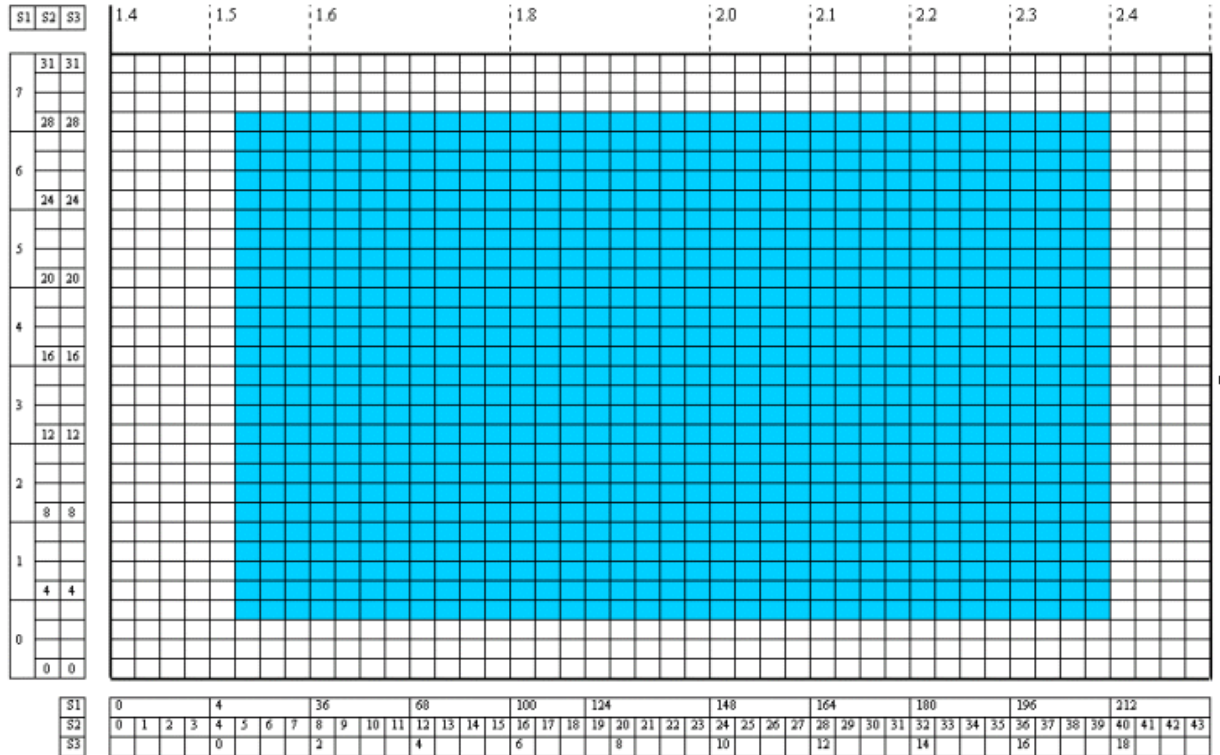


Figure 4.12: Segmentation of the outer wheel of an EMEC module. The blue region corresponds to the cluster central cells considered for this analysis.

## 4.5 Electron energy corrections

The end-cap calorimeter geometry produces several effects which degrade the uniformity. Hence, corrections should be applied to calibrated energies to reconstruct the electron response. They are performed at the cell level (as the high voltage correction and the capacitance correction) and at the cluster level (lateral leakage and  $\phi$ -modulation correction).

Module	ECC0	ECC1	ECC5
Scanned	874	910	844
Kept	763 (87%)	820 (90%)	761 (90%)

Table 4.2: Number of cluster central cells kept for the uniformity analysis.

### 4.5.1 High Voltage correction

The first correction applied to the cluster energy is the so called High Voltage (HV) correction. As we have seen the liquid Argon gap thickness of the EMEC decreases continuously when the pseudorapidity  $\eta$  increases (see section 3.2.1). This makes the cluster energy to grow along the pseudorapidity direction due to the explicit gap variation and the implicit change in the sampling fraction according the following relation

$$E \sim \frac{f_s}{g^{1+b}} U^b$$

where  $g$  is the liquid Argon gap thickness,  $f_s$  the sampling fraction, that is a function of the gap thickness, and  $U$  is the high voltage applied in the gap. The value for the exponent  $b$  is approximately 0.4 according to measurements performed in module 0 [27]. A continuously decreasing high voltage setting along  $\eta$  would partially compensate for this growth and imply an almost  $\eta$ -independent detector response. As we have already seen, for technical reasons a decreasing stepwise function for  $U$  is chosen instead defining 7 HV sectors for the outer wheel (2 for the inner wheel), see figure 4.13.

Since inside each sector the HV is constant, the cluster energy increases with  $\eta$  (see left plot of figure 4.14). To correct for the increase of the cluster energy inside HV sectors,  $\eta$ -dependent weights ( $\omega^{(s)}$ ) are applied to each cell:

$$\omega^{(s)}(\eta_j) = \beta^{(s)} / (1 + \alpha^{(s)} (\eta_j - \eta_c^{(s)}))$$

where for a given sampling layer (front, middle or back)  $\eta_j$  is the cell pseudorapidity and  $\eta_c^{(s)}$  the pseudorapidity at the centre of the HV sector  $s$ . The parameter  $\alpha^{(s)}$  is the slope of the energy dependence with  $\eta$  and the parameter  $\beta^{(s)}$  is a normalization factor accounting for inaccurate high voltage settings, which can also be observed in the left plot of figure 4.14.

We have used two methods in order to obtain both parameters  $\alpha^{(s)}$  and  $\beta^{(s)}$  from the test beam data.

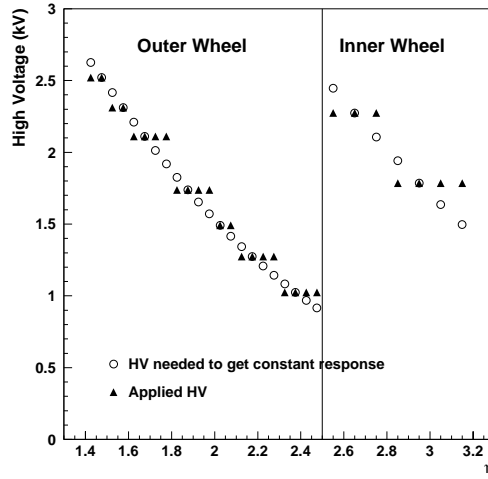


Figure 4.13: The open circles represent the continuously varying high voltage value needed for the response to be constant over  $\eta$ . The black triangles represent the nominal values applied in different sectors in  $\eta$ .

- **Method 1: Method of the independent sectors.**

This method consists of fitting inside each HV region  $s$  a linear dependence of the energy with  $\eta$ , obtaining the values of the parameters  $\alpha^{(s)}$  and  $\beta^{(s)}$ . However some difficulties arise using this procedure. The cluster near the boundary of a HV region contains cells of the neighbouring region and therefore the energy of such cluster is bias by the different HV settings. This makes the energy dependence with  $\eta$  deviates from linearity at the borders because of clustering effects. Therefore, we have to calculate the parameters in such a way that they are not influenced by these boundary points. A second iteration in the calculation of the parameters is needed in order to eliminate the residual dependence of the HV distribution on  $\eta$ . To overcome this difficulties, the method consists of two steps:

- Firstly, in each HV region  $s$ , we have made a linear fit to the test beam data, excluding the clusters near the boundary of a HV region (see left plot of figure 4.14). In the HV regions with too few points (for instance, the region between  $\eta_{cell} = 24$  and 27, in which there are only four), we have considered all the points in the fit. In this way, we have obtained a set of coefficients  $\alpha_{a_1}^{(s)}$  and  $\beta_{a_1}^{(s)}$ . Using these parameters the following weights can be constructed:

$$w_{a_1}^{(s)}(\eta_j) = \beta_{a_1}^{(s)} / [1 + \alpha_{a_1}^{(s)} \cdot (\eta_j - \eta_c^{(s)})]$$

- Secondly, we consider now the energy corrected by the weights  $w_{a_1}^{(s)}(\eta_j)$ . We fit the corrected energy to a line in each HV sector  $s$ , taking into account now



all the clusters (that is, including the points near the boundary of a region), see right plot of figure 4.14. The slope obtained in this way,  $\alpha_{b_1}^{(s)}$ , is very small but is enough to reduce the dispersion around the mean value for a  $\eta$  scan. In such a way, a second set of weights are computed:

$$w_{b_1}^{(s)}(\eta_j) = \beta_{b_1}^{(s)} / [1 + \alpha_{b_1}^{(s)} \cdot (\eta_j - \eta_c^{(s)})]$$

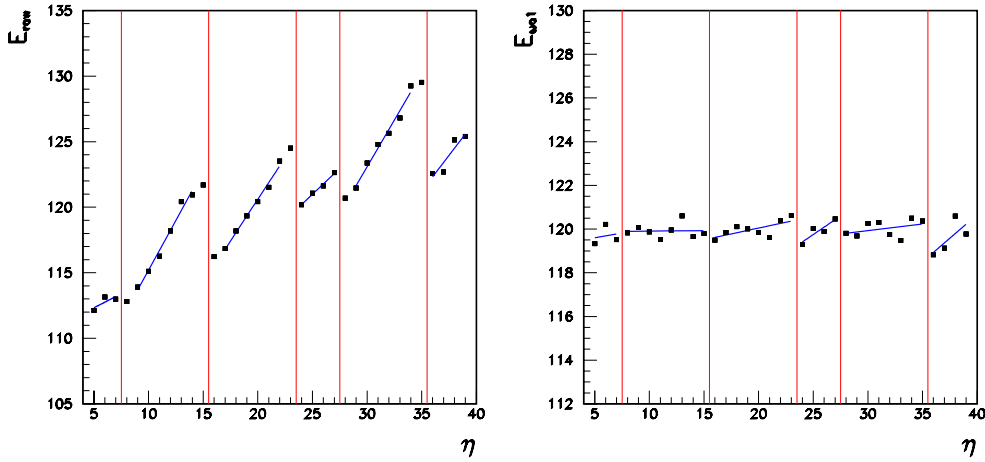


Figure 4.14: First (left) and second (right) step of the high voltage correction, using the method of the independent sectors. Energy (GeV) as a function of  $\eta$ , for  $\phi_{cell} = 16$ , without corrections (left) and corrected with the weights  $w_{a_1}^{(s)}(\eta_j)$  (right). The blue line is the result of a linear fit.

Therefore, the total high voltage correction is the product of both weights:

$$\begin{aligned} w_{a_1}^{(s)}(\eta_j) \cdot w_{b_1}^{(s)}(\eta_j) &= \beta_{a_1}^{(s)} \cdot \beta_{b_1}^{(s)} / \{ [1 + \alpha_{a_1}^{(s)} \cdot (\eta_j - \eta_c^{(s)})] \cdot [1 + \alpha_{b_1}^{(s)} \cdot (\eta_j - \eta_c^{(s)})] \} = \\ &= \beta_{a_1}^{(s)} \cdot \beta_{b_1}^{(s)} / [1 + (\alpha_{a_1}^{(s)} + \alpha_{b_1}^{(s)}) \cdot (\eta_j - \eta_c^{(s)}) + \alpha_{a_1}^{(s)} \cdot \alpha_{b_1}^{(s)} (\eta_j - \eta_c^{(s)})^2] \end{aligned}$$

The quadratic term is very small, so we can reject it, obtaining the resulting weights given by:

$$w_1^{(s)}(\eta_j) = w_{a_1}^{(s)}(\eta_j) \cdot w_{b_1}^{(s)}(\eta_j) \approx \beta_1^{(s)} / [1 + \alpha_1^{(s)} \cdot (\eta_j - \eta_c^{(s)})]$$

where  $\beta_1^{(s)} = \beta_{a_1}^{(s)} \cdot \beta_{b_1}^{(s)}$  and  $\alpha_1^{(s)} = \alpha_{a_1}^{(s)} + \alpha_{b_1}^{(s)}$ .

- **Method 2: Method of the interconnected sectors.**

Two difficulties arises using the previous procedure, namely

1. the cluster near the boundary of a region contains cells of two regions and therefore the energy of such cluster is biased by the different HV settings
2. some regions contain too few points (either because they are small or because there are too many “bad-behaved” cells) making it difficult to obtain the slope  $\alpha^{(s)}$  with accuracy.

We have developed a new method in which a global fit to all high voltage regions together is performed using a power law function  $a_1 + a_2 \eta^{a_3}$  (as we can deduce from the figure 4.13). This choice is motivated by the relation between the energy and the gap thickness  $g$ , given by  $E \sim \frac{I_s}{g} (\frac{U}{g})^b$ .

We have made two iterations:

- For a given  $\phi$ , we consider an  $\eta$  scan (without applying corrections). The response in each region ( $s$ ) is displaced by an amount  $k^{(s)}$  (see left side plot of figure 4.15) that depends on the region. We make a global fit using the function  $a_1 + a_2 \eta^{a_3}$  [25] (right side plot of figure 4.15) obtaining the values of  $a_i$  and of the parameters  $k^{(s)}$ . Afterwards, we subtract these parameters  $k^{(s)}$  to the fit curve (left of figure 4.16) and, finally, this fit curve is made linear in each region to obtain the parameters  $\alpha_{a_2}^{(s)}$  and  $\beta_{a_2}^{(s)}$  (see right of figure 4.16). In this way, we have obtained the weights  $w_{a_2}^{(s)}(\eta_j)$ :

$$w_{a_2}^{(s)}(\eta_j) = \beta_{a_2}^{(s)} / [1 + \alpha_{a_2}^{(s)} \cdot (\eta_j - \eta_c^{(s)})]$$

- Secondly, the same process is made, but using now the energy corrected with the former weights  $w_{a_2}^{(s)}(\eta_j)$  (see figure 4.17 and 4.18). The energy dependence on  $\eta$  is now very small, obtaining thus, in this second iteration, very small slopes  $\alpha_{b_2}^{(s)}$ .

The total high voltage correction, using this method of the interconnected sectors is given by the weights  $w_2^{(s)}(\eta_j)$ , obtained in a first order in the following way:

$$w_2^{(s)}(\eta_j) = w_{a_2}^{(s)}(\eta_j) \cdot w_{b_2}^{(s)}(\eta_j) \approx \beta_2^{(s)} / [1 + \alpha_2^{(s)} \cdot (\eta_j - \eta_c^{(s)})]$$

where  $\beta_2^{(s)} = \beta_{a_2}^{(s)} \cdot \beta_{b_2}^{(s)}$  and  $\alpha_2^{(s)} = \alpha_{a_2}^{(s)} + \alpha_{b_2}^{(s)}$

The resulting  $\alpha^{(s)}$  parameter, using any of the methods, is close to 0.5 for all regions, that results from the quadratic sum of two contributions, the power  $b$  and the dependence of

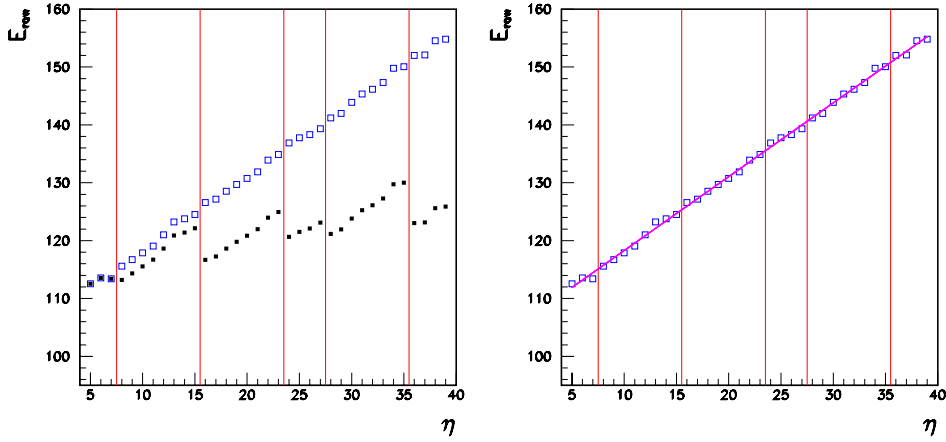


Figure 4.15: Left: energy (GeV) without corrections (black dots) as a function of  $\eta$ , for a given  $\phi$  ( $\phi_{\text{cell}} = 22$ ) and the outcome of adding the constants  $k^{(s)}$  to the energy (blue dots). Right: energy (GeV) without corrections with the addition of the  $k^{(s)}$  parameters (blue dots) as a function of  $\eta$  for  $\phi_{\text{cell}} = 22$ . The solid line represents the fit to the curve  $a_1 + a_2 \eta^{a_3}$ .

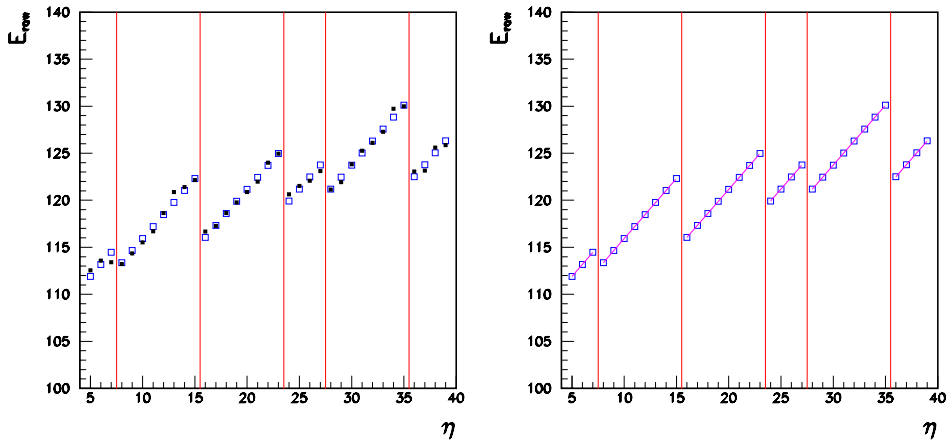


Figure 4.16: Left: energy (GeV) obtained from the fit to a curve  $a_1 + a_2 \eta^{a_3}$  and where the parameters  $k^{(s)}$  have been subtracted (blue dots), as a function of  $\eta$ , for  $\phi_{\text{cell}} = 22$ . The initial energy without corrections is shown as black dots. Right: energy (GeV) after the fit to a  $a_1 + a_2 \eta^{a_3}$  curve and after the subtraction of the  $k^{(s)}$  parameters (blue dots), as a function of  $\eta$ , for  $\phi_{\text{cell}} = 22$ . The solid line represents the result of a linear fit.

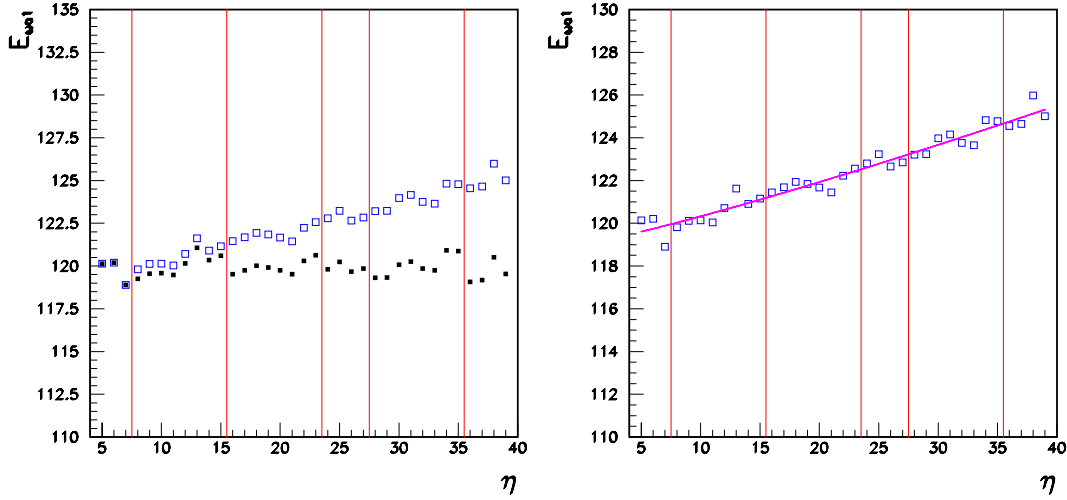


Figure 4.17: Left: energy corrected with the weights  $w_{a_2}^{(s)}(\eta_j)$  (black dots) and energy corrected with  $w_{a_2}^{(s)}(\eta_j)$  after adding the constants  $k'^{(s)}$  (blue dots), as a function of  $\eta$ , for  $\phi_{cell} = 22$ . Right: energy corrected with  $w_{a_2}^{(s)}(\eta_j)$  after adding the constants  $k'^{(s)}$  (blue dots), as a function of  $\eta$ , for  $\phi_{cell} = 22$ . The solid line represents the fit to a  $a'_1 + a'_2 \eta^{a'_3}$  curve.

the sampling fraction  $f_s$  with the gap size [57], see appendix A.

We can study the typical RMS of the deviation of the  $\eta$  scan energy from the mean value, for all  $\phi$ . The values computed with the two HV correction methods are shown in the table 4.3. Similar results are obtained with both methods. The small difference is due to the fact that in the first method a fit to each high voltage sector in particular is made, while in the second method a global fit to all regions is performed. Additionally, in the second method, the dependence on  $\eta$  of parameters  $\alpha_2^{(s)}, \beta_2^{(s)}$  is more uniform than one obtained with the first method. We have used this second method for our analysis.

The figures 4.19 and 4.20 show the  $\alpha^{(s)}$  and  $\beta^{(s)}$  parameters, computed using the second method, as a function of  $\phi$  and of the module for several HV regions. Both parameters are rather independent of  $\phi$  as expected. We can see the agreement between modules is good. These facts make possible to apply a universal HV correction independent of  $\phi$  and of the module.

The mean values of  $\alpha^{(s)}$  and  $\beta^{(s)}$ , computed with the second method, for all modules are shown in the figure 4.21. The normalization factor  $\beta$  decreases with  $\eta$  and can differ significantly from 1. This suggests that the simulation based on GEANT3 is not perfect

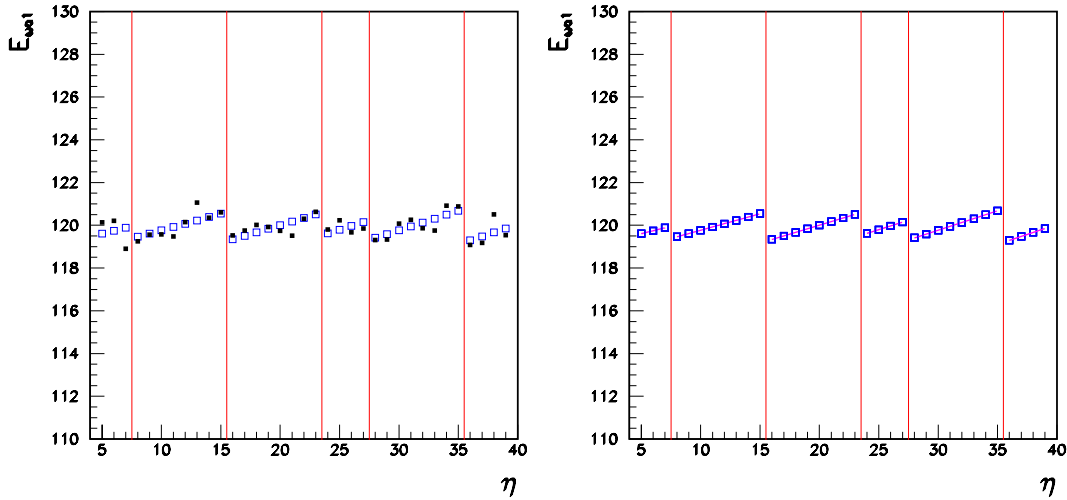


Figure 4.18: Left: energy (GeV) obtained from the fit to a curve  $a'_1 + a'_2 (\eta)^{a'_3}$  and where the parameters  $k^{(s)}$  have been subtracted (blue dots) as a function of  $\eta$ , for  $\phi_{cell} = 22$ . Black dots are the initial energy corrected by  $w_{a_2}^{(s)}(\eta_j)$ . Right: energy (GeV) after the fit to a  $a'_1 + a'_2 (\eta)^{a'_3}$  curve and after the subtraction of the  $k^{(s)}$  parameters, as a function of  $\eta$ , for  $\phi_{cell} = 22$ . The solid line represents the result of a linear fit.

and the HV settings will be adjusted. The  $\beta$  value for ECC1 sector B1 is a little big high due probably to an incorrectly high voltage setting. As the mean energy is normalized to the beam energy through the  $\beta^{(s)}$  parameters, no interpretation of the absolute energy scale can be made after the HV correction.

The distribution of the parameter  $\alpha^{(s)}$  over all  $\phi$ , all HV sectors and all modules is shown in figure 4.22. The mean value is 0.484, with a dispersion around 10%. The average value in  $\phi$  and in module of these parameters  $\alpha^{(s)}$  and  $\beta^{(s)}$  for each HV region  $s$  has been used finally to correct the data presented in this thesis (see table 4.4). When ATLAS starts, the knowledge of these correction parameters will then probably improve with time and data. As an example, the  $\beta$  parameters, which are intercalibration coefficients between HV regions, can be improved using  $Z^0 \rightarrow e^+e^-$  events [28].

## 4.5.2 Capacitance correction

The energy measured in beam test shows an unexpected non-uniformity along the  $\phi$  direction in the 3 modules tested (see figure 4.23, upper points), specially in ECC0 and ECC1 (the modules which were firstly constructed). This effect can be correlated with

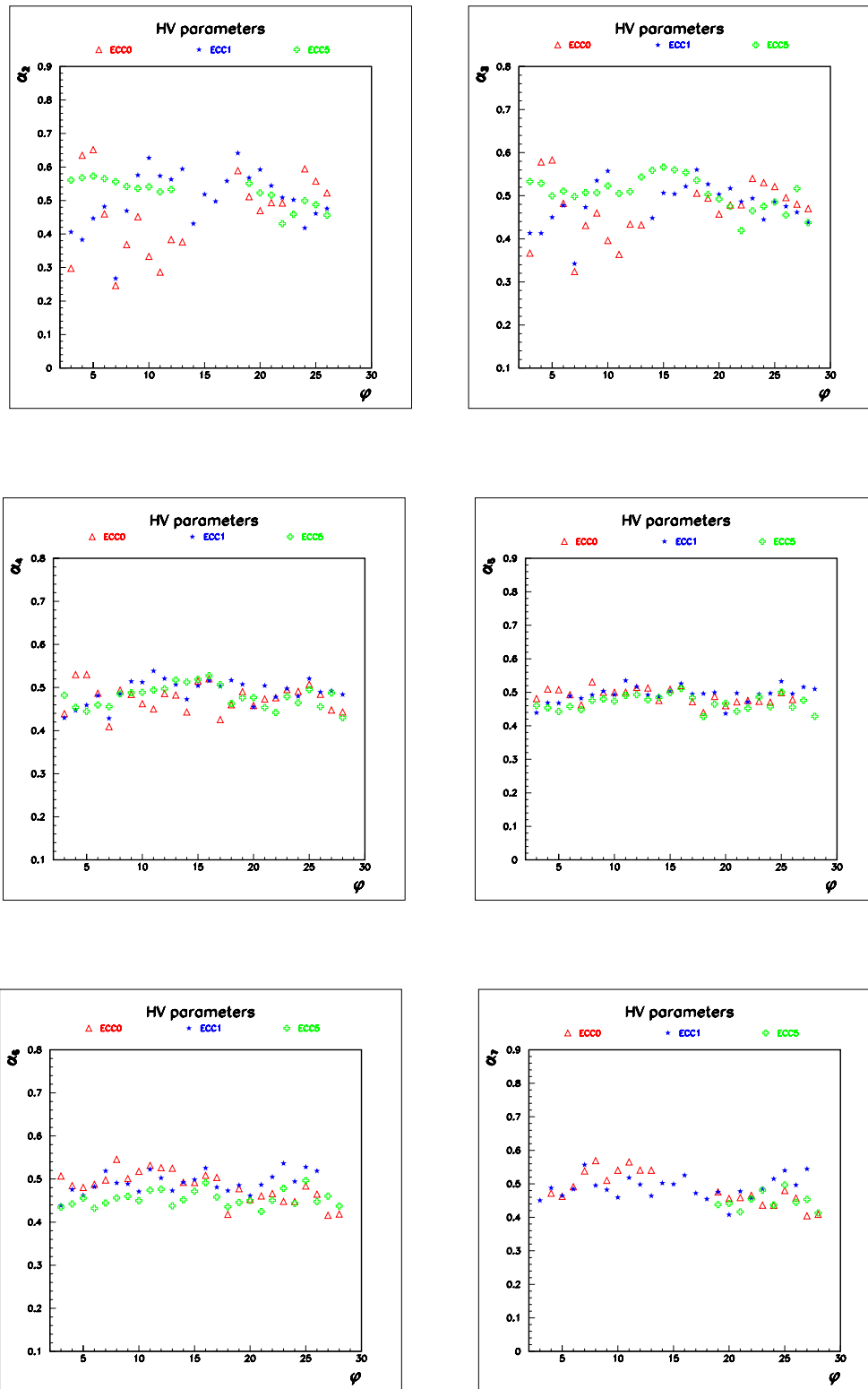


Figure 4.19: Parameters  $\alpha^{(s)}$  versus  $\phi_{cell}$  and versus module.

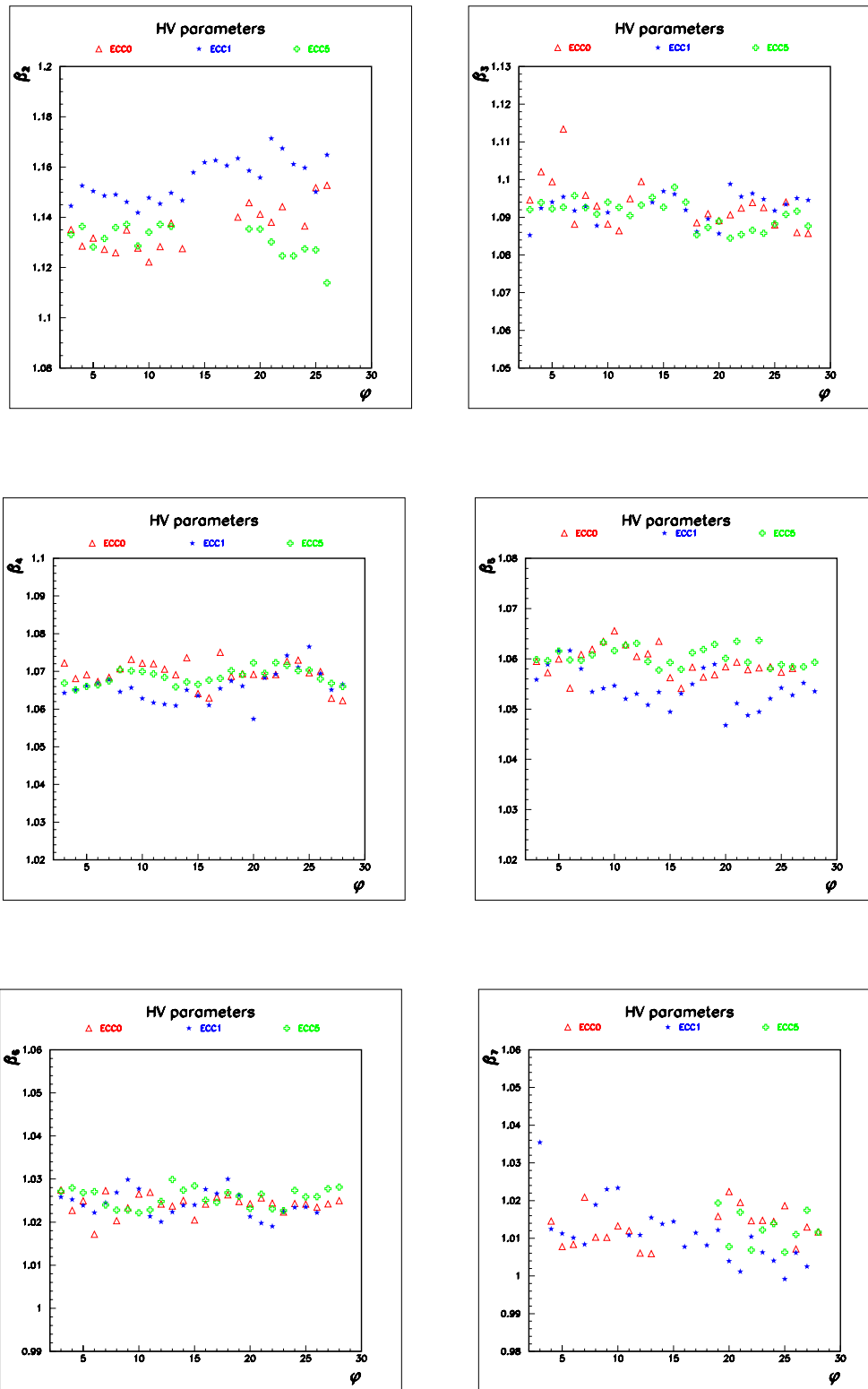


Figure 4.20: Parameters  $\beta^{(s)}$  versus  $\phi_{cell}$  and versus module.

HV correction method	ECC0	ECC1	ECC5
Method 1: first step	0.385	0.308	0.334
Method 1: second step	0.287	0.273	0.275
Method 2: first step	0.484	0.431	0.434
Method 2: second step	0.338	0.327	0.331

Table 4.3: RMS of the deviation of  $\eta$  scan energy from the mean value, integrated over all  $\phi$ , using several high voltage correction methods.

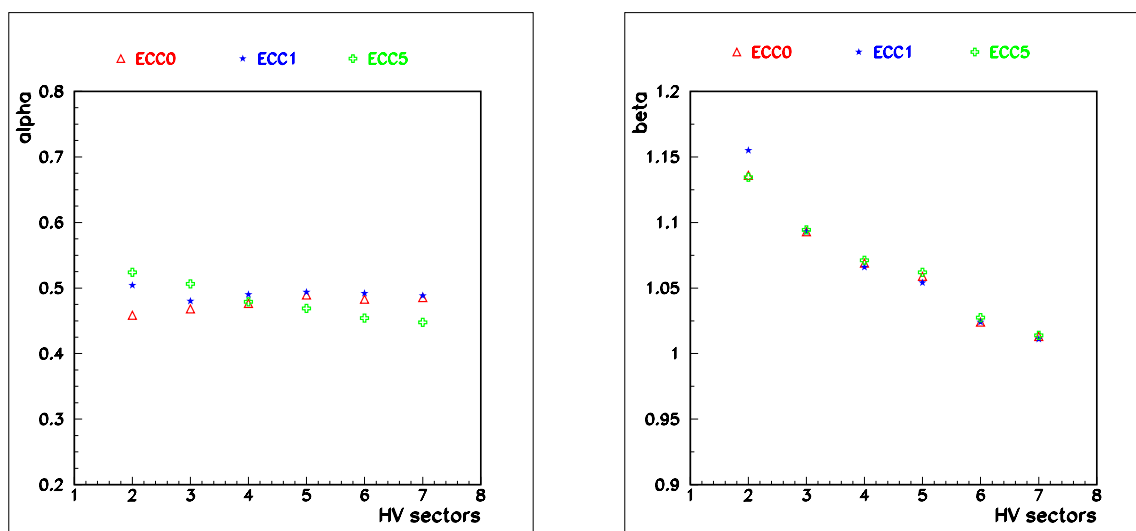


Figure 4.21: Mean values of the parameters  $\alpha^{(s)}$  and  $\beta^{(s)}$  versus HV sector  $s$  and versus module.

HV sector ( $\eta$ range)	B1 [1.5-1.6]	B2 [1.6-1.8]	B3 [1.8-2.0]	B4 [2.0-2.1]	B5 [2.1-2.3]	B6 [2.3-2.4]
$\alpha$	0.495	0.485	0.482	0.484	0.476	0.474
$\beta$	1.134	1.092	1.068	1.058	1.024	1.012

Table 4.4: Mean values of the high voltage correction parameters  $\alpha^{(s)}$  and  $\beta^{(s)}$  for several high voltage sectors averaged over the three tested modules.



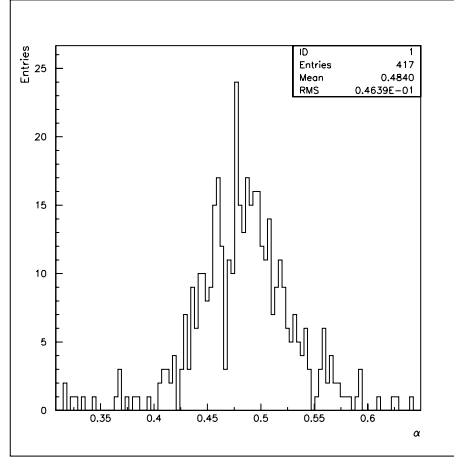


Figure 4.22:  $\alpha$  parameter distribution over all  $\phi$  values of the six HV zones studied, and for the three tested modules.

the middle cell capacitance  $C$  variation along  $\phi$  (see figure 4.23, lower points).

Since there is a relation between capacitance and gap thickness, the good correlation of the waving (fluctuating) behaviour between the energy and the capacitance (figure 4.23) leads to interpret this asymmetry in the calorimeter response as a consequence of local fluctuations of the gap thickness around the nominal value, generated during the module stacking. A theoretical explication could be the following.

We have seen the relation between energy and gap thickness, given by:

$$E \sim \frac{f_s}{g} \left(\frac{U}{g}\right)^b$$

where  $f_s$  is the sampling fraction,  $U$  is the HV applied in the gap,  $g$  is the liquid Argon thickness and  $b$  is approximately 0.4 according to measurements performed in module 0 [27].

The sampling fraction  $f_s$  can be expressed as:

$$f_s = \frac{g \left(\frac{dE}{dx}\right)_{Ar}}{g \left(\frac{dE}{dx}\right)_{Ar} + e \left(\frac{dE}{dx}\right)_{Absorber}}$$

where  $e$  is the absorber thickness<sup>11</sup>. Therefore we can write

---

<sup>11</sup> $e \left(\frac{dE}{dx}\right)_{Absorber} \approx e_{Pb} \left(\frac{dE}{dx}\right)_{Pb}$

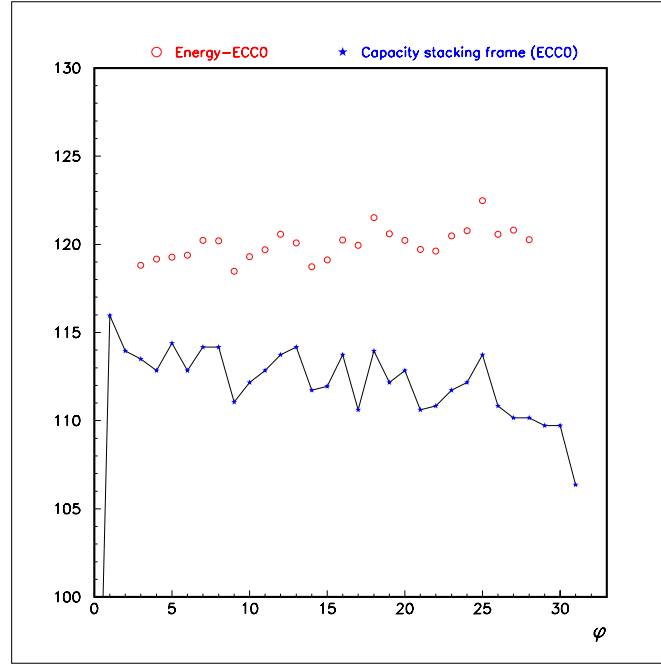


Figure 4.23: Variation along the  $\phi$  direction of the ECC0 energy measured in beam test for a cell with a fixed value of  $\eta = 1.8875$  (red circles) and capacitance measured at the stacking frame for this  $\eta$  (blue stars). The capacitance values have been multiplied by a factor in order to make easy the comparison between the energy and capacitance measurements, so the units of  $C$  are arbitrary. There is a good correlation between the cluster energy and capacitance measured at the stacking frame for each middle cell.

$$E \sim \frac{\left(\frac{dE}{dx}\right)_{Ar}}{g \left(\frac{dE}{dx}\right)_{Ar} + e \left(\frac{dE}{dx}\right)_{Absorber}} U^b \frac{1}{g^b}$$

Deriving it we find

$$\frac{dE}{dg} \sim -\left(E \frac{\left(\frac{dE}{dx}\right)_{Ar}}{g \left(\frac{dE}{dx}\right)_{Ar} + e \left(\frac{dE}{dx}\right)_{Absorber}} + bE \frac{1}{g}\right)$$

that is:

$$\frac{dE}{dg} \sim -E (f_s + b) \frac{1}{g}$$

So, the fluctuation around the mean can be written as

$$\frac{dE}{E} = -(f_s + b) \frac{dg}{g}$$

Such fluctuations in the gap thickness can be generated during the module stacking. The spacers were cut with a thickness lower than the nominal gap size between the electrode and the absorber, which results in variations in the gap thickness. The absorbers deflection due to the gravity and the variation on the position of the rings also affect to the gap. This effect is almost independent on  $\eta$ . Therefore, we must correct for the variations in the gap thickness around the nominal value in order to obtain a good uniformity.

The capacitance of a cell, in the planar approximation, is given by  $C = \varepsilon \frac{a}{g}$ , where  $a$  is the area of one cell of the electrode,  $g$  is the gap thickness and  $\varepsilon$  is the dielectric constant of the liquid Argon. Since  $a$  is a constant, a variation on  $g$  leads a variation on  $C$ . The fluctuations in the capacitance are of the order 1%, which means variations of about 10 microns (30 microns) for a 1 mm (3 mm) gap thickness.

Since  $C = \varepsilon \frac{a}{g}$ , we obtain

$$\frac{dC}{C} = -\frac{dg}{g}$$

and then

$$\frac{dE}{E} = (f_s + b) \frac{dC}{C}$$

That means that a correlation between energy fluctuations and capacitance fluctuations is observed. Therefore, the corrected cluster energy is obtained from the raw energy according to the following relation:

$$E_{capa-cor}^{cell} = E^{cell} / \left( \frac{C^{cell}}{\langle C^{cell} \rangle} \right)^\alpha$$

where  $\langle C^{cell} \rangle$  is the cell capacitance averaged over all  $\phi$ . The power  $\alpha$  corresponds to  $(f_s + b)$  that agrees with the slope of the HV correction. This agreement is consistent with the fact that both high voltage and capacitance corrections take into account the dependence of the energy with the gap thickness, the former along  $\eta$  and the latter along  $\phi$  ([57], [65]).

This correction is only applied to the signal of middle cells, since there are only C-measurements for this sampling. On the other hand, there is evidence that the front cells

keep the nominal gap thickness in the stacking frame (the deflection in front and back samplings is supposed to be small, due to screws located in the rings) [66]. Moreover, the middle sampling contributes with about 79% of the cluster energy, hence fluctuations in the middle cell energies dominate.

Many capacitance measurements were done at the stacking sites. For ten modules (all modules in ECA wheel and ECC0 and ECC3 in ECC wheel<sup>12</sup>), capacitance measurements for all  $\eta$  were performed at the middle cell level, on the summing boards [42]. For ECC5 module the capacitances were measured at the gap level, on the electrodes, at the stacking site. Unfortunately there is lack of such measurements for some modules, in particular for module ECC1. The results of these measurements in term of capacitance non-uniformity along  $\phi$  are summarized in figure 4.24.

A good correlation is observed for the oscillations at different  $\eta$  values (see figure 4.25). This leads to think that the gap deformation affects equally to the complete gap independent of  $\eta$ . There are capacitance measurements for the ECC wheel as well, but they are taken only at one  $\eta$  value ( $\eta_{cell} = 39$ ). The previous results justifies to use these measurements for the capacitance correction at all  $\eta$  values.

Unfortunately, these capacitance measurements on the ECC wheel were performed during fixes of bad behaved channels simultaneously, that is people touching, plug-in and unplug-in MB and SB, soldering, etc. These operations affected the ground of the capacimeter used for the measurements, hence its reference line. For instance, the step seen at  $\phi_{cell} = 24$  in the capacitance measured at  $\eta_{cell} = 39$  for ECC1 on the wheel (see figure 4.26) is interpreted as a change of the ground during the measurements of ECC1. In addition, a low quality probe had to be used, which made the measurements to experience larger fluctuations, as can be seen comparing the measurements for ECC0 on the wheel and in the stacking frame (figure 4.27). Therefore these measurements need to be taken with care when correcting the signal.

A summary of the kind of capacitance measurements performed for the three beam-tested modules, ECC0, ECC1 and ECC5, is given in table 4.5.

Two effects have been seen in the capacitance measurements at the stacking frame: a global decrease (global slope) and cell-to-cell fluctuations. The global slope is understood as produced by the stacking frame keeping the module under some mechanical constraints which are not present in the final wheel [67] [68]. In fact this slope is not present when the modules are integrated in the wheel in vertical position (see upper points of figure 4.27). Therefore the effect is of no concern for ATLAS. In contrast, the cell-to-cell fluctuation are also observed when the modules are integrated in the wheel. Figure 4.27 shows that

---

<sup>12</sup>When the importance of the capacitance measurements was established, the ECC wheel was already inserted in the cryostat, and only capacitance measurement at the middle cell level were done for ECC0 and ECC3 modules. For the ECA wheel, the capacitance was measured for all modules.

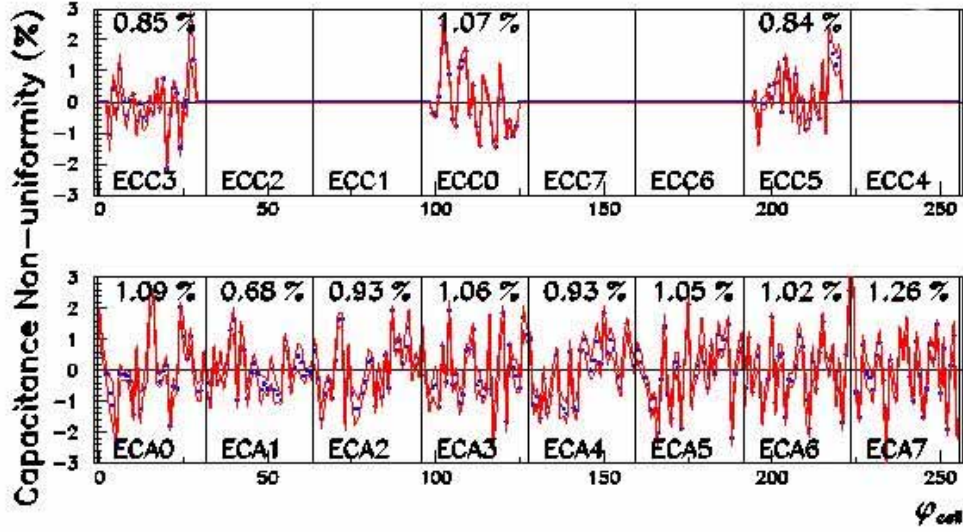


Figure 4.24: Measurement results of the middle cell capacitance non-uniformity along  $\phi$  for the ATLAS EMEC modules, at the stacking site. All capacitance measurements were performed at the middle cell level, on the summing boards, except for ECC5, whose measurements were performed at the gap level, on the electrodes. Five modules have not been measured. Only the relative variation with respect to the mean value is plotted. The dispersion is given for each module.

Module	ECC0	ECC1	ECC5
C stack	C SB-level	None	Capagap
C wheel $\eta_{cell} = 39$ MB level	Yes	Yes	Yes

Table 4.5:  $C$  measurements performed for the three beam-tested modules. For ECC0 the measurements at the stacking frame were done on the summing boards connectors, while for ECC5 module were measured at the gap level combining several sectors in  $\eta$ . The measurements at the wheel were done on the mother boards connectors. All measurements correspond to cells of the middle layer.

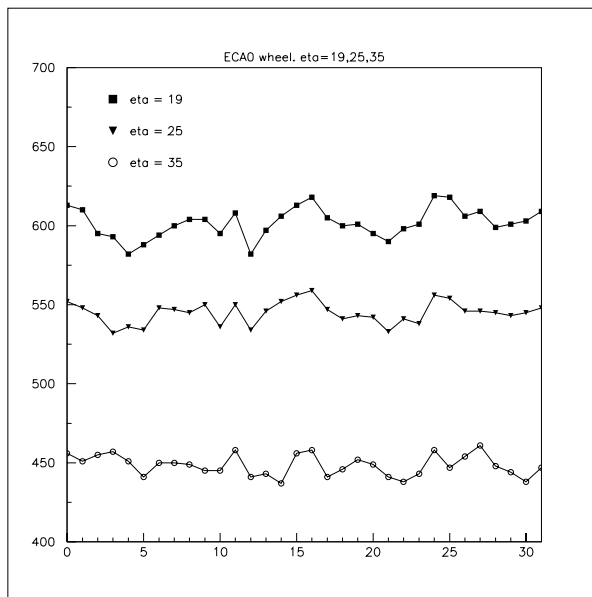


Figure 4.25: Capacitance measurements (in  $pF$ ) performed at the ECA wheel for several  $\eta_{cell}$ . A correlation between the measurements is observed.

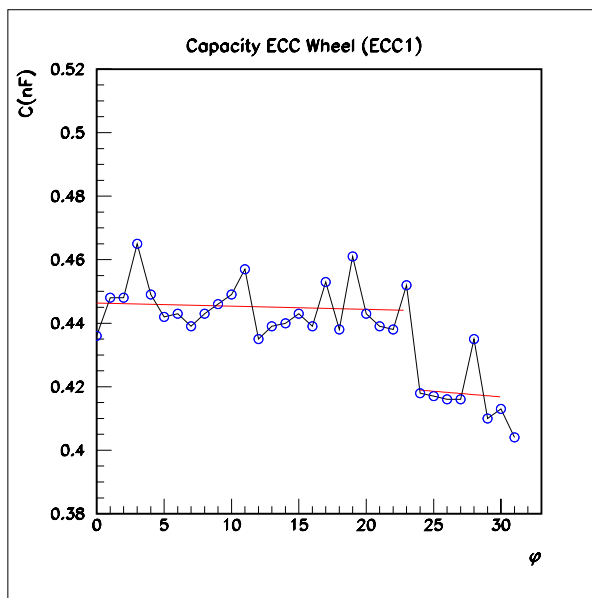


Figure 4.26: Capacitance measured at  $\eta_{cell} = 39$  for ECC1 (in middle cell units corresponds to  $\eta = 2.3875$ ) on the wheel. At  $\phi_{cell} = 24$  there is a step decrease due to a change in the grounding of the capacimeter used for the measurements.

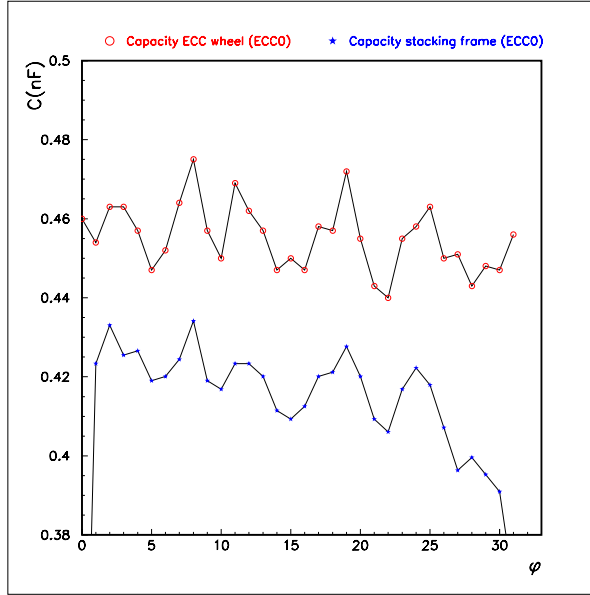


Figure 4.27: Capacitance measured at  $\eta_{cell} = 39$  (in middle cell units corresponds to  $\eta = 2.3875$ ) for ECC0 on the wheel (red circles) and on the stacking frame (blue stars).

the fluctuations of the capacitance remain at the same positions irrespective of whether the module is at the stacking frame or in the ECC wheel [45]. Therefore it is possible to use the measurements in the stacking frame (performed for all  $\eta$  and  $\phi$ ) to correct the data for these gap-to-gap fluctuations. The relation  $E_{capa-cor}^{cell} = E^{cell} / (\frac{C^{cell}}{\langle C^{cell} \rangle})^\alpha$  corrects both the waving behaviour and the slope (in case there exists).

There also exists measurements of the product  $LC$  performed on both ECA and ECC wheels using a network analyzer device. In this procedure a cosine input signal is injected through the calibration line for different frequencies and the output response is recorded as a function of the injected frequency. The minimum of the output function is obtained when the frequency equals  $\frac{1}{\sqrt{LC}}$  of the cell (see figure 4.28)). Unfortunately, the different methods applied to extract  $C$  from these measurements could not provide the required accuracy.

For each module the most accurate capacitance measurements are used. As it corrects for local stacking effect, the correction has to be specific for each cell and each module and mandatory at least for the 2 first produced modules (ECC0 and ECC1). Starting from the capacitance measurements, it could be refined in ATLAS by intercalibrating  $\phi$ -slices of the calorimeter with  $Z^0 \rightarrow e^+e^-$  events, in the same way as what is done in [28].

As already commented above, no accurate capacitance measurements exist for module

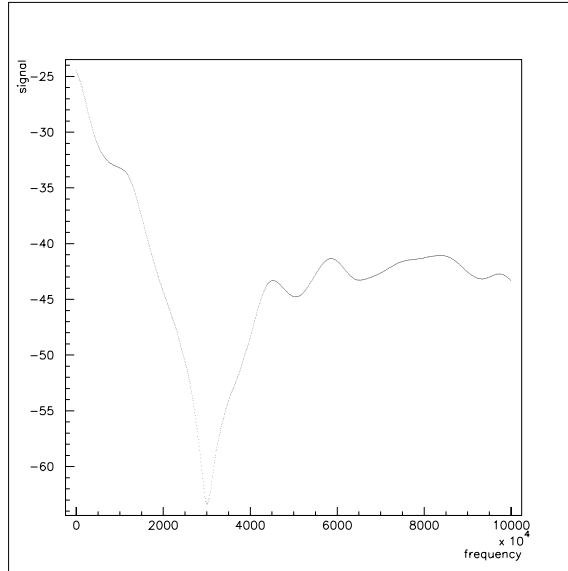


Figure 4.28: Response signal of the network analyzer as a function of the input frequency. The minimum of the output function is obtained when the frequency equals  $\frac{1}{\sqrt{LC}}$  of the cell.

ECC1. For this reason an ad-hoc correction has been extracted from the  $\phi$ -dependence of the TestBeam signal averaged over all  $\eta$ . In contrast, for module ECC0 the signal is corrected using the capacitance measurements performed at the stacking frame. Module ECC5 exhibits very small gap to gap fluctuations, hence no correction is applied for this module apart from the slight global slope that is corrected using the data itself.

### 4.5.3 Lateral leakage correction

The cluster size is large enough to contain the shower energy when the beam is incident right on the center of the cluster central cell. However, for each run, the beam has been tuned in such a way the point of incidence is uniformly distributed along a size larger than one middle cell in both directions  $\eta$  and  $\phi$ . Figure 4.29 shows the cluster energy as a function of the beam point of incidence along the  $\eta$  direction. The cluster central cell is  $\eta = 1.7625$  (cell 14 of the middle sampling).

The beam impact point is estimated with energy weighted barycentres in the front section for  $\eta$ :

$$\eta_{bar}^{S_1} = \sum_{j=1}^{N_j} \sum_{k=1}^{N_k} \frac{E_1(\eta_j, \phi_k) \times \eta_j}{E_{S_1}}$$



where  $\eta_j$  is the position of the cell  $j$ ,  $N_j \times N_k$  is the number of cells in a  $\Delta\eta \times \Delta\phi$  cluster of the front sampling  $S_1$  and  $E_1$  the energy deposited in the front cell  $(\eta_j, \phi_k)$ .

We can observe in the figure 4.29 that the measured energy is maximum for particles which hit the cell centre and decreases toward the cell edges due to lateral leakage outside the cluster (for events of the run where the electron is incident far from the center of the cluster central cell). The leakage is expected to increase with  $\eta$ , because the cell size decreases in cm. A parabolic fit  $1 + K(\eta - \eta_c)^2$ ,  $\eta_c$  being the centre of the cluster, describes well this  $\eta$  dependence of the cluster energy. Hence, the correction for this lateral leakage is obtained as follows:

$$E_{\eta-cor} = E/[1 + K(\eta - \eta_c)^2]$$

The parameter  $K$  represents the parabola curvature, which is related to the amount of leakage. In absolute values it increases with  $\eta_c$ , which indicates a decrease of the shower containment for larger  $\eta_c$  values. Its  $\eta$  dependence (averaged over  $\phi$  and over modules) has been parametrized by a line  $K = p_0 + p_1\eta$ , being  $p_0 = 68.3 \pm 7.6$  and  $p_1 = -59.6 \pm 4.0$  (see figure 4.30).

The cluster chosen, 5 by 5 middle cells, is larger along the  $\phi$  direction than along the  $\eta$  direction. This fact makes the leakage along  $\phi$  be negligible and therefore no correction is needed in this case.

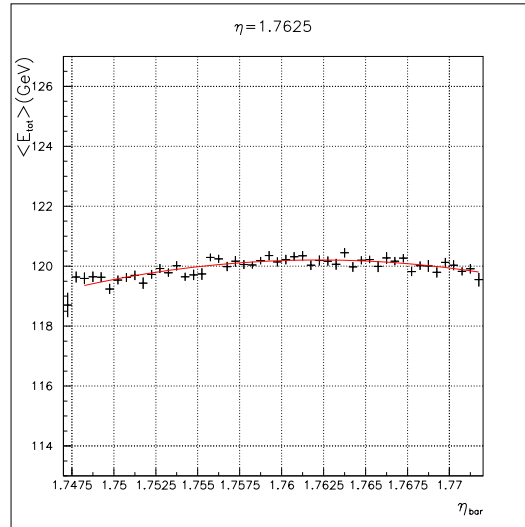


Figure 4.29: Cluster energy versus  $\eta$  incident position of the beam on cell 14 (middle cell units).

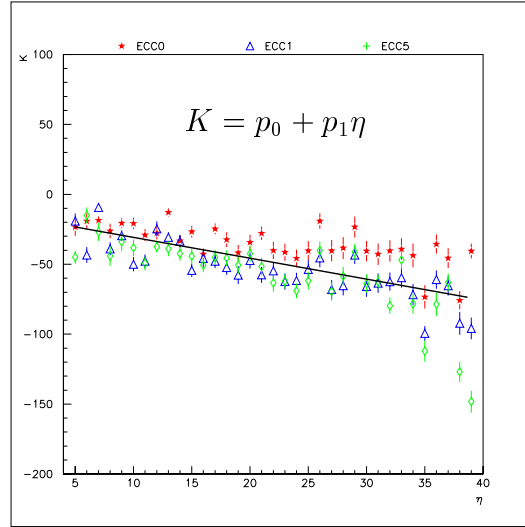


Figure 4.30: Parameter  $K$  of the lateral leakage correction, averaged over  $\phi$ , as a function of  $\eta$ , for ECC0, ECC1 and ECC5 modules. Its  $\eta$  dependence (averaged over  $\phi$  and over modules) has been parametrized by a line  $K = p_0 + p_1\eta$ , being  $p_0 = 68.3 \pm 7.6$  and  $p_1 = -59.6 \pm 4.0$ .

#### 4.5.4 $\phi$ -modulation correction

The accordion shape introduces non-uniformities of the electric field along  $\phi$  inside every gap between two consecutive absorbers. This translates to periodic non-uniformities on the cluster energy along the  $\phi$  direction ( $\phi$ -modulation), where the period is the distance between two consecutive absorbers, see figure 4.31. The particle impact position on the calorimeter is estimated with energy weighted barycentre in the middle sampling for  $\phi$  according the following formula:

$$\phi_{bar}^{S_2} = \sum_{j=1}^{N_j} \sum_{k=1}^{N_k} \frac{E_2(\eta_j, \phi_k) \times \phi_k}{E_{S_2}}$$

where  $N_j \times N_k$  is the number of cells in a  $\Delta\eta \times \Delta\phi$  cluster of the middle sampling  $S_2$ .

Figure 4.32 shows the cluster energy as a function of the  $\phi$ -barycentre for two  $\eta$  positions. The units of the  $\phi$ -barycentre refer to the thickness between 2 consecutive absorbers. The amplitude of the modulation decreases with the amplitude of the waves of the accordion geometry, that is when  $\eta$  increases (see figure 4.32).

The  $\phi$ -modulation is corrected using a Fourier polynomial with five parameters [69] in the following manner:

$$E_{\phi-cor} = E/[a_0 \cdot \left(1 + \sum_{k=1}^2 a_k \cdot \cos(2\pi k(\phi - \phi_0)) + b_1 \cdot \sin(2\pi(\phi))\right)]$$

where  $a_i$ ,  $b_1$  and the phase shift  $\phi_0$  are  $\eta$  dependent whereas  $a_0$  is a normalization parameter.



Figure 4.31: Photograph of an electrode sandwiched between two consecutive absorbers thanks to the spacers.

Figures 4.33 show the  $\eta$  dependence of these parameters for the three modules, averaged over  $\phi$ . The agreement between modules is very good for all parameters, leading to obtain a universal correction. We can see a smoothly dependence on  $\eta$  for all parameters, which reflects the geometry variation (accordion wave amplitude, folding angle, gap thickness). We have fitted the average value of the three modules ECC0, ECC1, and ECC5 to a polynomial, whose degree depends on the  $\eta$  region. The results of such fit are shown in table 4.6.

$a_1$	$a_1 = p_0 + p_1\eta + p_2\eta^2$ if $\eta < 2.4$ $a_1 = 0$ if $2.4 < \eta < 2.5$	$p_0 = 0.3365 \pm 0.0014$ $p_1 = -0.3360 \pm 0.0013$ $p_2 = 0.0818 \pm 0.0003$
$a_2$	$a_2 = p_0 + p_1\eta$ if $\eta < 2.0$ $a_2 = 0$ if $2.0 < \eta < 2.5$	$p_0 = 0.0349 \pm 0.0008$ $p_1 = -0.0173 \pm 0.0005$
$b_1$	$b_1 = 0$ if $\eta < 2.2$ $b_1 = p_0 + p_1\eta$ if $2.2 < \eta < 2.5$	$p_0 = -0.063 \pm 0.002$ $p_1 = 0.0284 \pm 0.0012$
$\phi_0$	$\phi_0 = p_0 + p_1\eta + p_2\eta^2$ if $\eta < 2.0$ $\phi_0 = p_0 + p_1\eta$ if $\eta > 2.0$	$p_0 = -2.237 \pm 0.011$ $p_1 = 2.670 \pm 0.009$ $p_2 = -0.775 \pm 0.003$ $p_0 = 0.13 \pm 0.05$ $p_1 = -0.06 \pm 0.02$

Table 4.6: Parameters of the  $\phi$ -modulation correction. We have fitted the average value of the three modules ECC0, ECC1, and ECC5 to a polynomial, whose degree depends on the  $\eta$  region.

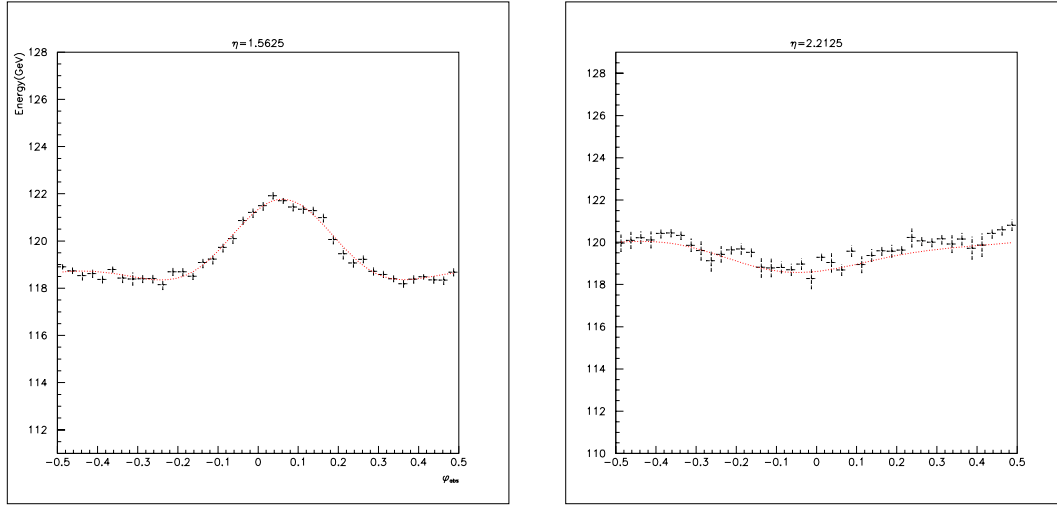


Figure 4.32: Cluster energy versus  $\phi$  for  $\eta = 1.5625$  (left) and  $\eta = 2.2125$  (right). The quantity  $\phi_{abs}$  is in units of the thickness between two consecutive absorbers. The solid line represents the results of a fit to a Fourier polynomial.

## 4.6 Uniformity results

We have represented the mean reconstructed cluster energy after all correction at every scan point as an histogram for each module in figure 4.34. There is an entry per cell of the region of analysis. We have used the capacitance measured at stacking frame for ECC0 and the test beam data (average response) for ECC1 to correct the  $\phi$ -asymmetry. For module ECC5 only the global slope is corrected using the test beam data since the gap to gap fluctuations are found to be small. The dispersion ( $\sigma/\text{mean}$ ) of those Gaussian distributions represents the non-uniformity of the module response.

We have computed the  $\eta$  non-uniformities as follows. For a given  $\eta$  scan ( $\phi$  is kept constant at  $\phi_k$ ) we determine the quantity

$$\Delta E_{\eta_i}^{(\phi_k)} = \frac{(E(\eta_i, \phi_k) - E_m^{(\phi_k)})}{E_m^{(\phi_k)}} \quad \eta_i = 1, \dots, n_\phi$$

where  $n_\phi$  is the number of points of the scan and  $E_m^{(\phi_k)} = \frac{1}{n_\phi} \sum_{\eta_i}^{n_\phi} E(\eta_i, \phi_k)$  is the mean energy for each  $\eta$  scan. This process is repeated for all  $\eta$  scan (for all  $\phi$  values) and the quantities  $\Delta E_{\eta_i}^{(\phi_k)}$  are histogrammed. If  $n_{scans}$  is the number of  $\eta$  scans, the number of entries on this histogram will be  $n_{scans} \times n_\phi$ . From a Gaussian fit to this distribution the non-uniformity along the  $\eta$  direction,  $\sigma_\eta / \langle E \rangle$ , is obtained. A similar procedure is followed to obtain  $\sigma_\phi / \langle E \rangle$  from the  $\phi$  scans.

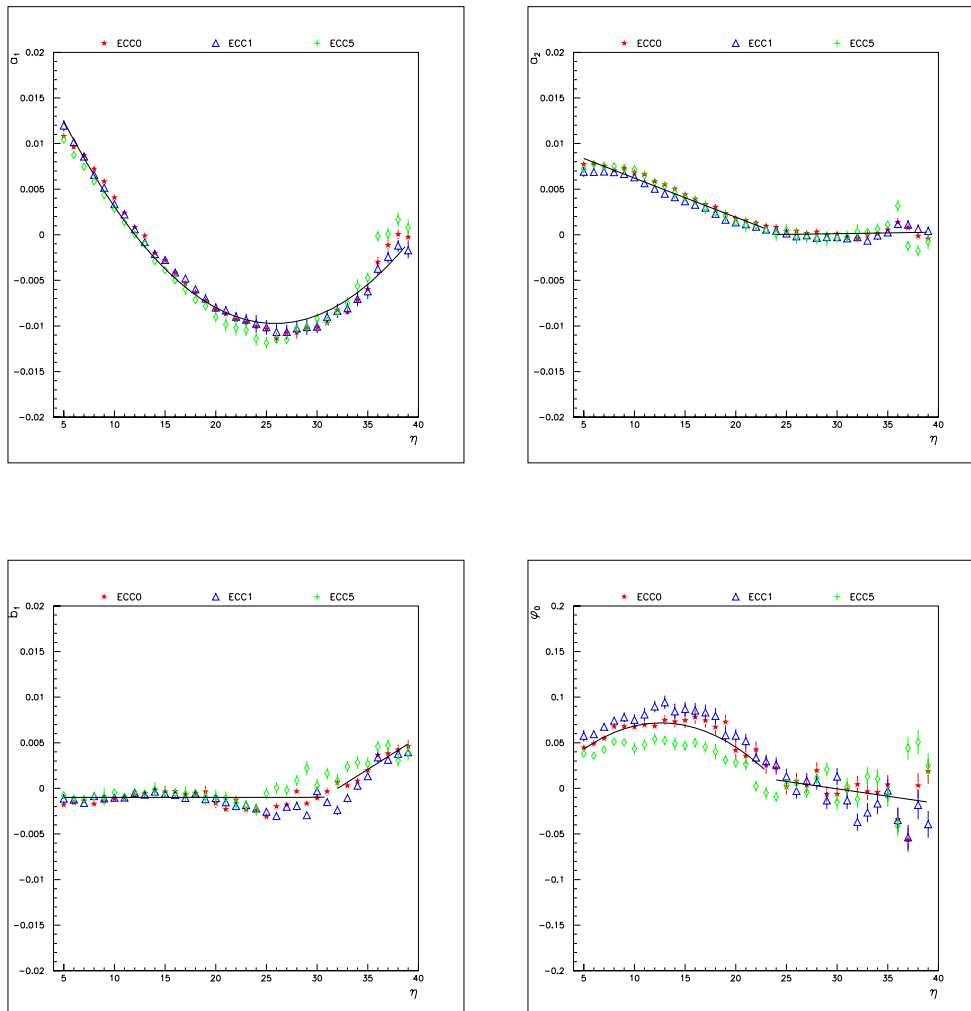


Figure 4.33:  $\phi$ -mean coefficient  $a_1$ ,  $a_2$ ,  $b_1$  and  $\phi_0$  of  $\phi$ -modulation versus  $\eta_{cell}$  and versus module. The dependence on  $\eta$  is fitted to polynomials, whose parameter values are in table 4.6.

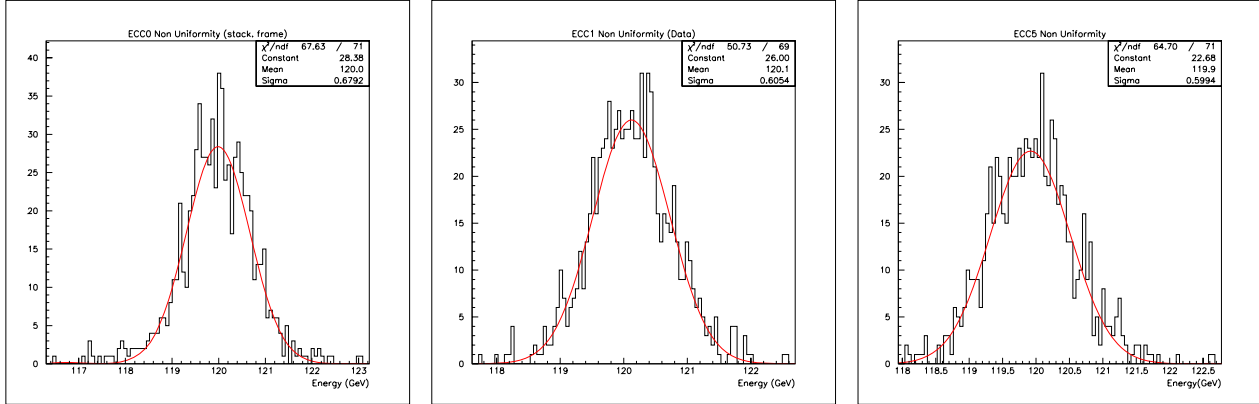


Figure 4.34: Distribution of the mean cluster energy for ECC0, ECC1 and ECC5.

The results for the non-uniformity are shown in the table 4.7. These values are less than 0.6% for each of modules. It is slightly better for ECC1 because an ad-hoc capacitance correction has been used. The numbers are in good agreement with an independent analysis done at CPPM [57] except for module ECC5 ( $\sigma / \langle E \rangle = 0.57\%$  for the CPPM analysis). We understand that the reason for this discrepancy comes from the procedure to correct the global slope: CPPM uses the capagap measurements and we use the test beam data (average response) for this module.

Module	ECC0	ECC1	ECC5
$\sigma / \langle E \rangle$	$0.57 \pm 0.02\%$	$0.51 \pm 0.02\%$	$0.50 \pm 0.02\%$
$\sigma_\eta / \langle E \rangle$	$0.42 \pm 0.02\%$	$0.49 \pm 0.02\%$	$0.43 \pm 0.02\%$
$\sigma_\phi / \langle E \rangle$	$0.47 \pm 0.02\%$	$0.43 \pm 0.02\%$	$0.38 \pm 0.02\%$

Table 4.7: Deviation from uniformity for the three modules analyzed.

We observe small differences in the non-uniformity along the orthogonal directions  $\eta$  and  $\phi$  (see table 4.7), which indicates a slight anisotropic performance of the module. We consider the following two sources of anisotropy:

- Along the  $\eta$ -direction we know that the regions near the cracks, at low and high  $\eta$  values, have a worse non-uniformity, which spoils the value of  $\sigma_\eta$ .
- Along the  $\phi$ -direction the gap to gap fluctuations, smaller for ECC5, and the procedure to correct them influences the final result on  $\sigma_\phi$ .

We study then by obtaining the non-uniformity in the  $\eta$ -region from  $\eta_{cell} = 8$  to 35, far away from the cracks, and by correcting the gap to gap fluctuations using the average response of the test beam data, module by module for the three modules. The results are shown in table 4.8. A very good agreement between between  $\sigma_\eta$  and  $\sigma_\phi$  is observed for the three modules. On the other hand, there remains a residual effect as indicated by the fact that  $\sigma$  is larger than  $\sigma_\eta$  (or  $\sigma_\phi$ ). The value is however very small and does not disturb the performance goal.

Module	ECC0	ECC1	ECC5
$\sigma / \langle E \rangle$	$0.45 \pm 0.02\%$	$0.45 \pm 0.02\%$	$0.42 \pm 0.02\%$
$\sigma_\eta / \langle E \rangle$	$0.39 \pm 0.01\%$	$0.41 \pm 0.01\%$	$0.36 \pm 0.01\%$
$\sigma_\phi / \langle E \rangle$	$0.40 \pm 0.01\%$	$0.41 \pm 0.01\%$	$0.34 \pm 0.01\%$

Table 4.8: Deviation from uniformity for the three modules analyzed. The  $\eta$  region is restricted to 8-35 in middle cell units and the gap to gap fluctuations is corrected using the test beam data.

Finally, we have also corrected the  $\phi$ -asymmetry using the capacitance measured manually on the ECC wheel in vertical position. This capacitance measurements were performed at one single  $\eta$  value ( $\eta_{cell} = 39$ ). The resulting non-uniformities and the comparison with the non-uniformities obtained previously are shown in table 4.9. The result is similar as the nominal for ECC0, obtained when the capacitance correction is done by using the C-measurements at the stacking frame. For a module like ECC1, where no C-measurements at stacking frame are available, the result is still at the limit of tolerance (0.6%).

Module	ECC0	ECC1
$\sigma / \langle E \rangle$	$0.57 \pm 0.02\%$	$0.51 \pm 0.02\%$
$\sigma / \langle E \rangle$ (C-wheel)	$0.58 \pm 0.02\%$	$0.62 \pm 0.02\%$

Table 4.9: Deviation from uniformity for ECC0 and ECC1. The  $\phi$ -asymmetry is corrected using capacitance measured at stacking frame for ECC0 and test beam data for ECC1 in the first raw and using capacitance measured in the wheel in the second raw.

An interesting analysis is how much each correction improves the uniformity. Before any correction is applied, the non-uniformity is around 4%. When the high voltage is corrected, the non-uniformity value is around 0.8% and finally the capacitance correction gives the final results. The effects in non-uniformity of the cluster level corrections (that is, lateral leakage and  $\phi$ -modulation corrections) are negligible. They basically improve the energy resolution.





# Chapter 5

## Dependence on signal reconstruction

In the previous analysis the LAPP method for the signal reconstruction has been used, which provides a description of the pulse shape at a level of better than 1%. We want to know if this level of description is enough for the uniformity studies and also which level can we tolerate in order to leave the uniformity unaffected. To study these subjects we have developed three methods to reconstruct the signal of ECC1 cells with different levels of descriptions [63]. In what follows we will refer to these methods as Hec, Hecref and Hecref2 $\omega$ . The level of signal description will be  $\pm 4.2\%$ ,  $\pm 1.3\%$  and  $\pm 0.8\%$  respectively. The name Hec comes from HEC calorimeter, since method Hec is a modification of the one developed by L. Kurchaninov to analyse the test beam data of the HEC calorimeter modules [70]. Hence, in what follows we will refer to Hec, Hecref and Hecref2 $\omega$  as HEC family methods.

The procedure to cancel out the common part of the readout circuit in the Laplace frequency space is the same for HEC's methods as for LAPP, already described in section 4.3.2. As we have studied in the previous chapter, there is a common part associated to the readout circuit for the calibration and physics signals, which can cancel out, obtaining the following relation:

$$\hat{g}_p(s) = \hat{B}(s)\hat{g}_c(s)$$

where

$$\hat{B}(s) = \frac{\hat{H}_p(s) I_p(s)}{\hat{H}_c(s) I_c(s)}$$

In more detail:

$$\hat{B}(s) = \frac{\omega^2}{s^2 + \omega^2} \frac{\hat{I}_p(0) \left( \frac{e^{-\tau_d s} - 1}{\tau_d^2 s^2} + \frac{1}{\tau_d s} \right)}{\hat{I}_c(0) \left( \frac{\tau_c(1-f)}{1+\tau_c s} + \frac{f}{s} \right)}$$

In HEC family methods, the way to obtain the physics pulse prediction  $g_p(t)$  in the time domain differs from the LAPP method:

- In the LAPP method, the function  $\hat{B}(s)$  is discretized in the frequency domain of the Fourier transform  $\tilde{B}(\nu)$  and afterwards the physics pulse  $g_p(t)$  in the time domain is predicted by applying the inverse Fourier transform using a Fast Fourier Transform numerical algorithm (see section 4.3.3).
- In the HEC's methods, an exact analytic inverse Laplace transform<sup>1</sup> of  $\hat{B}(s)$  (using some informatic program as *MATHEMATICA*) is done obtaining  $B(t)$ . After that, the following integral in the time domain is computed numerically in order to get  $g_p(t)$ , namely:

$$g_p(t) = \int_0^t B(t-t')g_c(t')dt'$$

where  $g_c(t)$  is constructed with the delay runs, subtracting DAC=0.

In order to complete the computation of  $g_p(t)$ , the knowledge of the parameters set is required. To obtain the unknown parameters of the circuit (the frequency  $\omega = \frac{1}{\sqrt{L_d C_d}}$  and the starting time of the calibration and physics signals, basically) two families of methods have been studied by different groups:

1. Methods that fit the predicted physics pulse  $g_p(t)$  to the physics wave form,  $g_d(t)$ , measured at the beam test.

LAPP and HEC methods belong to this family. In summary, the main differences between the HEC family and LAPP methods are the numerical treatment applied to obtain  $g_p(t)$  (in LAPP an inverse FFT is done whereas in HEC method an exact inverse Laplace transform plus numerical convolution is applied), and the kind of second order effects like reflections, additional resistors, etc, which are taken into account.

---

<sup>1</sup>In these method no regularization of divergences needs to be applied in contrast to the LAPP method that discretizes in the frequency domain.

2. Methods that use calibration pulses  $g_c(t)$  only (and therefore do not need the test beam data).

To the second family belong two methods from Milano group [54], namely FAM and RTM. In these methods parameters (and therefore the ionization signal prediction  $g_p(t)$ ) are directly retrieved from the calibration pulse analysis. The calibration of the detector is then completely self-consistent, since it does not rely on the acquisition of ionization signal events.

The RTM (*Response Transformation Method*) method bases its strategy to retrieve the parameters needed to complete the ionization signal prediction on the computation and analysis of what would be the response of the whole system (detector cell plus readout chain) to a signal different from the standard "exponential" calibration pulse. The system response can in fact be sensitive to a particular injected waveform, the output showing in some case easily recognizable characteristics. The  $f$  and  $\tau_c$  parameters can be obtained computing the response of the system to a step function, whereas to get the  $\omega$  parameter a monochrome cosine pulse is injected.

In the FAM (*Frequency Analysis Method*) method the parameter  $\omega$  can be extracted from a frequency analysis of the calibration signal emerging from the shaper, in such a way the transfer function of the detector has a minimum at the frequency  $\omega = \frac{1}{\sqrt{L_d C_d}}$ . The parameter  $\tau_c$  is extracted by fitting the log of calibration signal tail. A good agreement between both methods is obtained.

To use this technique, long delay runs are necessary. With the use of these runs, calibration signals have been acquired using 32 samples per event, so that the pulse shape has a resulting length of 800 ns, obtaining a precise analysis of the calibration signal shape. These runs have been taken only for the barrel electromagnetic calorimeter, but not for the end-cap, during the beam tests. Therefore, unfortunately, we can not use this method for the end-cap modules.

In this chapter we have developed methods in which the unknown parameters are obtained by fitting the predicted physics pulse  $g_p(t)$  to the test beam measured physics pulse,  $g_d(t)$ .

## 5.1 Method Hec

This method is the simplest realization of the HEC family procedures. The first one using this procedure was L. Kurchaninov to analyze test beam data of the HEC calorimeter modules [70].

An analytic inversion of the Laplace transform is applied to  $\hat{B}(s)$  in order to obtain  $B(t)$

in the time domain. Afterwards, the predicted physics pulse,  $g_p(t)$ , is obtained from the convolution

$$g_p(t) = \int_0^t B(t-t')g_c(t')dt'$$

The predicted  $g_p(t)$  is compared with the measured physics pulse  $g_d(t)$  corresponding to 120 GeV electrons. The fit of  $g_p$  to  $g_d$  allows to determine the unknown parameters in these expressions. This procedure is repeated for every cell of the calorimeter.

The parameters which take part in this analysis are the following:

### 1. Fixed parameters

- Parameter  $f$  of the calibration board (see section 4.3.3). The value of  $f$  for EMBarrel modules was obtained from the 32 samples data in the H8 test beam period [54]. Unfortunately, these long delay runs were not taken in the EMEC test beam. One should not expect great differences since the calibration boards were the same for EMBarrel and for EMEC tests. Therefore, in this analysis, we have taken as  $f$  the mean of the values obtained for the EMBarrel modules. This value is  $f = 0.069$  [55].
- $\tau_c$ , the characteristic decay time of the exponentially decreasing current generated by the calibration board. Again, we have chosen the mean of the values from the EMBarrel modules, being  $\tau_c = 333.8 \text{ ns}$  [55].
- $\tau_d$ , the drift time. Its value was obtained from measurements on the calorimeter prototype Module 0. The values of  $\tau_d$  depend on  $\eta$  because of the cell size and the gap variation with  $\eta$  of the EMEC modules. Figure 5.1 shows the  $\tau_d$  dependence on  $\eta$  for front, middle and back cells.

### 2. Free parameters

- Frequency  $\omega = \sqrt{\frac{1}{L_d C_d}}$ . The values of the  $\omega$  obtained from the fit of  $g_p$  to  $g_d$  are close to measurements performed using the network analyzer (figure 5.2). Typical values are 0.35 GHz for the front sampling, 0.18-0.25 GHz for middle and 0.13 GHz for the back sampling.
- Starting times of the calibration  $t_c^0$  and physics pulse  $t_p^0$ . The obtained values are about 5 ns for  $t_c^0$  and 15 ns for  $t_p^0$ .

The quality of the prediction for  $g_p(t)$  can be seen in figure 5.3. We define the residual as the relative difference between the prediction and the data histograms normalized to prediction peak, namely:

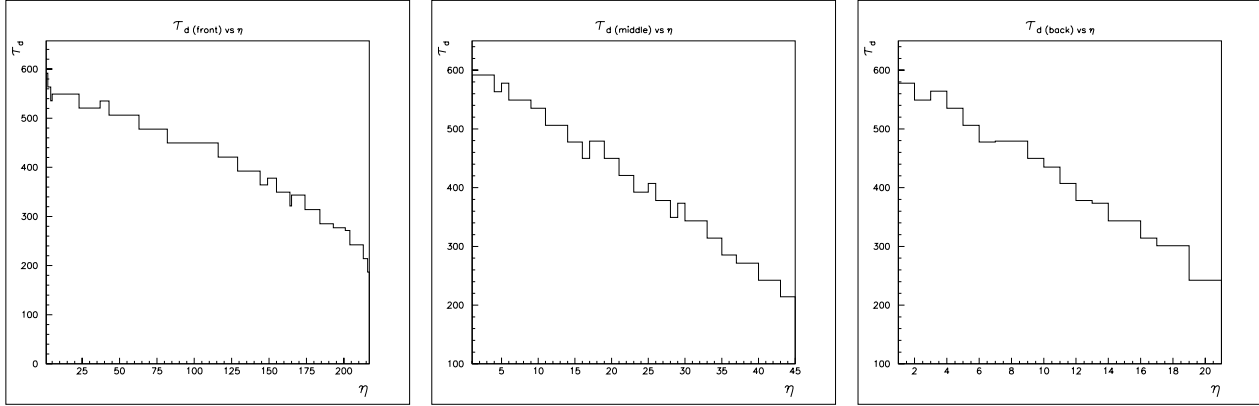


Figure 5.1: Drift time  $\tau_d$  dependence on  $\eta_{cell}$  for front, middle and back cells.

$$r^{(i)} = \frac{g_p^{(i)} - g_d^{(i)}}{\max(g_p^{(i)})} \quad i = 1, \dots, nbins$$

To avoid the lack of statistics of one run, several runs of a  $\phi$ -scan are combined to obtain an average residual. This residual is shown in figure 5.4, where the full line corresponds to method Hec. The maximum value for the residual ( $r_{max}$ ) is about 4.2%, which unfortunately is reached at the signal peak.

## 5.2 Method Hecref

In order to improve the description of  $g_d(t)$  we have designed a new method, which takes into account reflections in the calibration and signal lines. The predicted physics pulse shape is obtained from the following integral:

$$g_p(t) = \int_0^t (B(t-t') + K_r B(t-t'-t_r)) g_c(t') dt'$$

Notice that method Hecref becomes method Hec if  $K_r = 0$ . Two additional free parameters are introduced:

- $K_r$ , the amplitude of the reflection. The value obtained from the fit to the measured pulse  $g_d(t)$  is about 0.09 for a typical middle cell.

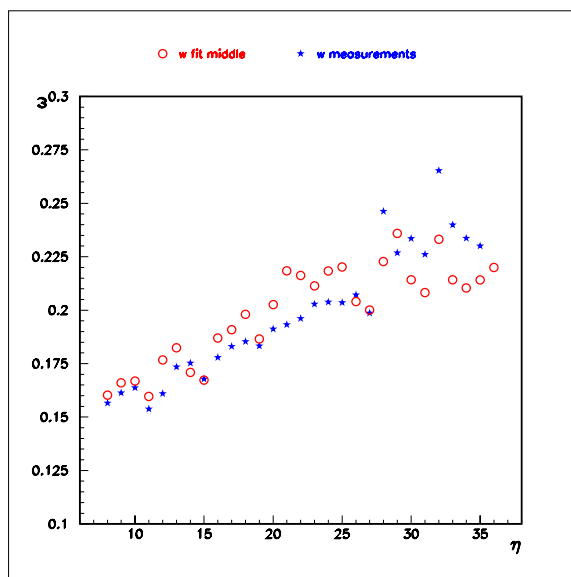


Figure 5.2: Comparison of frequency (GHz) obtained from a fit to test beam data using Hec method (red circles) and direct measurements (blue stars), for a given  $\phi_{cell}$  middle cell, as a function of  $\eta_{cell}$ . The measurements were performed on the ECC wheel using a network analyzer device.

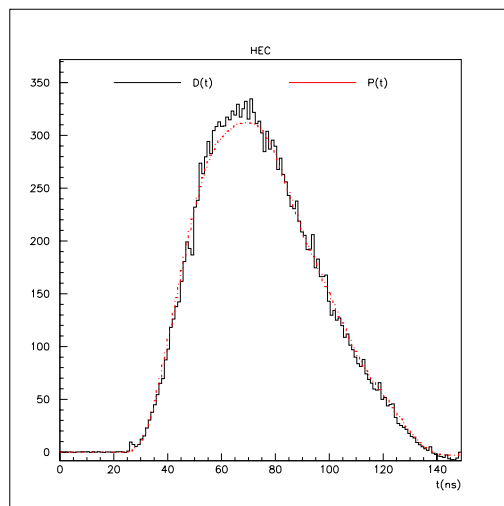


Figure 5.3: Comparison between predicted pulse using the Hec method (red line) and measured physics pulse (dark line), both in GeV, for 120 GeV electrons of the ECC1 beam test, for a middle cell ( $\eta_{cell} = 28$  and  $\phi_{cell} = 19$ ).

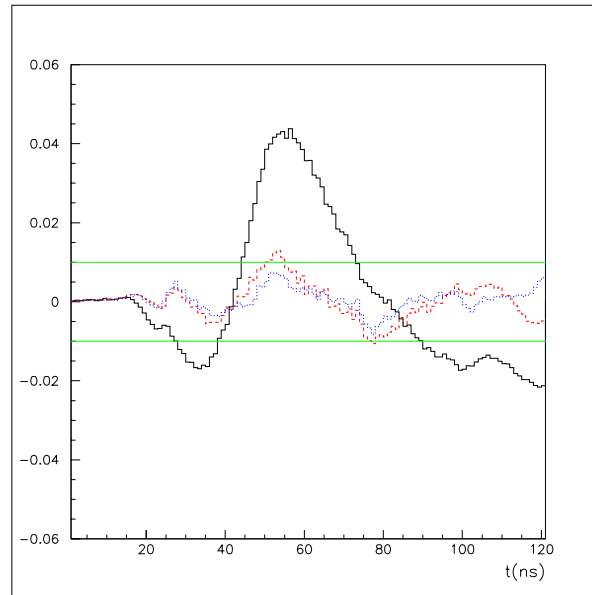


Figure 5.4: Residual  $r^{(i)}$  of middle cells for the three signal reconstruction methods Hec (black full line), Hecref (red dashed line) and Hecref2 $\omega$  (blue dotted line).

- $t_r$ , the delay of the reflection. The fit gives values about 20 ns for a typical middle cell.

The reasonable values of these parameters lead to think there can be reflections on the readout line for the data. The remaining free parameters have similar values than those obtained using Hec method. Figure 5.5 shows a comparison between the  $\omega$  obtained from this fit and measurements performed on the ECC wheel using a network analyzer device. The values of  $\omega$  correspond to middle cells of a  $\eta$ -scan. There is a good agreement for all cells what confirms the modeling of the circuit in the Hecref method. Therefore we can use the values of the  $LC$  measurements in the method instead of fitting the test beam data. This is important to predict the physics shape  $g_p$  for modules that did not pass through a beam test. We also notice that the agreement is worse using Hec method (see figure 5.2).

With the introduction of reflection we have obtained a better physics pulse shape reconstruction (see figure 5.6) than the reconstruction using the Hec method. The maximum residual  $r_{max}$  is at the level of 1.3% for middle cells of the ECC1 module (see dashed line of figure 5.4).



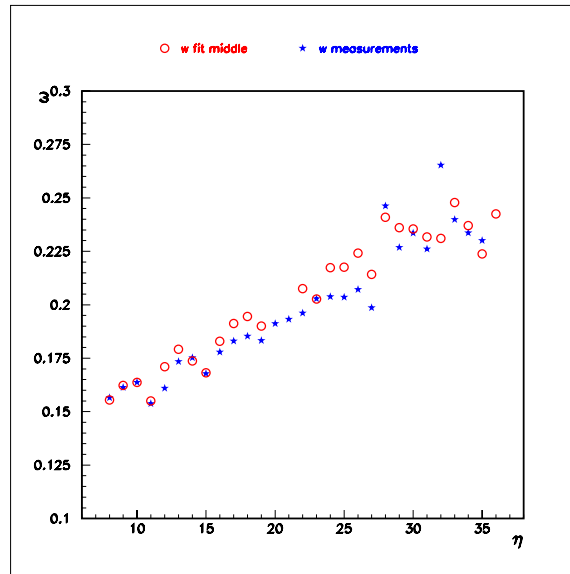


Figure 5.5: Comparison of frequency (GHz) obtained from a fit to test beam data using Hecref method (red circles) and direct measurements (blue stars), for a given  $\phi_{cell}$  middle cell, as a function of  $\eta_{cell}$ . The measurements were performed on the ECC wheel using a network analyzer device.

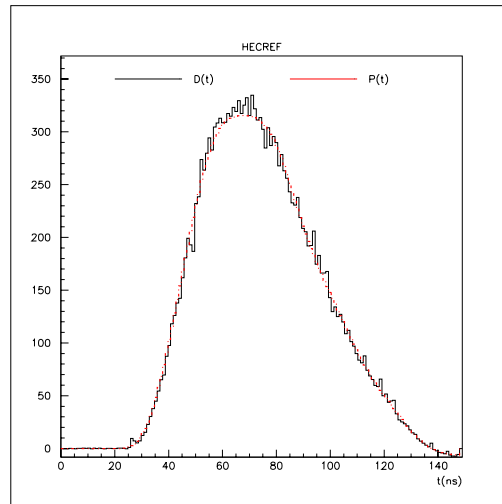


Figure 5.6: Comparison between predicted pulse using the Hecref method (red line) and measured physics pulse (dark line), both in GeV, for 120 GeV electrons of the ECC1 beam test, for a middle cell ( $\eta_{cell} = 28$  and  $\phi_{cell} = 19$ ).

### 5.3 Method Hecref2 $\omega$

In the former methods an oscillation on residuals were observed, which indicates the existence of an additional frequency not taken into account before. The method Hecref2 $\omega$  is like method Hecref but adding a parasitic LC in the readout circuit. This is considered by adding a second frequency  $\omega_2$  to the function  $\hat{B}(s)$ , that is adding the following  $\hat{B}_2(s)$  function:

$$\hat{B}_2(s) = \frac{\omega_2^2}{s^2 + \omega_2^2} \frac{\hat{I}_p(s)}{\hat{I}_c(s)}$$

where  $\omega_2 < \omega$ .

The predicted physics pulse includes the reflection as well:

$$g_p(t) = \int_0^t (B(t-t') + K_r B(t-t'-t_r) + K_2 B_2(t-t')) g_c(t') dt'$$

Notice that method Hecref2 $\omega$  becomes method Hecref if  $K_2 = 0$ . Two additional free parameters are now introduced:

- $\omega_2$ , the additional frequency, which typical values obtained from a fit to the measured pulse  $g_d(t)$  are about 0.12 GHz (that is  $0.5-0.7 \times \omega$ ) for middle cells.
- $K_2$ , the normalization constant of this additional term. Their values obtained from the fit are about 0.08 for middle cells.

The remaining free parameters ( $\omega$ ,  $K_r$ ,  $t_r$ ) values are also obtained from the fit and keep similar values as method Hecref, namely 0.18-0.25 GHz, 0.09 and 20 ns respectively.

The quality of the prediction for  $g_p(t)$  using the Hecref2 $\omega$  method can be seen in figure 5.7. The maximum residual  $r_{max}$  is at the level of 0.8% for middle cells (see dotted line of figure 5.4).

### 5.4 Several modifications

In order to improve the physics signal shape reconstruction, we have analyzed several effects:

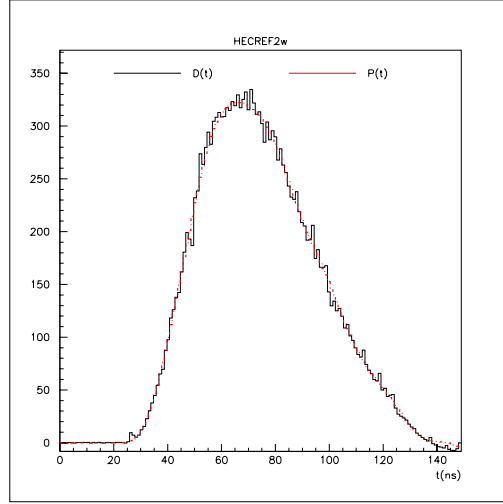


Figure 5.7: Comparison between predicted pulse using the Hecref2 $\omega$  method (red line) and measured physics pulse (dark line), both in GeV, for 120 GeV electrons of the ECC1 beam test, for a middle cell ( $\eta_{cell} = 28$  and  $\phi_{cell} = 19$ ).

- Skin effect: One difference between the path for the calibration pulse and for the ionization pulse is that the calibration pulse must travel over a cable of about 4 m in length to reach the mother board. So, a correction for the distortion in the cable must be made. The skin effect produces an attenuation proportional to  $e^{-\sqrt{t_{se}\omega}}$ , which gives rise to an error-function type integral in the time domain. The  $t_{se}$  value is given by the cable parameters as:

$$t_{se} = \frac{\mu}{32 \pi^2 \sigma Z_0^2} \left(\frac{l}{a}\right)^2$$

where  $\mu$  is the magnetic permeability,  $\sigma$  is the copper conductivity,  $Z_0$  the characteristic cable impedance,  $l$  the cable length and  $a$  is the radius of the inner conductor. Since our frequency is limited to approximately 20 MHz and  $t_{se}$  is less than 300 ps, the exponential can be approximated using Taylor series to:

$$e^{\sqrt{t_{se}s}} = 1 + \sqrt{t_{se}s} + \frac{t_{se}s}{2} + \frac{(t_{se}s)^{\frac{3}{2}}}{6} + \dots$$

The first term leads to a Dirac delta, while the third, proportional to  $s$ , produces a time shift. The second and fourth terms are responsible for the actual change in shape of the waveform due to the skin effect.

$$\sqrt{t_{se}s} + \frac{(t_{se}s)^{\frac{3}{2}}}{6} = \sqrt{t_{se}s} \left(1 + \frac{st_{se}}{6}\right) \approx \sqrt{t_{se}s} \frac{st_{se}}{6}$$

We calculate the correction by multiplying this expression by the waveform in frequency space. A significant improvement on the residuals was not found when we took into account the skin effect.

- A model with more than one reflections has been used to compute another analytical formula, but the fit converges hardly, due to the number of unknown parameters of the electrical path, left free in the fit. We have observed a negligible contribution.
- We can also take into account that the injected triangular current has an initial increasing slope. So, the injected current would be:

$$I_p(t) = I_p^0 Y(t - t_1) Y(\tau_d - t) \left(1 - \frac{t}{\tau_d}\right) + I_p^0 Y(t_1 - t) \frac{t}{t_1}$$

where  $t_1$  is the time of the increase. The inclusion of this effect does not lead to a visible improvement in the prediction.

- Finally, a small resistor can be added in series to  $L$  to deal with a resistive component of the paths. This resistor enters into the  $B(s)$  function as a frequency  $1/(rC)$  in a similar manner as  $1/\sqrt{LC}$ . It is likely that the second frequency introduced in method Hecref2 $\omega$  has its origin on that resistor, at least partially.

## 5.5 TDC dependence of the cluster energy

Related to the description of the pulse shape is the dependence of the cluster energy on the arrival of the beam particle or TDC trigger time. We will refer to it as TDC dependence of the cluster energy. In figures 5.8 and 5.9 the cluster energy is represented as a function of this TDC time for one middle cell and for the four signal reconstruction methods (Hec, Hecref, Hecref2 $\omega$  and LAPP). The cluster energy has an observable time dependence for the method Hec, while this dependence is negligible for methods Hecref2 $\omega$  and LAPP. Therefore the TDC dependence of the cluster energy decreases with the residual  $r_{max}$ . This can be explained by the fact that the maximum of the predicted physics signal has a bias when  $r_{max}$  is large. Hence the optimal filtering coefficients, obtained from that shape, produce a wrong value for the maximum of the signal when multiplying by the data samples. This depends on the data samples taken, hence on the TDC, for some sets the reconstruction of the maximum is more accurate than for others.

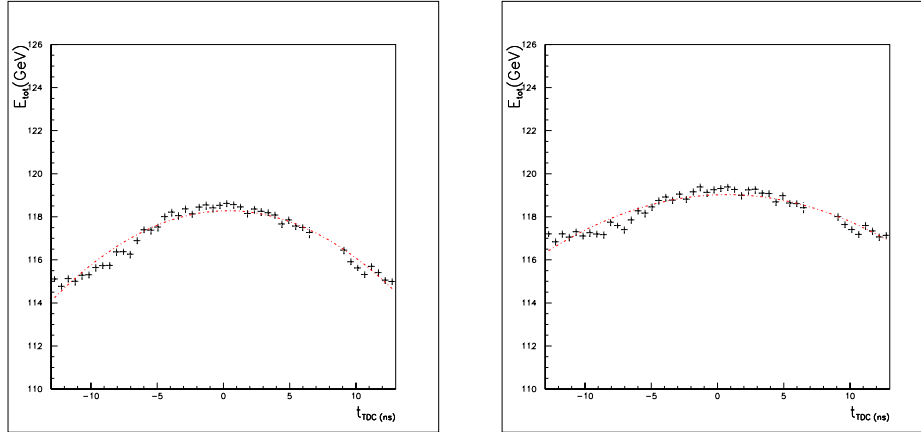


Figure 5.8: Cluster energy as a function of the TDC time using signal reconstruction method Hec (left) and method Hecref (right). The red line represents a parabolic fit.

This dependence can be parametrized by a second degree polynomial. The curvature  $C_t$  of this polynomial is given as a function of the signal reconstruction method in table 5.1. The curvature  $C_t$  decreases with the residual  $r_{max}$ . For the sake of comparison, the curvature for the parabola method is also shown in table 5.1 (see figure 5.10). In contrast to the OF-based methods, the residual  $r_{max}$  for the parabola method cannot be obtained in the whole range of 125 ns, but only in 75 ns around the maximum of the signal, since it uses the 3 samples of highest amplitude to fit a parabola. We have observed that  $C_t$  is slightly smaller for LAPP than for Hecref2 $\omega$ . This may be explained by the fact that the  $r^{(i)}$  around the peak is smaller for LAPP than for Hecref2 $\omega$ .

Method	$C_t$	$r_{max}$
Parabola	3.0%	5.0%
Hec	2.0%	4.2%
Hecref	1.5%	1.3%
Hecref2 $\omega$	1.3%	0.8%
LAPP	1.1%	0.8%

Table 5.1: Deviation from horizontal of TDC dependence of the cluster energy for the different signal reconstruction methods. For the parabola method only 75 ns around the signal maximum are used to obtain  $r_{max}$ . For the OF-based methods the whole range, 125 ns, is used to obtain  $r_{max}$ .

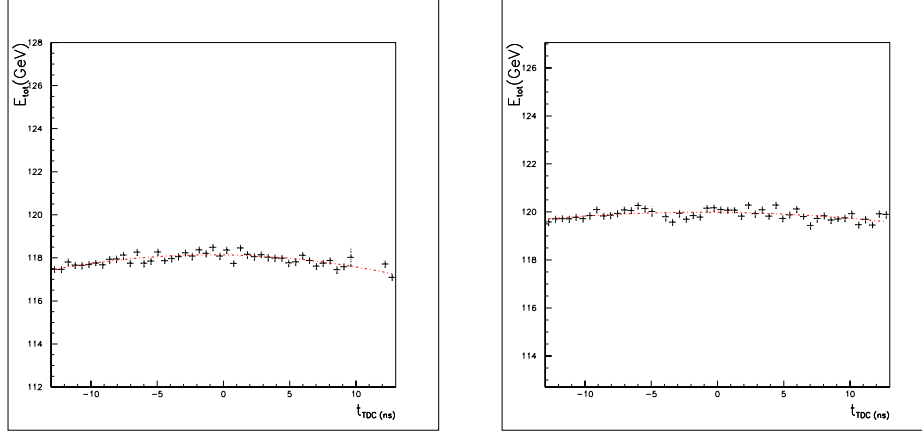


Figure 5.9: Cluster energy as a function of the TDC time using signal reconstruction method Hecref2 $\omega$  (left) and method LAPP (right). The red line represents a parabolic fit.

## 5.6 Uniformity dependence

We want to analyze if the uniformity depends on the signal reconstruction level. For that, we have studied the spatial non-uniformity for ECC1 module in two directions,  $\eta$  and  $\phi$ , for each signal reconstruction method. As we have seen in chapter four, several corrections must be applied to reconstruct the true energy of the electrons, namely, high voltage, lateral leakage,  $\phi$ -modulation and capacitance correction. For the last correction, as we did in the last chapter, we have used a correction extracted from the  $\phi$ -dependence of the energy averaged over  $\eta$  for this analysis. The four signal reconstruction methods show a similar behaviour for all corrections.

Table 5.2 shows the ECC1 non-uniformity for the different signal reconstruction methods. These values are obtained representing the distribution of the mean energy as an histogram for each module. The ratio  $\sigma / \langle E \rangle$  gives the non-uniformity value for each method. The non-uniformities for  $\eta$  and  $\phi$  scans are given as well. These are computed as follows. For a given  $\eta$  scan ( $\phi$  is kept constant at  $\phi_k$ ) we determine the quantity

$$\Delta E_{\eta_i}^{(\phi_k)} = \frac{(E(\eta_i, \phi_k) - E_m^{(\phi_k)})}{E_m^{(\phi_k)}} \quad \eta_i = 1, \dots, n_\phi$$

where  $n_\phi$  is the number of points of the scan and  $E_m^{(\phi_k)} = \frac{1}{n_\phi} \sum_{\eta_i}^{n_\phi} E(\eta_i, \phi_k)$  is the mean energy for each  $\eta$  scan. This process is repeated for all  $\eta$  scan (for all  $\phi$  values) and the quantities  $\Delta E_{\eta_i}^{(\phi_k)}$  are histogrammed. If  $n_{scans}$  is the number of  $\eta$  scans, the number of

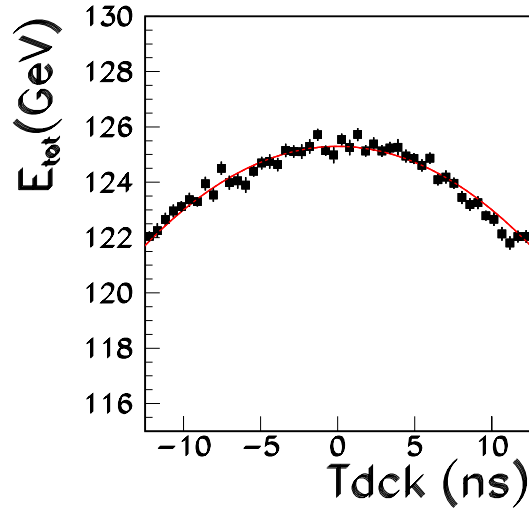


Figure 5.10: Cluster energy as a function of the TDC time using signal reconstruction method of parabola.

entries on this histogram will be  $n_{scans} \times n_{\phi}$ . From a Gaussian fit to this distribution the non-uniformity along the  $\eta$  direction,  $\sigma_{\eta}/\langle E \rangle$ , is obtained. A similar procedure is followed to obtain  $\sigma_{\phi}/\langle E \rangle$  from the  $\phi$  scans.

As we can see in table 5.2, the four methods give similar results for the ECC1 non-uniformity irrespective of the residual, keeping  $r_{max} \leq 4.2\%$ . This means that we could even use method Hec to obtain the non-uniformity of the modules. Similar conclusion is inferred for the non-uniformities  $\sigma_{\eta}$  and  $\sigma_{\phi}$ .

Method	$r_{max}$	$\sigma/\langle E \rangle$	$\sigma_{\eta}/\langle E \rangle$	$\sigma_{\phi}/\langle E \rangle$
Hec	4.2%	$0.58 \pm 0.04\%$	$0.54 \pm 0.03\%$	$0.47 \pm 0.03\%$
Hecref	1.3%	$0.54 \pm 0.05\%$	$0.51 \pm 0.02\%$	$0.43 \pm 0.03\%$
Hecref2 $\omega$	0.8%	$0.59 \pm 0.05\%$	$0.54 \pm 0.03\%$	$0.46 \pm 0.03\%$
LAPP	0.8%	$0.51 \pm 0.02\%$	$0.49 \pm 0.02\%$	$0.43 \pm 0.02\%$

Table 5.2: Deviation from uniformity for ECC1 as a function of the signal reconstructed method.

# Chapter 6

## Conclusions

Throughout this thesis, a detailed analysis of the electromagnetic end-cap calorimeter of ATLAS is done. In chapter 3 we have described in depth the stacking procedure of each module. All the steps were done with very accuracy in order to improve the uniformity of the calorimeter.

Chapter 4 has been devoted to an analysis of the test beam data on the uniformity of the three ECC modules. The modules are denoted as ECC0, ECC1 and ECC5. Only results for outer wheel are quoted. We have studied the calorimeter response, using the so called LAPP method to reconstruct the signal amplitude. Several corrections have been applied in order to reconstruct the electron response. For the High Voltage correction, we have used two different methods, leading both to similar results. We have corrected the  $\phi$ -modulation using a Fourier polynomial, whereas a parabolic fit corrects the lateral leakage. An unexpected non-uniformity along the  $\phi$  direction was observed. This effect can be corrected with the capacitance measurements. For ECC0, we have used the capacitance measured at the stacking frame, and for ECC1 the test beam data itself (average response). Since the gap to gap fluctuations are found to be small for ECC5, only the global slope has been corrected using the test beam data for this module. In summary, signal corrections are found to be independent of the module except for the above capacitance correction.

A cell to cell non-uniformity below 0.6% is found for the three modules, which is in accordance with the goal stated in the Technical Design Report. The results are in good agreement with an independent analysis done at CPPM. A slight anisotropy on the non-uniformity along the two orthogonal directions  $\eta$  and  $\phi$  is observed, that is due to the crack regions at low and high  $\eta$  and the quality of the capacitance correction. Additionally, we have seen that the capacitance correction using the C-measurements performed on the ECC wheel at  $\eta_{cell} = 39$  gives results which are still at the limit of tolerance.



The dependence of the uniformity on the signal reconstruction method has been shown in chapter 5. We have developed three additional methods which use time convolution to predict the physics pulse shape. The uniformity obtained by using them is found to be very similar. We have also seen that the TDC dependence of the cluster energy decreases with the residual  $r_{max}$ .

# Appendix A

## Calculation of parameter $\alpha$

We have seen the relation between energy and gap thickness, given by:

$$E \sim \frac{f_s}{g} \left(\frac{U}{g}\right)^b$$

where  $f_s$  is the sampling fraction,  $U$  is the HV applied in the gap,  $g$  is the liquid Argon thickness and  $b$  is approximately 0.4 according to measurements performed in module 0 [27].

Since the high voltage is constant in each sector, we can obtain:

$$\frac{\Delta E}{E} \sim \frac{\Delta f_{samp}}{f_{samp}} - (b + 1) \frac{\Delta g}{g}$$

We can express the relative variation of the gap  $g$  as a function of  $\eta$ . From the figure A.1 we can obtain:

$$g \sim r\phi$$

$$r \sim R\theta$$

and therefore

$$\frac{\Delta g}{g} \sim \frac{\Delta r}{r}$$

$$\frac{\Delta r}{r} \sim \frac{\Delta \theta}{\theta}$$

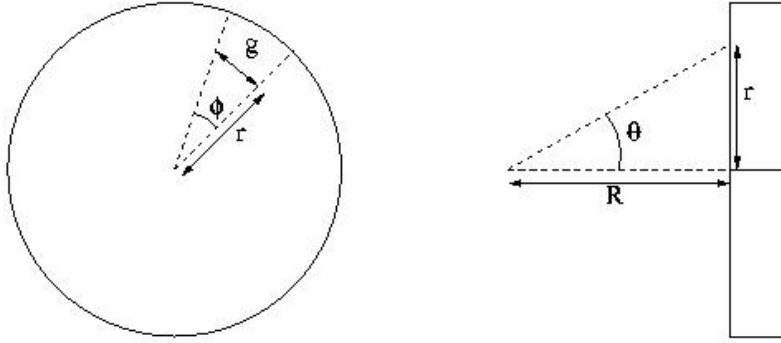


Figure A.1: Description of the parameters used for the calculation of  $\alpha$ : front (left picture) and profile (right picture) view of the wheel.

Moreover, we have

$$\eta = -\ln \left| \tan\left(\frac{\theta}{2}\right) \right| \sim -\ln \left| \frac{\theta}{2} \right|$$

and, from the last expressions, we get

$$\Delta\eta \sim -\frac{\Delta\theta}{\theta} \sim -\frac{\Delta r}{r} \sim -\frac{\Delta g}{g}$$

After a simple computation [71] the following expression can be obtained:

$$\frac{\Delta f_{samp}}{f_{samp}} \sim (1 - f_{samp}) \frac{\Delta g}{g}$$

Finally, with all the previous equations, we can find, at first order

$$\frac{\Delta E}{E} \sim \frac{\Delta f_{samp}}{f_{samp}} - (b + 1) \frac{\Delta g}{g} \sim (b + f_{samp}) \Delta\eta$$

Comparing with

$$E^{HV-corr} = E \frac{\beta^{(s)}}{(1 + \alpha^{(s)} (\eta_j - \eta_c^{(s)}))}$$

we obtain that, at first order,  $\alpha \sim b + f_{samp}$ .

# Appendix B

## Resumen en español

A continuación se adjunta un resumen en español de esta tesis.

### B.1 LHC y el proyecto ATLAS

#### B.1.1 Introducción

El Modelo Estándar ( $SM$ ) [1] proporciona en la actualidad la única descripción matemática consistente de las partículas fundamentales y de sus interacciones. Está basado en el grupo *gauge*  $SU(3) \times SU(2)_L \times U(1)$ , que incorpora tres interacciones fundamentales: la electrodinámica cuántica,  $QED$ , que describe las interacciones electromagnéticas, el modelo *Glashow-Weinberg-Salam*, que combina  $QED$  con una descripción de la interacción nuclear débil, y por último, la cromodinámica cuántica,  $QCD$ , la cual describe la interacción nuclear fuerte. Actualmente todavía no se ha incluido una descripción satisfactoria de la gravitación.

Hay dos tipos de partículas en el  $SM$ : los *fermiones*, partículas con espín 1/2 que constituyen toda la materia y que obedecen la ecuación de *Dirac* y los *bosones gauge*, partículas de espín entero que satisfacen la ecuación de *Klein-Gordon*. Los fermiones están a su vez divididos en dos grupos, los *quarks* y los *leptones*. Los leptones son sensibles a las interacciones débil y electromagnética, mientras que los quarks son adicionalmente sensibles a la interacción fuerte.

Los fermiones del modelo estándar interactúan con otros fermiones mediante el intercambio de *bosones gauge*. De este modo la interacción electromagnética está asociada a una partícula sin masa, el fotón, la interacción fuerte está asociada a los gluones, mientras

que la interacción débil ocurre mediante el intercambio de dos bosones pesados,  $Z^0$  y  $W^\pm$ . La partícula supuestamente asociada a la gravedad, el gravitón, no ha sido encontrada experimentalmente.

En el modelo estándar todas las partículas adquieren masa a través del mecanismo de Higgs [5], dentro del cual es importante el concepto de la ruptura espontánea de simetría. Esta implica que el lagrangiano del sistema mantiene su invarianza bajo una simetría, mientras que el vacío (estado de menor energía del sistema) no exhibe esta invarianza. Aplicando este mecanismo al modelo estándar se consigue dar masa tanto a los bosones de gauge como a los fermiones. Además existe un estado físico asociado con el campo de Higgs: el bosón Higgs. El mecanismo de Higgs no predice su masa, pero podemos limitarla a partir de cálculos teóricos. Así, por ejemplo, teorías de trivialidad dan un límite superior de la masa del Higgs alrededor de  $860 \text{ GeV}$ , mientras que argumentos de estabilidad del vacío dan un límite inferior aproximadamente de  $132 \text{ GeV}$ . Experimentalmente, el límite inferior más estricto proviene del LEP II y está alrededor de  $115 \text{ GeV}$ . De hecho la búsqueda del bosón de Higgs es el primer objetivo de la investigación que se realizará en el LHC, cuyo funcionamiento empezará el verano del 2007 en el CERN.

### B.1.2 El LHC

El acelerador de partículas LHC (*Large Hadron Collider*) está siendo actualmente construido en el túnel del antiguo acelerador LEP en el "Centre Européen de Physique Nucléaire", (CERN), en Ginebra, Suiza. En él se producirán colisiones protón-protón con una energía en el centro de masas de  $14 \text{ TeV}$ .

La aceleración de los protones y su acumulación en paquetes densos se realizará en cinco etapas, aprovechándose la cadena de aceleradores existentes en el CERN: el *LINAC2* acelerará los protones hasta  $50 \text{ MeV}$ , seguidamente el *BOOSTER* hasta  $1 \text{ GeV}$ , el *PS* hasta  $26 \text{ GeV}$  y el *SPS* hasta  $450 \text{ GeV}$ . Finalmente los protones se acelerarán hasta  $7 \text{ TeV}$  en el *LHC* (ver figura 1.5). Con el fin de mantener los haces de protones de  $7 \text{ TeV}$  alrededor de la circunferencia de  $27 \text{ km}$  se necesitan campos magnéticos extremadamente grandes ( $8.36 \text{ T}$ ).

Las colisiones de paquetes de protones tendrán lugar cada  $25 \text{ ns}$  a baja luminosidad ( $\mathcal{L}_0/10$ ) durante los tres primeros años y luego a alta luminosidad ( $\mathcal{L}_0 = 10^{34} \text{ cm}^{-2} \cdot \text{s}^{-1}$ ). Los paquetes tendrán una longitud de unos centímetros y una anchura de unas pocas micras. Cada uno de ellos contendrán  $1.05 \cdot 10^{11}$  protones y estarán separados espacialmente por  $7.5 \text{ metros}$ . Con estas características, se esperan alrededor de unas  $20$  interacciones en promedio por cada cruce, operando a alta luminosidad.

Se han elegido cuatro puntos para que interaccionen los protones de los paquetes, en los cuales se situarán cuatro experimentos de física: *ATLAS*, *CMS* (estos dos experimentos cubrirán todo tipo de física protón-protón), *LHC-b* (experimento que estudiará la física del quark  $b$ ) y *ALICE* (experimento sobre iones pesados).

Entre la amplia variedad de estudios físicos que se van a realizar en el LHC cabe destacar la búsqueda del bosón de Higgs. Para detectar el Higgs existen diversos canales de desintegración dependiendo de la masa de dicha partícula. En el rango  $m_Z < m_H < 2m_Z$  el canal dominante es la desintegración  $H \rightarrow b\bar{b}$ . Sin embargo, el nivel de fondo procedente de procesos de QCD imposibilita su uso. Así pues, el canal usado en este rango de masas es la desintegración del Higgs a dos fotones, lo cual requiere una excelente resolución energética en los calorímetros. Para el caso de Higgs más pesado,  $2m_Z < m_H \leq 700 \text{ GeV}$ , la desintegración ocurre mayoritariamente a través del proceso  $H \rightarrow ZZ \rightarrow l^+l^-l^+l^-$ , con  $l = e, \mu$ . Finalmente, para un rango mayor de masas,  $m_H \geq 700 \text{ GeV}$ , los únicos modos posibles de detección son  $H \rightarrow ZZ \rightarrow ll\nu\nu, H \rightarrow ZZ^* \rightarrow lljet - jet, H \rightarrow WW \rightarrow l\nu jet - jet$ .

Aparte de la búsqueda del Higgs, se realizarán otros estudios como, por ejemplo, estudios de nueva física (supersimetría o extradimensiones), estudios electrodébiles, física de hadrones B y análisis de interacciones fuertes.

### B.1.3 El detector ATLAS

ATLAS (A Toroidal LHC ApparatuS) [10] es uno de los cuatro experimentos del LHC. Tiene la forma de un cilindro de aproximadamente 44 metros de longitud y 22 metros de diámetro, centrado en el eje de los haces del LHC y colocado alrededor del punto de interacción. Se puede subdividir el detector en tres grandes grupos de subdetectores y dos grandes imanes.

El detector interno [11], situado en la parte más cercana al punto de interacción, permite determinar con gran precisión las trayectorias de las partículas cargadas y así determinar, entre otras cosas, la posición del punto de colisión. Además se le añade un cierto poder de identificación de electrones en el llamado detector de radiación de transición. Cubre la zona de pseudo-rapidez  $|\eta| < 2.5$  dedicada a las medidas de alta precisión.

El calorímetro electromagnético [12] permite medir la energía de los electrones (o positrones) y de los fotones. Se compone de dos semi-barriles cilíndricos centrados alrededor del eje del haz, y de dos tapones con forma de rueda que cubren el rango  $1.375 < |\eta| < 3.2$ . Gracias a su fina granularidad es capaz de separar los  $\gamma$  de los  $\pi^0$  (los cuales contribuyen al fondo del canal de desintegración del Higgs a dos fotones). Este subdetector, tema de esta tesis, se estudiará con detalle más adelante.

El calorímetro hadrónico permite identificar los chorros de partículas así como determinar

sus energías y direcciones. Junto con las secciones electromagnéticas este subdetector es fundamental para reconstruir la energía transversa perdida, clave para búsquedas supersimétricas. El calorímetro hadrónico cubre el rango  $1.5 < |\eta| < 3.2$ . Adicionalmente, para conseguir una buena hermeticidad, se usa un calorímetro delantero en el rango  $3.2 < |\eta| < 4.9$ .

Finalmente el espectrómetro de muones es muy importante para la búsqueda del Higgs en el canal de desintegración a cuatro leptones. Está constituido por un sistema de tres grandes imanes toroidales superconductores, detectores de trazas de precisión y un sistema de *trigger* potente.

Dado que en las colisiones protón-protón se produce un gran número de partículas (del orden de unos cuantos miles), es necesario un *trigger* [15] para distinguir los sucesos físicamente interesantes del fondo. En el experimento ATLAS se ha desarrollado un sistema *trigger* basado en tres niveles de selección. Cada nivel refina las decisiones previas, y cuando es necesario, aplica criterios adicionales. La tasa de sucesos interesantes pasa de 40 MHz a 100 Hz.

## B.2 Principios de detección de partículas

### B.2.1 Introducción

En este capítulo, vamos a repasar las interacciones básicas de las partículas con la materia, las cuales son la base de todos los detectores de partículas.

### B.2.2 Energía perdida por los partículas cargadas

Cuando los electrones o positrones atraviesan un bloque de materia pierden energía de dos maneras, cada una dominante en un rango de energía. A baja energía, la pérdida de energía ocurre básicamente por ionización mientras que a alta energía ocurre en su mayoría por radiación, proceso que solemos llamar también *bremstrahlung*.

La energía perdida por unidad de longitud debida a la ionización sigue la ley de Bethe-Bloch. Depende de la energía de la partícula incidente de tal modo que es proporcional a  $1/\beta^2$  (con  $\beta = v/c$ ) para valores bajos de  $\beta$ , alcanza un mínimo conocido como mínimo de ionización para valores medios de  $\beta$  y finalmente crece logarítmicamente hasta alcanzar un *plateau*.

La energía perdida por radiación se debe a colisiones con electrones atómicos. La sección eficaz es proporcional al cuadrado del número atómico del material atravesado (de ahí la elección de un material pasivo cuyo número atómico sea grande, como Fe, Cu o Pb). Los electrones y positrones son las partículas más afectadas por el fenómeno de *bremstrahlung*.

Existen en calorimetría dos constantes de gran importancia: la energía crítica y la longitud de radiación. Podemos definir la energía crítica como aquella para la cual las pérdidas de energía por radiación son iguales a las debidas a la ionización. Definimos la longitud de radiación como la distancia que necesita un electrón para penetrar en un bloque de materia de manera que su energía se reduzca en un factor  $e^{-1}$ .

### B.2.3 Dispersión de partículas cargadas

Cuando una partícula cargada atraviesa un bloque de materia, no solamente ocurren colisiones inelásticas con los electrones sino también colisiones coulombianas con el núcleo. Estos procesos dan lugar básicamente a un cambio en la trayectoria de la partícula. A pequeños ángulos de dispersión, una buena aproximación para la desviación angular es una distribución gaussiana.

### B.2.4 Interacciones de los fotones con la materia

Existen tres tipos de interacciones de los fotones con la materia, dominando cada uno en un rango diferente de energía. El efecto fotoeléctrico es dominante a energías pequeñas, hasta  $500\text{ keV}$ , mientras que el de producción de pares es dominante a alta energía, mayor que  $50\text{ MeV}$ . La dispersión Compton domina en el rango intermedio de energías.

El efecto fotoeléctrico tiene lugar cuando un fotón de energía  $k = h\nu$  atraviesa un bloque de materia y es absorbido por un electrón de la capa atómica. Si la energía del fotón es mayor que la energía de ligadura, el átomo se ioniza y se crea un electrón libre.

El proceso de creación de pares  $e^+e^-$  sólo puede ocurrir, por razones cinemáticas, a energías mayores que dos veces la masa de un electrón. Definimos el recorrido libre medio  $\lambda_{pair}$  como la distancia que un fotón tiene que atravesar para convertirse en un par  $e^+e^-$ .



### B.2.5 Cascadas electromagnéticas

Cuando un fotón o un electrón incide sobre un bloque de materia, se desarrolla una cascada electromagnética como resultado de la combinación de los procesos de *bremstrahlung* y de la producción de pares. Si, por ejemplo, un electrón incide sobre un bloque de materia con una energía mucho mayor que la energía crítica de ese material, el mecanismo de pérdida de energía dominante será la radiación. Por tanto se emitirá un fotón, que a su vez se convertirá en un par  $e^+e^-$  y así sucesivamente hasta que la energía sea menor que la energía crítica.

La energía perdida por ionización puede ser calculada gracias a programas de Monte Carlo pero básicamente es proporcional al recorrido total medio atravesado por las partículas de la cascada, es decir del orden de  $E_0/E_c$ , donde  $E_0$  es la energía del electrón incidente. De este modo, conociendo la energía perdida por ionización, recogida en el calorímetro, y conociendo la energía crítica, se puede calcular la energía del electrón incidente.

### B.2.6 Cascadas hadrónicas

El proceso de las cascadas hadrónicas está dominado por una sucesión de interacciones hadrónicas inelásticas. Están caracterizadas por la producción de múltiples partículas ( $\pi^0, \pi^\pm, K, \dots$ ) y la emisión de partículas procedentes de la desintegración nuclear de los núcleos excitados. Existe una componente electromagnética en las cascadas hadrónicas, debido a la frecuente creación de piones neutros.

## B.3 Calorímetro electromagnético de ATLAS

### B.3.1 Descripción del módulo

El calorímetro electromagnético es un calorímetro de muestreo cuyo material activo es el argón líquido, mientras que el pasivo es el plomo. Posee una alta granularidad y una geometría en forma de acordeón. El calorímetro electromagnético está dividido en dos partes, un barril y dos tapones. Adicionalmente, debido a las dos longitudes de radiación de material existentes enfrente del calorímetro (incluyendo el solenoide y el criotato), se usa un *presampler* con el fin de corregir por la pérdida de energía en la región  $\eta < 1.375$ .

A continuación limitaremos la descripción del calorímetro a los tapones o ruedas, los cuales son el tema de esta tesis.

La geometría en forma de acordeón fue escogida con el fin de construir un calorímetro

hermético. Una de las consecuencias de esta elección fue la necesidad de dividir el tapón en dos ruedas: la rueda interna, que cubre un rango de pseudorapidez entre  $\eta = 2.5$  y  $\eta = 3.2$ , y la rueda externa, cuyo rango se extiende entre  $\eta = 1.375$  y  $\eta = 2.5$ . Ambas ruedas están construidas con *absorbers* de plomo y acero intercalados con electrodos, todo ello con geometría de acordeón. Hay 768 electrodos y *absorbers* en la rueda externa, mientras que hay 256 en la interna. Para separar los electrodos y los *absorbers* se usan unos espaciadores o *spacers* con una estructura de nido de abejas, dando lugar a *gaps* de aproximadamente 4 mm. Una vez que el módulo está dentro del criostato, se llenan estos *gaps* con argón líquido.

La colaboración ATLAS escogió el plomo como material pasivo debido principalmente a su longitud de radiación de 0.56 cm, que permite un calorímetro compacto, y a su baja energía crítica. Entre las numerosas ventajas de usar argón líquido como material activo cabe destacar la baja energía para producir un electrón de ionización, su resistencia a las radiaciones y su bajo precio (comparado con el kriptón).

Las partículas incidentes depositarán la mayor parte de su energía en el *absorber*, dando lugar a una cascada electromagnética, cuyo número total de electrones será proporcional a la energía incidente. Estas partículas atravesarán el argón líquido, ionizándolo. De esta forma se crearán pares de electrones-iones, los cuales, debido al campo eléctrico, derivarán hacia el electrodo, donde se detectará la cascada. Con el fin de que la respuesta del calorímetro sea uniforme se necesita un alto voltaje que varíe uniformemente con  $\eta$ . Debido a razones técnicas, se ha escogido un alto voltaje que sigue una función escalón, definiendo siete zonas de alto voltaje en la rueda externa y dos en la interna.

Con respecto a la resolución energética, la colaboración ATLAS impuso que el término de muestreo fuera alrededor del 10%, el de ruido 400 MeV y el término constante aproximadamente 0.7%.

### B.3.2 Componentes mecánicos

Los *absorbers* de la rueda grande (pequeña) están hechos de placas de plomo de 1.7 mm (resp. 2.2 mm) de espesor y con forma de acordeón envueltas en placas de acero inoxidable de espesor 0.2 mm para asegurar la rigidez del conjunto. Las placas están pegadas gracias a un material compuesto llamado *prepreg*.

Para que la contribución al término constante sea menor del 0.3 %, se han impuesto tolerancias estrictas en el espesor de los *absorbers*, para lo cual se han realizado análisis durante toda la cadena de producción. Adicionalmente, se han pegado unas barras transversales a cada lado del *absorber*, con el fin de aumentar su rigidez y ayudar al posicionamiento de los *absorbers* con una precisión del orden de 0.1 mm.

Los electrodos de lectura de la señal son circuitos impresos flexibles con la misma geometría que los *absorbers*. Están formados por tres capas de cobre aisladas por dos hojas de poliamida de kaptón. La capa interna de cobre permite la recolección de la señal por acoplamiento capacitivo, mientras que las capas externas de cobre definen el alto voltaje. La estructura del circuito de cobre impreso en la capa de señal determina la segmentación del detector en  $\eta$  y en profundidad. De este modo, se definen tres secciones en profundidad, llamadas delantera, central y trasera.

Los espaciadores se usan con el fin de mantener cada electrodo centrado entre dos *absorbers* consecutivos. Están formados por celdas hexagonales, realizadas con papel NOMEX impregnado con resina *phenolic*.

### B.3.3 Montaje de los módulos

El montaje de los módulos tiene lugar en una sala limpia sellada. El peso total del detector se soporta principalmente con dos grandes anillos externos de aluminio. Adicionalmente se usan dos anillos intermedios en  $\eta = 2.5$  con el fin de minimizar el hueco entre la rueda externa e interna.

Como primer paso del montaje se aspira y se limpia con alcohol un *absorber*, situándolo seguidamente en la estructura, con la ayuda de un equipo elevador con ventosas. Se fija la posición de cada *absorber* mediante la inserción de pines y tornillos en los anillos de soporte. Seguidamente se coloca una primera capa de espaciadores, los cuales han sido sometidos a una prueba de voltaje. Después se coloca un electrodo que ha sido aspirado y limpiado con alcohol. Finalmente se añade otra capa de espaciadores y un *absorber*, completando de esta manera un primer gap. El resto del módulo se construye de la misma forma.

Una vez construídos todos los módulos, son integrados en las dos ruedas del calorímetro electromagnético.

### B.3.4 La electrónica

Se conectan dos tipos de tarjetas a los conectores de los electrodos: las tarjetas de alto voltaje y las sumadoras. Las primeras distribuyen el alto voltaje a los sectores en  $\phi$ , que consisten en 24 (8) electrodos en la rueda grande (pequeña respectivamente). Las tarjetas sumatorias definen la granularidad en  $\phi$  al sumar la señal de 3 (4) electrodos en la sección central y trasera en la rueda grande (resp. pequeña) y 12 electrodos en la sección delantera.

A continuación se conectan las tarjetas madre sobre las tarjetas sumatorias. Estas tarjetas madre distribuyen la señal física y aseguran la distribución de las señales de calibración

a través de una red de resistencias.

La electrónica caliente corresponde a la parte de la electrónica instalada en el exterior del criostato. Los cables de señal salen desde las tarjetas madre hacia el exterior, donde se encuentra la llamada *front end crate*, *FEC*. Esta contiene diversos tipos de tarjetas, como las *FEBs* y las tarjetas de calibración. Las primeras amplifican, dan forma, almacenan y digitalizan la señal. Las tarjetas de calibración, por su parte, generan los pulsos de calibración con gran precisión, de forma que la contribución al término constante de la resolución energética sea lo menor posible.

### B.3.5 Pruebas de validación de los módulos

Con el fin de controlar la calidad del montaje se han realizado una serie de pruebas, tanto a nivel mecánico como eléctrico.

En primer lugar, cada vez que se coloca un nuevo *absorber* se mide la altura relativa de cada onda a lo largo de cuatro líneas equidistantes, perpendiculares a la sección delantera. De esta manera se controlan las posibles deformaciones mecánicas del detector.

Adicionalmente se realizan tests de alto voltaje sobre cada gap, con el fin de comprobar la ausencia de impurezas en el gap y que soporta el voltaje nominal previsto cuando esté lleno de argón líquido. Estos tests de alto voltaje se repiten sobre diversos gaps conjuntamente a lo largo de todo el montaje. Así por ejemplo, se realizan pruebas de alto voltaje cada noche sobre los gaps montados durante ese día, cada fin de semana y se lleva a cabo un test final una vez el módulo se ha completado.

Otra prueba realizada es el test de baja frecuencia, el cual permite averiguar si algún conector o resistencia del electrodo está dañado.

Con el fin de controlar la uniformidad de la anchura del gap e identificar posibles problemas geométricos se han medido las capacidades del gap (*CAPA GAP*), una vez se ha construido todo el módulo. Adicionalmente, también se han medido las capacidades e inductancias de cada celda.

Todos estas pruebas son llevadas a cabo en los lugares de montaje. Una vez que los módulos están en el CERN, se realizan otros tests, como, por ejemplo, tests de alto voltaje adicionales y medidas de las resistencias.

## B.4 Estudios de la uniformidad

### B.4.1 Pruebas con el haz

De los 16 módulos EMEC de producción construidos en Marsella y en Madrid, tres fueron sometidos a pruebas con haces de electrones, con el fin de analizar la reproducibilidad de la respuesta y controlar la calidad de la producción de los detectores. Los módulos ECC0 (de Marsella) y ECC1 (de Madrid) fueron analizados en el verano del 2001 en la línea de haz H6 del CERN SPS, mientras que el módulo ECC5 (de Marsella) fue sometido a los haces de electrones en mayo-junio del 2002.

Para estudiar la respuesta del calorímetro en función del punto de incidencia se usó un haz de electrones de 120 GeV. Durante las pruebas se insertó el módulo en un criostato y se llenó con argón líquido. El uso de cámaras proporcionales y centelladores permitía seleccionar a los electrones entre las diversas partículas posibles así como medir las trayectorias y los tiempos de llegada,  $t_{tdc}$ .

Durante las pruebas con haces de electrones se tomaron datos de física así como pedestales, los cuales permiten medir el ruido de cada canal de la electrónica de lectura. Adicionalmente, se realizaron dos tipos de calibración: los llamados *delay runs*, en los cuales la amplitud del pulso de calibración es fija y el tiempo de inicio del pulso varía, y los *ramp runs*, donde el tiempo de inicio es fijo pero se varía la amplitud.

### B.4.2 Reconstrucción de la señal

Cuando una partícula atraviesa el calorímetro ioniza a los electrones del argón líquido, produciendo así una señal de ionización cuya forma es triangular. Cada celda del detector se puede representar como una capacidad  $C_d$  y una inductancia  $L_d$ . La señal de ionización es amplificada y modelada con un filtro multi-ganancia  $CR - RC$ . A continuación se realiza un muestreo de la señal cada 25 ns, de forma que al final se obtienen 7 muestras para cada una de las dos ganancias. Los pulsos de física se obtienen representando las muestras en función del tiempo reconstruido como  $t_{reco} = 25 \times i_{muestra} - t_{tdc}$ , donde  $t_{tdc}$  toma valores entre 0 y 24 ns e  $i_{muestra}$  es el número de las 7 muestras de la señal.

La señal de calibración producida en la tarjeta de calibración tiene una forma exponencial y se inyecta en las tarjetas madre, recorriendo luego el mismo camino que la señal de ionización. De este modo se obtienen de nuevo 7 muestras para cada señal de calibración. El pulso de calibración se obtiene representando estas muestras en función de  $25 \times i_{muestra} - t_{delay}$ , donde  $t_{delay}$  el tiempo de retraso de la inyección de la señal de calibración.

Dado que el máximo de la señal formada es proporcional a la energía depositada en una

celda, es muy importante reconstruir este máximo a partir de los puntos de muestreo con el fin de medir la energía depositada en el calorímetro. Hemos considerado principalmente dos métodos de reconstrucción de la señal, el *parabola fitting* y el *optimal filtering*. En el primer método se hace un ajuste parabólico a las tres muestras con mayor amplitud. La desventaja asociada a este procedimiento es una dependencia residual de la amplitud con el  $t_{tdc}$ . En el método de *optimal filtering*, el cual se usará a lo largo de esta tesis, se calcula el máximo de la señal a partir de una suma ponderada de las amplitudes de las muestras, minimizando la contribución del ruido. Para hacer uso de este método es necesario conocer la forma del pulso de física.

Sin embargo, la forma del pulso de física solamente se conoce para las celdas de los tres módulos sometidos a haces de electrones. Para solucionar este problema, se ha desarrollado un método que reconstruye el pulso de física a partir del pulso de calibración. En este procedimiento se toma en cuenta el hecho de que tanto el pulso de calibración como el de física recorren una parte común de la electrónica de lectura, evitando así tener que realizar una descripción eléctrica completa de todo el circuito.

Se han usado diversos tratamientos matemáticos para obtener la predicción del pulso de física a partir del de calibración, como por ejemplo realizar una transformada de Laplace inversa seguida de una integral numérica o realizar una transformada de Fourier inversa. Los parámetros desconocidos que intervienen en las expresiones se obtienen ajustando la predicción del pulso de física a los datos medidos en las pruebas con haces de electrones.

Una vez que hemos calculado el máximo de la señal de ionización mediante el uso del método de *optimal filtering* se aplican diversos factores para pasar de unidades ADC a unidades GeV. Con el fin de reconstruir la energía total de la cascada electromagnética, se define para las tres secciones, delantera, central y trasera, una ventana de celdas alrededor de la celda más energética de manera que toda la cascada esté contenida sin añadir ruido. La suma de las energías de las tres secciones será la energía depositada dentro del calorímetro.

### B.4.3 Análisis de la uniformidad

A continuación se presenta el análisis realizado por la Universidad Autónoma de Madrid (UAM) relativo a la uniformidad de los tres módulos sometidos a haces de electrones en el CERN. En este capítulo se ha usado el llamado método LAPP para la reconstrucción de la señal. En este método se discretizan los pulsos de calibración y la parte de la electrónica en el espacio de frecuencias de Fourier. El pulso predicho se ajusta a los datos medidos con los haces de electrones, obteniendo los parámetros desconocidos. Finalmente, mediante una transformada de Fourier inversa numérica se obtiene la predicción del pulso de física en el espacio de tiempo. Mediante este método se obtienen residuales de aproximadamente

1% alrededor del máximo del pulso.

Se ha analizado solamente la rueda externa, excluyendo zonas de no precisión, como, por ejemplo, los extremos en  $\eta$  y  $\phi$ .

#### B.4.4 Correcciones de la energía del electrón

Con el fin de reconstruir la energía de los electrones se deben aplicar varias correcciones, tanto a nivel de celda (correcciones de alto voltaje o de asimetría en  $\phi$ ) como a nivel de cluster (correcciones de fugas laterales y de modulación en  $\phi$ ).

- **Corrección de alto voltaje**

Conforme hemos explicado anteriormente, se ha adoptado, por razones técnicas, un alto voltaje que depende con  $\eta$  según una función escalón, definiendo así siete sectores de alto voltaje constante en la rueda externa. Como consecuencia, en cada sector la energía del cluster aumenta con  $\eta$ . Para corregir este efecto se usan unos pesos que son función de la pendiente de la energía en cada sector. Hemos desarrollado dos métodos para obtener dicha pendiente. En un primer método (método de los sectores independientes) ajustamos la energía en cada sector de alto voltaje a una recta, sin tener en cuenta los puntos cercanos a los extremos de cada sector. Seguidamente, se hace una segunda iteración. En el segundo método, de los sectores acoplados, se tiene en cuenta que en algunos sectores de HV hay pocos puntos, haciendo difícil obtener con precisión la pendiente. Para solucionarlo, se hace un ajuste conjuntamente a todas las regiones de alto voltaje y finalmente, se realiza de nuevo una segunda iteración.

Se ha comprobado que ambos métodos proporcionan resultados similares, obteniendo unas pendientes prácticamente independiente de  $\phi$  y de los módulos. Esto permite aplicar una corrección universal de alto voltaje. Para el resto del análisis hemos usado el método de los sectores acoplados.

- **Corrección con capacidades**

Se ha observado que la energía medida en el test beam muestra una inesperada no-uniformidad a lo largo de  $\phi$ , especialmente en los módulos ECC0 y ECC1. Además se ha comprobado que este efecto está correlacionado con las medidas de la capacidad en el sección central. Esto lleva a interpretar esta asimetría de la respuesta del calorímetro como una consecuencia de las fluctuaciones locales de la anchura del gap alrededor del valor nominal, las cuales se han generado durante el proceso de montaje. Para el módulo ECC0, este efecto se ha corregido con las medidas de la

capacidad de las celdas de la sección central, realizadas en el lugar de montaje para todo  $\eta$  y  $\phi$ . Para el caso del módulo ECC1 no se tomaron estas medidas, por lo cual se ha corregido esta asimetría en  $\phi$  con los datos del test beam. Por último, dado que las fluctuaciones gap a gap son muy pequeñas en el módulo ECC5, solamente se ha corregido en dicho módulo la pendiente global, mediante los datos medidos en las pruebas con haces de electrones. Adicionalmente se ha estudiado la corrección con las medidas de la capacidad realizadas en la rueda a  $\eta_{celda} = 39$ .

- **Corrección de las fugas laterales**

Debido al tamaño finito del cluster es posible que algunos electrones impacten fuera del centro de la celda central, dando lugar a fugas energéticas en los laterales del cluster. Este efecto, que aumenta con  $\eta$  debido a que el tamaño de la celda disminuye, se corrige mediante un ajuste parabólico.

- **Corrección de la modulación en  $\phi$**

La geometría en forma de acordeón introduce no-uniformidades a lo largo de  $\phi$  en el campo eléctrico dentro del gap entre dos absorbers consecutivos. Esto da lugar a no-uniformidades periódicas en la energía del cluster a lo largo de  $\phi$ . El ajuste a un polinomio de Fourier con cinco parámetros corrige este efecto. Se observa que el acuerdo entre módulos es muy bueno, permitiendo así una corrección universal.

### B.4.5 Resultados de la uniformidad

Hemos representado la energía reconstruida para cada cluster, después de aplicar todas las correcciones descritas anteriormente, en un histograma. La dispersión ( $\sigma / \langle E \rangle$ ) del ajuste a una gaussiana nos da el valor de la no-uniformidad de la respuesta del módulo. Adicionalmente también se ha estudiado la uniformidad en dos direcciones ortogonales,  $\eta$  y  $\phi$ . Como hemos dicho anteriormente, se ha corregido el módulo ECC0 con las medidas de capacidad realizadas en el lugar de montaje, el ECC1 con los datos del test beam y en el ECC5 solamente hemos corregido la pendiente con los datos. Todos los resultados están por debajo de 0.6%, como se requiere para ATLAS. Existe un buen acuerdo con el análisis independiente realizado por Marsella, salvo en el ECC5, debido a una corrección distinta de la asimetría en  $\phi$ .

Se observa una ligera anisotropía en el módulo, la cual es debida, por un lado, a que existen regiones a bajo y alto  $\eta$ , cerca de los cracks, que empeoran la uniformidad, y, por otro lado, a que el modo de corregir las fluctuaciones gap a gap influye en el resultado de la uniformidad. De hecho, hemos comprobado que si limitamos el rango en  $\eta$  a las zonas



de alta precisión y corregimos la asimetría en  $\phi$  con los datos medidos en el test beam, se obtiene que  $\sigma_\eta$  y  $\sigma_\phi$  toman valores muy similares, para todos los módulos.

Adicionalmente se han corregido los módulos ECC0 y ECC1 con las capacidades medidas en la rueda ECC. Se observa que no existe una diferencia apreciable en el ECC0 respecto a cuando se corrige con las capacidades medidas en el lugar de montaje. Para el ECC1, la uniformidad sigue siendo inferior a 0.6%.

## B.5 Dependencia con la reconstrucción de la señal

En el capítulo anterior hemos analizado el módulo ECC1 usando el método LAPP para la reconstrucción de la señal, el cual proporciona un nivel de descripción de aproximadamente 1% alrededor del máximo. A continuación se pretende analizar si este nivel de descripción de la señal es suficiente para estudiar la uniformidad y qué nivel se puede tolerar con el fin de que los resultados de uniformidad no se vean afectados. Para ello hemos estudiado el módulo ECC1 con tres posibles métodos desarrollados en Madrid.

### B.5.1 Diversos métodos

- **Método Hec**

En este método se realiza una transformada de Laplace inversa analítica y una integral numérica para obtener la predicción del pulso de física. Los parámetros desconocidos que intervienen en las expresiones se calculan mediante el ajuste a los datos medidos en las pruebas con haces de electrones. Entre ellos está la frecuencia  $\omega = \sqrt{\frac{1}{L_a C_a}}$ , cuyos valores ajustados son muy cercanos a los medidos con el *network analyser*. Este método tiene un residual máximo alrededor del 4.2%.

- **Método Hecref**

Con el fin de mejorar el método anterior, se han incluido reflexiones en las líneas de calibración y señal. Con esta modificación las frecuencias ajustadas están más de acuerdo con las medidas, y el residual máximo es aproximadamente 1.3%.

- **Método Hecref2 $\omega$**

La observación de una oscilación en los residuales de los métodos anteriores ha sugerido la existencia de una frecuencia adicional que no se había tomado en cuenta. Por ello en este método se ha añadido una componente LC adicional en el circuito. Esta nueva modificación da lugar a un residual máximo del 0.8%.

### B.5.2 Dependencia del TDC

A continuación hemos estudiado la dependencia de la energía de la ventana con el tiempo de llegada de las partículas, es decir, con  $t_{tdc}$ . Se ha representado la energía en función de dicho tiempo para los cuatro métodos estudiados a lo largo de esta tesis. Se observa que para el método Hec la energía tiene una dependencia no despreciable, pero es casi inexistente para los métodos Hecref2 $\omega$  y LAPP. De esta manera se puede concluir que la dependencia de la energía con el  $t_{tdc}$  disminuye con el residual  $r_{max}$ .

Esta dependencia puede ser parametrizada por un polinomio de segundo grado, cuya curvatura disminuye con el residual máximo. Se observa que la curvatura es ligeramente menor para el LAPP que para el método Hecref2 $\omega$ . Esto podría ser debido a que los residuales alrededor del pico del pulso son menores para el LAPP que para el Hecref2 $\omega$ , siendo este residual alrededor del máximo el que más contribuye a la curvatura.

### B.5.3 Dependencia de la uniformidad con la reconstrucción de la señal

A continuación se ha estudiado el módulo ECC1 con los tres métodos descritos anteriormente. Las correcciones aplicadas a la energía de los electrones son las mismas que las usadas en el capítulo anterior. Así pues se ha corregido por el alto voltaje mediante el método de los sectores acoplados, observando que todos los métodos estudiados de reconstrucción de la señal tienen un comportamiento similar. Lo mismo ocurre en la corrección de la modulación en  $\phi$  y de las fugas laterales en  $\eta$ . Para corregir por la asimetría en  $\phi$  hemos usado la energía medida en las pruebas con haces de electrones, como hicimos en el capítulo anterior.

Se observa que para todos los métodos de reconstrucción de la señal estudiados, se obtiene una uniformidad similar, siempre por debajo de 0.6%, independientemente del residual (cuyo máximo es menor que 4.2%).

## B.6 Conclusiones

A lo largo de toda la tesis se ha realizado un análisis detallado del calorímetro electromagnético de ATLAS.

En el capítulo tres hemos descrito en profundidad todos los pasos realizados en el montaje y en el cableado de los módulos, así como las pruebas de validación a las cuales han sido sometidos. Se ha mostrado que todo ha sido diseñado y realizado con la mayor precisión

posible, con el fin de no aumentar la no-uniformidad de los detectores.

La uniformidad de los módulos sometidos a haces de electrones (los módulos ECC0, ECC1 y ECC5) ha sido estudiada en el capítulo cuatro. Se ha usado el método LAPP para la reconstrucción de la señal. Para corregir el alto voltaje hemos desarrollado dos posibles métodos, los cuales proporcionan resultados similares. El efecto de modulación en  $\phi$  ha sido corregido mediante un polinomio de Fourier, mientras que las fugas laterales se han corregido con un ajuste parabólico. Adicionalmente, se ha comprobado que las medidas de la capacidad de las celdas del calorímetro permiten corregir una inesperada no-uniformidad observada a lo largo de  $\phi$ .

Los resultados de la no-uniformidad para todos los módulos se encuentran por debajo de 0.6%, lo cual está dentro de las especificaciones establecidas por el TDR. Adicionalmente se observa que la uniformidad sigue dentro de este margen incluso si corregimos con las medidas de la capacidad realizadas en la rueda ECC. Los resultados están de acuerdo con el análisis independiente realizado por CPPM. Se ha observado una pequeña anisotropía en la uniformidad a lo largo de dos direcciones ortogonales  $\eta$  y  $\phi$ , debida a los cracks a bajo y alto  $\eta$  y a la calidad de la corrección con las capacidades.

Con el fin de estudiar la dependencia de la uniformidad con el método de reconstrucción de la señal hemos desarrollado tres nuevos métodos, con diferente nivel de descripción de la señal. Se ha concluido que la dependencia de la energía con el TDC disminuye con el residual. Además se observa que los resultados de uniformidad son independientes del método de reconstrucción siempre y cuando los residuales estén por debajo del 4%.

# Bibliography

- [1] Mandl-Shaw, *Quantum Field Theory*, Wiley (1993).
- [2] *The Review of Particle Physics*, Particle Data Group (2006).
- [3] D. Decamp et al. (The ALEPH collaboration), *A precise determination of the number of families with light neutrinos and of the Z boson partial widths*, Phys. Letter B 539 (2002), 179-187.
- [4] M. Chemarin, *Number of neutrino families from LEP1 measurements.*, Nucl. Phys. Proc. Suppl. 85 (2000), 67-71.
- [5] P. W. Higgs, Phys. Lett. 12 (1964), 132.
- [6] G. Arnison et al., UA1 Collaboration, Phys. Lett. B122 (1983), 103.
- [7] ALEPH Collaboration, DELPHI Collaboration, L3 Collaboration, OPAL Collaboration and The LEP Working Group for Higgs Boson Searches, *Search for the Standard Model Higgs boson at LEP*, Phys. Lett. B565 (2003), 61-75.
- [8] The LEP Collaborations: ALEPH Collaboration, DELPHI Collaboration, L3 Collaboration, OPAL Collaboration, The LEP Electroweak Working Group, the SLD Electroweak, Heavy Flavour Groups, *A Combination of Preliminary Electroweak Measurements and Constraints on the Standard Model*, hep-ex/0312023.
- [9] *The Large Hadron cCollider*, CERN/AC/95-05 (1995).
- [10] *The ATLAS Technical Proposal*, CERN/LHCC/94-43 (1994).
- [11] The ATLAS Collaboration, *ATLAS Inner Detector Technical Design Report*, CERN/LHCC/97-17 (1997).
- [12] The ATLAS Collaboration, *Liquid Argon Calorimeter TDR*, CERN/LHCC/96-41 (1996).
- [13] The ATLAS Collaboration, *Tile Calorimeter TDR*, CERN/LHCC/97-17 (1997).

- [14] The ATLAS Collaboration, *Muon spectrometer TDR*, CERN/LHCC/97-22 (1997).
- [15] *ATLAS HLT, DAQ and DCS technical proposal*, Technical report, CERN (2000).
- [16] W. R. Leo, *Techniques for nuclear and particle physics experiments*, SpringerVerlag Berlin Heidelberg (1987).
- [17] R. M. Sternheimer, S. M. Seltzer, M. J. Berger, *Phys. Rev. B* 26, 6067 (1982).
- [18] J. Jackson, *Classical Electrodynamics*, New-York: Wiley (1962).
- [19] H. Bethe, J. Ashkin, *Experimental particle physics*, Cambridge University Press, (1986).
- [20] H. Bethe, J. Ashkin, *Passage of Radiations through Matter in Experimental Nuclear Physics*, Vol 1, ed. by E. Segre, John Wiley & Sons, New-York (1953).
- [21] R. Fernow, *Introduction to experimental particle physics*, Cambridge University Press (1986).
- [22] J. del Peso, E. Ros, *NIM A* 276 (1989) 456.
- [23] *Calorimeter performance TDR*, CERN/LHCC/96-40 (1996)
- [24] A. Chekhtman, D. Fouchez, E. Monnier, *The Accordion in the end-cap: geometry and characteristics*, ATLAS-LARG-NO-4 (1994).
- [25] O. Martin, E. Monnier, S. Tisserant, *Update of some Geometrical Parameters for the ATLAS EM End-Cap Calorimeter*, ATLAS-LARG-NO-47 (1996).
- [26] S. G. Klimenko, Yu. A. Tikhonov, A. I. Chekhtman, *The design of End-Cap EM Calorimeter with constant thickness of the absorber plates*, ATLAS Internal NOTE LARG-NO-025 (1995).
- [27] ATLAS Collaboration, *Performance of the End-Cap Module 0 of the ATLAS Electromagnetic Calorimeter*, Nucl. Inst. and Methods A500 (2003) 178-201.
- [28] F. Djama, *Using  $Z^0 \rightarrow e^+e^-$  for Electromagnetic Calorimeter Calibration*, ATLAS-LARG-2004-008 (2004).
- [29] B. Canton et al., *Analysis and results of the measurements of the plate thickness, done at the factory, during the production of the lead for the module 0 of the barrel and end-cap ATLAS electromagnetic calorimeter*, ATL-LARG-1997-076 (1997).
- [30] G. García et al., *NIM A*418 (1998) 513-521.

- [31] G. García, *Lead absorber production for the end-cap module 0*, ATL-LARG-1997-076 (1997).
- [32] G. García, *Two different cases of calorimetry in High Energy Physics: The ATLAS liquid argon electromagnetic end cap and the ZEUS Forward Plug Calorimeter*, Ph.D. Thesis, DESY-THESIS-200-010 (March 2000).
- [33] P. Romero, *Sobre algunos aspectos del diseño y construcción del calorímetro electro-magnético de argón líquido del experimento ATLAS*, Ph.D. Thesis (June 2000).
- [34] L. Labarga, P. Romero, *Analysis of the quality control measurements performed on the absorbers produced for the module 0 of the ATLAS Electromagnetic End-Cap Calorimeter*, ATL-LARG-1999-004 (1999).
- [35] F. Djama, L. Hervás, C.P. Marin, *Copper-polyimide multilayer electrodes for the end-cap electromagnetic calorimeter*, ATL-LARG-1998-088 (1998).
- [36] P. Dargent, F. Djama, *Bending of end-cap electrodes*, ATL-LARG-1998-108 (1998).
- [37] B. Aubert et al., *Development and construction of large size signal electrodes for the ATLAS electromagnetic calorimeter*, CERN-PH-EP/2004-019 (2004).
- [38] W. Bonivento, D. Lacour, *Acceptable values of resistances on electrodes of the ATLAS EM calorimeter*, ATL-LARG-1999-019 (1999).
- [39] ATLAS Electromagnetic Liquid Calorimeter Group, *Performance of the Barrel Module 0 of the ATLAS Electromagnetic Calorimeter*, Nucl. Inst. and Methods A500 (2003), 202.
- [40] J. Colas et al., *The LArg calorimeter calibration board*, ATL-LARG-2000-006 (2000).
- [41] P. Pralavorio and D. Sauvage, *Review of the cross-talk in the module 0 of the Electromagnetic End-Cap Calorimeter Cross-Talk*, ATL-LARG-2001-006 (2001).
- [42] P. Barrillon et al., *Electrical tests for the validation of the electromagnetic end-cap calorimeter modules*, ATL-LARG-2003-004 (2003).
- [43] N. Massol et al., *Test bench of the barrel calorimeter modules*, ATL-LARG-2001-007 (2001).
- [44] N. Massol, *These de l'Université de Savoie*, april 2000, LAPP-T-2000/02 (2000).
- [45] A.F. Barfuss, P. Pralavorio, *Analysis of electrical measurements of ATLAS Electromagnetic End-Cap Calorimeter*, Presentation at LAr week (September 2004).

- [46] L. Hinz, *Étude expérimentale des performances du module 0 du calorimètre électromagnétique bouchon d'ATLAS*, Thèse de doctorat de l'Université de la Méditerranée (June 2001).
- [47] P. Barrillon, *Construction du calorimètre électromagnétique d'ATLAS et études de ses performances*, Thèse de doctorat de l'Université Claude Bernard Lyon (September 2002).
- [48] P. Barrillon et al., *Uniformity Scan in the Outer Wheel of the Electromagnetic End-Cap Calorimeter*, ATL-LARG-2001-012 (2001).
- [49] H. Burkhardt, et al., *Nucl. Inst and Meth.*, A268 (1988) 116
- [50] M. Chalifour, et al., *Cryogenic system for the test facilities of the ATLAS liquid argon calorimeter modules*, CERN-LHC-Project-Report-23
- [51] L. Neukermans, P. Perrodo and R. Zitoun, *Understanding the ATLAS electromagnetic barrel pulse shapes and the absolute electronic calibration*, ATLAS LARG Internal Note, ATL-LARG-2001-008 (February 2001).
- [52] W. E. Cleland and E.G. Stern, *Signal processing considerations for liquid ionization calorimeters in a high rate environment*, Nucl. Inst and Meth. A338 (1994) 467-497.
- [53] P. Barillon, F. Djama, L. Hinz, P. Pravalorio, *Signal reconstruction in module 0 of the end-cap electromagnetic calorimeter and presampler*, ATLAS LARG Internal Note, ATL-LARG-2001-022 (December 2002).
- [54] D. Banfi, M. Delmastro, M. Fanti, *Cell response equalization of the ATLAS electromagnetic calorimeter without the direct knowledge of the ionization signals*, ATLAS LARG Internal Note, ATL-LARG-2004-004 (May 2004).
- [55] M. Delmastro, *Private Communication*.
- [56] P. Perrodo, *Presentation at LAR week*.
- [57] F. Hubaut, C. Serfon, *Response uniformity of the ATLAS electromagnetic end-cap calorimeter*, ATL-LARG-2004-015 (2004).
- [58] J. P. Meyer, *Effect of new calibration on ECC5*, Presentation at LAr week (September 2003), EM general meeting.
- [59] [http://atlas.web.cern.ch/Atlas/GROUPS/LIQARGON/EM\\_Calo/TestBeam/www\\_emtb/ec\\_diagnostic/](http://atlas.web.cern.ch/Atlas/GROUPS/LIQARGON/EM_Calo/TestBeam/www_emtb/ec_diagnostic/).
- [60] B. Dekhissi et al., *Crosstalk in production modules of the electromagnetic end-cap calorimeter*, ATL-LARG-2003-012 (2003).

- [61] J. Schwindling, *Correction of Resistive Cross-Talk for ECC5*, Private Communication (2004).
- [62] S. Rodier, *The Atlas Liquid Argon Electromagnetic End-Cap Calorimeter: Construction and tests*, Ph.D. Thesis, CERN-THESIS-2004-001 (September 2003).
- [63] C. Oliver, J. del Peso, *Outer Wheel Uniformity of the Electromagnetic End-Cap Calorimeter*, ATL-LARG-PUB-2005-002 (2005).
- [64] C. Serfon, *Résultats des tests en faisceau sur les bouchons du calorimètre électromagnétique d'ATLAS. Séparation électrons-jets.*, Thèse de doctorat (September 2005).
- [65] F. Hubaut, C. Serfon, *Presentation at LAr week*, EM general meeting (March 2004).
- [66] J. del Peso, *Capa measurement on ECA2*, Presentation at LAr week (April 2003), EM general.
- [67] A. F. Barfuss, *Overview of capa and LC measurement*, Presentation at LAr week (September 2004), EM general.
- [68] J. del Peso, *Production and stacking in Madrid (Capacitance studies on ECA4)*, Presentation at LAr week (September 2003), EM general.
- [69] G. Garcia, *Data analysis of the ATLAS EMEC module 0 calorimeter September 1998 beam test*, ATL-LARG-1999-017 (1999)
- [70] L. Kurchaninov, *Calibration and Ionization Signals in the Hadronic End-Cap Calorimeter of ATLAS*, IX International Conference on Calorimetry in Particle Physics (October 2000), Annecy (France).
- [71] C. de la Taille, L. Serin, *Temperature dependance of the ATLAS electromagnetic calorimeter signal. Preliminary drift time measurement*, ATL-LARG-95-029.